# Vers des copolymères supramoléculaires multifonctionnels

Yunjie Xiang

## To cite this version:

Yunjie Xiang. Vers des copolymères supramoléculaires multifonctionnels. Other. Université de Strasbourg, 2014. English. NNT : 2014STRAF015 . tel-01423845

HAL Id: tel-01423845
https://theses.hal.science/tel-01423845v1

Submitted on 1 Jan 2017

# UNIVERSITÉ DE STRASBOURG

*ÉCOLE DOCTORALE DE SCIENCES CHIMIQUES*

INSTITUT CHARLES SADRON – UPR22

# THÈSE présentée par :

**Yunjie XIANG**

soutenue le : **08 Juillet 2014**

pour obtenir le grade de : **Docteur de l'université de Strasbourg**

Discipline/ Spécialité : Chimie Organique

# Towards Multifunctional Supramolecular Copolymers

**THÈSE dirigée par :**

| | |
|---|---|
| **Mr Giuseppone Nicolas** | Professeur, Université de Strasbourg, Institut Charles Sadron, Strasbourg |

**RAPPORTEURS :**

| | |
|---|---|
| **Mme PASC Andreea** | Maitre de conférences, SRSMC UMR 7565, Nancy |
| **Mr BOUTEILLER Laurent** | Directeur de recherche, UPMC – Paris 6, Ivry sur Seine |

---

**AUTRES MEMBRES DU JURY :**

| | |
|---|---|
| **Mr RAWISO Michel** | Directeur de recherche, Institut Charles Sadron, Strasbourg |

INSTITUT CHARLES SADRON

UNIVERSITÉ DE STRASBOURG

THÈSE

présentée pour obtenir le grade de

DOCTEUR de l'UNIVERSITÉ DE STRASBOURG

par

Yunjie XIANG

# Towards Multifunctional Supramolecular Copolymers

Soutenue publiquement le 08 juillet 2014 devant le jury composé de:

Docteur Andreea Pasc (SRSMC UMR 7565, Nancy) – Rapporteur externe

Docteur Laurent Bouteiller (Université Pierre et Marie Curie, Ivry sur Seine) – Rapporteur externe

Docteur Michel Rawiso (ICS – CNRS, Strasbourg) – Examinateur

Professeur Nicolas Giuseppone (ICS, Université de Strasbourg – CNRS, Strasbourg) – Directeur de thèse

# Résumé en Français

Un des défis majeurs auquel est aujourd'hui confrontée la chimie aux interfaces avec la physique et la science des matériaux est de concevoir des systèmes fonctionnels à l'échelle mésoscopique.[1] Pour atteindre cet objectif, deux approches complémentaires majeures ont été envisagées. La première repose sur une stratégie « top-down », illustrée par des techniques comme la lithographie, la microfluidique, l'impression par microcontact, etc…[2] La seconde se fonde sur une approche dite « bottom-up » qui utilise l'auto-assemblage de molécules et permet la construction d'édifices à partir du nanomètre et jusqu'au micromètre.[3]

En pratique, pour contrôler ces systèmes, les outils de la Chimie Supramoléculaire[4] s'avèrent puissants et représenteront certainement une des technologies clef du 21e siècle. D'importants concepts comme l'auto-assemblage moléculaire, le repliement, la reconnaissance moléculaire, la chimie « hôte – invité », les architectures moléculaires mécaniquement entrelacées ou encore la chimie covalente dynamique sont fondés sur la chimie supramoléculaire. Les polymères supramoléculaires sont formés et contrôlés par la thermodynamique et la cinétique des associations non-covalentes intermoléculaires. De façon intéressante, ces matériaux devraient in fine être capables de combiner les propriétés des polymères conventionnels et les capacités de réversibilité et de réponse à l'environnement, conduisant à des propriétés d'adaptation et de réparation.

Parmi les questions les plus fondamentales posées par l'approche « bottom-up », l'une d'entre elles concerne la nanostructuration dynamique des molécules afin de produire des objets multifonctionnels.[5] Les copolymères supramoléculaires multifonctionnels peuvent être synthétisés en combinant ensemble différents monomères fonctionnels ou en mixant plusieurs polymères supramoléculaires fonctionnels. Si les espèces mixées conduisent à des objets incorporant simultanément les différents monomères, ce phénomène est connu sous le nom de « Social Self-Sorting » (triage de type social). Cependant, si le mélange des différentes espèces conduit à des objets distincts composés d'un monomère unique, ce processus est appelé « Narcissistic Self-Sorting » (triage narcissique).[6]

---

[1] «*There's plenty of room at the bottom*»: transcript of the classic talk that Richard Feynman gave on December 29th 1959 at the annual meeting of the *American Physical Society* at the *California Institute of Technology*.

[2] a) D. S. Ginger, H. Zhang, C. A. Mirkin, *Angew. Chem. Int. Ed.* **2004**, *43*, 30; b) P. Gartseki, M. J. Fuerstman, H. A. Stone, G. M. Whitesides, *Lab on a Chip*, **2006**, *6*, 207.

[3] G. M. Withesides, B. Grzybowski, *Science* **2002**, *295*, 2418.

[4] J.-M. Lehn, *Supramolecular Chemistry: Concepts and Perspectives* VCH, **1995**, New York.

[5] a) A. Pal, S. Karthikeyan and R. P. Sijbesma, *J. Am. Chem. Soc.* **2010**, *132*, 7842–7843; b) X. Zhang, Z. Chen and F. Würthner, *J. Am. Chem. Soc.* **2007**, *129*, 4886-4887.

[6] M. M. Safont Sempere, G. Fernandez and F. Würthner, *Chem. Rev.* **2011**, *111*, 5784-5814.

L'objectif de mon travail de thèse a consisté à développer une approche combinatoire dynamique utilisant des monomères présentant un cœur bis-urée ou pérylène bisimide (PBI) afin de comprendre la structuration des auto-assemblages constitués de divers monomères supramoléculaires fonctionnels et d'explorer potentiellement leur applications (Figure I). En utilisant diverses techniques de caractérisation physiques et physico-chimiques telles que la RMN, les spectroscopies U.V., I.R. voire de fluorescence, les microscopies TEM, SEM et AFM) et les mesures de diffusion du rayonnement (SANS, SAXS, SLS et DLS), nous avons étudié les morphologies et les propriétés des polymères supramoléculaires formés à partir de ces unités de base lorsqu'elles étaient décorées par divers groupements latéraux pouvant servir d'unité de structuration (PEG), de fluorescence ($Cy_3$ et $Cy_5$) ou de bioreconnaissance (peptides).

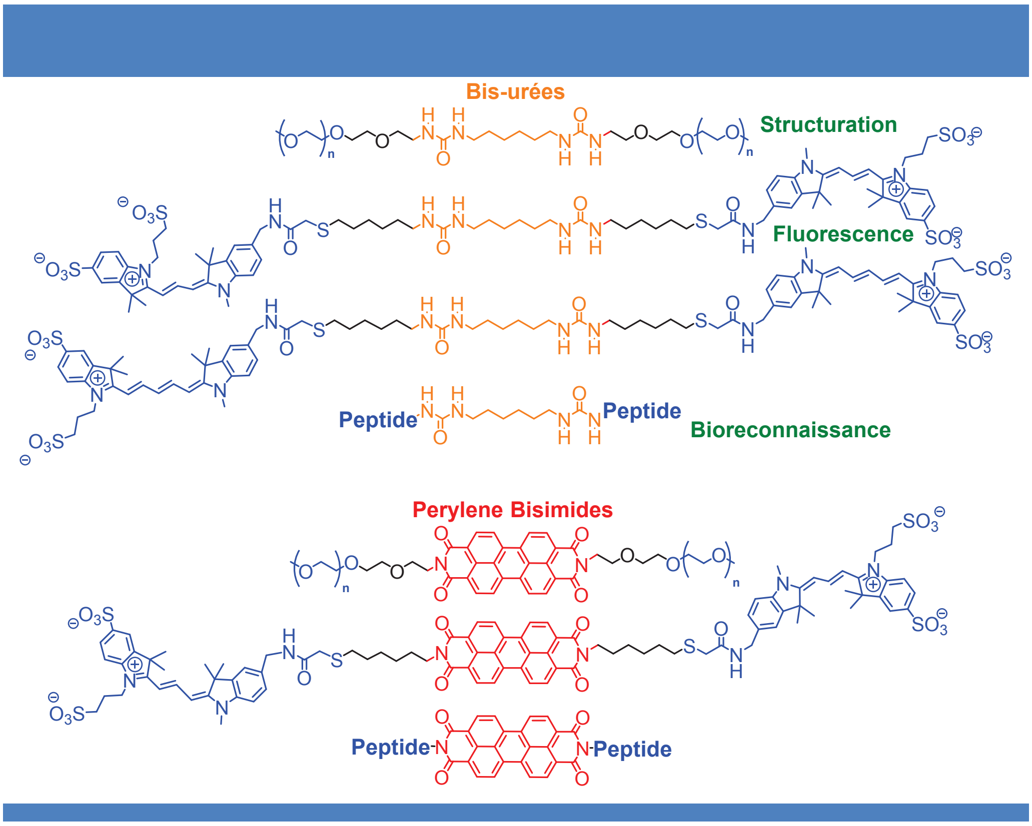

**Figure I** Structures chimiques des dérivés bis-urées et pérylènes bisimides.

Après avoir étudié individuellement tous les polymères obtenus à partir d'un monomère unique, nous avons commencé l'étude de leur comportement en mélange (uniquement pour la série bis-urée) afin d'étudier de possible changements de morphologies et/ou de propriétés. En particulier, nous avons souhaité utiliser le phénomène de FRET (Förster Resonance Energy Transfer) entre les cyanines $Cy_3$ et $Cy_5$ pour mieux comprendre les co-auto-assemblages.

Ce manuscrit de thèse est divisé en deux grands chapitres: une partie bibliographique divisée en 4 sous-parties et une partie "Résultats" divisée en 3 sous-parties et accompagnée d'une partie expérimentale décrivant les diverses techniques utilisées et les protocoles de synthèse.

La première partie correspond à un survol des concepts et des précédents récents de la littérature en relation avec le projet décrit ci-dessus. Les diverses interactions supramoléculaires intervenant dans les processus de polymérisation supramoléculaire, la caractérisation de ces polymères et leurs possibles applications sont décrites dans une première sous-partie. Les polymères supramoléculaires incorporant les motifs bis-urées et PBI sont ensuite présentés dans deux chapitres distincts. Une attention particulière est portée à la formation des auto-assemblages dans l'eau. Enfin, une quatrième sous-partie décrit les divers co-auto-assemblages supramoléculaires connus et principalement basés sur des motifs de reconnaissance de type bis-urée et benzène tricarboxamide (BTA). Seuls quelques rares exemples sont connus pour la formation de co-auto-assemblages utilisant le cœur PBI comme motif de reconnaissance.

Pour la partie "Résultats", le premier chapitre décrit la synthèse des diverses molécules nécessaires à ce projet. Plusieurs molécules présentant des cœurs bis-urées ou PBIs et incorporant diverses chaines latérales fonctionnelles ont été synthétisées (Figure I). Les molécules avec des chaines latérales PEG ont été obtenues pour deux longueurs de chaines différentes (n = 5 and 14). Pour les molécules avec des chaines latérales peptidiques, nous avons choisi la séquence AAAEEE qui était déjà connue pour induire la formation d'auto-assemblages.[7] Nous avons également introduit un espaceur hydrophobe entre le peptide et le cœur bis-urée ou PBI afin d'étudier son influence sur l'auto-assemblage. Pour les molécules avec des chaines latérales fluorescents, deux sondes de type cyanine $Cy_3$ et $Cy_5$[8] ont été accrochées sur le cœur bis-urées. Compte tenu de la complexité de la synthèse, seule la cyanine $Cy_3$ a été couplée au cœur PBI. Les structures de molécules obtenues après synthèse ont toutes été caractérisées par RMN du proton et du carbone ainsi que par spectrométrie de masse.

Le second chapitre de la partie "Résultats" concerne la caractérisation des auto-assemblages obtenus à partir des divers composes bis-urées dans différents systèmes de solvants et plus particulièrement dans l'eau, en utilisant les diverses techniques mentionnées précédemment. En particulier, nous avons démontré que les composés bisurée-PEG formaient

---

[7] E. T. Pashuck and S. I. Stupp *J. Am. Chem. Soc.* **2010**, *132*, 8819-8821.

[8] A. Toutchkine, P. Nalbant, and K. M. Hahn, Facile Synthesis of Thiol-Reactive Cy3 and Cy5 Derivatives with Enhanced Water Solubility. *Bioconjugate Chem.* **2002**, *13*, 387-391.

des auto-assemblages différents dans divers solvants (toluène, méthanol, acetonitrile, chloroforme et eau). En utilisant les techniques de diffusion des neutrons SANS et de la lumière SLS, nous avons démontré que les composés bisurée-PEG$_7$ et bisurée-PEG$_{16}$ conduisaient à des agrégats compacts dans l'eau et à des structures tubulaires dans le chloroforme alors qu'aucun auto-assemblage n'était observé dans l'acétonitrile, démontrant l'importance du solvant pour atteindre une morphologie précise (Figure II).

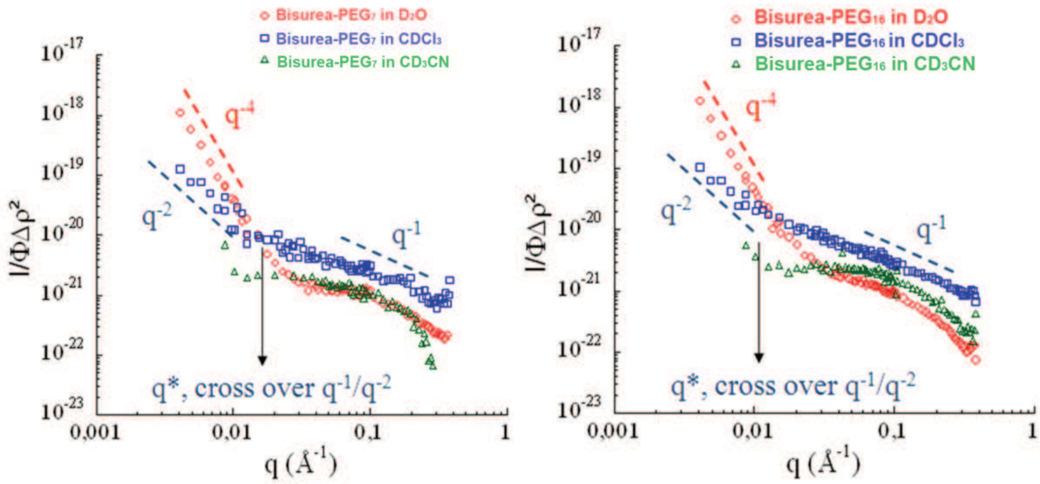

**Figure II** Spectres SANS des polymères supramoléculaires obtenus à partir de bisurée-PEG$_7$ (gauche) et bisurée-PEG$_{16}$ (droite) dans $D_2O$ (rouge), $CDCl_3$ (bleu), and $CD_3CN$ (vert).

Concernant les dérivés peptidiques et cyanines, pour des raisons de solubilité, leur comportement n'a été étudié que dans l'eau. La microscopie AFM démontre que la présence d'un espaceur entre la chaine peptidique et le cœur bis-urée joue un rôle important pour la structuration du système (Figure IIIa and IIIb), observations confirmées par les expériences SANS et LS (Figure IVa and IVb). Alors que des structures en feuillets ont été observées pour le composé bisurée-AAAEEE (Figure IIIa), les images AFM de l'auto-assemblage obtenu pour la molécule bisurée-espaceur-AAAEEE a révélé la présence de longues fibres branchées pouvant atteindre des longueurs micrométriques (Figure IIIb). Concernant le polymère supramoléculaire formé par la molécule bisurée-Cy$_3$, des rubans enroulés de plusieurs centaines de nanomètres ont été observés en milieu dilué, conduisant à l'enchevêtrement de ces rubans en structures tissées lorsque des plus fortes concentrations étaient utilisées (Figure IIIc). Les expériences de diffusion du rayonnement ont corroboré les observations effectuées par microscopie (Figure IV). Par ailleurs, les propriétés de fluorescence du compose bisurée-Cy$_3$ ont été étudiées.

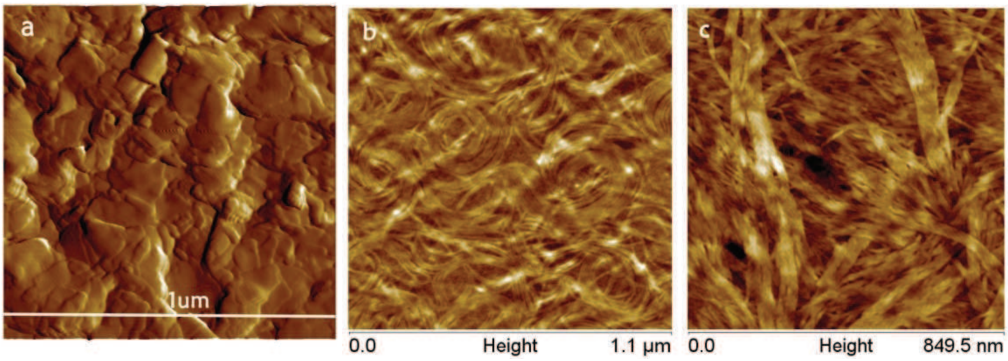

**Figure III** Images AFM des auto-assemblages obtenus pour les composés (a) bisurée-AAAEEE, (b) bisurée-espaceur-AAAEEE et (c) bisurea-Cy$_3$ dans l'eau.

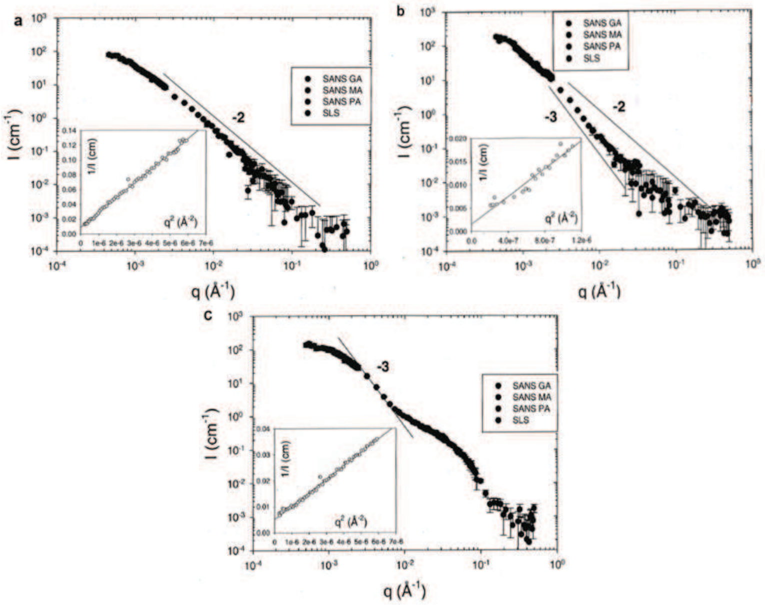

**Figure IV** Spectres SANS et SLS obtenus pour les auto-assemblages des composés (a) bisurée-AAAEEE, (b) bisurée-espaceur-AAAEEE et (c) bisurea-Cy$_3$ dans l'eau.

Nous avons également observé que les composés bisurée-AAAEEE, bisurée-Cy$_3$ et bisurée-Cy5 formaient des hydrogels à des concentrations critiques de gélation comprises entre 5 et 9% en masse en fonction de la molécule. Des études préliminaires ont démontré le caractère thermoréversible de ces gels. Cependant, des études plus approfondies du comportement en température (DSC) et des propriétés rhéologiques de ces matériaux doivent être réalisées afin de caractériser précisément ces matériaux. Enfin, ce deuxième chapitre se conclut sur les premiers résultats concernant la formation de co-auto-assemblages à partir de molécules de type bis-urée. En particulier, nous avons étudié les mélanges binaires faits de biurées-peptide et de bisurée-cyanine. Ces copolymères ont été étudiés par les analyses mentionnées précédemment. L'utilisation de la spectroscopie de fluorescence a permis de mettre en évidence la formation de co-auto-assemblages par un processus de "social self-sorting". Ces résultats ont été corroborés par des expériences de diffusion du rayonnement qui démontrent que la morphologie observée pour le mélange est dictée par le composé bisurée-$Cy_3$ (Figure V). Pour les mélanges bisurée-$Cy_3$ et bisurée-AAAEEE ou bisurée-espaceur-AAAEEE, la microscopie AFM a démontré que les morphologies observées initialement pour les monomères peptidiques n'étaient plus présentes, indiquant l'incorporation de ces unités au sein des polymères formés par les monomères bisurée-$Cy_3$.

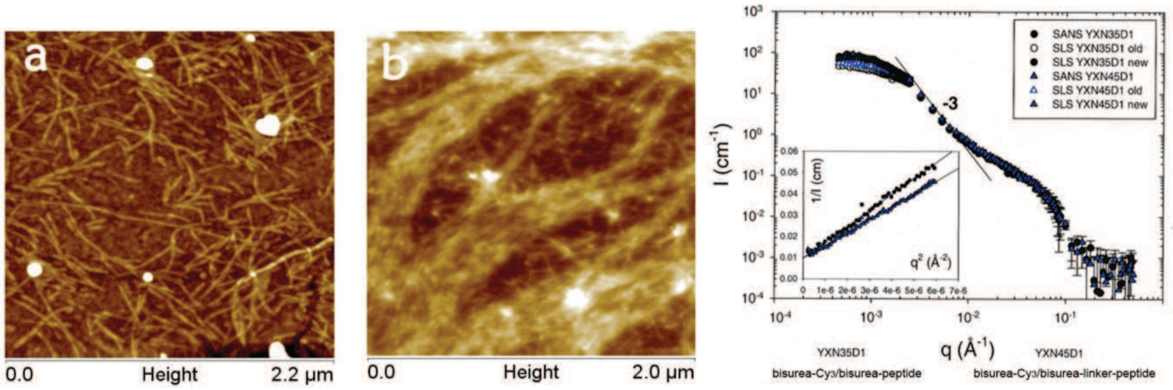

**Figure V** a, b: Images AFM des co-auto-assemblages observés pour les mélanges bisurée-AAAEEE/bisurée-$Cy_3$ (a) et bisurée-espaceur-AAAEEE/bisurée-$Cy_3$ (b) dans l'eau; c: Spectres SANS et SLS obtenus pour les mélanges bisurée-AAAEEE/bisurée-$Cy_3$ (YXN35D1) et bisurée-espaceur-AAAEEE/bisurée-$Cy_3$ (YXN45D1) dans l'eau.

De plus, une étude de fluorescence sur un mélange bisurée-$Cy_3$/bisurée-$Cy_5$ a mis en évidence l'intérêt de ce mélange pour l'étude des co-auto-assemblages. En effet, l'apparition d'un signal de FRET, caractéristique de la proximité spatiale des deux molécules, a été mise en évidence pour des concentrations de l'ordre de $10^{-4}$ M, suggérant également un phénomène de "social self-sorting" entre ces deux monomères.

Enfin, un troisième chapitre décrit les caractérisations des auto-assemblages obtenus pour les composés pérylènes bisimides. En particulier, nous avons étudié l'assemblage supramoléculaire et le comportement dynamique des composés PBIs-PEG en solution aqueuse en utilisant différentes techniques de diffusion du rayonnement (Figure VI).[9] En combinant des expériences de cinétique et en analysant l'effet de la température, de l'agitation et du vieillissement sur les solutions, nous avons démontré que les composés PBIs-PEG

---

[9] N. Jouault, Y. Xiang, E. Moulin, G. Fuks, N. Giuseppone and E. Buhler *Phys.Chem. Chem. Phys*, **2012**, *14*, 5718-5728.

s'auto-assemblaient spontanément en agrégats primaires composés d'un petit nombre de molécules. Ces agrégats primaires sont thermodynamiquement les objets les plus stables en solution et s'assemblent en agrégats denses de par l'interpénétration des chaines PEGs. Ensuite, au repos, ces nano-agrégats se dissocient lentement avec le temps en deux populations: agrégats primaires et agrégats moins denses encore présents en solution. De manière intéressante, l'agitation conduit à l'incorporation des agrégats primaires libres dans les assemblages globulaires.

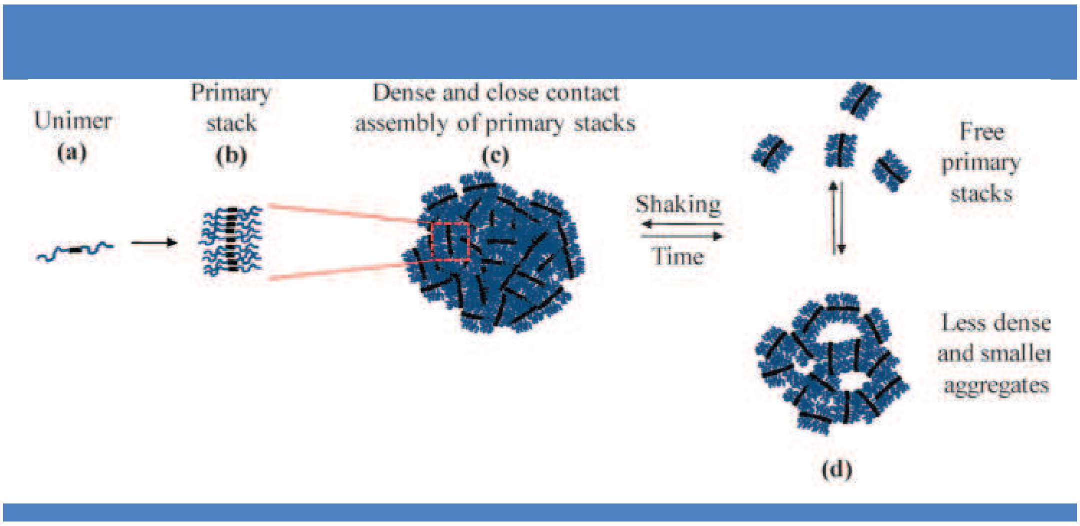

**Figure VI** Schéma décrivant l'effet du temps (ou, de façon équivalente, de la concentration) et de l'agitation sur la structure des systèmes PBIs-PEG.

Nous avons également démontré en utilisant la spectroscopie U.V. que ces composés PBI-PEGs s'auto-assemblaient selon un mécanisme coopératif dans les mélanges aqueux incorporant des solvants polaires comme le THF, le méthanol ou l'acétonitrile. Enfin, les composés PBI-peptides et PBI-Cy$_3$ ont été étudiés dans l'eau par spectroscopies U.V et de fluorescence, diffusion de la lumière et microscopie AFM, suggérant la présence d'agrégats de type H.

En résumé, ce travail enrichit le domaine encore peu étudié des co-auto-assemblages supramoléculaires et peut s'avérer prometteur pour l'obtention de copolymères supramoléculaires multifonctionnels. En effet, lorsque toutes les caractérisations des polymères et des gels présentés dans cette thèse auront été effectués, nous envisageons d'étendre ce travail à des combinaisons de 3 ou 4 monomères dans un même polymère et d'étudier la formation de copolymères à bloc supramoléculaires à partir des monomères pérylènes. De telles réalisations pourraient apporter de nouveaux outils pour construire des matériaux avancés purement organiques avec des applications potentielles dans le domaine de la médecine comme pour la bioreconnaissance ciblée. Les gels obtenus au cours de ces travaux pourraient être envisages comme matériaux thermosensibles pour le relargage, alors que les systèmes à base de pérylènes pourraient trouver des applications dans le domaine de l'électronique organique.

# ABSTRACT

Complex systems in Nature are an important source of inspiration for chemists who aim at mimicking biological nanostructures which are constructed from non-covalent interactions between building blocks and which follow hierarchical processes of organization. Because of their structure and dynamics, biological systems are able to respond and adapt to their environment, but also to multitask.

Supramolecular chemistry is a powerful tool to build artificial functional structures at mesoscale, following the so-called « bottom-up » approach going from nano- to micrometer scale by making use of programmed self-assembly of molecules. Among the most fundamental questions raised by this bottom-up approach, one rests on the use of dynamics of supramolecular nanostructures to produce multifunctional objects. Our goal in the present work is to understand the supramolecular organization and the possible dynamic rearrangement of multifunctional supramolecular copolymers.

To this end, we have developed a series of building blocks based on urea or perylene cores with various lateral side chains for combining structuring, fluorescence, and biorecognition properties in a single supramolecular polymer chain. Before going to mixtures of building blocks, we have first investigated the structures of supramolecular polymers based on a unique type of monomer. Using a combination of state-of-the-art analytical tools such as spectroscopy, scattering, and microscopy techniques, we have shown that molecules with a same core but different lateral chains can lead to the formation of various nanostructures such as, for instance, twisted ribbons, 2D plates, or branched fibers. We have also observed that solvent can be used to vary both the shape and size of self-assembled objects build from a same monomeric unit. Ultimately, by combining monomeric units with different functional side chains, multifunctional supramolecular copolymers have been obtained. Whereas scattering and imaging techniques were used to demonstrate that one of the monomer can dictate the formation of a preferential nanostructure, optical spectroscopies revealed that the polymerization process of our systems indeed occurs via social self-sorting.

The work reported in this manuscript is divided between two main parts: a) a bibliographical introduction on supramolecular polymers with a particular emphasis on the self-assemblies build from bisurea and perylene cores and, b) three chapters that cover the results obtained regarding the synthesis of the monomeric units (along with experimental protocols and characterization of the products) and the analyses of their self-assemblies and

co-self-assemblies using the aforementioned techniques.

# ACKNOWLEDGEMENTS

*First I would like to thank my PhD advisor Nicolas Giuseppone, Professor at the University of Strasbourg and director of the SAMS research group, where I was accepted to work. I have been grateful to work on the ambitious project he proposed me and I enjoyed the time we spent working, investigating, and thinking together. I thank him for the trust and encouragement he provided to me, for his patience, his knowledge, for the scientific formation and the advices I could benefit from his side, and for the multiple opportunities I was offered to improve and demonstrate my skills.*

*I greatly appreciated Dr. Emilie Moulin, permanent researcher of the SAMS team for her help, her advices, and the scientific and technical management she gave to me. She really helped me a lot and I appreciate all her help.*

*I thank Pr. J.M. Guenet, Director of Institute Charles Sadron, for his trust in the project and for greeting me inside the institute where I could benefit efficient facilities for my work.*

*I am grateful to Lemble Odile, Oberlé Virginie, and Lea Koch for the administrative support during my PhD period in the Institute Charles Sadron.*

*During my PhD work I was provided with various analysis equipments in ICS and I want to thank all the people in charge of these equipments, particularly Pr. Maaloum Mounir (AFM), Dr. Fuks Gad (TEM and SEM), and Dr. Yves Guilbert (NMR) and all the others.*

*I appreciated the collaboration of Pr. Eric Buhler and Dr. Nicolas Jouault from the university of Paris-Diderot 7 for light and neutron scattering experiments. Their scientific contribution allowed great advancements in the project.*

*I appreciated the technical support of Mélodie Archimbaud, Odile Gavat, and Celine Desvignes and I thank them for the daily work and maintaining of the SAMS laboratories.*

*I fully appreciated the good atmosphere in the SAMS team and thank all the people who had scientific or general discussion with me: Dr. Ruff Yves, Dr. Ellis Thomas, Dr. Busseron Eric, Dr. Domoto Yuya, Lutz Eric (PhD student), Dr. Misuraca Cristina, Wolf Adrian (PhD student), Armao Joe (PhD student), Li Quan (PhD student), Osypenko Artem (PhD student), Garavini Valentina (PhD student), Schneider Susanne (PhD student), Goujon Antoine (PhD student).*

*I also want to thank all the people from ICS for the advices and scientific discussions, and good moments we spared in the Institute: Dr. Lara Tauk, Dr. Johanna Davila, and other researchers and students who worked in ICS.*

*I would greatly thank my parents, my sister, and all the people in my family who encouraged me in my will to make this PhD.*

*I also thank my friends (Dr. Fuchao Jia, Dr. Yuefeng Liu, Dr. Jingjie Luo, Li Fu, Qing Cao, Ting Liang, Jing Feng, Xiaofeng Ling, Hebin Hu and et al.) for their help and all the good moments we spared in Strasbourg.*

*I want to thank the University of Strasbourg where I performed my PhD, the China Scholarship Council (CSC) and European Research Council (ERC) for funding my work for those four years.*

*Finally, I would like to thank Dr. Andreea PASC, Dr. Laurent BOUTEILLER and Dr.Michel RAWISO, for examinating my work and I am honoured by their attention.*

# ABBREVIATIONS AND SYMBOLS

| | |
|---|---|
| Å | ångström |
| Ac | acetyl |
| AcOH | acetic acid |
| $Ac_2O$ | acetic anhydride |
| Boc | *tert*-butyloxycarbonyl |
| °C | celsius degree |
| COSY | correlation spectroscopy |
| $\delta$ | chemical shift |
| DCM | dichloromethane |
| DIAD | diisopropylazodicarboxylate |
| DIPEA | diisopropylethylamine |
| DMF | dimethylformamide |
| DMSO | dimethylsulfoxide |
| DLS | dynamic light scattering |
| eq ou equiv. | equivalent |
| ESI-MS | mass spectrometry with electrospray ionization |
| EtOAc | ethyl acetate |
| FRET | Förster Resonance Energy Transfer |
| h | hour |
| HPLC | high performance liquid chromatography |
| HRMS | high resolution mass spectrometry |
| ITC | isothermal titration calorimetry |
| $J$ | coupling constant |
| K | Kelvin |
| $K_d$ | dissociation constant |
| L | liter |
| c | Contour length |
| LC/MS | liquid chromatography coupled to mass spectrometry |
| $\lambda_{max}$ | maximum of emission/absorption wavelength |
| MALDI-TOF | matrix-assisted laser desorption/ionization – time of flight |
| µL | microliter |
| µm | micrometer |
| MCH | methylcyclohexane |
| mL | milliliter |
| $M_L$ | linear mass density |
| µmol | micromole |
| mmol | millimole |
| MS | mass spectrometry |

| | |
|---|---|
| nm | nanometer |
| NMR | nuclear magnetic resonance |
| NMP | *N*-methylpyrrolidinone |
| NIR | near infrared |
| ppm | parts per million |
| PEG | poly(ethylene glycol) |
| PTCDA or PDA | perylene-3,4:9,10-tetracarboxylic acid dianhydride |
| PTCDI or PBI | perylene-3,4:9,10-tetracarboxylic acid diimide |
| $R_f$ | retardation factor |
| $R_g$ | gyration radius |
| $R_H$ | hydrodynamic radius |
| r.t. | room temperature |
| SAS | small angle scattering |
| SANS | small angle neutron scattering |
| SAXS | small angle X-ray scattering |
| SLS | static light scattering |
| T | temperature |
| TEA or $NEt_3$ | triethylamine |
| TEM | transmission electronic microscopy |
| TFA | trifluoroacetic acid |
| THF | tetrahydrofuran |
| TIPS | triisopropylsilane |
| TLC | thin layer chromatography |
| Ts | tosyl |
| UPLC | ultra performance liquid chromatography |
| UV | ultra-violet |
| Vis | visible |

# GENERAL INTRODUCTION AND OBJECTIVES

Compared to their covalent counterparts, supramolecular polymers present unique characteristics due to the reversible association of their monomers. Their stability being controlled by thermodynamics, the resulting materials can combine properties of conventional polymers with additional adaptive and self-healing properties. Another interesting aspect of these objects is their spontaneous formation by simple mixing of monomers which share complementary recognition units for supramolecular polymerization. Going further, one can think that by mixing several monomers sharing the same type of complementary recognition units, but having various pending functionalities, different kinds of polymers could be produced. In particular, supramolecular copolymers could be envisioned along such an approach, with the potentiality to access multifunctional co-self-assemblies having combined or enhanced properties. This approach is relatively recent in the literature and the work presented here contributes to produce the necessary fundamental knowledge to study and make use of such complex materials.

Our methodology will consist first in synthesizing a series of functional molecules among two families that share similar structuring units: *i*) bisurea for a polymerization using hydrogen bonds, and *ii*) perylene diimides for a polymerization using π-π stacking interactions. Within each series, structuring units have been decorated with either *i*) polyethylene glycol chains (for further structuration properties and water solubility, or *ii*) peptides (for further structuration properties and for their potential bioactivity), or *iii*) cyanine dyes (for their fluorescence properties).

In a second step, we will envision to produce supramolecular homopolymers from the various individual monomers and in order to characterize them and to use them as references for further studies within mixtures. In particular, we will analyze the stabilities and the morphologies of these supramolecular polymers by an extended set of physical-chemistry techniques such as NMR, U.V.-Vis, I.R., and fluorescence spectroscopies; TEM, SEM, and AFM microscopies, as well as light, neutron, and X-ray scattering techniques.

In a third step, we will start analyzing the structural behavior of supramolecular polymers when mixing structuring units having different functional groups in a sort of dynamic constitutional approach. Several possibilities will be examined: narcissistic self-sorting or social self-sorting and, within this latter, the possibility to obtain alternated, random, or block copolymers (see General Figure).

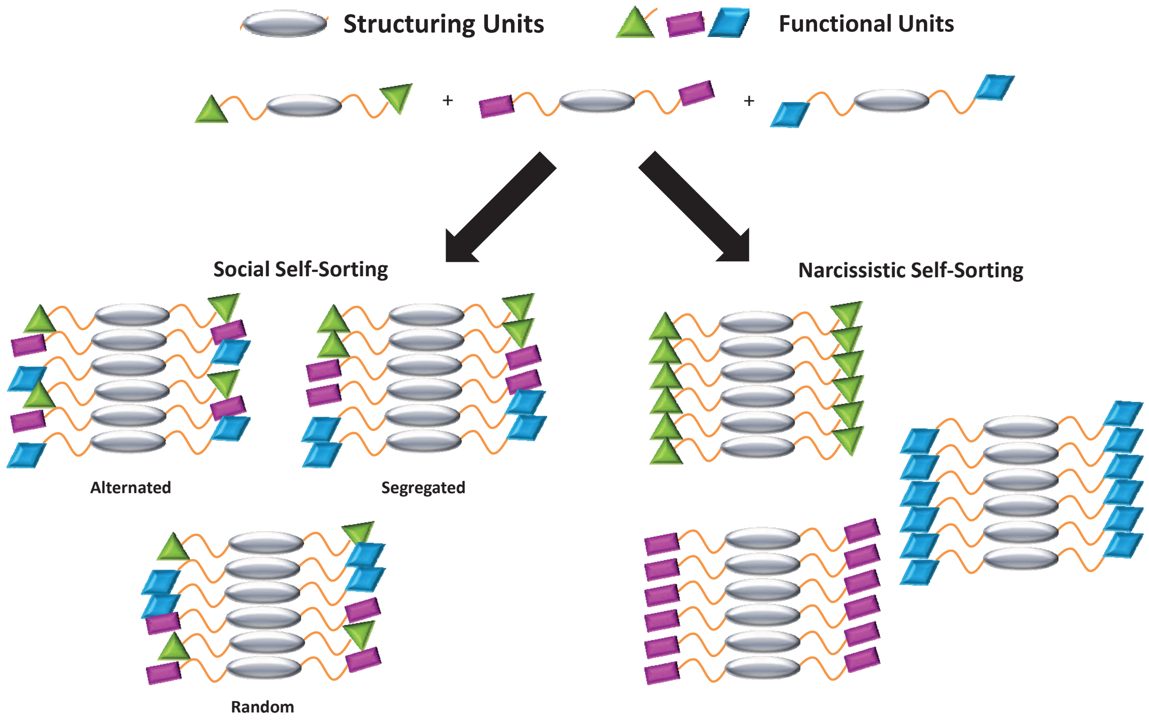

**General Figure|** Schematic representation of the possible supramolecular polymerizations with the possible production of multifunctional co-self-assembly. Perylene and bisurea cores will be used as primary structuring units, while PEG chains, peptides, and Cyanine dyes will be used as supplementary functional units.

# BIBLIOGRAPHICAL PART

# Generalities

Supramolecular chemistry relates to the field of chemistry beyond that of individual molecules and focuses on chemical systems made up of a discrete number of molecular subunits or components. Whereas molecular chemistry is established on the covalent bond, supramolecular chemistry deals with the weaker and reversible non-covalent interactions between molecules. These interactions may vary from weak (Van der Waals' forces for example) to strong (dipole-ion interactions for instance).[10] However, when several interactions are cooperatively combined, a stable supramolecular architecture can exist. Other important concepts, such as molecular self-assembly, molecular recognition, host-guest chemistry, mechanically-interlocked molecular architectures, and dynamic covalent chemistry also recently emerged from supramolecular chemistry.[11]

Since 1987 when the Nobel Prize in chemistry was awarded to Jean-Marie Lehn, Donald J. Cram and Charles J. Pedersen "for their development and use of molecules with structure-specific interactions of high selectivity", the field of supramolecular chemistry has been growing up constantly. For example, huge effects have been devoted to discover selective host-guest complexes, in which a host molecule recognizes and selectively binds a certain guest. These achievements now find important applications in the field of environmental science for the development of (bio)chemical sensor. In the 1990s, supramolecular chemistry started being used as a tool to develop complex systems with increasing functions. As a starting point, molecules incorporating functional motifs such as, for instance, electrochemical or photochemical groups are synthesized but do not present any function. However, when these single molecules are combined in a supramolecular architecture, functions arising from the design of the single molecules can emerged. These advances have led to the development of emerging research fields such as supramolecular electronics or synthetic ion channels.

Biology and medicine have also benefited from the development of supramolecular chemistry. Indeed, non-covalent interactions are known to play a crucial role in many biological processes. By better understanding these interactions at protein binding sites, chemists have been able to develop new pharmaceutical therapies with better activities and selectivities. For example, some supramolecular systems have been designed to selectively disrupt some protein-protein interactions and therefore to modify the associated cellular

---

[10] (a) Lehn, J. M. Supramolecular Chemistry. *Science* **1993**, *260*, 1762-1763; (b) Lehn, J.M. Supramolecular Chemistry. Wiley-VCH, 1995.

[11] Oshovsky, G. V.; Reinhoudt, D .N. and Verboom, W. Supramolecular Chemistry in Water. *Angew. Chem. Int. Ed.* **2007**, *46*, 2366-2393.

functions.[12] Drug delivery has also progressed thanks to supramolecular chemistry with, for instance, the design of new capsules to deliver drugs in a controlled manner at specific sites.

Recently, supramolecular chemistry has been considered as a 'bottom up' approach to construct nanostructures in the nanometer scale as an alternative to the 'top down' approaches such as nanolithography or inkjet printing which require intense efforts to produce nanostructures and/or devices in the range below 100 nm.[13] This 'bottom up' approach, which rests on the self-assembly of individual molecules, may open new routes to nanostructures that are not currently accessible by the 'top down' methodologies. The combination of several identical molecular units by supramolecular interactions leads to the formation of a so-called supramolecular polymer, which can take advantage of non-covalent interactions to adapt its self-assembly depending on the environment (solvent, temperature, *etc.*). The formation of these polymers is controlled by the thermodynamics and the kinetics of non-covalent interactions. This new family of polymers has attracted a lot of attention as the reversibility of the non-covalent interactions induces adaptive properties to the system.[14]

---

[12] Bertrand, N., Gauthier, M. A.; Bouvet, C.; Moreau, P.; Petitjean, A.; Leroux, J. C. and Leblond, J. New Pharmaceutical Applications for Macromolecular Binders. *J. Control. Release* **2011**, *155*, 200-210.

[13] Whitesides, G.; Mathias, J. and Seto, C. Molecular Self-Assembly and Nanochemistry: A Chemical Strategy for the Synthesis of Nanostructures. *Science* **1991**, *254*, 1312-1319.

[14] Huang, F. and Scherman, O. A. Supramolecular Polymers. *Chem. Soc. Rev.* **2012**, *41*, 5879-5880.

# Chapter 1: Supramolecular polymers

Supramolecular polymers have been defined in 2001 by Meijer and co-workers as ***"polymeric arrays of monomeric units that are brought together by reversible and highly directional secondary interactions, resulting in polymeric properties in dilute and concentrated solutions, as well as in the bulk. The monomeric units of the supramolecular polymers themselves do not possess a repetition of chemical fragments. The directionality and strength of the supramolecular bonding are important features of systems that can be regarded as polymers and that behave according to well-established theories of polymer physics."***[15]

Considering the important number of publications in this new field of polymer science, it became important to classify supramolecular polymers according to their main features. Therefore, three possible classifications have been proposed:[16]

i. Thermodynamical classification, i.e. based on the evolution of the Gibbs free energy of the polymer as a function of its conversion
ii. Monomeric classification, i.e. single monomers with self-complementary interactions, two or more different bifunctional monomers, *etc.*
iii. Supramolecular interactions classification, i.e. physical nature of the non-covalent force that induces the formation of the polymer.

Another important point in supramolecular polymers relates to their characterization. Indeed, owing to the dynamic nature of the non-covalent interactions, the characterization techniques used for covalent polymers are not always suitable for their supramolecular counterparts.

In the following parts of this chapter, we will highlight the different supramolecular interactions that are involved in the polymerization process and the different techniques that have been used to characterize these dynamic self-assemblies.

## 1. Interactions involved in supramolecular polymerization

Non-covalent interactions, such as hydrogen bonding, metal–ligand coordination, electrostatic interactions, π–π stacking, and other hydrophobic interactions, whose strength varies from 4 to 400 kJ.mol$^{-1}$ (Figure 1), can be considerably weaker than their covalent

---

[15] Brunsveld, L.; Folmer, B. J. B.; Meijer, E. W. and Sijbesma, R. P. Supramolecular Polymers. *Chem. Rev.* **2001**, *101*, 4071-4097.

[16] De Greef, T. F. A.; Smulders, M. M. J.; Wolffs, M.; Schenning, A. P. H. J.; Sijbesma, R. P. and Meijer, E. W. Supramolecular Polymerization. *Chem. Rev.* **2009**, *109*, 5687-5754.

counterpart (150 to 450 kJ.mol$^{-1}$ for a single bond). Initially, these weak non-covalent interactions were applied to the formation of host-guest complexes such as crown ethers or cryptands with metal cations.[17]

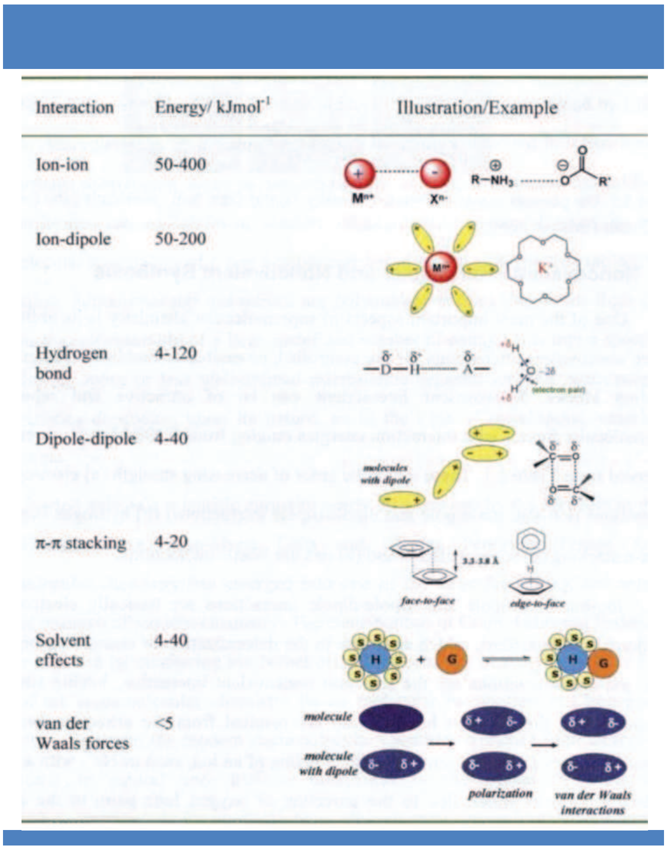

| Interaction | Energy/ kJmol$^{-1}$ | Illustration/Example |
|---|---|---|
| Ion-ion | 50-400 | |
| Ion-dipole | 50-200 | |
| Hydrogen bond | 4-120 | |
| Dipole-dipole | 4-40 | |
| π-π stacking | 4-20 | |
| Solvent effects | 4-40 | |
| van der Waals forces | <5 | |

**Figure 1 |** Average interaction energies of various noncovalent interactions frequently used in supramolecular chemistry (Cations (M), anions (X). electronegative element (D), elements with lone pair of electrons (A), host (H) and guest (G)).

Several years later, the group of Lehn reported the first supramolecular main-chain polymer using triple hydrogen bonding interactions.[18] Nowadays, advanced functional supramolecular polymers can be built using a combination of these non-covalent interactions.[19] For instance, the group of Huang recently combined host-guest and metal-ligand interactions to produce a multiresponsive supramolecular network gel.[20] In the following sections, we will describe these various non-covalent interactions and highlight some related examples of supramolecular polymers.

---

[17] (a) Pedersen, C. J. Cyclic polyethers and their complexes with metal salts. *J. Am. Chem. Soc.* **1967**, *89*, 7017-7036; (b) Dietrich, B.; Lehn, J.-M. and Sauvage, J. P. Les Cryptates. *Tetrahedron Lett.* **1969**, *10*, 2889-2892.

[9] Fouquey, C.; Lehn, J.-M. and Levelut, A.-M. Molecular recognition directed self-assembly of supramolecular liquid crystalline polymers from complementary chiral components. *Adv. Mater.* **1990**, *2,* 254–257.

[19] Li, S.-L.; Xiao, T.; Lin, C. and Wang, L. Advanced supramolecular polymers constructed by orthogonal self-assembly. *Chem. Soc. Rev.* **2012**, *41*, 5950-5968.

[20] Yan, X.; Xu, D.; Chi, X.; Chen, J.; Dong, S.; Ding, X.; Yu, Y. and Huang, F. A Multiresponsive, Shape-Persistent, and Elastic Supramolecular Polymer Network Gel Constructed by Orthogonal Self-Assembly. *Adv. Mater.* **2012**, *24*, 362–369.

### a. Hydrogen bonding

Hydrogen bond is ubiquitous in nature going from water to biological systems such as DNA and proteins. It has been recently redefined by IUPAC as "***an attractive interaction between a hydrogen atom from a molecule or a molecular fragment X–H in which X is more electronegative than H, and an atom or a group of atoms in the same or a different molecule, in which there is evidence of bond formation***."[21] The molecule or molecular fragment X-H is usually denoted as hydrogen-bond donor (D) whereas the atom or group of atoms, with which it interacts, is commonly described as the hydrogen-bond acceptor (A). This bond (4 to 120 kJ/mol) is weaker than ion-ion interactions or covalent bonds but stronger than van der Waals or π-π interactions.

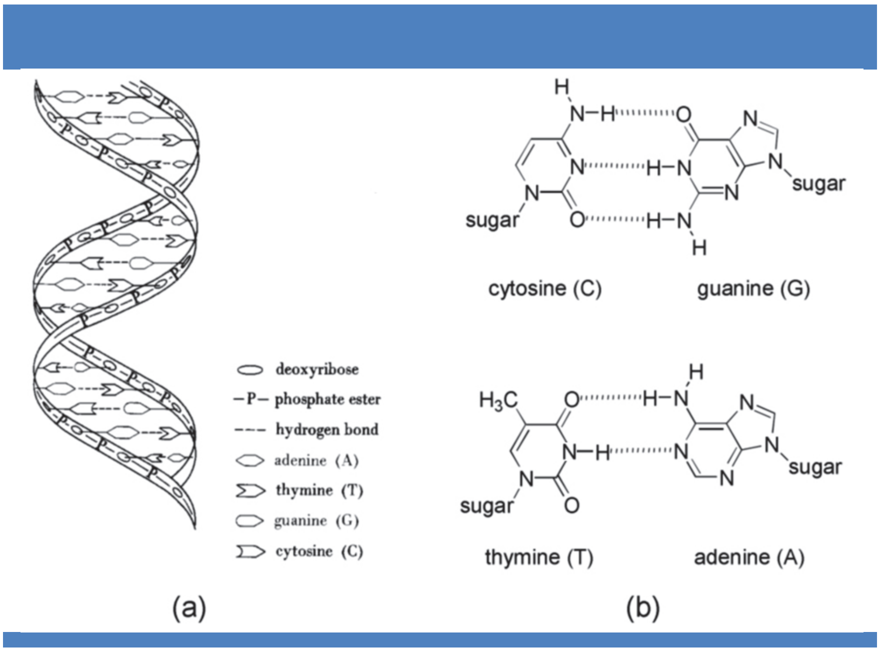

**Figure 2 |** a) Double Helix of DNA and complementary base pair; b) Hydrogen bonded base pair in DNA.[22]

In biological systems, double helical DNA is probably the best known self-assembling structure and uses hydrogen bonds to bind together two single strands. Here, while acidic hydrogen atoms act as hydrogen bond donors, oxygen and nitrogen atoms from the purine and pyrimidine bases play the role of hydrogen bond acceptor (Figure 2a). In the DNA double helix, the guanine-cytosine and the adenine-thymine combinations are particularly specific as they maximize the number of interactions with cytosine (C) forming a triple hydrogen bond motif with guanine (G) and thymine (T) forming a double hydrogen bond pattern with adenine (A) (Figure 2b). Inspired by the nucleobases and the strength that they confer to DNA

---

[21] Arunan, E. et al. Definition of the hydrogen bond (IUPAC Recommendations 2011). *Pure Appl. Chem.* **2011**, *83*, 1637–1641.

[22] Petrucci, R.H. General Chemistry: Principles and Modern Applications. Fifth ed. Macmillan Publishing Company, New York, 1989.

structures, chemists have developed synthetic molecules, whose structures mimic the motifs encountered in the purine and pyrimidine bases. For example, Lehn and co-workers took advantages of a hydrogen bonding pattern to enforce the self-assembly of 2-oxopyrimido[4,5,d]pyrimidin-5-(6H)-ones into a cyclic hexamer rather than the corresponding linear structure (Figure 3a).[23] For that, they designed Janus-type molecules which display a DDA pattern on one face and an AAD motif on the other one. Gel permeation chromatography (GPC) and vapor pressure osmometry (VPO) were used to confirm the formation of the cyclic assembly.

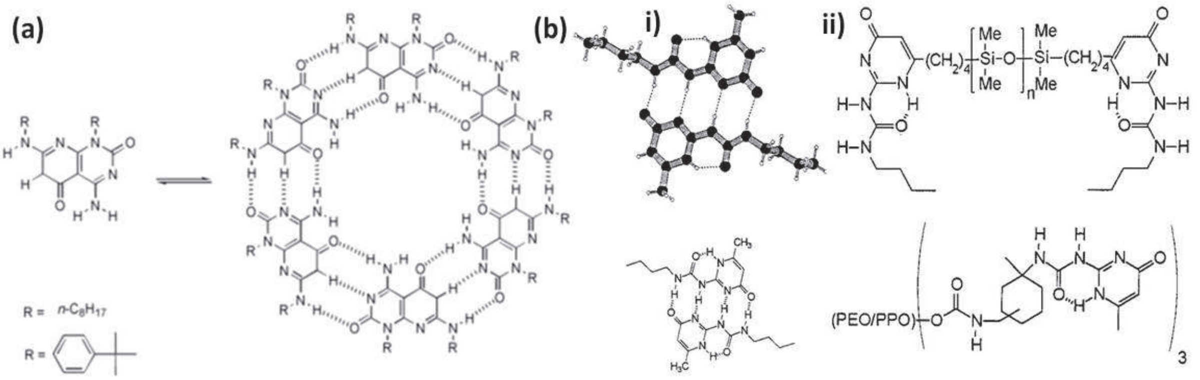

**Figure 3 |** a) Structure of the cyclic hexamer formed from the self-assembly of 2-oxopyrimido[4,5,d]pyrimidin-5-(6H)-ones; b) (i) X-ray structure of 2-butylureido-6-methylpyrimidone; (ii) Covalent polymers modified with 2-ureido-pyrimidone end groups.

One year later, the group of Meijer reported the formation of supramolecular polymers using a quadruple hydrogen bond motif called 2-ureido-pyrimidone which dimerizes with a very high association constant ($K_{dim} > 10^6$ $M^{-1}$ in $CHCl_3$) (Figure 3b).[24] Owing to this large dimerization constant, polymers with DP up to 700 units could be produced. Some covalent polymers such as polysiloxanes or a block copolymer made of poly(ethylene oxide) and poly(propylene oxide) were then decorated with these supramolecular units as end groups. Interestingly, in both cases, the mechanical properties of the supramolecular polymers were different than the ones observed for their covalent counterpart and could be modulated reversibly as a function of the temperature.

---

[23] Marsh, A.; Silvestri, M. and Lehn, J. M. Self-Complementary Hydrogen Bonding Heterocycles Designed for the Enforced Self-Assembly into Supramolecular Macrocycles. *Chemical Communications*, 1996, **13**, 1527-1528.

[24] Sijbesma, R. P.; Beijer, F. H.; Brunsveld, L.; Folmer, B. J. B.; Hirschberg, J. H. K. K.; Lange, R. F. M.; Lowe, J. K L. and Meijer, E. W. Reversible Polymers Formed from Self-Complementary Monomers Using Quadruple Hydrogen Bonding. *Science* **1997**, *278*, 1601-1604.

## b. Electrostatic interactions

Electrostatic interactions are based on the Coulombic attraction between opposite charges and have been divided in three main categories: (i) ion-ion, (ii) ion-dipole and (iii) dipole-dipole interactions. Among these ones, ion-ion interactions are the strongest with binding energies raging from 100 to 350 kJ.mol$^{-1}$ but are not directional. Conversely, ion-dipole and dipole-dipole interactions prove to be directional but their strengths vary from moderate (50-200 kJ.mol$^{-1}$) to weak (5-50 kJ.mol$^{-1}$) respectively, depending on the structure of the molecule. Electrostatic interactions have been widely used to construct layer-by-layer self-assemblies made of polyelectrolytes.[25] To a less extend, supramolecular polymers whose self-assembly is governed by these interactions have also been described.

In 2004, the group of Würthner reported the supramolecular polymerization of merocyanine dyes via dipole-dipole interactions.[26] In THF, polymers/oligomers arising from the antiparallel pairing of the dyes are formed. When solvents with low polarity such as methylcyclohexane are used, the increased strength of the electrostatic interactions leads to the hierarchical self-assembly of these polymers into rod-shaped fibers.

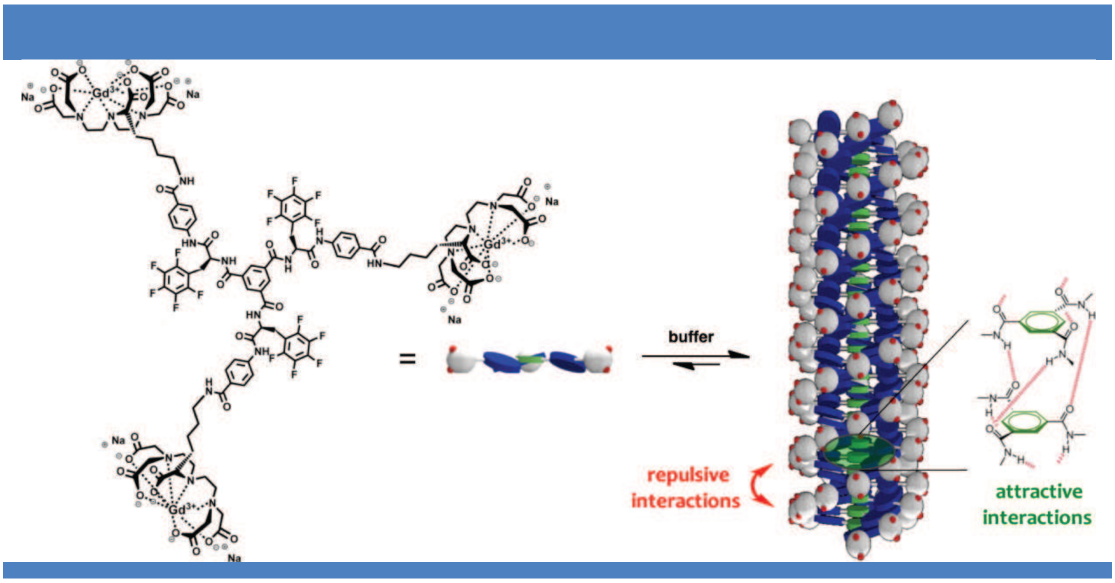

**Figure 4 |** Molecular structure of the $C_3$-symmetrical discotic amphiphile ($C_3$DA) and the schematic representation of the self-assembly into a helically ordered architecture.[27]

Another example of polymerization directed by electrostatic interactions was reported in 2010 by Meijer and co-workers using ionic discotic amphiphiles, so called $C_3$-symmetric discotic amphiphile ($C_3$DA), based on a benzene-1,3,5-tricarboxamide (BTA) core coupled to peripheral negatively charged Gd(III)-DTPA (DTPA =diethylenetriaminepentaacetic acid)

---

[25] Decher, G. Fuzzy Nanoassemblies: Toward Layered Polymeric Multicomposites. *Science* **1997**, *277*, 1232-1237.

[26] Yao, S.; Beginn, U.; Gress, T.; Lysetska, M. and Würthner, F. Supramolecular Polymerization and Gel Formation of Bis(Merocyanine) Dyes Driven by Dipolar Aggregation. *J. Am. Chem. Soc.* **2004**, *126*, 8336-8348.

(Figure 4).[27] Using small-angle X-ray scattering (SAXS) and diffusion ordered spectroscopy (DOSY) experiments, they demonstrated that the length of the rod-like assemblies is controlled by the electrostatic repulsive forces between the charged Gd(III)-DTPA moieties. Going further, they showed that the mechanism of self-assembly is changed from anti-cooperative to cooperative (see section 1. 3.) when an equimolar amount of salt (NaCl) is added. This change was accompanied by a morphological change from discrete spherical objects to high-aspect ratio rod-like self-assemblies. This example clearly demonstrates that Coulomb interactions do not only affect the structure of the aggregates but also their nucleation from the monomeric to the aggregated state.

### c. Metal–ligand interactions

Metal–ligand interaction, also known as coordination bond, is a highly directional non-covalent interaction that has been used by both inorganic and supramolecular chemists to built metal-organic frameworks (MOFs) and metallo-supramolecular polymers, respectively.[28] Whereas MOFs are usually crystalline materials, the latter are soluble 1D polymeric chains constructed from alternating metal ions and organic molecules incorporating two ligand units. One important factor for reaching a high degree of polymerization (DP) is to use metal-ligand couples with a high binding constant and therefore, the combination of terpyridine with metal ions such as $Zn^{2+}$ or $Fe^{2+}$ has been widely used. For instance, our group recently achieved the polymerization of [c2] daisy chain rotaxane using such combination (Figure 5).[29]

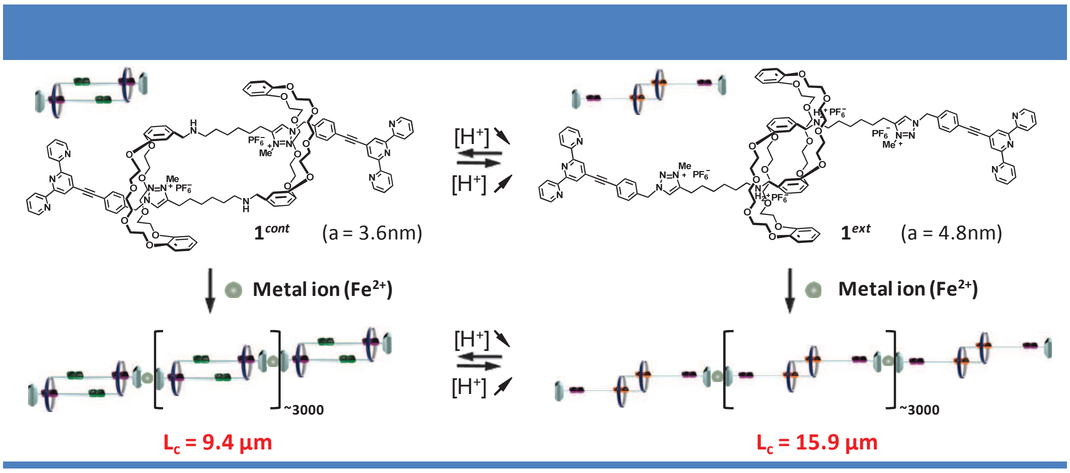

**Figure 5 |** Molecular structures of pH-responsive bistable [c2]daisy chain rotaxanes and of their supramolecular polymerization using metal ions such as iron(II).

---

[27] Besenius, P.; Portale, G.; Bomans, P. H. H.; Janssen, H. M.; Palmans, A. R. A. and Meijer, E. W. Controlling the growth and shape of chiral supramolecular polymers in water. *Proc. Nat. Acad. Sci. USA* **2010**, *107*, 17888-17893.

[28] Dobrawa, R.; Würthner, F. Metallosupramolecular Approach toward Functional Coordination Polymers. *J. Polym. Sci. Part A: Polym. Chem.* **2005**, *43*, 4981-4995.

[29] Giuseppone, N., et al. Muscle-like Supramolecular Polymers: Integrated Motion from Thousands of Molecular Machines. *Angew. Chem. Int. Ed.* **2012**, *51*, 12504 –12508.

Interestingly, when $Zn^{2+}$ ions were used, a DP of ~2000 was reached whereas a polymer of ~3000 units was obtained when $Fe^{2+}$ ions were used. This result clearly highlights how the binding constant affects the degree of polymerization of a metallosupramolecular polymer (log $K_1$= 6.0 $M^{-2}$ ($Zn^{2+}$) and 20.9 $M^{-2}$ ($Fe^{2+}$) in water).[30] The length of the polymers obtained in this study was long enough to demonstrate the possibility to integrate the translational motion of thousands of molecular machines up to the micrometric scale. Although the group of Schubert developed many metallosupramolecular polymers based on the terpyridine ligand,[31] some other ligands have been recently used to produce some polymers. For instance, the group of Higuchi reported the synthesis of high-molecular weight supramolecular polymers based on the 1,10-phenanthroline ligand using $Cu^{II}$ as metal ions ($M_w$=7.3*$10^6$ Da, $M_w/M_n$=1.1).[32]

### d. π interactions

π interactions refer to weak electrostatic interactions that involve π systems such as aromatic molecules, alkenes, etc. They can be categorized in three main groups: (i) cation-π, which corresponds to the binding of a cation to the π-electrons of a molecule; (ii) anion-π, which appears as counterintuitive but is favored between electron-deficient aromatics and anions; and (iii) π-π stacking, which is the most common and involves interactions between aromatic molecules.[33] The latter corresponds to the attraction between the negatively charged π-electrons of one conjugated system and the positively charged σ-framework of the neighboring molecule.[34] π-π stacking interactions can be of two types: (i) face-to-face, i.e. two molecules interact parallel to each other with a distance of ~3.5Å or (ii) edge-to-face, i.e. two molecules interact perpendicular to each other with the hydrogen atom of one pointing toward the center of the other aromatic ring. In this section, we will only highlight two examples of supramolecular polymers that involve π interactions as Chapter 3 is dedicated to supramolecular polymers based on perylene moieties.

In 2006, Ajayaghosh and co-workers studied the concentration-dependent morphologies observed for a short oligo (p-phenyleneethynylene) (OPE) derivative with two hydroxyl end groups (Figure 6). They showed that various supramolecular assemblies ranging from

---

[30] Martell, A. E.; Smith, R. M. Critical Stability Constants, Plenum, New York, 1974.

[31] (a) Schubert, U. S. and Eschbaumer, C. Macromolecules Containing Bipyridine and Terpyridine Metal Complexes: Towards Metallosupramolecular Polymers. *Angew. Chem. Int. Ed.* **2002**, *41*, 2892-2926; (b) Chiper, M.; Hoogenboom, R. and Schubert, U. S. Toward Main Chain Metallo-Terpyridyl Supramolecular Polymers: "The Metal Does the Trick". *Macromol. Rapid Commun.* **2009**, *30*, 565–578.

[32] Hossain, M. D.; Sato, T. and Higuchi, M. A Green Copper-Based Metallo-Supramolecular Polymer: Synthesis, Structure, and Electrochromic Properties. *Chem. Asian J.* **2013**, *8*, 76–79.

[33] Salonen, L. M.; Ellermann, M. and Diederich, F. Aromatic Rings in Chemical and Biological Recognition: Energetics and Structures. *Angew. Chem. Int. Ed.* **2011**, *50*, 4808–4842.

[34] Martinez, C. R. and Iverson, B. L. Rethinking the term "pi-stacking". *Chem. Sci.* **2012**, *3*, 2191-2201.

nanoparticles and micro-spherical nanostructures to large fibrous aggregates can be obtained by increasing the concentration of unimer thanks to π-π stacking interactions.[35] For concentrations lower than the critical gelation concentration (CGC < $1\times10^{-4}$ M), microspheres were observed whereas extended superstructures associated with gelation properties were reached when the concentration was higher than the CGC ($3.4\times10^{-3}$ M).

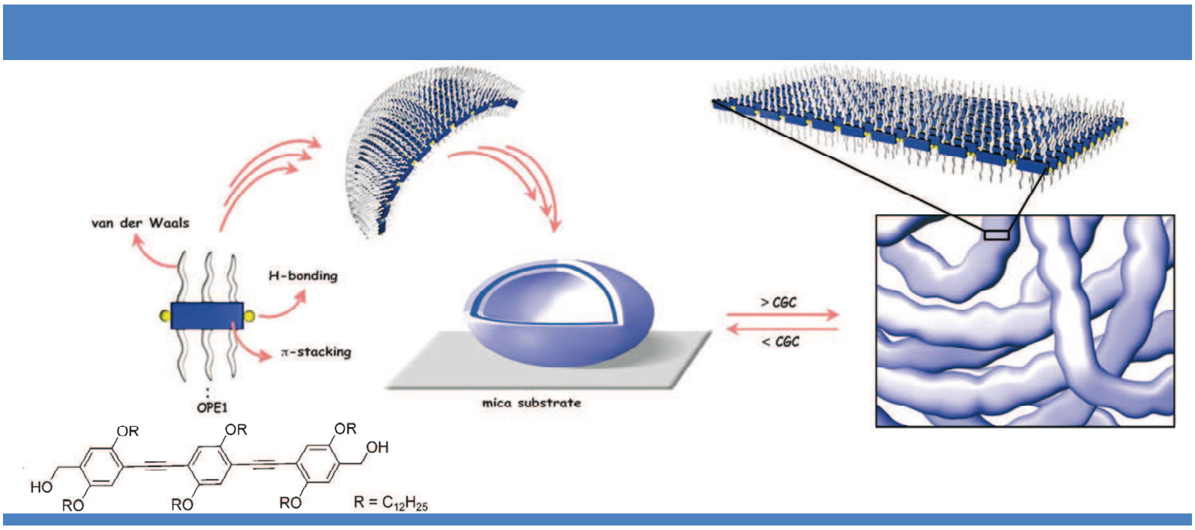

**Figure 6 |** Schematic representation of the self-assembly processes of *p*-phenyleneacetylenes organogelators. The mode of molecular arrangements in a single layer of the spherical and the extended self-assemblies are also shown.

Recently, Avinash and Govindaraju reported the aggregation of tryptophane-modified naphthalene diimides in either J-type or H-type aggregates in acetonitrile or an aqueous solution, respectively.[36] In the aqueous medium, cation-π interactions were shown to be the driving force for the self-assembly, whereas hydrophobic effect as the driving force in acetonitrile.

### e. Charge transfer interactions

Charge-transfer (CT) interactions represent a particular case of π-π stacking in which an electron donor interacts with an electron acceptor. A charge transfer complex typically arises from an electronic transition from the HOMO of the donor to the LUMO of the acceptor.[37] These CT complexes have been used to form a large variety of nanostructures ranging from vesicles to nanotubes or even foldamers. However, their high association constants remain to be improved to compete with hydrogen-bonding or π-stacking supramolecular polymers.

As an example of such polymer, Xi Zhang and co-workers developed bolaamphiphiles

---

[35] Ajayaghosh, A.; Varghese, R.; Praveen, V. K. and Mahesh, S. Evolution of Nano- to Microsized Spherical Assemblies of a Short Oligo(P-Phenyleneethynylene) into Superstructured Organogels. *Angew. Chem. Int. Ed.* **2006**, *45*, 3261-3264.

[36] Avinash, M. B. and Govindaraju, T. A bio-inspired design strategy: Organization of tryptophan-appended naphthalenediimide into well-defined architectures induced by molecular interactions. *Nanoscale* **2011**, *3*, 2536-2543.

[37] Das, A. and Ghosh, S. Supramolecular Assemblies by Charge-Transfer Interactions between Donor and Acceptor Chromophores. *Angew. Chem. Int. Ed.* **2014**, *53*, 2038 – 2054.

which consist in electron-rich naphthalene (BNAPH and IBNAPH, which are the 1,5- and 2,6-substituted naphthalene respectively) and electron-deficient naphthalene diimide (BNDI) groups and can form different nanostructures in aqueous solution (Figure 7).[38]

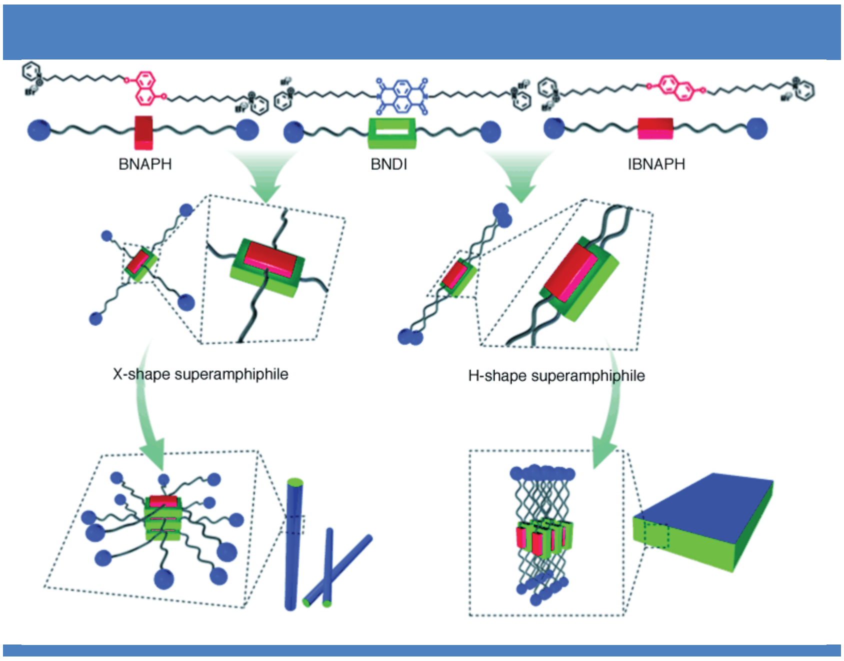

**Figure 7 |** Schematic representation of the X- and H-shape superamphiphiles and their assembly into one dimensional and two-dimensional nanostructures respectively.

In aqueous medium, BNDI and BNAPH were shown to form fibrillar and spherical micellar nanostructures respectively. Interestingly, when BNDI was mixed with BNAPH or IBNAPH units, different morphologies were observed, showing that the substitution of the naphthalene unit strongly influence the charge transfer interaction to form X-shape and H-shape amphiphiles, respectively. At the supramolecular level, these two superamphiphiles led either to a 1D supramolecular nanostructure such as a tubular assembly or to a 2D one such as a sheet-like structure.

### f. Other hydrophobic interactions

Hydrophobic interactions exist when non-polar molecules aggregate in aqueous solution and exclude water molecules.[39] The best example of such effect is the separation of a mixture of water and oil into two phases. From a thermodynamic point of view, the hydrophobic effect is composed of both an enthalpic component (replacement of water by the guest) and an entropic one (combination of several molecules to create an organic "hole" in water). This hydrophobic effect plays an important role in biological events such as protein-small

---

[38] Liu, K.; Wang, C.; Li, Z. and Zhang, X. Superamphiphiles Based on Directional Charge-Transfer Interactions: From Supramolecular Engineering to Well-Defined Nanostructures. *Angew. Chem. Int. Ed.* **2011**, *50*, 4952-4956.

[39] (a) Southall, N. T.; Dill, K. A. and Haymet, A. D. A view of the hydrophobic effect. *J. Phys. Chem. B* **2002**, *106*, 521-533; (b) Chandler, D. Interfaces and the Driving Force of Hydrophobic Assembly. *Nature* **2005**, *437*, 640-647.

molecule interactions, folding of protein, formation of lipid bilayers and micelles.[40] In supramolecular chemistry, it was shown to play an important role in host-guest chemistry, i.e. for instance in the binding of organic molecules by large macrocyclic molecules such as cyclophanes or cyclodextrins in aqueous solutions.[41] In supramolecular polymerization, the hydrophobic effect has been considered as an additional driving force for the self-assembly in water.

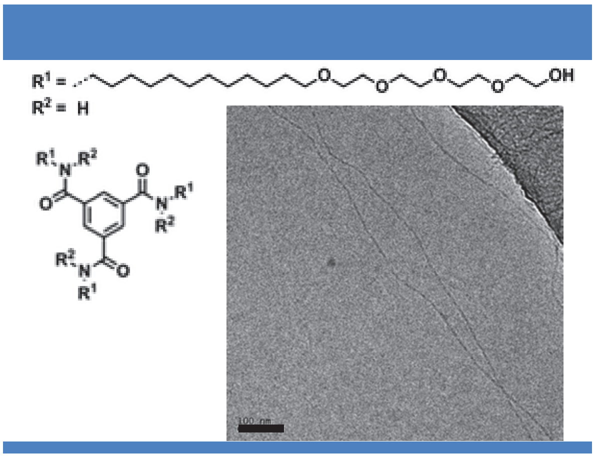

**Figure 8 |** Molecular structure of a BTA derivative substituted by alkyl spacer with tetraethylene glycol end group, and cryo-TEM image of its self-assembly in water (bar scale: 100 nm).

For example, the group of E. W. Meijer synthesized the N,N',N''-trialkyl-benzene -1,3,5-tricarboxamides (BTAs) derivative substituted on the amide moiety by an alkyl spacer followed by a tetraethylene glycol unit and studied its self-assembly in water (Figure 8).[42] Although examples of BTA-based supramolecular polymers in water are scarce, the alkyl spacer serves as the hydrophobic part to protect the hydrogen-bonding unit from water, and tetraethylene glycol end units provide solubility in water. Following a precise protocol (heating up the derivative in water at temperature above 80 °C, and then cooling down to 20 °C), they reached a clear viscous solution which displays long thin fibers with a high aspect ratio (micrometric in lengths and nanometric in diameters) as displayed in Figure 8.

## g. Van der Waals interactions

Van der Waals interactions are described by the IUPAC as "*the attractive or repulsive forces between molecular entities (or between groups within the same molecular entity) other than those due to bond formation or to the electrostatic interaction of ions or of ionic groups*

---

[40] Tanford, C. The Hydrophobic Effect: Formation of Micelles and Biological Membranes, 2nd ed.; Wiley: New York, 1980.

[41] Ferguson, S. B.; Seward, E. M.; Sanford, E. M.; Hester, M.; Uyeki, M.and Diederich, F. Molecular recognition by cyclophane hosts. *Pure App. Chem.* **1989**, *61*, 1523-1528.

[42] Leenders, C. M. A. ; Albertazzi, L.; Mes, T.; Koenigs, M. M. E.; Palmans, A. R. A. and Meijer, E. W. Supramolecular Polymerization in Water Harnessing Both Hydrophobic Effects and Hydrogen Bond Formation. *Chem. Commun.* **2013**, *49*, 1963-1965.

*with one another or with neutral molecules*”.[43] Their strength is usually lower than 5 kJ.mol$^{-1}$, providing them as the weakest non-covalent interactions involved in supramolecular polymerization. Although the combination of several of them might lead to strong interactions, they are usually combined with stronger interactions such as hydrogen bonds to produce supramolecular polymers. For instance, our group recently described the formation of supramolecular polymers based on a triarylamine core, thanks to the combined association of π-π stacking, hydrogen-bonding and van der Waals interactions.[44] Importantly, when the latter were suppressed, no self-assembly was observed, confirming that these interactions can play an important role in the stabilization of supramolecular polymers.

### h. Host–guest interactions

Host-guest chemistry can be defined as *the study of large "host" molecules that are capable of enclosing smaller "guest" molecules via non-covalent interactions*.[45] Therefore, host-guest interactions cannot be considered as a supramolecular interaction by itself. However, these complexes have been widely used to form supramolecular polymers and deserve to be mentioned as they are built from most of the non-covalent interactions mentioned previously.[46] For instance, the group of Zhang took advantage the stabilization of charge transfer interactions by a cucurbit[8]uril host to form a water soluble supramolecular polymer with a high DP.[47] Interestingly, whereas both the host and the guest molecules were poorly soluble in water, the supramolecular polymer displayed remarkably good water solubility. Although the degree of polymerization could not be precisely determined, the combination of several analytical techniques such as UV-Vis, light scattering and microscopies were used to confirm the formation of the polymer.

## 2. Characterization of supramolecular polymers

Supramolecular polymers are composed of monomers which are bound together by non-covalent interactions. Obviously, the occurrence of polymerization relies on these interactions which are often difficult to characterize. Nuclear magnetic resonance (NMR)

---

[43] http://goldbook.iupac.org/V06597.html

[44] Moulin, E.; Niess, F.; Maaloum, M.; Buhler, E.; Nyrkova, I. and Giuseppone, N. The Hierarchical Self-Assembly of Charge Nanocarriers : A Highly Cooperative Process Promoted by Visible Light. *Angew. Chem. Int. Ed.* **2010**, *49*, 6974-6978.

[45] Steed, J. W.; Turner, D. R. and Wallace, K. J. Core Concepts in Supramolecular Chemistry and Nanochemistry, 1st ed.; John Wiley & Sons: Chicester, England, 2007.

[46] (a) Dong, S.; Zheng, B.; Wang, F. and Huang, F. Supramolecular Polymers Constructed from Macrocycle-Based Host−Guest Molecular Recognition Motifs. *Acc. Chem. Res.* **2014**, *47*, DOI:10.1021/ar5000456; (b) Loh, X. J. Supramolecular host–guest polymeric materials for biomedical applications. *Mater. Horiz.* **2014**, *1*, 185-195.

[47] Liu, Y.; Yu, Y.; Gao, J.; Wang, Z. and Zhang, X. Water-soluble supramolecular polymerization driven by multiple host-stabilized charge-transfer interactions. *Angew. Chem., Int. Ed.* **2010**, *49*, 6576−6579.

spectroscopy, mass spectrometry (MS), infrared (IR), ultraviolet-visible (UV-Vis), fluorescence and circular dichroism (CD) spectroscopies are the common techniques used to confirm the presence of polymers, as differences with the monomer are expected. Scattering and microscopy techniques will then be complementary used to establish the structure of those supramolecular polymers. Additionally, calorimetry experiments such as isothermal titration calorimetry (ITC) or differential scanning calorimetry (DSC) will provide information on the thermodynamic parameters of the system. Of course, a combination of several characterization methods is mandatory to complete the full study of a supramolecular polymer.[48]

### a. Nuclear magnetic resonance (NMR) spectroscopy

Nuclear magnetic resonance (NMR) is a spectroscopic technique that plays an important role for the characterization of supramolecular polymers. By exploring the magnetic environment of any individual atomic nucleus, information about the structures and dynamics of the formed supramolecular polymers can be obtained. In particular, NMR spectra can be used to determine the chemical regions that are crucial for the stability of supramolecular polymers. Characteristic data such as binding constants or equilibrium constants can also be extracted from such analyses. So NMR appears as a very convenient technique to characterize supramolecular polymers at the molecular scale.

#### *i. $^1$H NMR spectroscopy*

$^1$H NMR spectroscopy probes the magnetic environment of hydrogen nuclei on molecules, reporting on their structures and interactions. Therefore, changes in chemical shifts of protons can be used to investigate the interactions between molecules within supramolecular polymers and can supply structural information about the corresponding self-assemblies. Temperature- and concentration-dependant $^1$H NMR spectra are a valuable tool to provide convincing evidence for the formation of intermolecular aggregation. For instance, in order to elucidate the aggregation of a well-designed perylene bisimide (PBI) derivative, the group of Würthner investigated its concentration-dependent $^1$H NMR spectra from 0.02 to 40 mM in a mixture of $CDCl_3$/[$D_{14}$]Methylcyclohexane (MCH) (v:v=1:5) at ambient temperature (Figure 9).[49]

---

[48] Liu, Y.; Wang, Z. and Zhang, X. Characterization of Supramolecular Polymers. *Chem. Soc. Rev.* **2012**, *41*, 5922-5932.

[49] Shao, C.; Grüne, M.; Stolte, M. and Würthner, F. Perylene Bisimide Dimer Aggregates: Fundamental Insights into Self-Assembly by Nmr and Uv/Vis Spectroscopy. *Chem. Eur. J.* **2012**, *18*, 13665-13677.

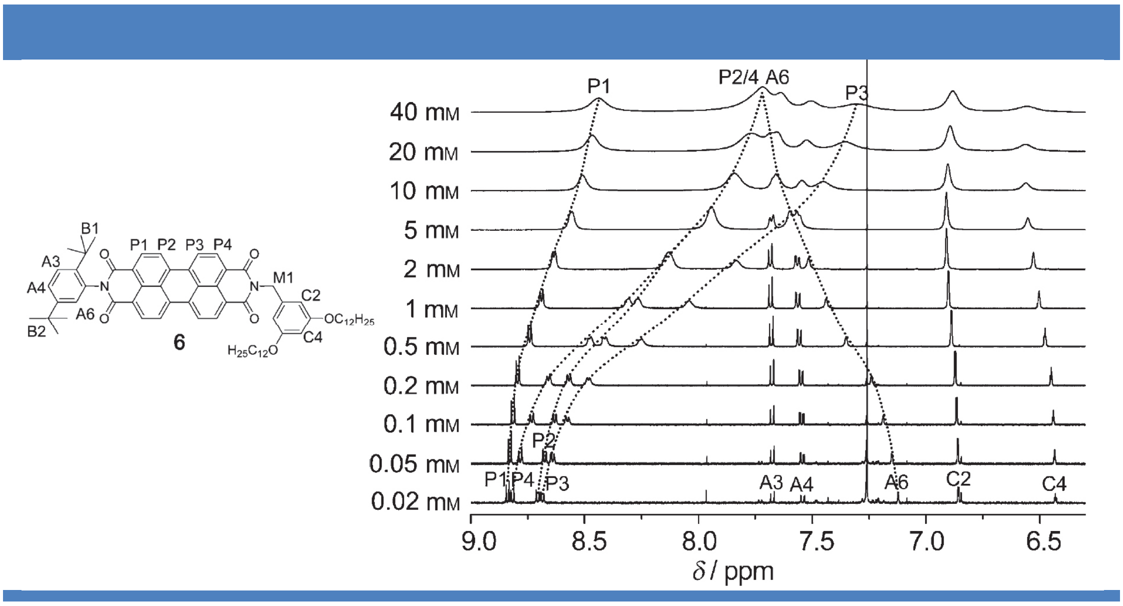

**Figure 9 |** Left: Molecular structure of PBI 6 with its marked protons; Right: Aromatic range of concentration-dependent $^1$H NMR spectra of PBI 6 from $2\times10^{-5}$ to $4\times10^{-2}$ M in $CDCl_3$/[$D_{14}$]MCH (v:v=1:5) conducted with 600 MHz NMR at 20 °C. The dotted lines follow the resonance shifts of protons P1–P4 and A6 with the concentration changes.

The major challenge in this study was to design a molecule that displays well-defined $^1$H NMR signals as PBI self-assemblies often suffer from broadened NMR chemical shift signals which limit their analyses.[50] As concentration increases, the chemical shifts of perylene's P1–P4 protons are all moving to higher field (Figure 9), which reflects the interactions between PBI chromophores by π–π interactions. Interestingly, the larger chemical shift of protons P4 and P3 indicates that the π–π stacking interaction is not centered on the perylene backbone but displaced towards P4 and P3 protons, probably because of the bulky tert-butyl substituents (B1 and B2). Additionally, the lower-field displacement of the A6 proton observed, simultaneously corresponds to the formation of a weak C-H···O hydrogen bond between the A6 proton and a carbonyl oxygen atom.[51] However, as proton A6 is located out of the perylene plane, this interaction can only occur with the carbonyl group from a neighboring molecule. Considering all the resonance variations observed in these concentration-dependant experiments, a dimerization model was proposed and nonlinear

---

[50] (a) Dehm, V.; Büchner, M.; Seibt, J.; Engel, V. and Würthner, F. Foldamer with a Spiral Perylene Bisimide Staircase Aggregate Structure. *Chem. Sci.* **2011**, *2*, 2094-2100; (b) Ahrens, M. J., *et al.* Self-Assembly of Supramolecular Light-Harvesting Arrays from Covalent Multi-Chromophore Perylene-3,4:9,10-Bis(Dicarboximide) Building Blocks. *J. Am. Chem. Soc.* **2004**, *126*, 8284-8294; (c) Rybtchinski, B.; Sinks, L.E. and Wasielewski, M.R. Photoinduced Electron Transfer in Self-Assembled Dimers of 3-Fold Symmetric Donor−Acceptor Molecules Based on Perylene-3,4:9,10-Bis(Dicarboximide). *J. Phys. Chem. A* **2004**, *108*, 7497-7505; (d) Ahrens, M. J.; Kelley, R. F.; Dance, Z. E. and Wasielewski, M. R. Photoinduced Charge Separation in Self-Assembled Cofacial Pentamers of Zinc-5,10,15,20-Tetrakis (Perylenediimide)Porphyrin. *Phys. Chem. Chem. Phys.* **2007**, *9*, 1469-1478.

[51] (a) Desiraju, G. R. The C-H···O Hydrogen Bond in Crystals: What Is It? *Acc.Chem. Res.* **1991**, *24*, 290-296; (b) Raymo, F. M.; Bartberger, M. D.; Houk K. N. and Stoddart, J. F. The Magnitude of [C−H···O] Hydrogen Bonding in Molecular and Supramolecular Assemblies. *J. Am. Chem. Soc.* **2001**, *123*, 9264-9267; (c) Steiner, T. The Hydrogen Bond in the Solid State. *Angew. Chem. Int. Ed.* **2002**, *41*, 48-76; (d) Senes, A.; Ubarretxena-Belandia, I. and Engelman, D. M. The Cα—H···O Hydrogen Bond: A Determinant of Stability and Specificity in Transmembrane Helix Interactions. *Proc. Nat. Acad. Sci. USA* **2001**, *98*, 9056-9061.

least-squares analysis of the data allowed the extraction of dimerization constant of the system. Additional 2D ROESY NMR and molecular modeling confirmed the head-to-tail dimer structure with a rotational angle of about 30°. This example clearly highlights the power of $^1$H NMR spectroscopy to monitor the formation of supramolecular structures.[52]

### ii. Diffusion ordered NMR spectroscopy (DOSY)

A valuable 2D NMR technique for the characterization of supramolecular self-assemblies is the diffusion-ordered $^1$H NMR spectroscopy (DOSY), first introduced by K. F. Morris in 1992,[53] which can directly measure the diffusion coefficient of the solutes. In a typical 2D DOSY spectrum, the horizontal dimension corresponds to the $^1$H chemical shift signals of the molecules in solution whereas the vertical dimension displays the diffusion behavior of the physical species (molecular or supramolecular) in solution.[54] The self-diffusion coefficient ($D_t$) extracted by DOSY is related to the Brownian motion of the species in their environment and is therefore influence by temperature, viscosity, *etc*. Some great advantages of DOSY NMR concern its non-invasive nature and the virtual separation of the different species in a mixture and the subsequent access to the different diffusion coefficients of the components. According to the Stokes-Einstein equation ($D_t = \frac{kT}{6\,\pi\eta r_s}$ where $k$ is the Boltzmann constant, $T$ the temperature, $\eta$ the viscosity of the liquid and $r_s$ the (hydrodynamic) radius of the molecule) and to the measured $D_t$, accurate hydrodynamic dimensions as well as thermodynamic parameters ($\Delta G^0$ of the assembling process and equilibrium constant) of the self-assemblies can be determined. Importantly, this equation can only be used if the studied object is considered as a spherical particle of colloidal dimension, i.e. much larger than that of the solvent. Such DOSY NMR experiment was used in the previous example on PBI derivatives to corroborate the exclusive formation of dimers. At a concentration where the degree of aggregation reaches around 90%, $D_t$ was determined to be $2.11*10^{-10}$ $m^2$ $s^{-1}$, which corresponds to a hydrodynamic diameter of 3.2 nm and confirms the absence of aggregates larger than dimeric species.

---

[52] (a) Brown, S.P. and Spiess, H.W. Advanced Solid-State Nmr Methods for the Elucidation of Structure and Dynamics of Molecular, Macromolecular, and Supramolecular Systems. *Chem. Rev.* **2001**, *101*, 4125-4156; (b) Hu, J.; Xu, T. and Cheng, Y. NMR Insights into Dendrimer-Based Host–Guest Systems. *Chem. Rev.* **2012**, *112*, 3856-3891; (c) Schneider, H. J.; Hacket, F. and Rüdiger, V. NMR Studies of Cyclodextrins and Cyclodextrin Complexes. *Chem. Rev.* **1998**, *98*, 1755-1786.

[53] (a) Morris, K. F. and Johnson, C. S. Resolution of Discrete and Continuous Molecular Size Distributions by Means of Diffusion-Ordered 2d NMR Spectroscopy. *J. Am. Chem. Soc.* **1993**, *115*, 4291-4299; (b) Johnson, C. S. Diffusion Ordered Nuclear Magnetic Resonance Spectroscopy: Principles and Applications. *Prog. Nuc. Mag. Res. Sp.* **1999**, *34*, 203-256.

[54] Macchioni, A.; Ciancaleoni, G.; Zuccacia, C. and Zuccaccia, D. *Diffusion Ordered NMR Spectroscopy (DOSY)* in Supramolecular Chemistry: From Molecules to Nanomaterials, Gale, P. A. and Steed, J. W. eds, Wiley-VCH, 2012, pp 319-330.

### b. Mass spectrometry

Mass spectrometry (MS) has been used to study conventional polymer for a long time in order to determine end-group structures and chemical compositions. Advances in mass spectrometers, in particular soft ionization technologies or improved analyzers, such as electrospray ionization (ESI) or matrix-assisted laser desorption ionization with time-of-flight analyzer (MALDI-TOF), helped in analyzing these polymers. However, considering the non-covalent nature of the interactions between monomers, it still remains a challenge to study the molecular weight of supramolecular polymers accurately by MS and mostly short units or oligomers are measured. For instance, Würthner and co-workers recently reported the formation of hydrogen-bonding supramolecular polymers using merocyanine dyes.[55] Whereas UV-Vis experiments indicated a high degree of polymerization, only dimers could be detected by MALDI-TOF MS. In 2005, the group of Harada reported the formation of supramolecular polymers formed by host-guest interactions.[56] Using turbo ion spray TOF MS, they were able to identify a polymer with 14 units, which is in good agreement with results obtained by vapor pressure osmometry.

### c. Optical spectroscopy

#### *i. Ultraviolet-visible spectroscopy*

Ultraviolet-visible spectroscopy (UV-Vis) is an absorption spectroscopy in the ultraviolet-visible range of the electromagnetic spectrum (200 to 750 nm). In this region, the molecule undergoes electronic transitions after absorbing light. This technology is therefore used to detect transitions of molecules from their ground state to their excited state. Molecules containing non-bonding electrons (n-electrons) or π-electrons can absorb the energy given by ultraviolet or visible light and electrons will be excited to higher anti-bonding molecular orbitals. If the electrons are easily excited, which corresponds to a small energy gap between the LUMO and the HOMO, they will then absorb light at a longer wavelength. UV-Vis spectroscopy can be used to qualitatively measure the formation of different objects such as, for instance, the formation of complexes between terpyridine and metal ions.[57] Indeed, when terpyridine ions are complexed by Zn(II) ions, a characteristic ligand-centered band is observed at 318 nm. When Fe(II) ions are used, an additional metal-to-ligand charge transfer

---

[55] Schmidt, R.; Stolte, M.; Grüne, M. and Würthner, F. Hydrogen-Bond-Directed Formation of Supramolecular Polymers Incorporating Head-to-Tail Oriented Dipolar Merocyanine Dyes. *Macromolecules* **2011**, *44*, 3766–3776.

[56] Miyauchi, M.; Takashima, Y.; Yamaguchi, H. and Harada, A. Chiral Supramolecular Polymers Formed by Host−Guest Interactions. *J. Am. Chem. Soc.* **2005**, *127*, 2984-2989.

[57] Hofmeier, H.; Hoogenboom, R.; Wouters, M. E. L. and Schubert, U. S. High Molecular Weight Supramolecular Polymers Containing Both Terpyridine Metal Complexes and Ureidopyrimidinone Quadruple Hydrogen-Bonding Units in the Main Chain. *J. Am. Chem. Soc.* **2005**, *127*, 2913-2921.

band is observed at 558 nm. UV-Vis experiments have also been used to quantitatively measure the thermodynamics parameters of self-assembled systems. Considering the perylene bisimide presented in Figure 9, concentration-dependant UV-Vis experiments have been used to quantify the dimerization constant of the system, which was in good agreement with the one determined by $^1$H NMR spectroscopy. These experiments were also used to determine that the self-assembly proceeds through an isodesmic mechanism in $CDCl_3$/[$D_{14}$] MCH (v:v = 1:5) and through a cooperative mechanism in pure methylcyclohexane (MCH) (see section 1. 3.).

### *ii. Fluorescence spectroscopy*

Fluorescence spectroscopy is a complementary technique to UV-Vis absorption spectroscopy as it deals with transitions from the excited state to the ground state.[58] Practically, in fluorescence spectroscopy, molecules are first excited to one of the vibrational states of the first singlet excited electronic state by a beam of light which results in the absorption of a photon. Upon collision with other molecules, the excited ones relax to a lower vibrational state of the singlet excited electronic state and then potentially to one of the various vibrational state of the ground electronic state along with emission of a photon. This relaxation mechanism is well-described by a Jablonski diagram which shows how fluorescence occurs due to the relaxation to the vibrational levels of the ground state (Figure 10).[59] Recently, the group of Haag used fluorescence spectroscopy to characterize the optical properties of a series of novel polyglycerol-dendronized rylene bisimide dyes.[60] Whereas PBI are known as good fluorescent emitters with high quantum yields, the introduction of PEG dendrons at the imide positions was shown to alter their fluorescence. Furthermore, hardly no fluorescence was detected for the quaterrylenebis(dicarboximide) homologue. One particular aspect of fluorescence spectroscopy deals with the through space energy transfer, also known as Förster Resonance Energy Transfer (FRET).[61] This phenomenon typically occurs for distances ranging from 10 to 100 Å and when the fluorescence spectrum of a donor overlaps with the absorbance spectrum of the acceptor. For instance, the group of Meijer used the FRET pair $Cy_3/Cy_5$ to monitor the proximity of BTA-based monomers at the molecular scale.[62] Upon addition of a single strand of DNA, a spatiotemporal rearrangement of the

---

[58] Guilbault, G. G. (Ed.). (1990). *Practical fluorescence* (Vol. 3). CRC Press.

[59] Jabłoński, A. Efficiency of Anti-Stokes Fluorescence in Dyes. *Nature* **1933**, *131*, 839-840.

[60] Heek, T., Würthner, F. and Haag, R. Synthesis and Optical Properties of Water-Soluble Polyglycerol-Dendronized Rylene Bisimide Dyes. *Chem. Eur. J.* **2013**, *19*, 10911–10921.

[61] Clegg, R. M. Fluorescence resonance energy transfer. *Curr. Opin. Biotechnol.* **1995**, *6*, 103-110.

[62] Albertazzi, L.; Martinez-Veracoechea, F. J.; Leenders, C. M. A.; Voets, I. K.; Frenkel, D. and Meijer, E. W. Spatiotemporal control and superselectivity in supramolecular polymers using multivalency. *Proc. Nat. Acad. Sci. USA* **2013**, *110*, 12203–12208.

monomers could be observed thanks to FRET events which demonstrate the dynamic nature of their self assembled system.

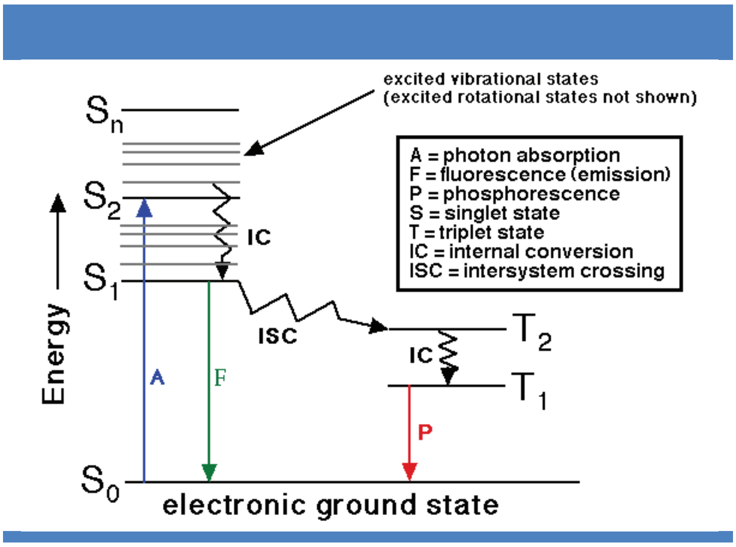

**Figure 10 |** Jablonski diagram

### *iii. Infrared spectroscopy*

Infrared (IR) rays are part of the electromagnetic spectrum at wavelengths that are longer than that of visible light. Infrared spectroscopy has been used extensively, in both inorganic and organic chemistry, to confirm the structure of molecules. It has also been applied to investigate the mechanism of formation of supramolecular polymer and understand the non-covalent interactions that are important for the self-assembly process.[63] For instance, the group of Bouteiller used Fourier-Transform InfraRed (FTIR) spectroscopy to determine the self-assembly mechanism of bis-urea-based supramolecular polymers.[64] By monitoring the FTIR spectra in the N-H region (i.e. from 3100 to 3500 nm$^{-1}$) as a function of concentration in $CDCl_3$, they demonstrated that the self-assembly process displays cooperativity at both the molecular level (synergistic association of the two urea functions for a bis-urea molecule) and the supramolecular level (the formation of long oligomers I favored compared to dimers).

### *iv. Circular dichroism spectroscopy*

Circular dichroism (CD) is based on the differential absorption of right and left-handed circularly polarized light. Whereas an achiral object absorbs both left and right handed circularly polarized light equally leading to a ‘zero’ CD spectrum, a chiral sample

---

[63] (a) Suzuki, M.; Yumoto, M.; Shirai, H. and Hanabusa, K. Supramolecular Gels Formed by Amphiphilic Low-Molecular-Weight Gelators of Nα,Nε-Diacyl-L-Lysine Derivatives. *Chem. Eur. J.* **2008**, *14*, 2133-2144; (b) Yang, M.; Zhang, Z.; Yuan, F.; Wang, W.; Hess, S.; Lienkamp, K.; Lieberwirth, I. and Wegner, G. Self-Assembled Structures in Organogels of Amphiphilic Diblock Codendrimers. *Chem. Eur. J.* **2008**, *14*, 3330-3337.

[64] Simic, V.; Bouteiller, L. and Jalabert, M. Highly Cooperative Formation of Bis-Urea Based Supramolecular Polymers. *J. Am. Chem. Soc.* **2003**, *125*, 13148-13154.

differentially absorbs the two polarized lights, resulting in either a negative or a positive CD spectrum. CD is powerful to study the conformation and configuration of chiral molecules or supramolecules, such as proteins, DNA, etc. Usually, CD spectra of isolated molecules have relatively low ellipticities, whereas chiral self-assembled structures display chirality to a much larger extent. In 2012, Meijer and co-workers reported the use of circular dichroism to probe the self-assembly mechanism of three different supramolecular polymers.[65] This study was performed by adding a good solvent to a preformed supramolecular polymer and monitoring the decay in CD intensity. Interestingly, their study revealed that, for a cooperative mechanism, the depolymerization process proceeds until a critical solvent composition whereas a continuous disassembly process takes place for an isodesmic mechanism. Overall, CD is a very soft and sensitive technique, which requires submicrogram-scale sample to probe the intermolecular and intramolecular interactions between molecules. Obviously, as it is the case for all optical spectroscopies, temperature-dependent CD experiments represent a very powerful tool to study the thermal responsiveness of chiral self-assemblies.[66]

### d. Scattering techniques

Scattering techniques are very useful tools for soft matter scientists to characterize the structure of polymeric assemblies in solution.[67] The most common scattering techniques used in solution are small-angle X-ray and neutron scattering (SAXS and SANS) and dynamic and static light scattering (DLS and SLS).[68] The general principle consists in illuminating a sample with an incident monochromatic ray at a known wavelength and to analyze the scattering radiation at a given angle with respect to the incident radiation. Whereas SAXS and SANS provide information at the mesoscopic scale, i.e. from 1 nm up to 30-100 nm, light scattering experiments, which are complementary to small angle scattering (SAS) techniques, provide information on structures in the 20-300 nm range for SLS and 1-300 nm for DLS (or even larger objects if they are compact). Additionally, whereas X-rays are electromagnetic radiations which are scattered by the electrons of the solution, neutrons are diffused by the

---

[65] Korevaar, P. A.; Schaefer, C.; de Greef, T. F. A. and Meijer, E. W. Controlling Chemical Self-Assembly by Solvent-Dependent Dynamics. *J. Am. Chem. Soc.* **2012**, *134*, 13482-13491.

[66] (a) Brizard, A.; Oda, R. and Huc, I. *Chirality Effects in Self-Assembled Fibrillar Networks*, in *Low Molecular Mass Gelator*. 2005, Springer Berlin Heidelberg, 167-218; (b) Jonkheijm, P.; van der Schoot, P.; Schenning, A. P. H. J. and Meijer, E. W. Probing the Solvent-Assisted Nucleation Pathway in Chemical Self-Assembly. *Science* **2006**, *313*, 80-83; (c) Smulders, M. M. J.; Schenning, A. P. H. J. and Meijer, E. W. Insight into the Mechanisms of Cooperative Self-Assembly:  The "Sergeants-and-Soldiers" Principle of Chiral and Achiral C3-Symmetrical Discotic Triamides. *J. Am. Chem. Soc.* **2007**, *130*, 606-611.

[67] Patterson, J. P.; Robin, M. P.; Chassenieux, C.; Colombani, O. and O'Reilly, R. K. The analysis of solution self-assembled polymeric nanomaterials. *Chem. Soc. Rev.* **2014**, *43*, 2412-2425.

[68] (a) Higgins, J. S.; Benoît, H. C. Polymers and Neutrons Scattering. *Ed. Clarenden press, Oxford* (1994); (b) Cummins, H. Z.; Pike, E. R. Photon Correlation and Light Beatimg Spectroscopy. *Ed. Plenum Press, New York and London* (1974); (c) Linder, P.; Zemb, T. Neutron, X-ray and Light Scattering: Introduction to Investigate Tool for Colloidal and Polymeric Systems. *Ed. North Holland* (1991); (d) Schmitz, K. S. An introduction to Dynamic Light Scattering by Macromolecules. *Ed. Academic Press inc., San Diego* (1990).

cores of the different atoms in the sample. Additionally, for light, these scatterers are the dipole moment of the monomers. Therefore, LS, SAXS and SANS are complementary techniques as their elementary diffusers are different for the three techniques. Typically, the complete characterization of large supramolecular aggregates requires the combined use of LS and SAS to determine the properties of the global object and its internal structure, respectively.[69] Usually, all elastic scattering experiments are represented as the scattered intensity $I(q)$ as a function of the magnitude of the scattering vector $q$ (which is inversely proportional to the length scale $1/q$):

$$q = \frac{4\pi n}{\lambda} \sin\left(\frac{\theta}{2}\right) \qquad \text{(eqn 1)}$$

where λ is the wavelength of the incident beam, θ is the scattering angle and n is the refractive index of the solvent for light scattering.

For SAXS and SANS, $q = \frac{4\pi}{\lambda} \sin\left(\frac{\theta}{2}\right)$

For spherical objects, the plot $I(q)$ versus $q$ is characterized by two main regions: (i) the Guinier region (defined for $qR_g \ll 1$ where $R_g$ is the gyration radius) at low $q$ which give information about the overall size of the particle and (ii) the Porod region (defined for $qR_g > 1$) at higher $q$ which provide information about the morphology of the sample (Figure 11).

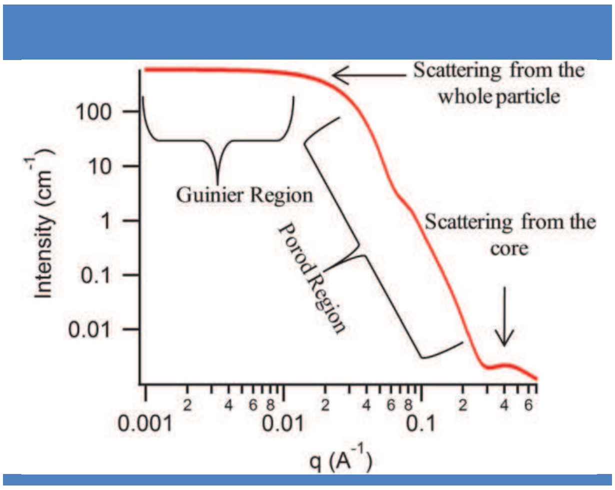

**Figure 11 |** SAS model showing *I(q)* vs. *q* for a polydisperse spherical particle with a core–shell structure.

For dilute solutions in which interactions can be neglected, the radius of gyration and the scattering intensity $I(0)$ can be easily obtained using the following Guinier approximation:

$$I(q) = I(0)\, exp\left(\frac{-q^2 R_g^2}{3}\right) \qquad \text{(eqn 2)}$$

---

[69] Jouault, N.; Nguyen, R.; Rawiso, M.; Giuseppone, N. and Buhler, E. SANS, SAXS, and Light Scattering Investigations of Ph-Responsive Dynamic Combinatorial Mesophases. *Soft Matter* **2011**, *7*, 4787-4800.

Importantly, this Guinier approximation is only valid in the so-called Guinier regime defined for $qR_g \ll 1$. The usual equation for absolute neutron scattering combines the intraparticle scattering $S_1(q) = V_{chain}\Phi_{vol}P(q)$ form factor with the interparticle scattering $S_2(q)$ factor:

$$I(q) = \frac{1d\sigma}{Vd\Omega} = (\Delta\rho)^2\big(S_1(q) + S_2(q)\big)$$

$$= (\Delta\rho)^2\big(V_{chain}\Phi_{vol}P(q) + S_2(q)\big)$$

where $(\Delta\rho)^2 = (\rho_{monomer} - \rho_{solvent})^2$ is the contrast per unit volume between the polymer and the solvent, which was determined from the known chemical composition. $\rho = \Sigma n_i b_i/(\Sigma n_i m_i v \times 1.66 \times 10^{-24})$ represents the scattering length per unit volume; $b_i$ is the neutron scattering length of the species $i$, $m_i$ is the mass of species $i$, and $v$ is the specific volume of the monomer or the solvent (i.e., 0.9026 cm$^3$/g for $D_2O$). $P(q)$ is the form factor, $V_{chain} = Nvm \times 1.66 \times 10^{-24}$ is the volume of $N$ monomers (of mass $m$) in a chain, and $\Phi_{vol}$ is the volume fraction of monomer. In the high $q$-range, the scattering is assumed to arise from isolated chains, that is, $S_2(q) = 0$, and thus $I(q) \propto P(q)$.

In most cases, for non-spherical objects, the spectrum shows an intermediate regime (for $1/q > R_g$) which provide the local structure of the object. This regime corresponds to a probed range smaller than the scattering objects so that the scattering radiation is probing the local structure and provides information about the "fractal dimension" of the scattered objects.[70] In this $q$ range, the scattered intensity can be approximated by the following equation:

$$I(q) = \frac{A}{q^n} + B \qquad \text{(eqn 4)}$$

where A and B are some constants related to the system.

From this equation, the slope $n$ of the plot $I(q)$ versus $q$ provides information on the shape of the object:

| **N** | 1 | 2 | 5/3 | 3 | 4 |
|---|---|---|---|---|---|
| **Shape** | Rigid rod | Gaussian chain (linear or branched) or smooth 2D object | Fully swollen coils | Collapsed polymer coils or 3D aggregates | Smooth surface |

When the slope $n$ is between 2 and 3, the local structure is composed on branched systems or networks, whereas a slope $n$ between 3 and 4 indicates the presence of 3D objects with fractal surfaces.

### i. Small-angle X-ray scattering

Small-angle X-ray scattering (SAXS) is mainly established on the elastic scattering of X-ray photons by aggregates present in solution and whose intensity is further recorded as a

---

[70] http://www.ncnr.nist.gov/staff/hammouda/distance_learning/chapter_22.pdf

function of the scattering angle.[71] The recorded scattering profile is typically used to determine the global structure and conformation of (supramolecular) polymers under study. In particular, SAXS can provide critical information on the objects, such as the radius of gyration ($R_g$), the molecular weight ($M_w$) and the maximum intramolecular distance ($D_{max}$). For instance, the group of Meijer used SAXS to determine the size and the shape of their discotic BTA amphiphiles.[27] From the slope of the $I(q)$ versus $q$ plot, they determine that their neutral discotic amphiphile forms rod-like shaped objects ($n = 1$) without interacting cylinders. Using the appropriate form factor for monodisperse cylindrical objects, they could estimate the radius of their objects to 3.1 nm and the associated length was shown to vary from 25 nm at 0.25 mM up to 75 nm at 1 mM.

#### *ii. Small-angle neutron scattering*

Small-angle neutron scattering (SANS) is mainly established on the elastic scattering of neutrons by aggregates present in solution and whose intensity is further recorded as a function of the scattering angle.[72] To a large extent, SANS is therefore very similar to SAXS. For SANS, the neutrons are elastically scattered by interaction with the magnetic moments of unpaired electrons or nuclear interaction with the nuclei, whereas for SAXS, the information is obtained from the photons that interact with electron clouds. Compared with SAXS, advantages of SANS are the strong scattering by magnetic moments, its sensitivity to light elements and the absence of sample damage. However, due to the lower flux of neutrons compared to X-ray (at the Synchrotron), the time of acquisition is usually much longer than for SAXS in order to obtain data with reasonable statistics. As SANS depends on the differential scattering between hydrogen and deuterium, the use of deuterated solvents allow a greater contrast between the solute and the solvent by SANS. For this reason, SANS experiments on polymeric and colloidal systems are usually performed in deuterated solvents and represent a great asset for the study of soft matter systems in solution. It should be mentioned that the structural information accessible by SANS are almost identical to the one obtained by SAXS.

Our group used SANS to follow the structural evolution of a library of amphiphilic dynamic block copolymers (dynablocks) upon pH modulation.[73] At any pH, scattering curves displayed the same overall behavior, namely a Guinier regime at low $q$, a $q^{-1}$ regime in the

---

[71] Chu, B.; Hsiao, B. S. Small-Angle X-ray Scattering of Polymers. *Chem. Rev.* **2001**, *101*, 1727-1761.

[72] Hollamby, M. J. Practical applications of small-angle neutron scattering. *Phys. Chem. Chem. Phys.* **2013**, *15*, 10566-10579.

[73] (a) Nguyen, R.; Buhler, E. and Giuseppone, N. Dynablocks: Structural Modulation of Responsive Combinatorial Self-Assemblies at Mesoscale. *Macromolecules* **2009**, *42*, 5913-5915; (b) Nguyen, R.; Allouche, L.; Buhler, E. and Giuseppone, N. Dynamic Combinatorial Evolution within Self-Replicating Supramolecular Assemblies. *Angew. Chem. Int. Ed.* **2009**, *48*, 1093-1096.

intermediate region, another Guinier regime at higher $q$ and a last $q^{-1}$ regime in the high $q$ range, which is typical for a cylindrical micelle. Several information such as $R_g$, $M_w$, the linear mass density ($M_L$), or even the radius of gyration of the section ($r_c$) were all shown to be highly dependent on the pH, whereas the shape of the objects was not affected.

### *iii. Light scattering*

Light scattering is a powerful technique to monitor the size (1-300 nm) and morphology of both covalent and supramolecular polymers as it is a non-invasive technique.[67] Two different but complementary experiments can be set: static or elastic light scattering (SLS) and dynamic or quasi-elastic light scattering (DLS). Whereas SLS is monitoring the absolute value of the intensity of the scattered light as a function of q, DLS is recording the auto-correlation function of the scattered intensity. Typically, SLS experiments provide information on form and structure factors. This technique is sometimes used in complement to SANS and SAXS when the Guinier regime is not accessible in their available $q$-range. Therefore, structural information such as $R_g$, $M_w$, or even the aggregation number $N_{agg}$ are available from SLS experiments. On the other hand, DLS gives the characteristic relaxation times of the system through the measurement of the auto-correlation function measurement and thus allows studying the dynamic properties of polymers. Indeed, performing time-dependent DLS experiments provides information on the possible particle aggregation over time. For cooperative mechanisms, a DLS experiment is used to determine the hydrodynamic radius $R_H$ of the studied objects from their cooperative diffusion coefficient $D_c$ using the Stokes-Einstein equation (see section 2.a.ii. on DOSY NMR). Thus, the combined use of SLS and DLS give access to the $R_g/R_H$ ratio, which provides information on the morphology of the sample. Importantly, for a sphere, $R_H$ corresponds to the theoretical radius of a perfect hard sphere, $R_g$ is defined as the mass weighted average distance from the core of a molecule to each mass element in the molecule. For hard homogeneous spheres, $R_H$ corresponds to the geometric radius R and $R_g/R_H = 0.775$, whereas, for hollow spheres, a $R_g/R_H$ ratio of 1 is observed. Additionally, for Gaussian polymer chains without excluded volume interactions, the $\rho$ ratio equals 1.505. Recently, the group of Lehn reported that double dynamic hydrogen-bonded polymers form Gaussian coils using a combination of SLS and DLS.[74] The group of Bouteiller also reported on the combined use of SLS and DLS to demonstrate that the molar mass of bis-urea based supramolecular polymer can be efficiently

---

[74] Schaeffer, G.; Buhler, E.; Candau, S. J. and Lehn, J.-M. Double Dynamic Supramolecular Polymers of Covalent Oligo-Dynamers. *Macromolecules* **2013**, *46*, 5664−5671.

tuned by the addition of a chain stopper.[75] From SLS experiments, both $R_g$ and $M_w$ could be determined whereas $R_H$ was determined using DLS. The calculated $R_g/R_H$ ratio was in agreement with the formation of long and rigid fibrillar species.

### e. Microscopy techniques

Microscopy techniques are complementary to scattering ones as they provide a direct imaging of the self-assembled species, typically after deposition on a grid or a substrate. Microscopes can be divided into three categories: optical, electron and scanning probe. However, for the purpose of this thesis, we will only describe the last two categories.

#### *i. Transmission electron microscopy*

Transmission electron microscopy (TEM) is based on an electron microscope which uses a beam of electrons which interact and pass through the studied sample. It thus highlights the interactions between the scanning electrons and the sample and provides images from the subnanometric up to micrometric scales depending on the resolution of the apparatus. TEM has been widely used to observe supramolecular systems, ranging from the self-assembly of lipid molecules to the characterization of self-assembled hydrogels.[76] Classical TEM imaging is usually performed on copper grid after drop-casting a solution of the sample and further drying. One main drawback on this procedure is the possible disruption of the structure observed in solution after drying. In order to circumvent this problem, freeze-fracture and cryogenic TEM have been developed. Whereas both provide 3D information on the microscopic structure of the objects, freeze-fracture TEM is providing an image of the replica of the frozen object. The main advantage of Cryo-TEM over freeze-fracture is the possibility to observe the inner structure of the visualized objects. However, both techniques require additional specific apparatus which are not routinely available.

#### *ii. Atomic force microscopy*

Atomic force microscopy (AFM) is a powerful tool for imaging supramolecular polymers at surfaces with high resolution but also for probing molecular forces.[77] AFM is considered as a scanning probe microscopy as an AFM tip is continuously scanning the surface and its mechanical deflection is then optically detected by a laser beam to further reconstruct the image of the surface. Several imaging modes are available in order to

---

[75] Lortie, F.; Boileau, S.; Bouteiller, L.; Chassenieux, C. and Lauprêtre, F. Chain Stopper-Assisted Characterization of Supramolecular Polymers. *Macromolecules* **2005**, *38*, 5283-5287.

[76] Kikuchi, J. and Kazuma, Y. *Transmission Electron Microscopy (TEM)* in Supramolecular Chemistry: From Molecules to Nanomaterials, Gale, P. A. and Steed, J. W. eds, Wiley-VCH, 2012, pp 633-645.

[77] Hyotyla, J. T. and Lim, R. Y. H. *Atomic Force Microscopy (AFM)* in Supramolecular Chemistry: From Molecules to Nanomaterials, Gale, P. A. and Steed, J. W. eds, Wiley-VCH, 2012, pp 659-668.

characterize the surface. The most common one is the *contact mode* in which the surface of the sample is scanned constantly with the tip under contact. Another common mode is the *tapping mode* in which the tip is continuously "tapping" the surface. One advantage of this mode is that it damages less the surface of the sample and it provides qualitative information on the material properties. However, one limitation of AFM is that the size of the tip greatly affects the resolution of the image and that soft structures can be flatten which make them display shallower and wider than they are actually.

### *iii. Scanning electron microscopy*

Scanning electron microscopy (SEM) provides images of the sample surface which has been scanned by a beam of electrons.[78] The image obtained by SEM corresponds to the interaction between scanning electrons and the atoms of the sample, giving therefore information about the sample's composition and surface topography. SEM has been widely used to characterize the morphology and size of supramolecular polymers and provide 3D information on the scanned samples. However, this technique also lacks the possibility to image solution-phase samples as they are usually drop-casted on conducting surfaces. The main differences between SEM and TEM regard: (i) the lower resolution (typically 5 nm) and (ii) the lack of information on the internal structure as the electron are collected by a back scattered detector (and not transmitted as for TEM). Importantly, TEM, AFM and SEM are regularly combined to fully study the morphology of the samples. For instance, the groups of Aida and Fukushima reported the use of these three techniques to fully characterize their supramolecular linear heterojunction based on gemini-shaped hexa-peri-hexabenzocoronene derivatives.[79] Whereas SEM revealed the presence of long micrometric nanotubular objects with bright and dark segments (Figure 12a), TEM confirmed the presence of two different block segments with different contrasts (Figure 12c). Finally, AFM in the tapping mode showed that both segments have different height profiles which correspond to the two different monomers used for these self-assembled objects (Figure 12b).

---

[78] Li, Z.-T. and Zhao, X. *Atomic Force Microscopy (AFM)* in Supramolecular Chemistry: From Molecules to Nanomaterials. Gale, P. A. and Steed, J. W. eds, Wiley-VCH, 2012, pp 619-631.

[79] Zhang, W.; Jin, W.; Fukushima, T.; Saeki, A.; Seki, S.; Aida, T. Supramolecular Linear Heterojunction Composed of Graphite-Like Semiconducting Nanotubular Segments. *Science* **2011**, *334*, 340-343.

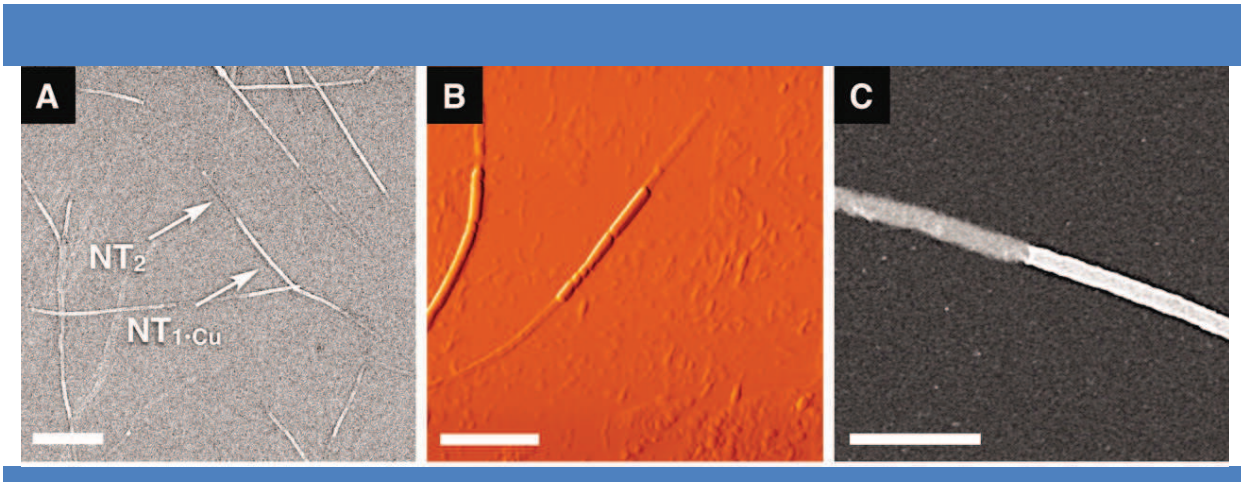

**Figure 12 | (A)** SEM (scale bar, 500 nm), (**B**) tapping-mode AFM (scale bar, 200 nm), and (**C**) scanning TEM (scale bar, 50 nm) micrographs of supramolecular linear heterojunction based on gemini-shaped hexa-peri-hexabenzocoronene derivatives.[79]

Finally, we would like to stress that other characterization methods such as rheology,[80] viscosimetry,[48] thermal analyses (isothermal titration calorimetry (ITC)[81] and differential scanning calorimetry (DSC)) have also been used to characterize supramolecular polymers. Whereas rheology and viscosimetry provide information on the mechanical properties of the self-assembled systems, ITC is used to determine the thermodynamic parameters of the non-covalent interactions in solution such as, for instance, binding affinity ($K_a$) and enthalpy changes ($\Delta H$) and DSC is a common method to probe phase transition and determine melting ($T_m$) or gel formation ($T_g$) temperature.

## 3. Mechanisms of supramolecular polymerization

Polymerization by covalent bond is mostly kinetically controlled because the potential barrier for the depolymerization reaction is often much larger than for the forward reaction. Whereas heating or diluting a macromolecule will not lead to a decrease of its molecular weight and degree of conversion, the situation is very different in supramolecular polymerization. Indeed, owing to the reversibility of the non-covalent interactions, the extent of reaction is directly related to thermodynamic factors such as temperature, concentration and the ratio of the monomers.

Depending on the equilibrium constant at each step of the polymerization, three main growth mechanisms have been described: isodesmic, ring-chain and cooperative

---

[80] Chassenieux, C. and Bouteiller, L. *Rheology* in Supramolecular Chemistry: From Molecules to Nanomaterials, Gale, P. A. and Steed, J. W. eds, Wiley-VCH, 2012, pp 517-528.

[81] Schmidtchen, F. P. *Isothermal Titration Calorimetry in Supramolecular Chemistry* in Supramolecular Chemistry: From Molecules to Nanomaterials, Gale, P. A. and Steed, J. W. eds, Wiley-VCH, 2012, pp 275-296.

supramolecular polymerization (Figure 13). However, as ring chain polymerization has been particularly observed for monomers presenting two reversible end groups connected via a flexible linker, we have decided to focus this introduction on isodesmic and cooperative polymerization mechanisms.

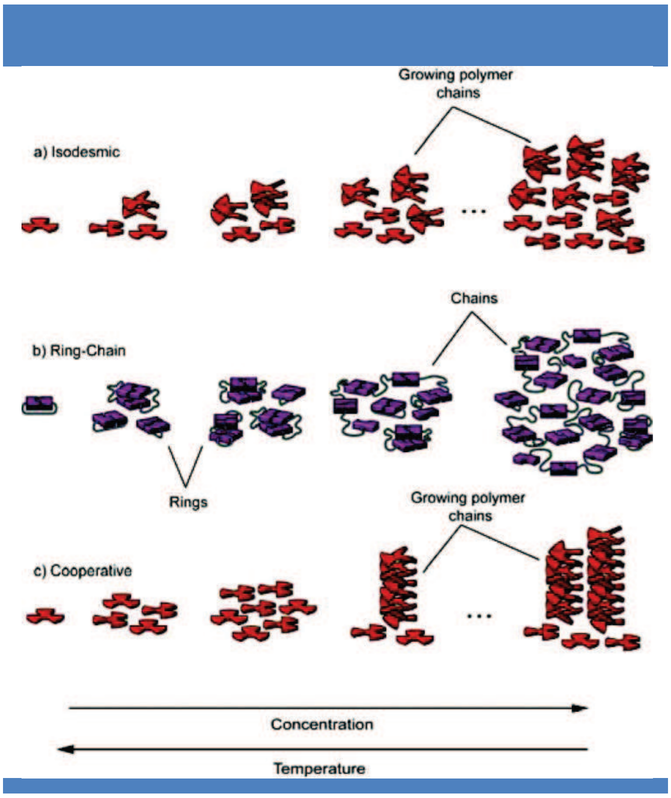

**Figure 13 |** Graphical representation of the three growth mechanisms by which a monomer can polymerize into a supramolecular polymer: a) isodesmic, b) ring-chain and c) cooperative supramolecular polymerization.

Isodesmic supramolecular polymerization occurs when the reversible formation of a noncovalent bond is identical at all steps in the polymerization process (Figure 14). This means that the addition of new monomeric units to the supramolecular polymer does not affect the reactivity of the end groups during the polymerization process. From the thermodynamic point of view, the molar equilibrium constant K is identical at each step of the self-assembly pathway. This results in an increase of the thermodynamic stability by the same amount at each step of the polymerization process.[16,82] Furthermore, as each step is equivalent, isodesmic polymerization is characterized by the absence of critical concentration or critical temperature for the self-assembly.

---

[82] De Greef, T. F. A. and Meijer, E. W. Supramolecular Polymerization. *Nature* **2008**, 453, 171-173.

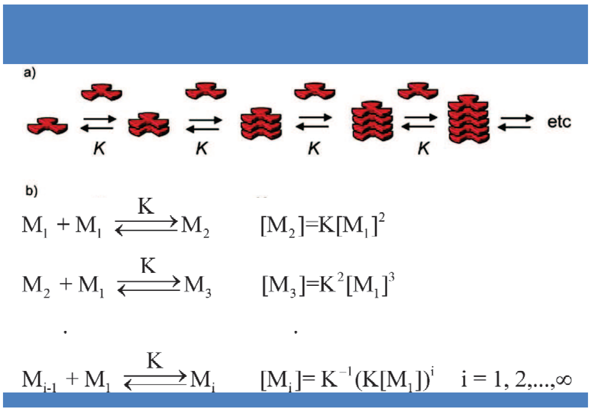

$$M_1 + M_1 \xrightleftharpoons{K} M_2 \qquad [M_2]=K[M_1]^2$$

$$M_2 + M_1 \xrightleftharpoons{K} M_3 \qquad [M_3]=K^2[M_1]^3$$

$$\cdot \qquad\qquad \cdot$$

$$M_{i-1} + M_1 \xrightleftharpoons{K} M_i \qquad [M_i]= K^{-1}(K[M_1])^i \quad i = 1, 2,\ldots,\infty$$

**Figure 14 |** a) Schematic representation of isodesmic supramolecular polymerizations of a rigid discotic molecule into a linear supramolecular polymer; b) Chemical equilibria involved in an isodesmic supramolecular polymerization. In both cases, *K* represents the intermolecular equilibrium constant, which, for an isodesmic supramolecular polymerization, is independent of the chain length.

For instance, the group of Würthner took advantage of various analytical experiments such as UV-Vis or NMR to demonstrate that PBI self-assemblies occurs predominantly via an isodesmic mechanism.[83]

Cooperative supramolecular polymerization, also called nucleation–growth polymerization, occurs through at least two different stages, resulting in either a cooperative or an anticooperative growth (Figure 15). In both cases, each stage is characterized by an isodesmic polymerization but with a different association constant K. For the cooperative growth, the first stage consists in an isodesmic polymerization with an association constant $K_n$ until a nucleus formed. The continuous additon of monomer to this nucleus then occurs with an association constant $K_e$ which is higher than $K_n$. For the anticooperative growth, the process is reverse, namely the first stage occurs with an association constant $K_n$ which is higher than the elongation one $K_e$. Therefore, a cooperative supramolecular polymerization is characterized by at least two different association constants which result in a critical concentration or temperature at which the supramolecular polymer starts growing.

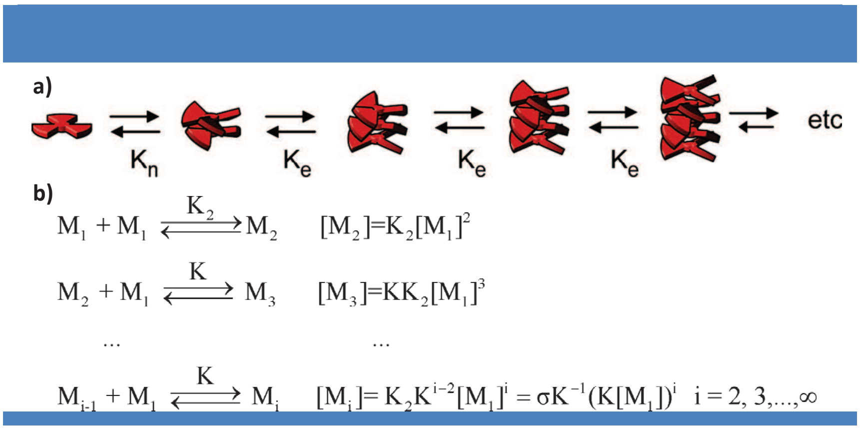

$$M_1 + M_1 \xrightleftharpoons{K_2} M_2 \qquad [M_2]=K_2[M_1]^2$$

$$M_2 + M_1 \xrightleftharpoons{K} M_3 \qquad [M_3]=KK_2[M_1]^3$$

$$\ldots \qquad\qquad \ldots$$

$$M_{i-1} + M_1 \xrightleftharpoons{K} M_i \qquad [M_i]= K_2K^{i-2}[M_1]^i = \sigma K^{-1}(K[M_1])^i \quad i = 2, 3,\ldots,\infty$$

**Figure 15 |** a) Schematic representation of a cooperative ($K_n < K_e$) supramolecular polymerization of a

---

[83] Chen, Z.; Lohr, A.; Saha-Möller, C. R. and Würthner, F. Self-assembled π-stacks of functional dyes in solution: structural and thermodynamic features. *Chem. Soc. Rev.* **2009**, *38*, 564–584.

rigid discotic molecule. In this cartoon, the dimer is the nucleus. b) Chemical equilibria involved in a cooperative supramolecular polymerization in which the dimer is the nucleus.

Models for cooperative polymerization processes using a variable nucleus size have been developed by Goldstein and Stryer.[84] However, most of the examples of cooperative supramolecular polymerizations analyzed so far consider a nucleus size of 2. One important parameter to estimate the degree of cooperativity is the σ parameter which can be defined as the ratio of $K_2/K$ where $K_2$ is the dimerization constant and K is the equilibrium constant for the elongation process. Therefore, when $\sigma < 1$, the process is cooperative and when $\sigma > 1$, the process is anticooperative. It should be noted that high degree of polymerization can be achieved not only by increasing K but also by decreasing σ. Finally, we would like to stress that the cooperativity in polymer growth is typically arising from three main origins: (i) electronic effects such as short-range polarization and long-range electrostatic effects, (ii) structural effects such as the formation of helical/tubular structures or allosteric effects and (iii) the hydrophobic effect.

The group of Bouteiller has developed the use of ITC to evidence the cooperative supramolecular polymerization of bis-urea monomers (see Chapter 2).[85] In that case, the cooperativity was driven by electronic effects, namely the polarization of the urea function after formation of dimers. The group of Meijer also had a great impact in the analysis of supramolecular polymerization mechanism.[16] In particular, they studied the cooperative supramolecular polymerization of properly-designed chiral oligo(*p*-phenylenevinylenes) into one-handed quasi 1D helical structures using temperature-dependant CD and UV-Vis spectroscopy.[66b] In this example, allosteric effects, namely the rearrangement of the monomeric structure to a thermodynamically less favored conformation, are probably at the origin of the cooperative growth. Obviously, most of the experimental techniques described in the previous chapter can be used to investigate the supramolecular polymerization mechanism. Compared with the experimental techniques, very few computational investigations exist to investigate the polymerization mechanism.[86] Up to now, only atomistic simulations and density functional theory (DFT)-based calculations have been used.[87]

---

[84] Goldstein, R. F. and Stryer, L. Cooperative polymerization reactions. Analytical approximations, numerical examples, and experimental strategy. *Biophys. J.* **1986**, *50*, 583-599.

[85] Arnaud, A. and Bouteiller, L. Isothermal Titration Calorimetry of Supramolecular Polymers. *Langmuir* **2004**, *20*, 6858-6863.

[86] Maiti, P. K.; Lansac, Y.; Glaser, M. A. and Clark, N. A. Isodesmic Self-Assembly in Lyotropic Chromonic Systems. *Liquid Cryst.* **2002**, *29*, 619-626.

[87] (a) Grimme, S.; Antony, J.; Schwabe, T. and Mück-Lichtenfeld, C. Density Functional Theory with Dispersion Corrections for Supramolecular Structures, Aggregates, and Complexes of (Bio)Organic Molecules. *Org. Biomol. Chem.* **2007**, *5*, 741-758; (b) Grimme, S. Supramolecular Binding Thermodynamics by Dispersion-Corrected Density Functional Theory. *Chem. Eur. J.* **2012**, *18*, 9955-9964.

# 4. Functional supramolecular polymers

Over the last two decades, supramolecular chemistry has been extensively developed towards functional supramolecular systems.[88] In particular, supramolecular polymers have been shown to produce structures that can be achieved by classical covalent polymers along with processability, recycling and/or self-healing properties owing to the reversibility of their non-covalent linkages.[89] These strong and directional interactions impart high degrees of internal order and dynamic to the supramolecular polymers, which have become promising candidates for applications in the fields of biomedicine, sensing, catalysis, and organic electronics.[88] In the following sections, we will briefly highlight some selected examples of functional supramolecular polymers in these active domains of applications.

## a. Supramolecular polymers for biomedical applications

Inspired by biological systems that extensively used non-covalent interactions, supramolecular polymers have been developed for biomedical applications along three main topics: (i) diagnostic and biomedical sensing, (ii) gene and drug delivery and (iii) regenerative medicine and tissue engineering. For instance, the group of Lee developed some synthetic functional analogs of filamentous viruses based on β-sheet peptides, which self-assemble into nanoribbons that interact with siRNA to form filamentous complexes.[90] When decorated with sugars, these bioinspired structures have been shown to enhance endocytosis in cancer cells, which promote them as potential candidates for gene or drug delivery. The group of Stupp has been very active in the development of peptide amphiphiles for biomedical applications, particularly in the field of regenerative medicine.[91] For instance, they developed a peptide amphiphile that contains a series of 23 amino-acids and whose self-assembled nanostructure mimics the activity of one of the most potent angiogenic signaling proteins (VEGF).[92] The self-assembled nanofibers were indeed shown to promote angiogenesis *in vitro* and to repair ischemic hind-limb tissue in mouse *in vivo*. These examples clearly highlight the potential of self-assembled systems for biomedical applications and because of their kinetic lability, they offer some great advantages such as self-construction and degradability.

---

[88] Busseron, E.; Ruff, Y.; Moulin, E. and Giuseppone, N. Supramolecular self-assemblies as functional nanomaterials. *Nanoscale* **2013**, *5*, 7098-7140.

[89] Aida, T.; Meijer, E. W. and Stupp, S. I. Functional Supramolecular Polymers. *Science* **2012**, *335*, 813-817.

[90] Lim, Y.-B.; Lee, E.; Yoon, Y.-R.; Lee, M. and Lee, M. Filamentous Artificial Virus from a Self-Assembled Discrete Nanoribbon. *Angew. Chem. Int. Ed.* **2008**, *47*, 4525–4528.

[91] Boekhoven, J. and Stupp, S. I. 25th Anniversary Article: Supramolecular Materials for Regenerative Medicine. *Adv. Mater.* **2014**, *26*, 1642–1659.

[92] Webber, M. J.; Tongers, J.; Newcomb, C. J.; Marquardt, K.-T.; Bauersachs, J.; Losordo, D. W. and Stupp, S. I. Supramolecular nanostructures that mimic VEGF as a strategy for ischemic tissue repair. *Proc Natl Acad Sci USA* **2011**, *108*, 13438–13443.

### b. Supramolecular polymers for sensing

Sensing is a major issue both in biomedical science to detect markers of diseases or active species and in environmental science for the detection of chemical analytes in water or food for instance. Many approaches developed in biomedicine take advantage of nanoparticles which changes their optical properties upon sensing.[88] Some strategies based on self-assembled nanostructures have also emerged and hydride materials have also been considered for such applications. For instance, Hamachi and coworkers described a hybrid hydrogel based on supramolecular fibers (formed by the cooperative action of four non-covalent interactions) and fluorescent dyes absorbed on montmorillonite to sense spermidine and spermine in artificial urine.[93] One great advantage of this hybrid sensor is that it can be used as a rapid naked-eye detector for polycationic amines. Self-assembled structures such as the one depicted on Figure 4 have also been used as contrast-enhanced MRI probes both *in vitro* and *in vivo* for imaging the mouse brain vasculature at Gd(III) doses far below those of clinical contrast agents.[94] The high stability of these supramolecular structures (mainly driven by electrostatic interactions) along with their good clearance rate and nanometric size (6 nm) seem very promising for future development in molecular imaging.

### c. Supramolecular polymers for catalysis

Inspired by enzymes which perform catalytic reactions in confined and well-structured environment and concerned by the reduction of costs and wastes in chemical processes, supramolecular chemists have developed supramolecular polymers that can enhance the efficiency and selectivity of chemical reactions. For instance, the group of Shimizu developed some porous crystals arising from the self-assembly of bis-urea macrocycles to promote the selective photopolymerization of coumarin.[95] Importantly, the stabilization of the host coumarin via π-π interactions led to an unexpected anti head-to-head dimer with a very high selectivity. The group of Miravet took advantage of the thermoresponsive gelation of a low-molecular weight pseudopeptidic hydrogelator incorporating two proline residues to enhance the yield of the Henry nitroaldol reaction between 4-nitrobenzaldehyde and nitromethane.[96] Importantly, owing to the reversible nature of the hydrogen-bonding

---

[93] Ikeda, M.; Yoshii, T.; Matsui, T.; Tanida, T.; Komatsu, H. and Hamachi, I. Montmorillonite−Supramolecular Hydrogel Hybrid for Fluorocolorimetric Sensing of Polyamines*. J. Am. Chem. Soc.* **2011**, *133*, 1670-1673.

[94] Besenius, P.; Heynens, J. L. M.; Straathof, R.; Nieuwenhuizen, M. M. L.; Bomans, P. H. H.; Terreno, E.; Aime, S.; Strijkers, G. J.; Nicolay, K. and Meijer, E. W. Paramagnetic Self-Assembled Nanoparticles as Supramolecular MRI Contrast Agents. *Contrast Media Mol. Imaging* **2012**, *7*, 356-361.

[95] Dawn, S.; Dewal, M. B.; Sobransingh, D.; Paderes, M. C.; Wibowo, A. C.; Smith, M. D.; Krause, J. A.; Pellechia, P. J. and Shimizu, L. S. Self-Assembled Phenylethynylene Bis-urea Macrocycles Facilitate the Selective Photodimerization of Coumarin. *J. Am. Chem. Soc.* **2011**, *133*, 7025–7032.

[96] Rodríguez-Llansola, F.; Escuder, B. and Miravet, J. F. Switchable Perfomance of an L-Proline-Derived Basic Catalyst Controlled by

interactions involved in the self-assembly process, the catalytic activity could be easily controlled by modulating the temperature.

### d. Supramolecular polymers for organic electronics

Finally, owing to the importance of electronics in our everyday life, organic electronics appear as a promising field to produce flexible and low-cost electronic devices. In particular, supramolecular organic electronics has become very popular to build up nanometric objects with good conducting properties and easy processability.[97] Additionally, owing to the reversible nature of the non-covalent interactions, various morphologies can be reached from a single building and lead to different conducting properties. This was indeed the case for the group of Bouvet who describes an amphiphilic PBI whose nanostructures vary depending on the solvent used for its solution-phase processing.[98] Importantly, the 1D nanobelts obtained from methanol (which favors π-π stacking interactions between perylene rings) showed one order of magnitude higher conductivity than the 2D nanoleaves obtained from hexane. The group of Meijer reported also that the supramolecular copolymerization of fluorene, oligo(p-phenylenevinylene) and perylene through quadruple hydrogen bonding interactions can generate white light emitting devices when an appropriate ratio of oligomers is used.[99] This example clearly demonstrates that multicomponent systems are promising for functional optoelectronic materials and we will see in Chapter 4 that they have also been used for biological applications.

---

Supramolecular Gelation. *J. Am. Chem. Soc.* **2009**, *131*, 11478–11484.

[97] (a) Moulin, E.; Cid, J. J. and Giuseppone, N. Advances in Supramolecular Electronics – from Randomly Self-Assembled Nanostructures to Addressable Self-Organized Interconnects. *Adv. Mater.* **2013**, *25*, 477-487; (b) Babu, S. S.; Prasanthkumar, S. and Ajayaghosh, A. Self-Assembled Gelators for Organic Electronics. *Angew. Chem. Int. Ed.* **2012**, *51*, 1766-1776; (c) Hasegawa, M. and Iyoda, M. Conducting Supramolecular Nanofibers and Nanorods. *Chem. Soc. Rev.*. **2010**, *39*, 2420-2427.

[98] Chen, Y.; Feng, Y.; Gao, J. and Bouvet, M. Self-assembled aggregates of amphiphilic perylene diimide–based semiconductor molecules: Effect of morphology on conductivity. *J. Coll. Int. Sci.* **2012**, *368*, 387-394.

[99] Abbel, R.; Grenier, C.; Pouderoijen, M. J.; Stouwdam, J. W.; Leclère, P. E. L. G.; Sijbesma, R. P.; Meijer, E. W. and Schenning, A. P. H. J. White-Light Emitting Hydrogen-Bonded Supramolecular Copolymers Based on π-Conjugated Oligomers. *J. Am. Chem. Soc.* **2009**, *131*, 833–843.

# Chapter 2: Supramolecular polymers based on bisurea motifs

Among all the non-covalent interactions used to build supramolecular polymers, the hydrogen bond has been widely used to access various supramolecular structures ranging from finite-sized assemblies to three-dimensional (3D) networks.[100] Although the strength of a single hydrogen bond is not sufficient to drive the formation of a self-assembly, its combination with other interactions/forces or the use of multiple-hydrogen bonding motifs have led to the development of numerous examples of supramolecular polymers incorporating this highly directional non-covalent interaction. As mentioned previously, Lehn was the first one to build up such polymers based on diaminopyridine and uracil units.[18] A couple of years later, the group of Meijer reported the first hydrogen-bonded polymer that incorporate a urea motif within a quadruple hydrogen bonding unit.[24] The group of Feringa was then the first one to report the formation of a functional supramolecular polymer based on a bis-urea small molecule which presents gelation properties.[101] The main driving force for the self-association of urea motifs is the formation of a 6-membered hydrogen bonded ring based on two donors and one carbonyl acceptor. Up to now, the bisurea motif has been widely used to construct self-assembled structures that possess gelation properties.[102] However, in the following sections of this chapter, we will focus only on monofunctional bis-urea molecules which incorporate polyethyleneglycol (PEG), fluorescent or peptidic chains on the external nitrogen atoms.

## 1. Bisurea-polyethylene glycol supramolecular polymers

The first example of bis-urea based supramolecular polymer that incorporate PEG units as side chains was described by the group of Sijbesma in 2005.[103] An amphiphilic triblock molecule was designed with a hydrophobic core that incorporates the bis-urea groups and hydrophilic PEG units as side chains (Figure 16a). A combination of FTIR, cryo-TEM, viscosimetry and DLS experiments was used to reveal the formation of cylindrical micelles which aggregate in water. Compared to a similar amphiphilic molecule that do not incorporate

---

[100] (a) Armstrong, G. and Buggy, M. Hydrogen-bonded supramolecular polymers: A literature review. *J. Mater. Sci.* **2005**, *40*, 547– 559; (b) Bouteiller, L. Assembly via Hydrogen Bonds of Low Molar Mass Compounds into Supramolecular Polymers. *Adv. Polym. Sci.* **2007**, *207*, 79–112.

[101] van Esch, J.; Kellogg, R. M.; Feringa, B. L. Di-urea compounds as gelators for organic solvents. *Tetrahedron Lett.* **1997**, *38*, 281-284.

[102] Steed, J. W. Anion-tuned supramolecular gels: a natural evolution from urea supramolecular chemistry. *Chem. Soc. Rev.* **2010**, *39*, 3686–3699.

[103] Chebotareva, N., Bomans, P. H. H.; Frederik, P. M.; Sommerdijk, N. A. J. M; and Sijbesma, R. P. Morphological Control and Molecular Recognition by Bis-Urea Hydrogen Bonding in Micelles of Amphiphilic Tri-Block Copolymers. *Chem. Commun.* **2005**, *39*, 4967-4969.

the bis-urea motif, the hydrogen-bonding interactions constrain the packing of the hydrophobic part and the PEG chains are forced to stretch, which results in a larger diameter for the core and a shorter length of the cylindrical micelles.

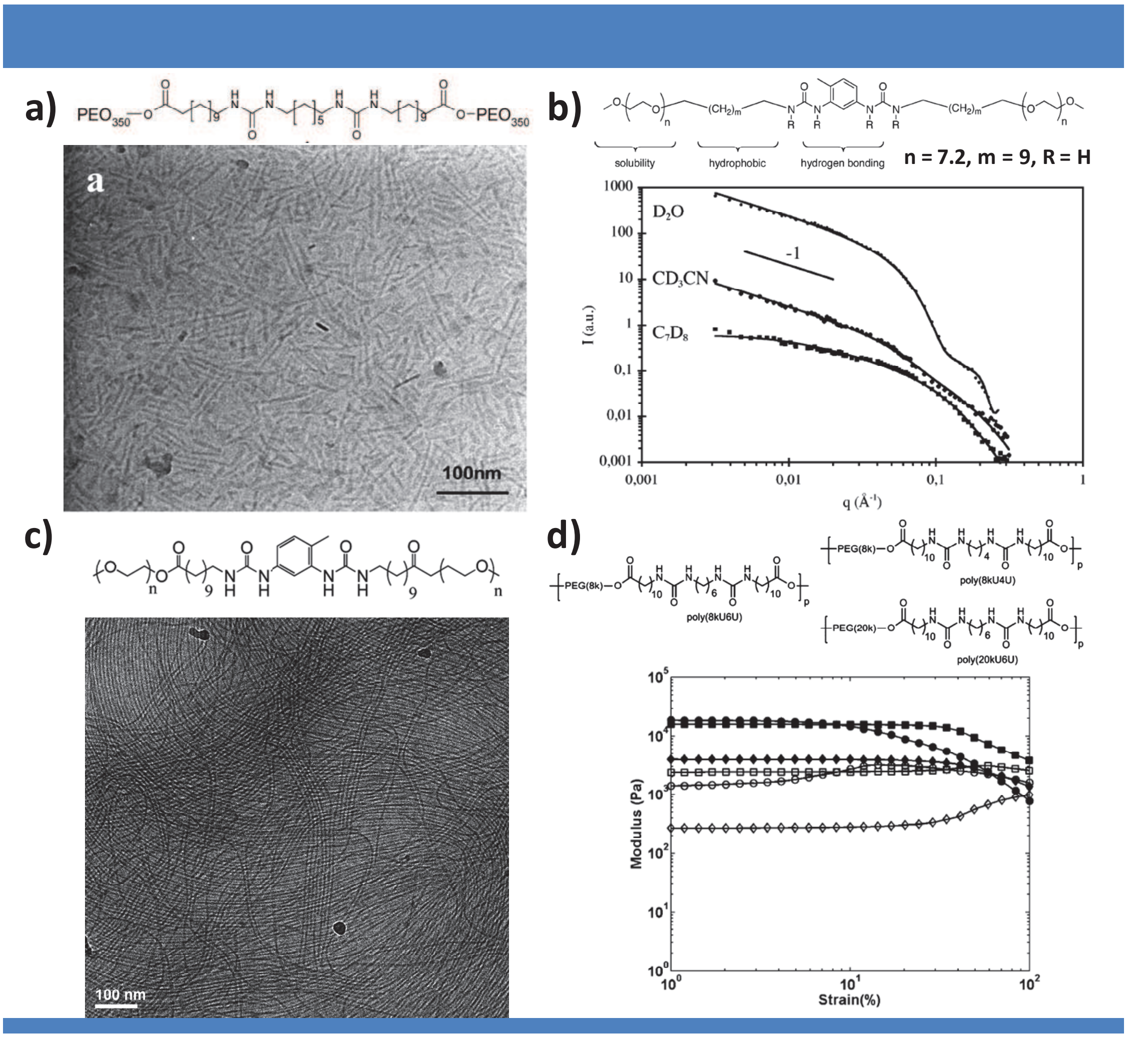

**Figure 16 |** a) (i) Molecular structure of a bisurea-PEG compound synthesized by Sijbesma and co-workers; (ii) Cryo-TEM images of 1 wt% micellar solutions of this compound; b) (i) Structure of bisurea-PEG compound synthesized by Bouteiller *et al.*; (ii) SANS intensity (*I*) versus scattering vector (*q*) for solutions of this compound in $D_2O$, $d_3$-acetonitrile, and $d_8$-toluene at 5 g/L (4 mM) and 22 °C; c) (i) Molecular structure of an oligomer with 4 bisurea units synthesized by Bouteiller and co-workers; (ii) Cryo-TEM of a 0.25% water solution of this monomer; (d) i) Molecular structures of segmented copolymers used by Sijbesma *et al.*; (ii) Yielding behavior in oscillatory rheological measurements. Strain sweeps at a frequency of 1 rad/s for poly(8kU4U) (G′ (■), G″ (□)), poly(8kU6U) (G′ (●), G″ (○)), and poly(20kU6U) (G′ (□), G″ (◊)), performed at 10 wt % concentration.

Shortly after, Bouteiller and co-workers reported the synthesis of bisurea-PEG derivatives with a similar design, namely a hydrophobic core with the bis-urea groups and PEG side chains (Figure 16b).[104] The self-assemblies of these compounds were studied in various solvent ranging from water to toluene. In all kinds of solvents (protic and aprotic polar, non polar), elongated filaments with a cross-section close to the dimension of the

---

[104] Obert, E., Bellot, M.; Bouteiller, L.; Andrioletti, F.; Lehen-Ferrenbach, C. and Boué, F. Both Water- and Organo-Soluble Supramolecular Polymer Stabilized by Hydrogen-Bonding and Hydrophobic Interactions. *J. Am. Chem. Soc.* **2007**, *129*, 15601-15605.

molecular unit were formed as demonstrated by SANS experiments but difference in their packing mode could be observed. Indeed, whereas the filament with the largest cross-section was formed in water because of the hydrophobic interactions, the more compact structure was observed in toluene where both hydrophobic and solvophobic forces are absent. Interestingly, the results obtained from SANS could be corroborated by a qualitative analysis of ITC experiments. Later, based on a similar design, the same group synthesized several oligomers with up to 9 bis-urea units on the macromolecule (Figure 16c).[105] Interestingly, none of these oligomers were soluble in water, except the one with only a single bis-urea motif whereas the best solubility for all samples was observed in methanol. In that solvent, oligomers with 2 and 3 bis-urea units were shown to display gelation properties. Using a combination of SANS and cryo-TEM, the presence of long and rigid filaments was observed for the oligomer in water and for the oligomers that induce gelation.

The group of Sijbesma also reported concomitantly the formation of hydrogels from high-molecular weight copolymers with segmented hydrophobic bisurea hard segments and hydrophilic PEG segments (Figure 16d).[106] In this work, DSC measurements reveal the presence of two transitions arising from the melting points of the PEG segments (T~50°C) and the hydrogen-bonded hydrophobic segments (T > 170°C). Importantly, the combined use of AFM and SAXS did not permit to precisely establish the structure of the objects. Extensive rheological experiments demonstrated that the length of the PEG segments affects the modulus of the hydrogel. From the application point of view, these hydrogels were shown to be injectable, biocompatible, and biodegradable as demonstrated by a toxicity XTT assay.

Finally, we would like to mention the work of Meijer who reported the formation of transient supramolecular network *via* hydrogen bonding in water.[107] In that case, the PEG unit was modified at both end by an alkyl spacer (C6 to C12) and used as linker between the two urea motifs. Although the main driving force for the self-assembly is the presence of ureidopyrimidinone as end groups on the bis-urea scaffold, these latter groups provide additional lateral interactions which results in the formation of high aspect ratio nanofibers as demonstrated by cryo-TEM, AFM, DLS and SLS. These supramolecular polymers could be loaded with dyes and proteins and were successfully used as protein delivery carriers in kidney regeneration.

---

[105] Tharcis, M.; Breiner, T.; Belleney, J.; Boué, F. and Bouteiller, L. Hydrogen Bonded Supramolecular Polymers in Protic Solvents: Role of Multitopicity. *Polym. Chem.* **2012**, *3*, 3093-3099.

[106] Pawar, G. M., Koenigs, M.; Fahimi, Z.; Cox, M.; Voets, I. K.; Wyss, H. M. and Sijbesma, R. P. Injectable Hydrogels from Segmented Peg-Bisurea Copolymers. *Biomacromolecules* **2012**, *13*, 3966-3976.

[107] Dankers, P. Y. W. et al. Hierarchical Formation of Supramolecular Transient Networks in Water: A Modular Injectable Delivery System. *Adv. Mater.* **2012**, *24,* 2703–2709.

## 2. Fluorescent bisurea-based supramolecular polymers

As described in the previous chapter, building supramolecular polymers with a precise function has become a major issue. Here, we would like to present some selected example of bis-urea supramolecular polymers which present fluorescent properties. In 2005, the group of Ajayasghosh reported the synthesis of bisurea tethered oligo(phenylenevinylene)s (OPVs) monomers which form self-assembled structures in non polar solvents such as cyclohexane as demonstrated by UV-Vis and fluorescence experiments (Figure 17a).[108] Interestingly, whereas the monomeric unit displayed fluorescence in chloroform, this fluorescence was quenched in cyclohexane due to both H-bonding between the urea groups and π-stacking between the aromatic moieties. Importantly, this fluorescence could be restored upon addition of fluorine ions as a result of the competition of halide anions with urea hydrogen-bonds. This example clearly shows that the non-covalent interactions between monomers induce properties that the monomer itself does not have. Whereas the OPV moiety in this example was incorporated in between the two urea units, Yagai and co-workers designed a bis-urea monomer with OPV groups as side chains (Figure 17b).[109] The formation of long fibrous aggregates in methylcyclohexane (MCH) was demonstrated using DLS, AFM and SEM experiments, as a result of van der Waals interactions of the alkyl side chains, hydrogen-bonding of the ureas and π-π stacking of the OPVs. UV-Vis and fluorescent experiments were also used to study the monomer in THF, the stabilities of supramolecular polymers in mixtures of THF/MCH, and the temperature-dependent transition from aggregated state to monomeric units in MCH. Additionally, these molecules displayed gelation and fluorescent properties in various organic solvents, whereas the corresponding mono-urea monomer did not give rise to gelation in most of the solvents considered.

---

[108] Varghese, R.; George, S. J. and Ajayaghosh, A. Anion Induced Modulation of Self-Assembly and Optical Properties in Urea End-Capped Oligo(P-Phenylenevinylene)S. *Chem. Commun.* **2005**, 593-595.

[109] Yagai, S., Kubota, S.; Iwashima,T.; Kishikawa, K.; Nakanishi, T.; Karatsu, T. and Kitamura, A. Supramolecular Polymerization and Polymorphs of Oligo(P-Phenylene Vinylene)-Functionalized Bis- and Monoureas. *Chem. Eur. J.* **2008**, *14*, 5246-5257.

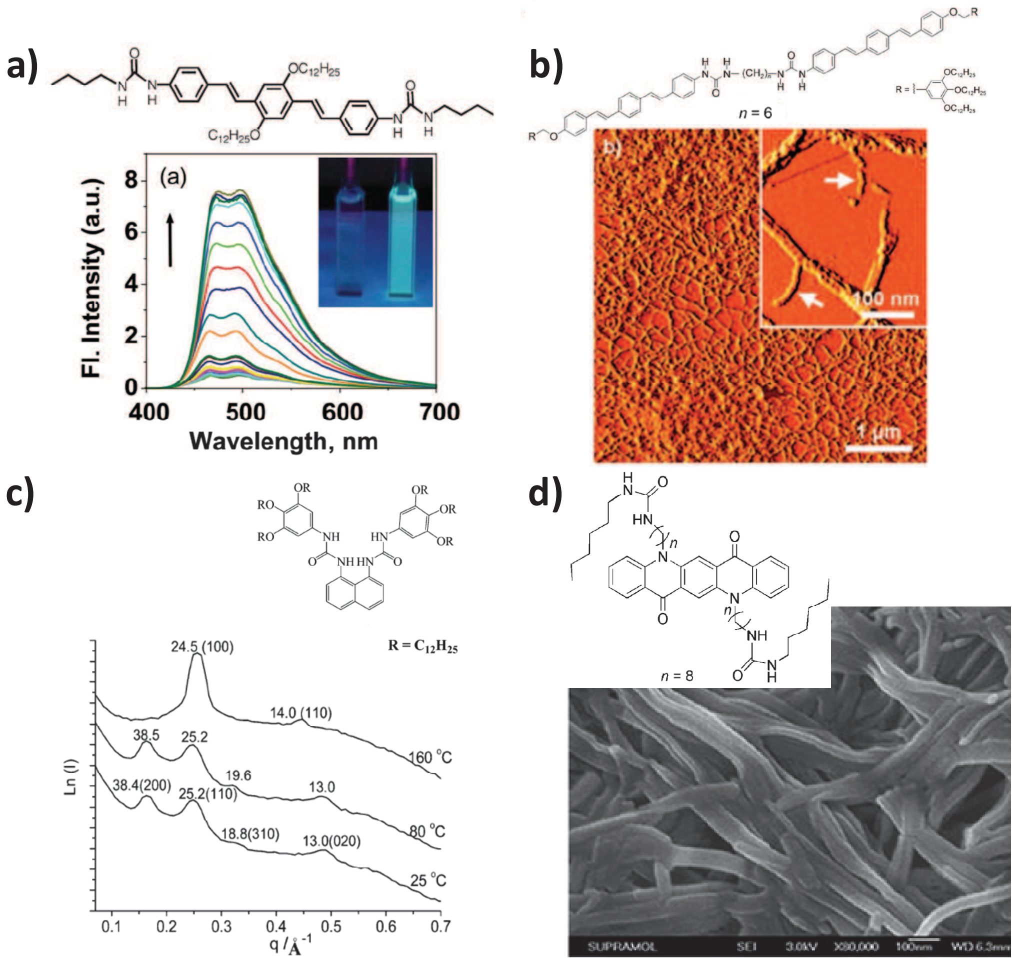

**Figure 17 |** a) Molecular structure of bisurea tethered OPV (BU-OPV) molecules studied by the group of Ajayasghosh and Changes in the emission spectra of BU-OPV (1.1 × $10^{-5}$ M) in $C_6H_{12}$–$CHCl_3$ (16:1) upon increasing addition of TBAF. Inset: photograph under UV light showing emission of BU-OPV (left) and strong emission of BU-OPV/TBAF complex (right); b) Molecular structures of OPV-functionalized bisureas studied by Yagai and co-workers and AFM phase images of this molecule spin coated on HOPG from a MCH dispersion (c= 5.0 × $10^{-5}$ M). Inset show a high-resolution image. Arrows indicate a single supramolecular polymer; (c) Molecular structure of a bisurea derivative with a naphthalene spacer studied by the groups of Yi and Li and Variable-temperature SAXS patterns of this molecule; (d) (i) Bisurea derivative studied by Zhang, Wang and co-workers and FE-SEM image of the corresponding xerogel in DMF after rapid cooling. Scale bars: 100 nm.

Two other stimuli-responsive fluorescent organogels driven by hydrogen-bonding of bis-urea units and π-π stacking interactions have been reported.[110] In the first one, the groups of Yi and Li synthesized bisurea derivatives with a naphthalene spacer and showed their gelation properties in various solvents (Figure 17c).[110a] Compared to the solution state, a strong fluorescent emission appeared in the gel state or upon addition of fluoride anions to the solution. The gel-sol transition was shown to be sensitive to temperature and fluoride anions

---

[110] (a) Yang, H., Yi, T.; Zhou, Z.; Zhou, Y.; Wu, J.; Xu, M.; Li, F. and Huang, C. Switchable Fluorescent Organogels and Mesomorphic Superstructure Based on Naphthalene Derivatives. *Langmuir* **2007**, *23*, 8224-8230; (b) Dou, C., Wang, C.; Zhang, H.; Gao, H. and Wang, Y. Novel Urea-Functionalized Quinacridone Derivatives: Ultrasound and Thermo Effects on Supramolecular Organogels. *Chem.Eur. J.* **2010**, *16*, 10744-10751.

whereas the addition of TFA to a solution with fluorine anions led to the recovery of the gel state with different morphologies and optical properties. Additional SAXS experiments were performed to determine the different structure parameters as a function of the temperature. In the other example, Zhang, Wang and co-workers reported the synthesis of bis-urea monomers with a quinacridone chromophore between the hydrogen-bonding units (Figure 17d).[110b] These compounds were shown to respond to temperature and ultrasound irradiation to form stimuli-responsive organogels. SEM, DSC, $^1$H NMR and FTIR experiments were used to characterize the gelation properties and the role of the non-covalent interactions for these properties. Additional UV-Vis, XRD and fluorescence experiments supported the possible face-to-face arrangement of the monomers and the directionality of the hydrogen bonds. All these examples highlight the potential of fluorescent bis-urea-based supramolecular polymers as multiresponsive materials and for chemical sensing in particular.

Finally, we would like to mention the work by Jia, Wei and co-workers who described the organogelation properties of a bis-urea monomer with a 2,2'-diaminobiphenyl linker as fluorescent probe and a dipeptide (glycine-glutamic-acid) as side end groups.[111] In ethanol and isopropanol, this molecule is forming gels made of intertwined fibers with larger aspect ratio as demonstrated by TEM and confirmed by SAXS. Interestingly, the addition of fluorine anions to an acetonitrile solution of this molecule induced a conformational change of the self-assembled structure (proved by CD) which resulted in strong blue fluorescence under classical UV light.

## 3. Bisurea-based supramolecular polymers with amino-acid residues

Oligomeric peptidomimetics containing urea motifs in their backbone have been studied for more than 15 years as potential inhibitors of protein-protein or protein-RNA interactions, neuropeptides analogues or even as potential disrupting agents of bacterial membranes.[112] However, although most of these molecules were shown to arrange in supramolecular structures such as α-helices, their self-assembly in main-chain supramolecular polymers have not been mentioned. It is important to mention that, except the example presented in the previous section, mostly single amino-acid units have been incorporated on bis-urea scaffolds

---

[111] Teng, M.; Kuang, G.; Jia, X.; Gao, M.; Lia, Y. and Wei, Y. Glycine-glutamic-acid-based organogelators and their fluoride anion responsive properties. *J. Mater. Chem.* **2009**, *19*, 5648–5654.

[112] Fischer, L. and Guichard, G. Folding and self-assembly of aromatic and aliphatic urea oligomers: Towards connecting structure and function. *Org. Biomol. Chem.* **2010**, *8*, 3101-3117.

as end groups. For instance, the group of Hamilton was the first one to describe the synthesis bis-urea molecules with incorporate aspartic acid moieties at both ends (Figure 18a).[113] Depending on the ester groups introduced on the amino acid residue, such compounds were able to form gel in supercritical carbon dioxide[113a] but also in buffers at pH ranging from 5.9 to 7.9.[113b] SEM was then used to determine the morphology of the aggregates. In most cases, fibrillar materials were observed and the fibers formed in water could even be seen using classical optical microscope. Interestingly, as demonstrated by CD experiments and potentiometric titrations in water, the gelation property was greatly affected by pH modulation due to the presence of one free carboxylic acid on each aspartic acid residue, but hydrophobic interactions were shown to be the main driving force for gelation. Some years later, this was confirmed by the elucidation of the molecular arrangement of these hydrogelators using a combination of cryo-TEM and X-ray diffraction techniques.[114]

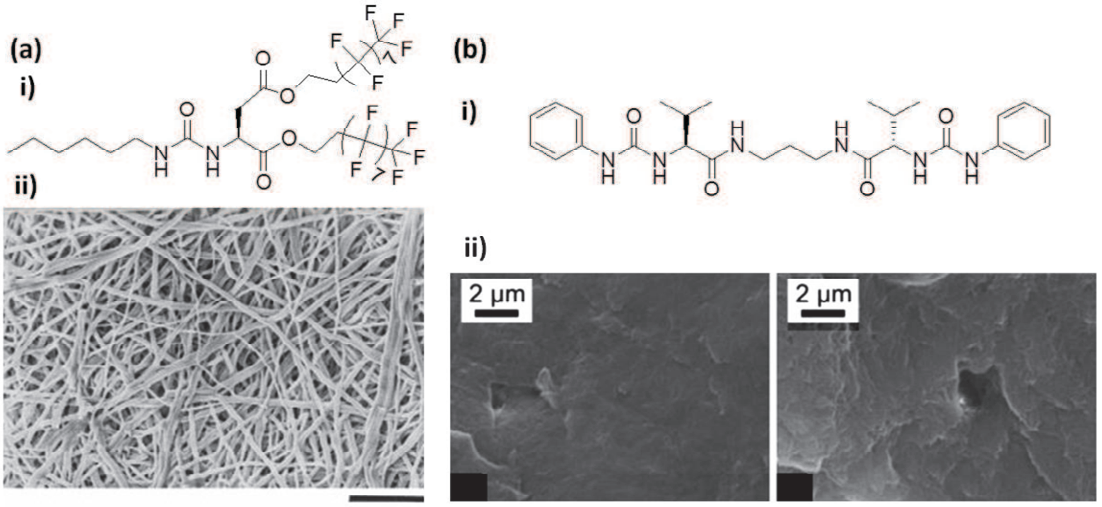

**Figure 18 |** a) (i) Molecular structure of one bisurea molecule with aspartic acid end groups studied by Hamilton *et al.,* (ii) SEM image of the corresponding foam produced at 2.2% initial composition in $CO_2$, scale bars: 5 mm; (b) (i) Bisurea derivatives studied by the group of Luis; (ii) SEM micrographs of this molecules grown from: (left) $CHCl_3$, (right) $CHCl_3$+5% MeOH.

In 2010, Steed and co-workers reported the synthesis of several bis-urea gelators, one of them incorporating one phenylalanine residue at each end.[115] Using SEM, the dried xerogels obtained from this latter compound in various solvents showed all fibrillar morphologies and rheology measurements demonstrated that the addition of acetate anions results in the

---

[113] (a) Shi, C.; Huang, Z.; Kilic, S.; Xu, J.; Enick, R. M.; Beckman, E. J.; Carr, A. J.; Melendez, R. E. and Hamilton, A. D. The Gelation of $CO_2$: A Sustainable Route to the Creation of Microcellular Materials. *Science* **1999**, *286*, 1540-1543; (b) Estroff, L. A. and Hamilton, A. D. Effective Gelation of Water Using a Series of Bis-urea Dicarboxylic Acids. *Angew. Chem. Int. Ed.* **2000**, *39*, 3447–3450.

[114] Estroff, L. A.; Leiserowitz, L.; Addadi, L.; Weiner, S. and Hamilton, A. D. Characterization of an Organic Hydrogel: A Cryo-Transmission Electron Microscopy and X-Ray Diffraction Study. *Adv. Mater.* **2003**, *15*, 38-42.

[115] Foster, J. A.; Piepenbrock, M.-O. M.; Lloyd, G. O.; Clarke, N.; Howard, J. A. K. and Steed, J. W. Anion-Switchable Supramolecular Gels for Controlling Pharmaceutical Crystal Growth. *Nature Chem.* **2010**, *2*, 1037-1043.

breakdown of the gel. These gels were ultimately used to grow crystals from several pharmaceutical compounds such as ibuprofen or paracetamol. By slowing down the crystallization process, larger and more uniform crystals were obtained in comparison to solution-phase crystallization without the formation of gelator-substrate co-crystal.

Recently, the group of Luis synthesized various bisurea pseudopeptidic compounds with two amino acids (phenylalanine or valine) located at both ends of a spacer in between the two urea units (Figure 18b).[116] Most of the compounds with a flexible aliphatic linker displayed gelation properties in a large variety of organic solvents (from DMF to chloroform). $^1$H NMR and DSC experiments were used to demonstrate that these gels are thermally stable even at high temperatures (above 100 °C). The comparison with similar compounds that lack the bis-urea groups and do not gelify clearly demonstrates the importance of the hydrogen bonding interactions in the self-assembling process.

Finally, we would like to point out the work of DiMasi and Sommerdijk who reported the formation of self-organizing surfactants which consist in an alkyl chain connected via a bisureido-heptylene unit to an amino acid head group.[117] These molecules were shown to form monolayers whose density is altered by the choice of the amino acid. Whereas glycine and alanine based surfactants formed very rigid monolayers, valine and leucine ones led to more flexible monolayers that reorganize their structure upon complexation of calcium ions. Importantly, although all surfactants were active for the nucleation of $CaCO_3$, they led to different nucleation phase depending on the rigidity of the monolayer.

## 4. Other bisurea-based supramolecular polymer

In the previous sections, we have seen that many supramolecular polymers that incorporate the bis-urea motif have been decorated with PEG chains, fluorescent units or even amino-acid residues. Most of these polymers are forming organo- or hydrogels and can be potentially used as sensors or as an inert matrix to grow crystals. In this section, we would like to highlight some selected examples of hydrophobic bisurea-based supramolecular polymer that have been used as functional materials. In 1997, Feringa and coworkers described a series of bisurea-based compounds (Figure 19a), which assembled into ribbons on graphite as demonstrated by scanning tunneling microscopy and fibers in various solvents, as

---

[116] Rubio, J., Martí-Centelles, V.; Burguete, M. I. and Luis, S. V. Synthesis and Organogelating Ability of Bis-Urea Pseudopeptidic Compounds. *Tetrahedron* **2013**, *69*, 2302-2308.

[117] Popescu, D. C. et al. Template Adaptability Is Key in the Oriented Crystallization of $CaCO_3$. *J. Am. Chem. Soc.* **2007**, *129*, 14058-14067.

confirmed by electron microscopy and X-ray powder diffraction.[118] Interestingly, these fibers formed an extended three-dimensional network in solution leading to efficient gelation properties in *p*-xylene, for instance. The gels are shown to be stable even at 100 °C by DSC experiments, but can be readily disrupted by mechanical stirring.

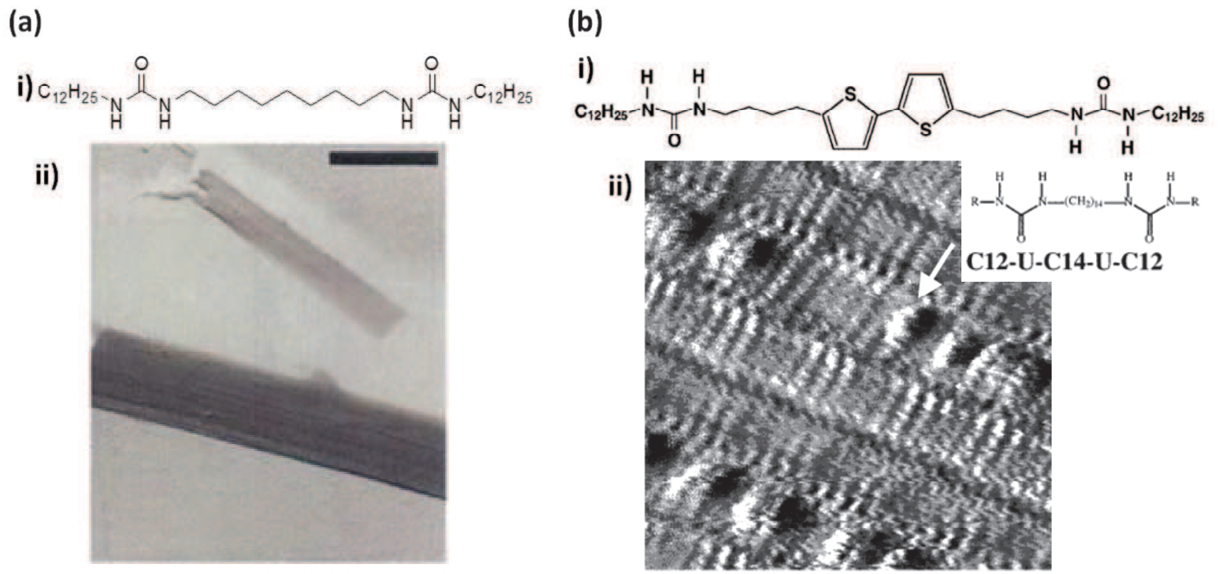

**Figure 19 |** a) (i) Molecular structure of the bisurea compound studied by Feringa and co-workers; (ii) Electron micrograph of the corresponding gel in tetralin, scale bars: 500 nm; b) (i) Molecular structure of the thiophene bisurea derivatives studied by the same group; (ii) STM image of mixed T2/C12-U-C14-U-C12 monolayers at the 1-phenyloctane/graphite interface. Image size is 10.0 x 10.0 nm$^2$. $I_{set}$ = 1.0 nA, $V_{bias}$ = 0.6 V. Individual T2 molecules can be recognized in the C12-U-C14-U-C12 matrix, as indicated by the arrow.

Based on this initial work, the same group synthesized two bisurea compounds that incorporate thiophene units between the urea groups (Figure 19b).[119] In solution, these molecules self-assembled into fibers stabilized by hydrogen bonds with different morphologies and lengths depending on the concentration, temperature and solvent. Upon deposition on several substrates, such as mica, $SiO_2$ and graphite, substrate-dependant morphologies were reached but all were corresponding to tilted 1D arrays as demonstrated by XRD. De Schryver and coworkers then studied the electronic properties of the molecule with two thiophene units by scanning tunneling microscopy and spectroscopy (STM and STS) at the solution/graphite interface.[120] Interestingly, current-voltage experiments showed a clear zero conductance band gap (0.45 ± 0.08 eV) and the shape of the I(V) curve revealed the

---

[118] van Esch, J.; De Feyter, S.; Kellogg, R. M.; De Schryver, F. and Feringa, B. L. Self-Assembly of Bisurea Compounds in Organic Solvents and on Solid Substrates. *Chem. Eur. J.* **1997**, *3,* 1238–1243..

[119] Rep, D. B. A.; Roelfsema, R.; van Esch, J. H.; Schoonbeek, F. S.; Kellogg, R. M.; Feringa, B. L.; Palstra, T. T. M. and Klapwijk, T. M. Self-Assembly of Low-Dimensional Arrays of Thiophene Oligomers from Solution on Solid Substrates. *Adv. Mater.* **2000**, *12,* 563–566.

[120] Gesquière, A.; De Feyter, S.; De Schryver, F. C.; Schoonbeek, F.; van Esch, J.; Kellogg, R. M. and Feringa, B. L. Supramolecular π-Stacked Assemblies of Bis(urea)-Substituted Thiophene Derivatives and Their Electronic Properties Probed with Scanning Tunneling Microscopy and Scanning Tunneling Spectroscopy. *Nano Letters* **2001**, *1*, 201-206.

semiconductive behavior of this molecule. When similar I(V) experiments were performed on isolated molecules, a larger band gap was observed (0.65 ± 0.11 eV). This result demonstrates that an effective conjugation is induced by the $\pi$-stacked and hydrogen-bonded ribbons at the surface.

Some years later, Bouteiller and coworkers described a new series of bisurea based supramolecular polymers that display viscoelastic properties in various solvents at room temperature (Figure 20). FTIR spectroscopy was used to probe the mechanism of the self-assembly process, which was shown to be cooperative at both the molecular and supramolecular levels. Indeed, after precise assignment and analyses of the N-H bonds, the authors could demonstrate that the association of the two ureas motifs from a same molecule is highly synergistic, and that the formation of short oligomers triggers the formation of the corresponding supramolecular polymers.[121]

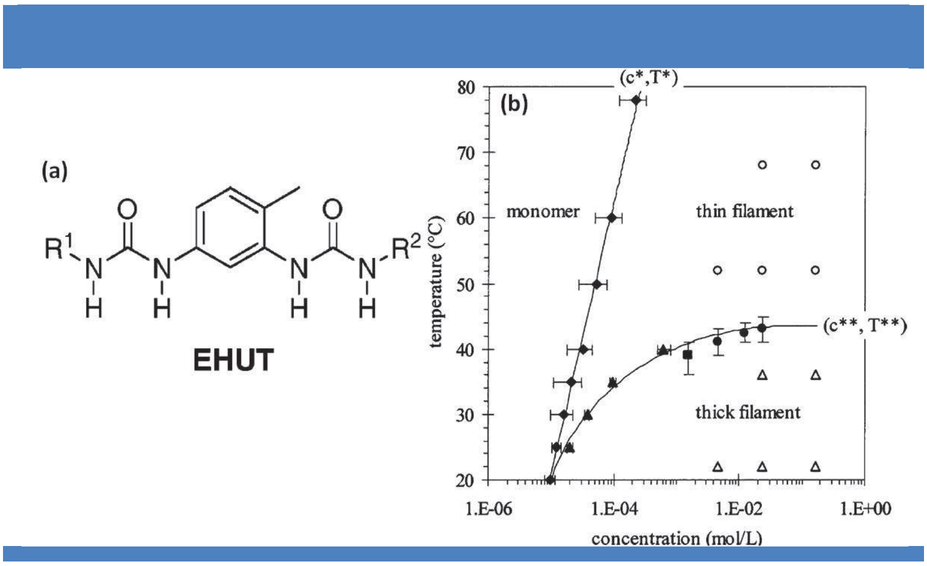

**Figure 20 |** a) Molecular structure of **EHUT**; (b) Pseudophase diagram for **EHUT** solutions in toluene. Transition between monomers and thin supramolecular filaments determined by ITC (◆). Transition between thin and thick supramolecular filaments determined by ITC (▲), viscosimetry (■), and FTIR (●). The error bars reflect the width of the transition. SANS characterization of the thin (○) and thick (△) supramolecular filaments.

The self-assembly process was then studied on gold surfaces at low temperature using STM.[122] After thermal annealing, STM images revealed the formation of assemblies of paired molecules which form ordered but randomly oriented zipperlike lines. Regarding the self-assembly process, they could conclude that, while hydrogen bonds are essential for the formation of the linear supramolecular polymer, additional van der Waals interactions between the alkyl side chains are responsible for the arrangement at larger scale. To be more

---

[121] Simic, V.; Bouteiller, L. and Jalabert, M. Highly Cooperative Formation of Bis-Urea Based Supramolecular Polymers. *J. Am. Chem. Soc.* **2003**, *125*, 13148-13154.

[122] Vonau, F.; Suhr, D.; Aubel, D.; Bouteiller, L.; Reiter, G. and Simon, L. Evolution of Multilevel Order in Supramolecular Assemblies. *Phys. Rev. Lett.* **2005**, *94*, 066103.

general, this example demonstrates that several non-covalent interactions of different strengths are usually required to build hierarchical self-assemblies. Whereas these long filaments were observed at high temperature, long and rigid nanotubes were observed at lower temperatures as demonstrated by SANS experiments and confirmed by FTIR.[123] Using a combination of DSC and ITC experiments, Bellot and Bouteiller proposed a model which permits the determination of the proportion and length of the different structures present in the system at any temperature and concentration.[124] Using viscosimetry and rheology experiments, the same group demonstrate that anions such as $H_2PO_4^-$ or $F^-$ can be used to control the degree of polymerization of the supramolecular polymers without affecting the nature of the self-assembly.[125]

Finally, we would like to mention the work of Shimizu who reported the tubular self-assembly of bis-urea macrocycles *via* intermolecular hydrogen bonds and edge-to-face π-stacking between the diphenyl ether linkers, as demonstrated by $^1$H NMR and X-ray diffraction (Figure 21).[126]

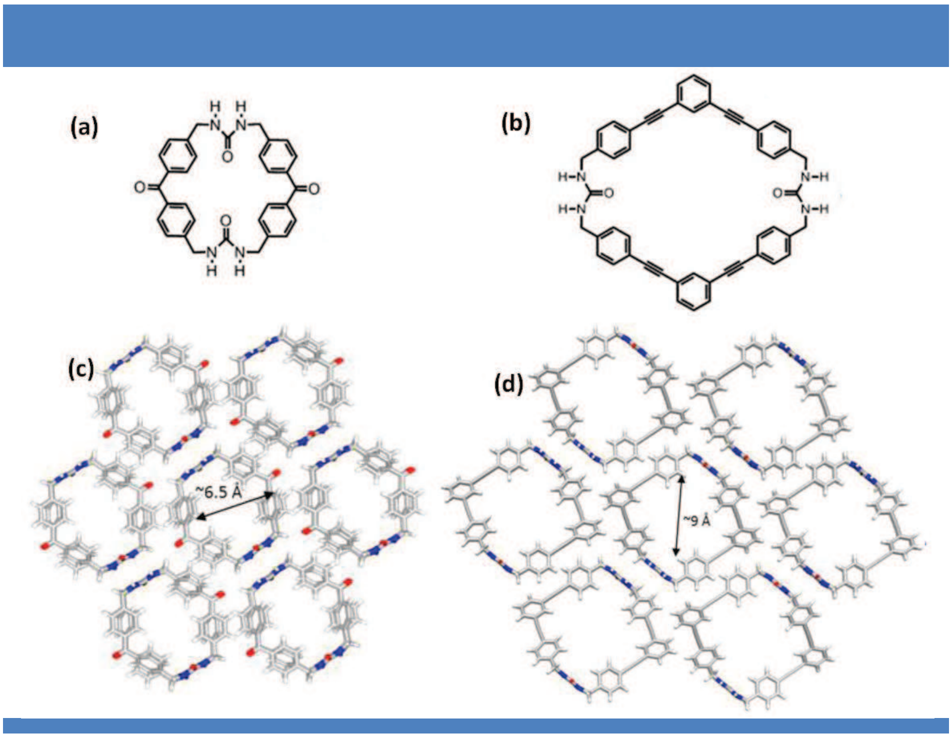

**Figure 21 |** a, b) Molecular structure of two bisurea macrocycles; c, d) Columnar assembly and subsequent packing of the columns affords aligned one-dimensional channels. These are viewed down the *b*-axis of seven hydrogen-bonded tubes of the assembled macrocycle reported in a) and b), respectively.

---

[123] Bouteiller, L.; Colombani, O.; Lortie, F.; Terech, P. Thickness Transition of a Rigid Supramolecular Polymer. *J. Am. Chem. Soc.* **2005**, *127*, 8893–8898.

[124] Bellot, M. and Bouteiller, L. Thermodynamic Description of Bis-urea Self-Assembly: Competition between Two Supramolecular Polymers. *Langmuir* **2008**, *24*, 14176-14182.

[125] Pinault, T.; Cannizzo, C.; Andrioletti, B.; Ducouret, G.; Lequeux, F. and Bouteiller, L. Anions as Efficient Chain Stoppers for Hydrogen-Bonded Supramolecular Polymers. *Langmuir* **2009**, *25*, 8404-8407.

[126] Shimizu, L. S.; Hughes, A. D.; Smith, M. D.; Davis, M. J.; Zhang, B. P.; zur Loye, H.-C. and Shimizu, K. D. Self-Assembled Nanotubes that Reversibly Bind Acetic Acid Guests. *J. Am. Chem. Soc.* **2003**, *125*, 14972-14973.

Initially, these supramolecular polymers were used to successively load and release guests such as acetic acid. A large variety of bis-urea macrocycles have now been synthesized and the corresponding self-assembled nanotubes with various channel sizes have been characterized using mostly powder X-ray diffraction.[127] Applications of these supramolecular polymers range from the storage of small molecule to molecular transport up to catalysis in confined environments.

---

[127] Shimizu, L. S.; Salpage, S. R. and Korous, A. A. Functional Materials from Self-Assembled Bis-urea Macrocycles. *Acc. Chem. Res.* **2014**, *47*, doi:10.1021/ar500106f.

# Chapter 3: Supramolecular polymers based on perylene bisimide scaffolds

Among the numerous molecular units which could be used to construct materials through supramolecular polymerization and self-assembly processes, the rylene dyes are very attractive building blocks due to their photophysical properties leading to applications in photonics and organic electronics.[128] Regarding the work performed during my PhD, we have decided to focus this introduction on perylene bisimides (PBIs) without substituents on the core. Such PBIs are blue fluorescent dyes having a molar extinction coefficient up to 95000 $M^{-1}$ $cm^{-1}$ at 526 nm and a quantitative fluorescence quantum yield of 0.94.[129] These dyes have a strong tendency to π-stack in non-polar solvents producing dynamic self-assemblies which, depending on concentration and temperature, modify their emission properties.[130,83] The hydrophobic perylene core has also been decorated with hydrophilic substituents to develop amphiphilic perylene bisimides.[131] Such water-soluble PBI-derivatives have been used for instance as efficient fluorescent DNA-intercalating probes for diagnostic applications or as dispersive agent for grapheme sheets. Other PBI derivatives were also reported to form gels[132] and liquid crystals with enhanced electronic properties.[133] Overall, PBI molecules represent a well-known class of pigments, fluorescence sensors as well as organic photon- and electron-carriers used in a number of optoelectronic devices.[134] Over the last few years, intensive researches on PBIs self-assemblies have been carried out. However, we will focus this introduction on water-soluble PBIs, as most of our work on PBIs will deal with such compounds. Although the first report on water-soluble PBIs dates back to the mid 1980s,[135] the development of such molecules essentially started ten years ago. The most common

---

[128] Weil, T.; Vosch, T.; Hofkens, J.; Peneva, K. and Müllen, K. The Rylene Colorant Family—Tailored Nanoemitters for Photonics Research and Applications. *Angew. Chem. Int. Ed.* **2010**, *49*, 9068-9093.

[129] Würthner, F. Perylene Bisimide Dyes as Versatile Building Blocks for Functional Supramolecular Architectures. *Chem.Commun.* **2004**, 1564-1579.

[130] Huang, C.; Barlow, S. and Marder, S.R.. Perylene-3,4,9,10-Tetracarboxylic Acid Diimides: Synthesis, Physical Properties, and Use in Organic Electronics. *J. Org. Chem.* **2011**, *76*, 2386–2407

[131] Görl, D.; Zhang, X.; and Würthner, F. Molecular Assemblies of Perylene Bisimide Dyes in Water. *Angew. Chem. Int. Ed.* **2012**, *51*, 6328-6348.

[132] (a) Sugiyasu, K.; Fujita, N. and Shinkai, S. Visible-Light-Harvesting Organogel Composed of Cholesterol-Based Perylene Derivatives. *Angew. Chem. Int. Ed.* **2004**, *43*, 1229–1233; (b) Li, X.-Q.; Stepanenko, V.; Chen, Z.; Prins, P.; Siebbeles, L. D. A. and Würthner, F. Functional organogels from highly efficient organogelator based on perylene bisimide semiconductor. *Chem. Commun.* **2006**, *37*, 3871-3873.

[133] (a) Hansen, M. R.; Schnitzler, T.; Pisula, W.; Graf, R.; Müllen, K. and Spiess, H. Cooperative Molecular Motion within a Self-Assembled Liquid-Crystalline Molecular Wire: The Case of a Teg-Substituted Perylenediimide Disc. *Angew. Chem. Int. Ed.* **2009**, *48*, 4621-4624; (b) Chen, Z. *et al.* Photoluminescence and Conductivity of Self-Assembled π–π Stacks of Perylene Bisimide Dyes. *Chem. Eur. J.* **2007**, *13,* 436–449.

[134] Zhan, X., et al. Rylene and Related Diimides for Organic Electronics. *Adv. Mater.* **2011**, *23*, 268-284.

[135] (a) Ford, W. E. Photochemistry of 3,4,9,10-perylenetetracarboxylic dianhydride dyes: visible absorption and fluorescence spectra and fluorescence quantum yields of the mono(n-octyl)imide derivative in aqueous and non-aqueous solutions. *J. Photochem.* **1986**, *34*, 43-54; (b) Ford, W. E. Photochemistry of 3,4,9,10-perylenetetracarboxylic dianhydride dyes: visible absorption and fluorescence of the di(glycyl)imide derivative monomer and dimer in basic aqueous solutions. *J. Photochem.* **1987**, *37*, 189-204.

strategy used to build water-soluble PBIs has been the introduction of hydrophilic groups such as PEG units, peptides or amino-acids, sugars or even ionic side chains at the imide functional group. Such water-soluble derivatives possess strongly hydrophobic π-surfaces which induce in water the formation of well-defined aggregates such as micelles, vesicles or nanofibers. In the following sections, we will describe some selected examples of water-soluble PBI derivatives that incorporate the various hydrophilic groups mentioned above and highlight the properties of the resulting supramolecular polymers.

## 1. Perylene bisimide-polyethylene glycol supramolecular polymer

Poly- and oligoethylene glycol (PEG and OEG) chains are well-known hydrophilic molecules that have been incorporated by different groups on the PBI scaffold. However, most of the studies have been carried out in organic solvents.[136] One of the first study in water was reported by Würthner and coworkers who studied the self-assembly behavior of four wedge- and dumbbell-shaped amphiphilic PBIs in water with 2% THF.[137] SEM and TEM imaging showed that the formation of spherical micelles of 4 to 6 nm for wedge-shaped PBIs in such solvents, whereas the dumbbell-shaped PBI arranged in rod aggregates with a 4 nm diameter (Figure 22a). Further UV-Vis experiments on this dumbbell-shaped PBI even at nanomolar concentrations in pure water indicated very high aggregation constant K and Gibbs free energy changes -ΔG° ($K > 10^8$ $M^{-1}$ and $-\Delta G° > 45$ kJ.mol$^{-1}$).[138] These values indicate that the dye is strongly aggregated even at low concentrations and that an unusually strong hydrophobic effect is occurring in water. Recently, using a combination of TEM, cryo-SEM and AFM imaging, the water-soluble dumbbell-shaped PDI was shown to sequentially grow from nanorods (as observed previously) to nanoribbons with a width of 20 to 60 nm with increasing concentration in water (Figure 22b).[139] Counterintuitively, the fluorescence quantum yield of the nanoribbons which results from a higher concentration of the dyes was considerably increased compared to the nanorods, promoting these molecules as potentially useful aggregation induced emission materials.

---

[136] See for instance: (a) Shaller, A. D.; Wang, W.; Li, A.; Moyna, G.; Han, J. J.; Helms, G. L. and Li, A. D. Q. Sequence-Controlled Oligomers Fold into Nanosolenoids and Impart Unusual Optical Properties. *Chem. Eur. J.* **2011**, *17*, 8350–8362 and references therein; (b) Bodapati, J. B. and Icil, H. Highly soluble perylene diimide and oligomeric diimide dyes combining perylene and hexa(ethylene glycol) units: Synthesis, characterization, optical and electrochemical properties. *Dyes Pigm.* **2008**, *79*, 224–235.

[137] Zhang, X.; Chen, Z. and Würthner, F.Morphology Control of Fluorescent Nanoaggregates by Co-Self-Assembly of Wedge- and Dumbbell-Shaped Amphiphilic Perylene Bisimides. *J. Am. Chem. Soc.* **2007**, *129*, 4886-4887.

[138] Chen, Z.; Fimmel, B. and Würthner, F. Solvent and substituent effects on aggregation constants of perylene bisimide π-stacks – a linear free energy relationship analysis. *Org. Biomol. Chem*. **2012**, *10*, 5845-5855.

[139] Zhang, X.; Görl, D.; Stepanenko, V. and Würthner, F. Hierarchical Growth of Fluorescent Dye Aggregates in Water by Fusion of Segmented Nanostructures. *Angew. Chem. Int. Ed.* **2014**, *53*, 1270–1274.

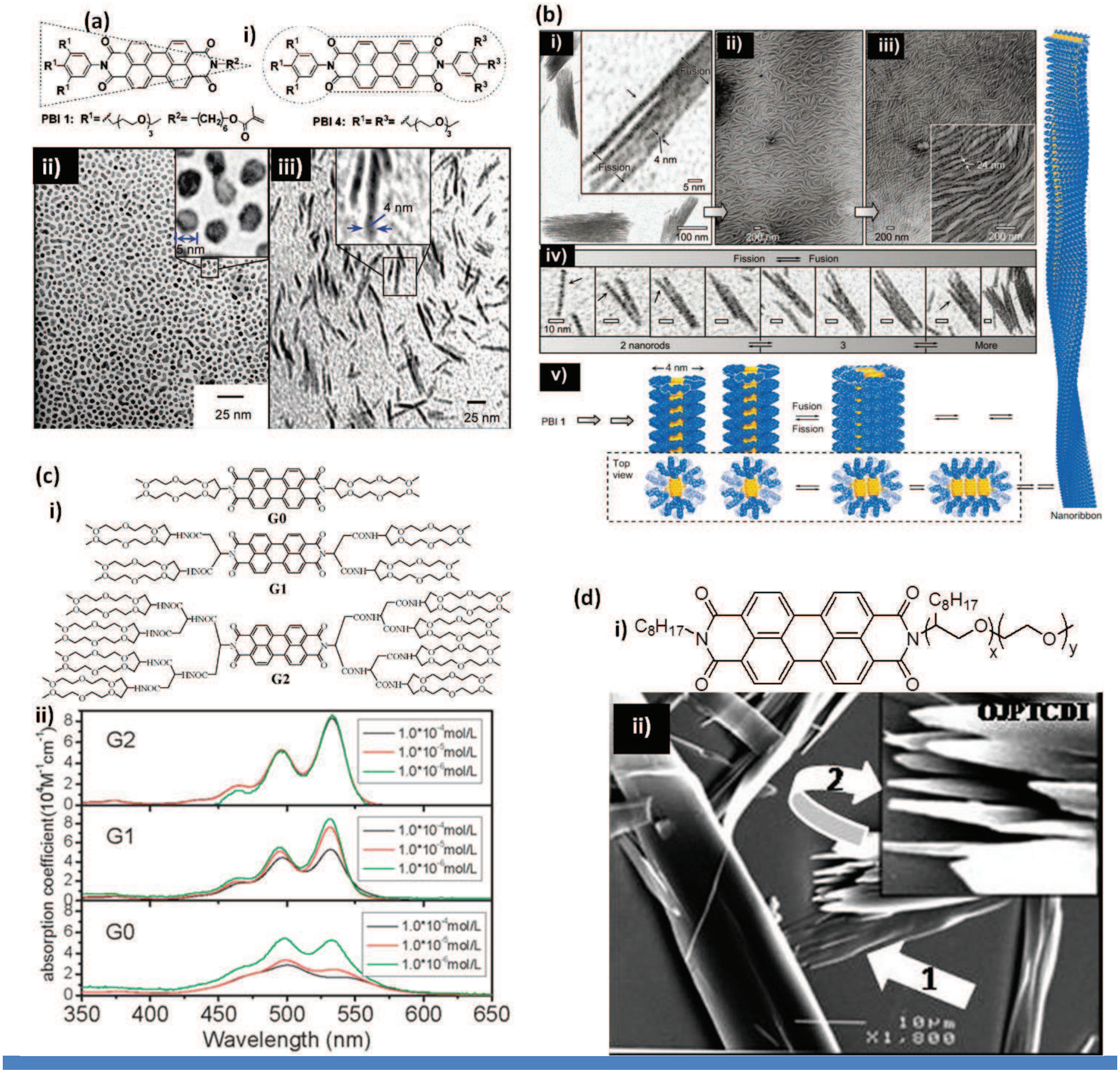

**Figure 22 |** a) (i) Molecular structure of wedge-shaped **PBI 1** and dumbell-shaped **PBI 4**, (ii, iii) TEM images of (ii) **PBI 1** and (iii) **PBI 4** self-assembled in THF-containing water (2%, v/v); b) (i – iii) TEM images of **PBI 1** aggregates prepared from water at different concentrations ((i): 0.25 mg/mL, (ii): 0.76 mg/mL and (iii) 1.0 mg/mL), (iv) TEM images of the fusion and fission of two, three, or more nanorods; scale bar: 10 nm, (v) Schematic illustration based on space-filling (CPK) models for the hierarchical self-assembly from nanorods to nanoribbons by fusion and fission; c) (i) Chemical structures of dendritic PBI molecules synthesized by the group of Gao; (ii) Concentration-dependent UV-Vis absorption spectra of these molecules in aqueous solution at different concentrations; d) (i) Molecular structure of the unsymmetric amphiphilic PDI derivative studied by Sundararajan; (ii) SEM image of a drop casted sample obtained by tilting the sample by 47 °C to reveal the tubular nature of the fibers.

The group of Gao synthesized three generations of dendritic PBI molecules with hexaethylene glycol chains as dendrons (Figure 22c).[140] In water, only the first generation showed aggregation over the whole concentration range, whereas the first generation showed

---

[140] Gao, B.; Li, H.; Liu, H.; Zhang, L.; Bai, Q. and Ba, X. Water-Soluble and Fluorescent Dendritic Perylene Bisimides for Live-Cell Imaging. *Chem. Commun.* **2011**, *47*, 3894-3896.

only partial aggregation at high concentration ($10^{-4}$ M) as demonstrated by UV-Vis experiments. The lack of aggregation of the second generation resulted in strong fluorescence in water (quantum yield of 93%) and these molecules could be used as fluorescent probes in Hela cells with low cytotoxicity. Similarly, although not functionalized with PEG chains but with glycerol units, the groups of Würthner and Haag also reported the synthesis of water-soluble PBI derivatives that incorporates polyglycerol dendrons up to the fourth generation.[141] UV-Vis and cryo-TEM experiments revealed that only one PBI derivative, i.e. the one with the smallest dendron, self-assembles in water in small fibers with ~ 1.6 nm diameter. In both examples, the lack of self-assembly for the largest dendrons is probably due to an inhibition of the aggregation of the perylene unit by shielding the π-faces.

Finally, we would like to mention the work of Sundararajan who synthesized unsymmetric amphiphilic PDI derivatives monofunctionalized on one imide side by a hydrophilic propylene oxide–ethylene oxide copolymer (PO–EO copolymer) so called Jeffamine® (Figure 22d).[142] Whereas no self-assembly was observed in organic solvents, aggregation was observed in water and water mixtures with acetone or methanol, as demonstrated by UV-Vis experiments. However, whereas H-type aggregates were observed in water, J-type aggregates were obtained in water mixtures. Using SEM imaging, they showed that hollow tubes with micrometric diameters are formed from water, mainly driven by π-stacking and van der Waals interactions along one direction, and only weak van der Waals forces along the other two.

## 2. Perylene bisimide-peptide supramolecular polymer

Owing to their various properties (biocompatibility, pH sensitivity, available range of hydrophobicity and hydrophilicity, *etc.*), amino acids have been considered as potential side chains for PBIs in order to reach functional supramolecular polymers for applications in electronics or biomedicine.[143] One of the first reports that mention the study of peptide-modified PBIs in water is very recent.[144] In this work, the group of Tovar studied the self-assembly behavior of a pentapeptide-modifed PBI (Figure 23a). At low pH (when all carboxylic acid residues are protonated), the formation of hydrogels with low peptide weight

---

[141] Heek, T.; Fasting, C.; Rest, C.; Zhang, X.; Würthner, F. and Haag, R. Highly fluorescent water-soluble polyglycerol-dendronized perylene bisimide dyes. *Chem. Commun.* **2010**, *46*, 1884–1886.

[142] Islam, M. R. and Sundararajan, P. R. Self-assembly of a set of hydrophilic–solvophobic– hydrophobic coil–rod–coil molecules based on perylene diimide. *Phys.Chem. Chem. Phys.* **2013**, *15*, 21058-21069.

[143] Avinash, M. B. and Govindaraju, T. Amino Acid Derivatized Arylenediimides: A Versatile Modular Approach for Functional Molecular Materials. *Adv. Mater.* **2012**, *24*, 3905–3922.

[144] Vadehra, G. S.; Wall, B. D.; Diegelmann, S. R. and Tovar, J. D. On-resin dimerization incorporates a diverse array of π-conjugated functionality within aqueous self-assembling peptide backbones. *Chem. Commun.* **2010**, *46*, 3947–3949.

percents was observed, which consisted in flat tape 1D nanostructures with a diameter of ~2 nm as demonstrated by AFM imaging. Upon decreasing the pH from neutral to acidic, complete quenching of the fluorescence occurred, which is in good agreement with a strong π-π stacking of the PBI units. Two years later, Hodgkiss and coworkers described the use of penta- and heptapeptidic units to control the assembly of PBI molecules (Figure 23b).[145] Using UV-Vis spectroscopy, molecules containing glutamic acid residues were shown to be very sensitive to pH and at acidic pH, CD and DLS experiments reveal the presence of ~20 nm chiral aggregates. Additionally, the presence of ions such as $Zn^{2+}$ was shown to affect the self-assembly process by increasing the H-type aggregation of the PBI molecules due to the coordination of the ions to glutamate residues from neighboring molecules.

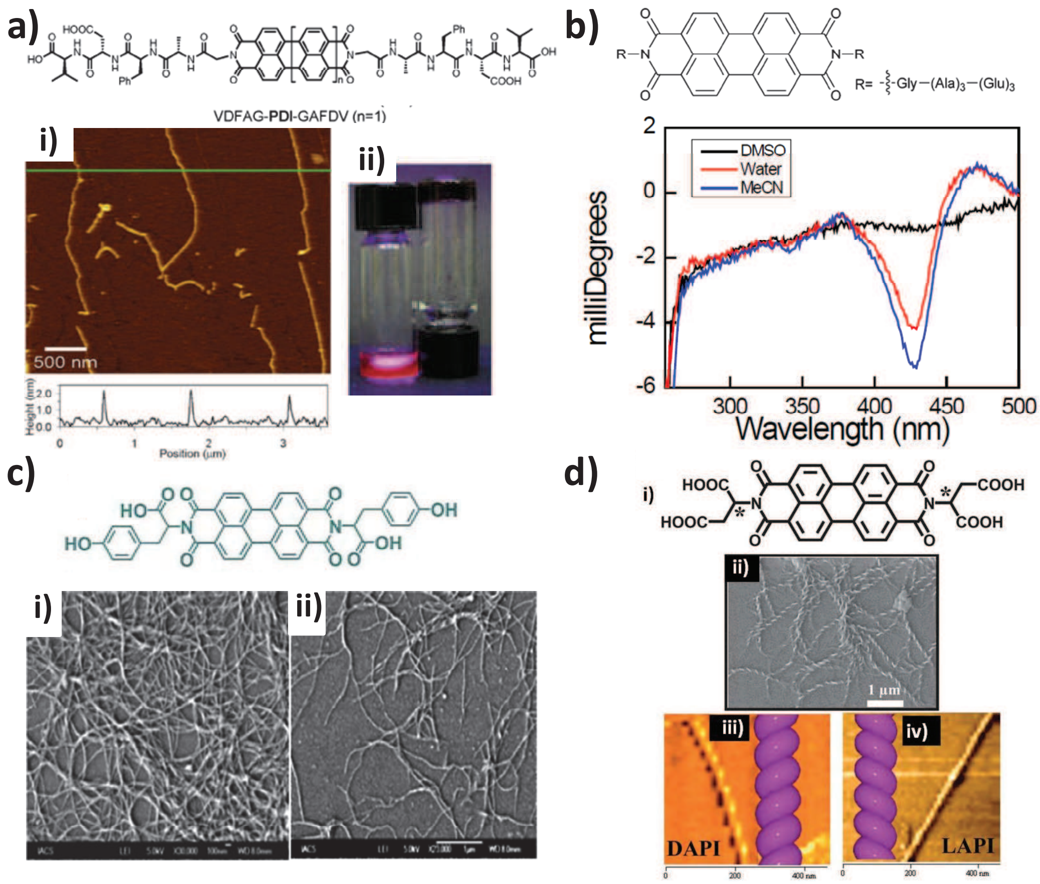

**Figure 23 |** a) Molecular structure of pentapeptide-modifed PBI studied by Tovar *et al.*, (i) Tapping-mode AFM image obtained from a assembled sample of this molecule deposited on mica. Line profile of the *z*-axis height is depicted below the image, (ii) representative photo of molecularly dissolved aqueous peptide solution (left) and of hydrogels formed after assembly (right) during irradiation with 365 nm light.; b) Molecular structure of haptapeptide-modifed PBI studied by Hodgkiss and coworkers, and CD spectra of this molecule ($3.0 \times 10^{-6}$ M) in DMSO, MeCN and $H_2O$; (c) Molecular structure of tyrosine-modified PBI; (i, ii) FE-SEM images of a diluted smaple the corresponding hydrogel at a concentration of $4.4 \times 10^{-5}$ M; d) (i) Molecular structure of an aspartic acid appended

---

[145] Gallaher, J. K.; Aitken, E. J.; Keyzers, R. A. and Hodgkiss, J. M. Controlled Aggregation of Peptide-Substituted Perylene-Bisimides. *Chem.Commun.* **2012**, *48*, 7961-7963.

perylene derivative; (ii) Typical FE-SEM image of a dried gel; AFM topology of (iii) D- gel and (iv) L-gel prepared on a freshly cleaved mica surface.

Two more recent works reported the decoration of PBI units with single amino acids, namely tyrosine[146] and aspartic acid.[147] In both cases, pH-dependant hydrogels were observed. FE-SEM, TEM, FT-IR and X-ray diffraction experiments demonstrated that the tyrosine gel consists in cross-linked nanofibers of 3 to 8 nm diameter which arise from both π-π stacking and intermolecular hydrogen-bonding interactions (Figure 23c). Additionally, the corresponding xerogel displayed excellent photoswitching properties in a single conducting device with lateral geometry. For the aspartic acid PBI derivative, both L- and D-amino acids were used, which resulted in the formation of self-assemblies with left-handed and right-handed helical fibers respectively, as demonstrated by both FE-SEM and AFM imaging (Figure 23d). Importantly, this chiral aggregation was shown to occur only in the gel state at low pH and relatively high concentration ($10^{-4}$ M) as demonstrated by UV-Vis, fluorescence and several CD experiments. Additionally, using MTT assays, these PBI derivatives were shown to be biocompatible and could be used to monitor the pH in cellular environments *in vivo*. Subsequently, these aspartic acid PBIs were reported as potential fluorescent sensor[148] for selective detection $Cu^{2+}$ and ATP and two-electron transfer reagent for use in water photolysis.[149]

## 3. Other water-soluble PBI-based supramolecular polymer

Three other approaches have been reported for the formation of water-soluble PBI supramolecular polymers involving (i) molecular units with carboxylic acid groups, (ii) sugar moieties and (iii) ionic side chains. Noteworthily, some charged and sugar-based PBI derivatives have been particularly useful to probe the presence of G-quadruplexes in telomeric DNA structures but they have been used as single fluorescent molecule and their self-assembly in water was not reported.[131]

Similar to the works mentioned previously with dendronized PEG and polyglycerol units, the group of Hirsch reported the incorporation of 1G- and 2G-Newkome dendrons (3 and 9 carboxylic acid residues respectively) on the PBI core and their resulting aggregation in

---

[146] Roy, S.; Maiti, D. K.; Panigrahi, S.; Basak, D. and Banerjee, A. A new hydrogel from an amino acid-based perylene bisimide and its semiconducting, photo-switching behavior. *RSC Adv.* **2012**, *2*, 11053–11060.

[147] Sukul, P. K.; Singh, P. K.; Maji, S. K. and Malik, S. Aggregation Induced Chirality in a Self Assembled Perylene Based Hydrogel: Application of the Intracellular pH Measurement. *J. Mater. Chem. B* **2013**, *1*, 153-156.

[148] Zhong, L.; Xing, F.; Bai, Y.; Zhao, Y. and Zhu, S. Aspartic acid functionalized water-soluble perylene diimide as ''Off–On''fluorescent sensor for selective detection $Cu^{2+}$ and ATP. *Spectrochim. Acta A* **2013**, *115*, 370–375.

[149] Zhong, L.; Xing, F.; Shi, W.; Yan, L.; Xie, L. and Zhu, S. Synthesis, Spectra, and Electron-Transfer Reaction of Aspartic Acid-Functionalized Water-Soluble Perylene Bisimide in Aqueous Solution. *ACS Appl. Mater. Interfaces* **2013**, *5*, 3401−3407.

water.[150] Using optical and TEM microscopies, the 1G-dendronized molecules were shown to form stronger aggregates than the 2G-PB molecules, an observation in good agreement with other works on dendron-decorated PBIs. Fluorescence quenching in buffered water at pH 7.2 confirmed the aggregation of these PBI derivatives, which form micellar aggregates whose diameters range from 4 to 40 nm depending on the structure of the molecule. The groups of Rowan, Beljonne, and Malik also reported the formation of a hydrogel from the 1:2 mixture of a PBI derivative bearing phenyl-3,5-dicarboxylic acid side groups and melamine (Figure 24a).[151] SEM imaging of the xerogels revealed the formation of long and bundled fibers with diameters ranging from 20 to 200 nm while AFM imaging of loose gel showed the presence of individual nanofibers with a diameter of ~12 nm. Further UV-Vis, fluorescence, XRD experiments and molecular modeling demonstrated that melamine molecules prevent the close contact between PBI units, and fluorescence emission in water is therefore induced via exciton emission rather than excimer emission.

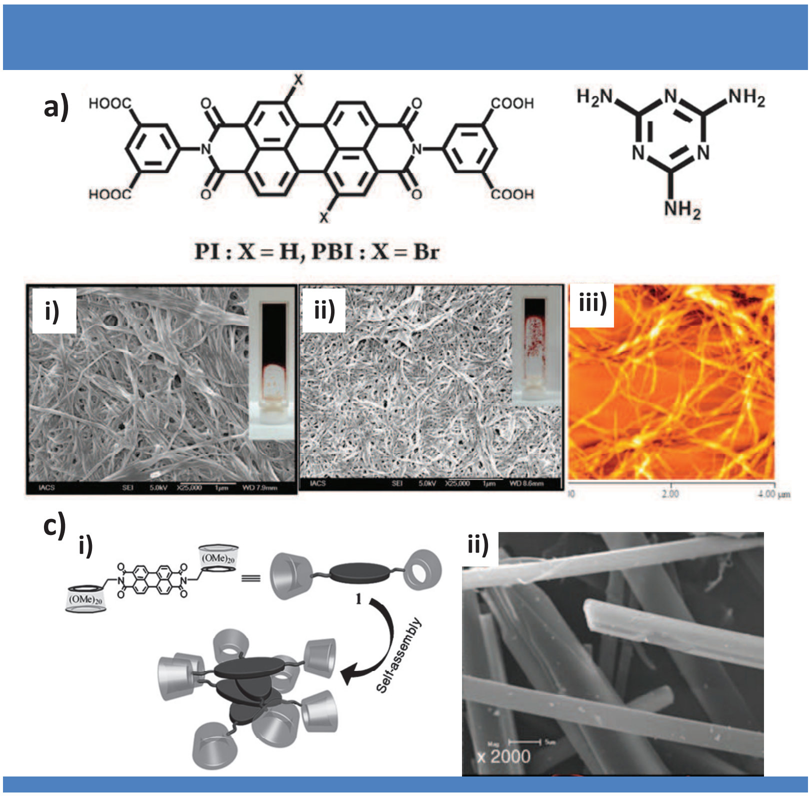

**Figure 24 |** a) Molecular structure of PBI derivative bearing phenyl-3,5-dicarboxylic acid side groups (PI) and melamine (MM), (i) FE-SEM images of dried gels [PI]/[MM]= 1 : 2 and (ii) [PBI]/[MM]= 1 : 2 [PI] or [PBI] = 2 x $10^{-2}$ M and [MM] = 4 x $10^{-2}$ M [inset: picture of an inverted quartz cuvette of 10 mm pathlength], (iii) AFM topology of loose gel [PI]/[MM] = 1 : 2 directly cast on a freshly cleaved mica surface; b) (i) Structural illustration of the self-assembly of perylene molecules decorated at both ends by permethyl-β-cyclodextrins; (ii) SEM image of the corresponding nanorods.[152]

---

[150] Schmidt, C. D.; Böttcher, C. and Hirsch, A. Synthesis and Aggregation Properties of Water-Soluble Newkome-Dendronized Perylenetetracarboxdiimides. *Eur. J. Org. Chem.* **2007**, 5497–5505.

[151] Sukul, P. K. *et al.* Assemblies of perylene diimide derivatives with melamine into luminescent hydrogels. *Chem. Commun.* **2011**, *47*, 11858–11860.

[152] (a) Liu, Y.; Wang, K.-R.; Guo, D.-S. and Jiang, B.-P. Supramolecular Assembly of Perylene Bisimide with β-Cyclodextrin Grafts as a

In 2009, Liu and coworkers reported the supramolecular assembly of perylene decorated at both ends by permethyl-*β*-cyclodextrins through π-π stacking interactions, as demonstrated by UV-Vis, fluorescence and $^1$H NMR experiments in water (Figure 24b). Whereas SEM and TEM imaging demonstrated the formation of 1D nanorods, XRD experiments revealed that these PBIs self-assemble into well-ordered crystals with a π-π stacking distance of 4.02 Å. This larger stacking distance is due to the steric hindrance of the cyclodextrin units which force an alternating rotation stacking of the perylene units. These PBI-cyclodextrin self-assemblies were shown to be good fluorescent sensors in the solid state for aromatic amines[152a] and in solution for charged aromatic molecules.[152b] PBI units have also been recently decorated with D-lactose units and reported to form strong chiral aggregates in water even at low concentration as suggested by spectroscopy experiments.[153] Cryo-SEM confirmed the formation of right-handed nanofibers with ~20 nm diameter. This bio-decorated PBI self-assembly was then successfully used for the sensing of lectins using turbidity assays.

Alternatively, PBI units have been decorated with charged side chains to produce water-soluble derivatives. For instance, the group of Tam-Chang reported the incorporation of tertiary ammonium groups on PBI units, which were shown to display different liquid crystalline phases depending on the counterion.[154] Although UV-Vis experiments demonstrated that the structures of both the side chain and the counterion were not influencing the formation of H-aggregates, polarized optical microscopy indicated the formation of either nematic or hexagonal phases depending on the counterion. Finally, Würthner and coworkers reported the synthesis of highly water-soluble fluorescent bolaamphiphiles from spermine-functionalized PBI dyes.[155] The formation of H-type aggregates was demonstrated by spectroscopy techniques and AFM and TEM imaging revealed the formation of large rod-like aggregates with diameters up to 6 nm and length up to 200 nm for PBI derivatives with the longer linkers. At low concentrations, these dyes were predominantly in their monomeric form and displayed fluorescent quantum yields up to 90%. Importantly, these dyes have been used to sense DNA/RNA secondary structure as shown by

---

Solid-State Fluorescence Sensor for Vapor Detection. *Adv. Funct. Mater.* **2009**, *19*, 2230-2235; (b) Wang, K.-R.; Guo, D.-S.; Jiang, B.-P.; Sun, Z.-H. and Liu, Y. Molecular Aggregation Behavior of Perylene-Bridged Bis(β-cyclodextrin) and Its Electronic Interactions upon Selective Binding with Aromatic Guests. *J. Phys. Chem. B* **2010**, *114*, 101–106.

[153] Wang, K.-R.; An, H.-W.; Wu, L.; Zhang, J.-C. and Li, X.-L. Chiral self-assembly of lactose functionalized perylene bisimides as multivalent glycoclusters. *Chem. Commun.* **2012**, *48*, 5644–5646.

[154] Tam-Chang, S.-W.; Helbley, J. and Iverson, I. K. A Study of the Structural Effects on the Liquid-Crystalline Properties of Ionic Perylenebis(dicarboximide)s Using UV-Vis Spectroscopy, Polarized Light Microscopy, and NMR Spectroscopy. *Langmuir* **2008**, *24*, 2133-2139.

[155] Rehm, S.; Stepanenko, V.; Zhang, X.; Rehm, T. H. and Würthner, F. Spermine-Functionalized Perylene Bisimide Dyes—Highly Fluorescent Bola-Amphiphiles in Water. *Chem. Eur. J.* **2010**, *16*, 3372–3382.

fluorescence and DNA melting experiments.[156] Additional CD experiments demonstrated that only PBI dimers aggregate within DNA/RNA grooves with high sensitivity due to the steric properties of the binding site. Overall, water-soluble PBI derivatives show great potential for applications from materials science to medicine.

---

[156] Rehm, T. H.; Radić Stojković, M.; Rehm, S.; Škugor, M.; Piantanida, I. and Würthner, F. Interaction of spermine-alanine functionalized perylene bisimide dye aggregates with ds-DNA/RNA secondary structure. *Chem. Sci.* **2012**, *3*, 3393-3397.

# Chapter 4: Supramolecular co-self-assemblies

Supramolecular polymers are built from monomers using reversible noncovalent interactions, which induce properties such as self-healing and ease of processability that conventional polymers do not possess. Additionally, multifunctional supramolecular copolymer can be generated either by combining multifunctional monomers or by intermixing different functional supramolecular polymers.[157] From a terminology point of view, supramolecular co-self-assemblies can be considered as *self-sorting* systems.[158] Self-sorting is nowadays related to self-recognition phenomena in multicomponent systems.[159] In such systems, if a monomer shows affinity for others, the assembly process is called *social self-sorting*. On the contrary, if the monomer shows only affinity for itself, then the process can be called *narcissistic self-sorting*. Here, we will summarize the studies concerning bisurea and perylene bisimides-based multicomponent self-assemblies. We will also highlight some recent examples on fluorene, benzene tricarboxamide (BTA) and peptide-based co-self-assemblies. In particular, we will focus on the mechanisms of self-assembly and the possible applications of these supramolecular polymers.

## 1. Bisurea based co-self-assembly

In 2005, Sijbesma and coworkers reported the first example of mixed assemblies based on bisurea motifs as recognition units.[103] Using cryo-TEM imaging, they demonstrated that bisurea-based pyrene molecules are incorporated in micelles made of bisurea-based PEG without disrupting their self-assembly. Based on fluorescence spectroscopy, they could determine that these dyes are held apart in the structure made of bisurea molecules due to hydrogen-bonding interactions, whereas they stay aggregated when the micellar assembly does not incorporate bisurea recognition units. The same year, the group of Sommerdijk reported the co-self assembly of surfactant bis-urea molecules, which form well-defined (highly ordered) ribbon-like bilayer aggregates in water, with bis-urea molecules containing either an azobenzene dye or a biotin unit.[160] Using UV-Vis spectroscopy, they demonstrated

---

[157] (a) Petkau-Milroy, K. and L. Brunsveld. Supramolecular Chemical Biology; Bioactive Synthetic Self-Assemblies. *Org. Biomol. Chem.* **2013**, *11*, 219-232; (b) Petkau-Milroy, K.; Sonntag, M. H. and Brunsveld, L. Modular Columnar Supramolecular Polymers as Scaffolds for Biomedical Applications. *Chem. Eur. J.* **2013**, *19*, 10786-10793.

[158] Safont-Sempere, M. M.; Fernández, G.and Würthner, F. Self-Sorting Phenomena in Complex Supramolecular Systems. *Chem.Rev.* **2011**, *111*, 5784-5814.

[159] Wu, A. X. and Isaacs, L. Self-Sorting: The Exception or the Rule? *J. Am. Chem. Soc.* **2003**, *125*, 4831-4834.

[160] Vos, M. R. J. *et al.* The Bis-urea Motif as a Tool To Functionalize Self-Assembled Nanoribbons. *J. Am. Chem. Soc.* **2005**, *127*, 16768-16769.

that the dye that present a matching size of the linker between the two urea units was efficiently incorporated in the ribbon. Incorporation of the bis-urea molecule containing the biotin unit was confirmed by TEM microscopy which shows the selective anchoring of gold nanoparticles labeled with streptavidin on the ribbons (Figure 25a).

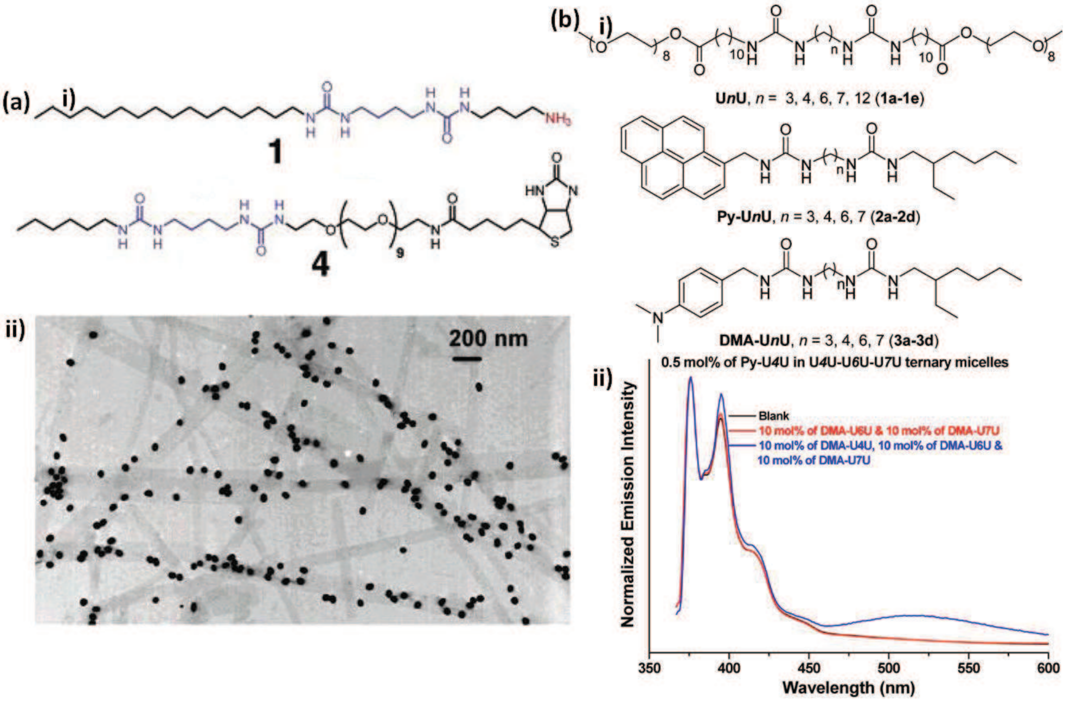

**Figure 25 |** a) (i) Molecular structure of a surfactant bisurea molecule (**1**) and a bisurea molecule functinalized by a biotin unit (**4**); ii) TEM image of biotin functionalized ribbons with 25 nm gold-labeled streptavidin selectively bound to the pendant biotin groups; b) (i) Molecular structure of bisurea compounds used for self-sorting experiments; (ii) Fluorescence emission spectra of ternary micellar solution of U*4U-U6U-U7U* containing different combinations of DMA (*DMA-U4U*, *DMAU6U* and *DMA-U7U)* and pyrene bisurea guest molecules Py-U*4U.*

Some years later, the group of Sijbesma studied the influence of the spacing between urea groups on self-sorting in aqueous solution.[161] For that, four oligoethylene glycol-bisurea bolaamphiphiles with different spacer lengths between the urea motifs were synthesized, which formed stable micelles in water. Probes made of either a pyrene unit or a dimethylaniline (DMA) unit with the same spacer lengths were then used to monitor the dynamic of the micelles. Indeed, when both probes are in close contact, an exciplex band is observed by fluorescence spectroscopy. Interestingly, when two micellar solutions with the same spacer length and incorporating either the pyrene or the DMA unit were mixed, the exciplex band appeared, demonstrating the dynamic nature of the self-assembly process. However, when two micellar systems with non-matching spacers were used, no exciplex

---

[161] Pal, A.; Karthikeyan, S. and Sijbesma, R.P. Coexisting Hydrophobic Compartments through Self-Sorting in Rod-Like Micelles of Bisurea Bolaamphiphiles. *J. Am. Chem. Soc.* **2010**, *132*, 7842-7843.

formation was observed, suggesting that the two rod-like micelles coexist in solution. Using a six-component mixture (3 amphiphiles, 1 pyrene and 2 non matching DMA probes), a self-sorting process was also observed, which efficiency decreased with increasing the length of the spacer (Figure 25b). Following a similar approach, the same group demonstrated the self-sorting of chiral bolaamphiphiles, which form segregated dynamic rods in water as demonstrated by SAXS and cryo-TEM experiments.[162] Although exciplex formation could be satisfyingly used to monitor this phenomenon, a high loading of probes (up to 15%) was necessary. To circumvent this problem, a naphthalene probe was used in combination with the pyrene one and the fluorescence energy transfer (FRET) was monitored. Gratifyingly, an increase in the fluorescence of the pyrene unit was observed for the matching system, which indicates the presence of naphthalene units in the close vicinity of the pyrene moieties. In this example, thanks to FRET, quantities as low as 0.5 mol% of the fluorescent probes could be used to monitor the chiral self-sorting.

Sijbesma and co-workers then extended this work to bisurea thermoplastic elastomers made of poly(tetrahydrofuran) (pTHF) soft segments ($M_n$ = 1100) and uniform bisureido-alkylene (butyl to heptyl) hard segments.[163] In their initial study, they showed that dyes whose size matches the size of the hard segment of the elastomers are preferentially and efficiently incorporated in the hard blocks as suggested by dye extraction and dye deformation experiments.[163a] Additionally, they have shown by AFM that thin films of these elastomers retain their fiber-like morphology when the size of the guest (distance between urea motifs) matches with the one of the elastomers (Figure 26).[163b] Fluorescence experiments on these films further indicated that the pyrene guest is randomly dispersed in the matching fibers whereas it aggregates in the non-matching polymers. Further work demonstrates the high level of self-sorting in polymer films when non matching polymers are mixed.[163c] This study was performed thanks to the use of fluorescent probes and FRET experiments demonstrated that self-sorting occurs at two levels of self-assembly (the formation of ribbons from the self-assembly of the bis-urea units and their consecutive aggregation into fibers). All these studies demonstrate that a methodology initially developed for small molecules can be readily extended to macromolecular systems and their resulting materials.

---

[162] Pal, A.; Besenius, P. and Sijbesma, R. P. Self-Sorting in Rodlike Micelles of Chiral Bisurea Bolaamphiphiles. *J. Am. Chem. Soc.* **2011**, *133*, 12987-12989.

[163] (a) Koevoets, R. A.; Versteegen, R. M.; Kooijman, H.; Spek, A. L.; Sijbesma, R. P. and Meijer, E. W. Molecular Recognition in a Thermoplastic Elastomer. *J. Am. Chem. Soc.* **2005**, *127*, 2999-3003; (b) Botterhuis, N. E.; Karthikeyan, S.; Veldman, D.; Meskers, S. C. J. and Sijbesma, R. P. Molecular recognition in bisurea thermoplastic elastomers studied with pyrene-based fluorescent probes and atomic force microscopy. *Chem. Commun.* **2008**, 3915-3917. (c) Botterhuis, N. E.; Karthikeyan, S.; Spiering, A. J. H. and Sijbesma, R. P. Self-Sorting of Guests and Hard Blocks in Bisurea-Based Thermoplastic Elastomers. *Macromolecules* **2010**, *43*, 745-751.

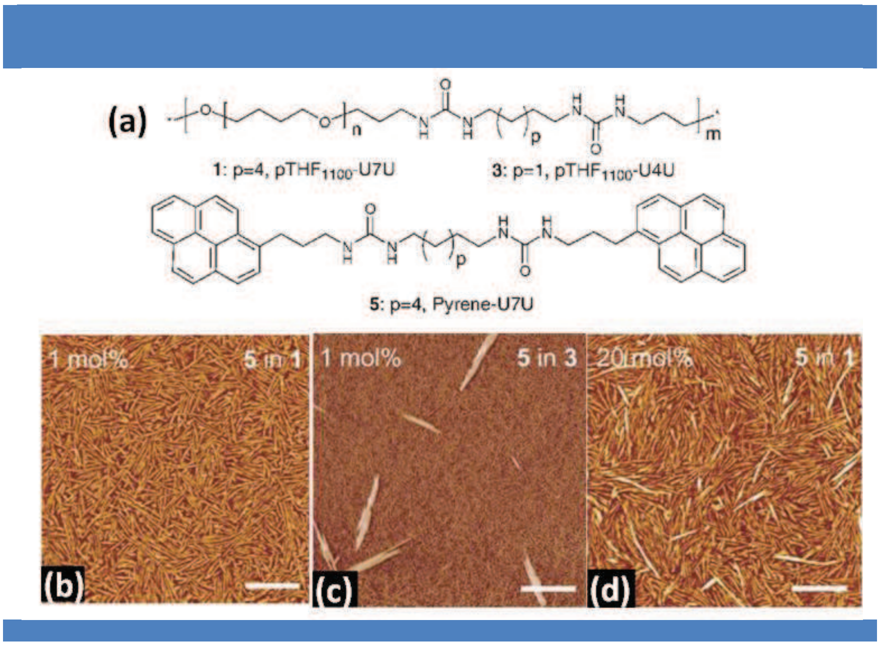

**Figure 26 |** a) Molecular structure of bisurea derivatives studied by Sijbesma and coworkers; b-d) Intermittent contact mode AFM phase images. Thin films of 1 mol% **5** in **1** (b) and **3** (c). Thin film of 20 mol% (d) **5** in **1**. Samples in b and d were annealed for 30 min at 110 °C prior to AFM imaging. Scale bars: 200 nm.

Inspired by the initial work of Sijbesma on thermoplastic elastomers, the group of Meijer reported the co-self-assembly of poly(ε-caprolactone) (PCL) elastomers with either bisureidoalkylene azobenzene dyes or a peptidic recognition unit based on the RGD sequence known for its cell-binding properties.[164] Similarly to other works, the azobenzene dyes with the good matching linker was reported to be released at a much slower rate than the nonmatching one using UV-Vis spectroscopy. The bisurea-peptidic molecule was also shown to be released at a lower rate when embedded in the PCL-based poly(urea) then when mixed with a classical PCL. This controlled release of the RGD-peptide can be potentially useful for tissue engineering.

Two other works have been reported recently on the preparation of mixed bis-urea supramolecular polymers. The group of Steed reported on the mixing of bis-urea based organogelators.[165] In that case, mixed gels with matching linker size presented both different morphologies and rheological characteristics compared to their parent gels, resulting in a kind of social self-sorting. Importantly, mixing of gels with non-matching linker size resulted in the formation of gels with intermediate rheological properties compared to the parent gels. Finally, Bouteiller and coworkers took advantage of the co-self-assembly of bis-urea

---

[164] Wisse, E., *et al.* Molecular Recognition in Poly(ε-Caprolactone)-Based Thermoplastic Elastomers. *Biomacromolecules* **2006**, *7*, 3385-3395.

[165] Lloyd, G.O.; Piepenbrock, M.-O. M.; Foster, J. A. ; Clarke, N. and Steed, J. W. Anion Tuning of Chiral Bis(Urea) Low Molecular Weight Gels. *Soft Matter* **2012**, *8*, 204-216.

monomers to study the thermodynamics of their self-assembly into tubular structures.[166] Using time-resolved fluorescence spectroscopy, a tetrazine labeled monomer was shown to be a good reporter to probe the self-assembly process. Importantly, the phase diagram obtained by this technique was shown to be almost identical to the one obtained by DSC and ITC.[124]

## 2. Perylene bisimide based co-self-assembly

Although examples of multicomponent supramolecular polymers based on bis-urea monomers are numerous, such examples with perylene units are scarce. In 2007, Würthner and co-workers reported the co-self-assembly of both amphiphilic wedge- and dumbbell-shaped PBIs in THF/$H_2O$ mixtures.[137] Whereas the wedge-shape PBI forms micelles of 4~6 nm in 2% v/v THF/$H_2O$, its co-self-assembly with the dumbbell-shaped one leads to hollow bilayer vesicles with diameter ranging from 94~133 nm depending on the ratio (higher diameter for higher amphiphilic PBI content). This difference in shape and size was attributed to a difference in spontaneous curvature, due to a change in the hydrophilic/hydrophobic ratio. This control of self-assembly by spontaneous curvature was already observed in biology for lipid membranes for example (Figure 27a). These self-assembled vesicles could be then loaded with energy-donor molecules and subsequently used as very sensitive fluorescent pH sensors in aqueous solutions.[167]

Subsequently, the same group synthesized a series of PBIs with linear and branched alkyl side chains and studied their self-sorting behavior.[168] Whereas PBI derivatives with linear alkyl side chain formed H-type aggregates and red gels, most PBI derivatives with branched alkyl side chain resulted in J-type aggregates and green gels (Figure 27b). Interestingly, when both linear and branched PBIs were mixed with a maximum content of 44% of the J-type molecule, the formation of mixed H-type aggregates was observed by UV-Vis and CD spectroscopy, resulting in a kind of social self-sorting. Beyond this critical ratio, a narcissistic self-sorting process occurred leading to the formation of both H-type and J-type aggregates. Finally, we would like to mention the work of Li who examined the self-sorting behavior of a mixture containing three bay-substituted PBI dyes which lead to different twisted angles of their core.[169] Using $^1H$ NMR and UV-Vis spectroscopy, they showed that

---

[166] Ribagnac, P., Cannizzo, C.; Méallet-Renault, R.; Clavier, G.; Audebert, P.; Pansu, R. and Bouteiller, L. Fluorescent Labeling of a Bisurea-Based Supramolecular Polymer. *J. Phys. Chem. B* **2013**, *117*, 1958-1966.

[167] Zhang, X.; Rehm, S.; Safont-Sempere, M. M. and Würthner, F. Vesicular Perylene Dye Nanocapsules as Supramolecular Fluorescent Ph Sensor Systems. *Nature Chem.* **2009**, *1*, 623-629.

[168] Ghosh, S., Li, X. Q.; Stepanenko, V. and Würthner, F. Control of H- and J-Type Π Stacking by Peripheral Alkyl Chains and Self-Sorting Phenomena in Perylene Bisimide Homo- and Heteroaggregates. *Chem. Eur. J.* **2008**, *14*, 11343-11357.

[169] Shaller, A. D.; Wang, W.; Gan, H. Y. and Li, A. D. Q. Tunable Molecular Assembly Codes Direct Reaction Pathways. *Angew. Chem. Int.*

molecules preferentially self-discriminate into segregated nanostructures in the presence of other building blocks.

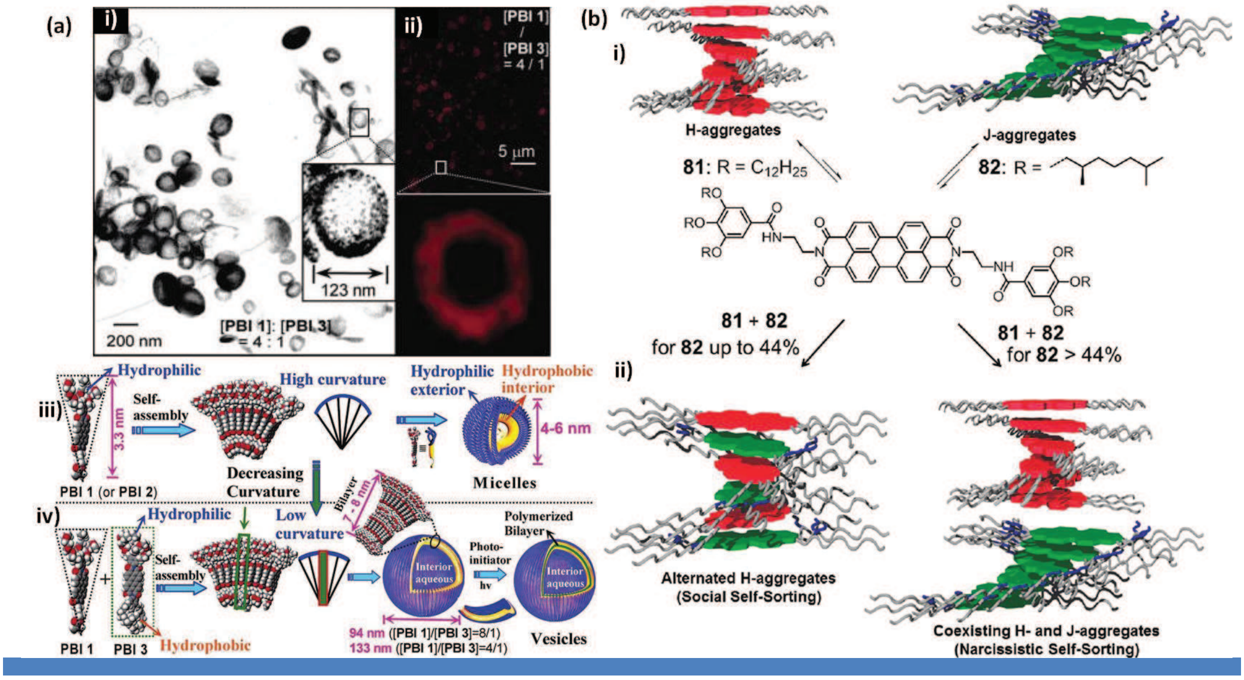

**Figure 27 |** a) TEM (i) and confocal fluorescence images (ii) of coaggregates of amphiphilic wedge- and dumbbell-shaped PBIs in a 4:1 molar ratio in THF-containing water (2%, v/v); (iii) Schematic Illustration for the formation of micelles from the wedge-shaped PBI; (iv) Bilayer vesicles from the co-self-assembly of wedge- and dumbbell-shaped PBIs; (b) (i) Chemical structures and independent self-assembly pathways for perylene bisimides with linear or branched side chains; (ii) Self-sorting processes in mixtures of linear or branched perylene bisimides depending on the relative concentration of the components in the mixture.

## 3. Other co-self-assemblies

Finally, we would like to conclude this bibliographic introduction with some selected examples of multifunctional co-self-assemblies based on π-π stacking or H-bonding interactions and that incorporate monomers with biorecognition groups. The first example relies on the self-assembly of π-conjugated fluorene units which form fluorescent nanoparticles with an average size of 40-50 nm in water as demonstrated by DLS and TEM experiments.[170] In their initial work, the group of Brunsveld and Schenning build up nanoparticles from two amphiphiles presenting either mannose or biotin functional units and so-called dual-targeting nanoparticles. Importantly, using FRET experiments, these dual nanoparticles displayed affinity for both concanavalin A and streptavidin with similar

---

*Ed.* **2008**, *47*, 7705-7709.

[170] Petkau, K.; Kaeser, A.; Fischer, I.; Brunsveld, L. and Schenning, A. P. H. J. Pre- and Postfunctionalized Self-Assembled π-Conjugated Fluorescent Organic Nanoparticles for Dual Targeting. *J. Am. Chem. Soc.* **2011**, *133*, 17063–17071.

efficiency than the individual nanoparticles. Subsequently, the group of Schenning studied the stability, fluorescence, dynamics, and self-sorting properties of these nanoparticles using two sets of monomers with various side chains using two sample preparation methods.[171] Overall, three different kinds of nanoparticles were observed (Figure 28a). Depending on the preparation method, i.e. mixing of preformed nanoparticles or formation of nanoparticles from a mixed solution of the monomers, either separate particles or mixed particles were respectively formed in most cases. When oligomers with different side chains were mixed, self-sorting occurred in all cases, resulting in either separate particles or mixed ones with self-sorting within the particles. This work shows that the dynamics and self-sorting properties of multifunctional co-self-assemblies can be tuned by appropriately designing monomers.

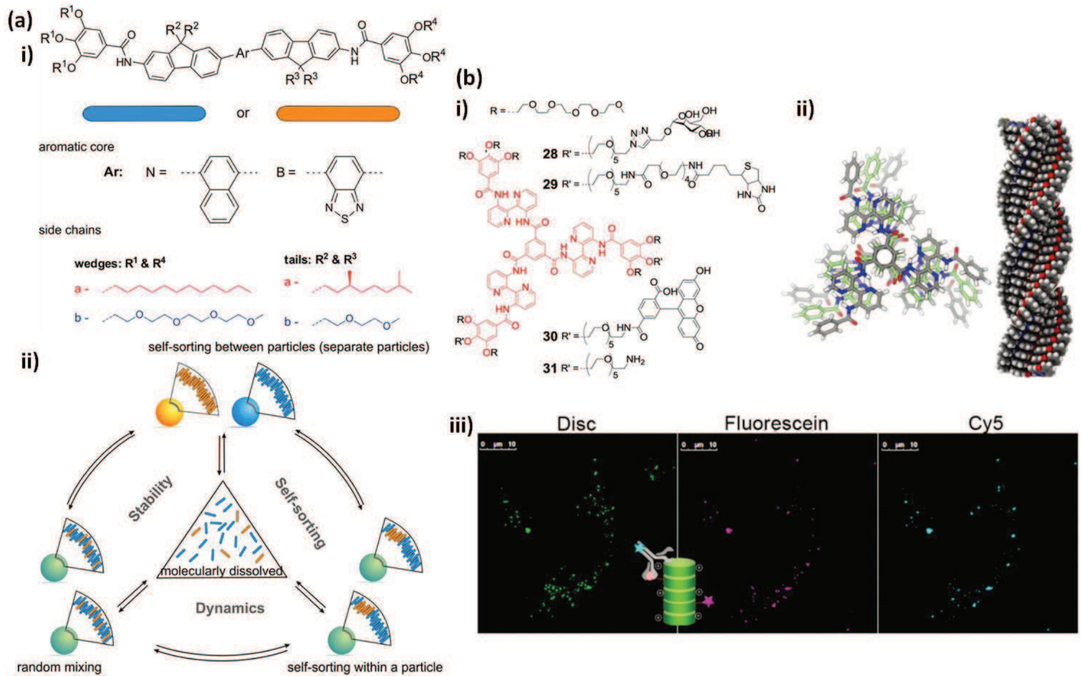

**Figure 28 |** a) (i) Molecular structures of nonionic fluorene based co-oligomers used for the formation of fluorescent nanoparticles in water. The bars represent the emission color of the π-conjugated core while the colors of the side chains refer to polarity; (ii) Different self-assembled states of bi-component nanoparticles, consisting of N and B derivatives, which have been observed in this study. Equilibriums exist between these states and the two monomers, showing the dynamics between nanoparticles, within a particle, and between particles and monomers; b) (i) Structures of BTA-based molecules decorated with mannose, biotin or PEG ligands; (ii) Self-assembly of these amphiphiles in water, (iii) Confocal images of HeLa cells incubated for 1 h with a 5 μM ternary mixture of these molecules (**31**/**30**/**29:** 80 : 10 : 10). To visualize the biotin functionalized discotic **29**, after 24 h the cells were fixed and stained with a Cy5-labelled anti-biotin antibody.

---

[171] Kaeser, A.; Fischer, I.; Abbel, R.; Besenius, P.; Dasgupta, D.; Gillisen, M. A. J.; Portale, G.; Stevens, A. L.; Herz, L. M. and Schenning, A. P. H. J. Side Chains Control Dynamics and Self-Sorting in Fluorescent Organic Nanoparticles. *ACS Nano* **2013**, *7*, 408-416.

Brunsveld and coworkers reported also the multicomponent self-assembly of BTA-based molecules decorated with PEG or mannose ligands and which form columnar aggregates at diluted concentration in water.[172] Although the formation of columnar aggregates and their auto-fluorescence was established based on previous works on BTA molecules,[173] fluorescence microscopy of bacterial assays revealed the strong fluorescence of the bacterial aggregates only in presence of the mannose derivative. Importantly, when self-assemblies were built from a limited number of mannose-functionalized monomers, an optimal binding of the bacteria was observed. Compared to covalent polymers, the supramolecular nature of the polymer is obviously a great asset to finely tune its composition depending on the application. The same group further extended this work to imaging in living cells (Figure 28b).[174] In this study, a cell-penetrating discotic molecule was combined with two non-cell-permeable ones, namely a fluorescent and a bio-labeled one and the resulting copolymer was incubated with cells. Confocal microscopy revealed that the three molecules were taken up by the cells and all colocalized inside the cell. This example clearly highlights the potential of multifunctional supramolecular polymers for biomedical applications. Similarly, the group of Meijer reported the multicomponent self-assembly of BTA molecules incorporating various pendant groups such as peptides, Gd(III) chelates and fluorescein groups.[175] The formation of single nanorods of more than 50 nm length was evidenced by cryo-TEM experiments. Additional CD experiments confirmed the formation of the supramolecular copolymerization following a cooperative mechanism. These polymers could be potentially used as targeted MRI labels.

Finally, we would like to mention the multicomponent self-assembly of peptides, which is becoming a useful method to construct multifunctional biomaterials.[176] In 2011, Gasiorowski and Collier studied the co-self-assembly of different Q-11 peptides, which are capable of forming fibrils, and their potential applications in cell culture.[177] The authors compared the properties of self-assemblies arising from intermixing between peptides and from separately assembled fibrils. Using TEM, immunoelectron microscopy and CD

---

[172] Müller, M. K. and Brunsveld, L. A Supramolecular Polymer as a Self-Assembling Polyvalent Scaffold. *Angew. Chem. Int. Ed.* **2009**, *48*, 2921 –2924.

[173] Brunsveld, L.; Zhang, H.; Glasbeek, M.; Vekemans, J. A. J. M. and Meijer, E. W. Hierarchical Growth of Chiral Self-Assembled Structures in Protic Media. *J. Am. Chem. Soc.* **2000**, *122*, 6175-6182.

[174] Petkau-Milroy, K.; Sonntag, M. H.; van Onzen, A. H. A. M.; Brunsveld, L. Supramolecular Polymers as Dynamic Multicomponent Cellular Uptake Carriers. *J. Am. Chem. Soc.* **2012**, *134*, 8086-8089.

[175] Besenius, P.; Goedegebure, Y.; Driesse, M.; Koay, M.; Bomans, P. H. H.; Palmans, A. R. A.; Dankers, P. Y. W. and Meijer, E. W. Peptide functionalised discotic amphiphiles and their self-assembly into supramolecular nanofibres. *Soft Matter* **2011**, *7*, 7980–7983.

[176] Tsutsumi, H. and Mihara, H. Soft materials based on designed self-assembling peptides: from design to application. *Mol. BioSyst.* **2013**, *9*, 609-617.

[177] Gasiorowski, J. Z. and Collier, J. H. Directed Intermixing in Multicomponent Self-Assembling Biomaterials. *Biomacromolecules* **2011**, *12*, 3549−3558.

experiments, protofibrils with *β*-sheet structure were obtained from intermixed peptides with similar morphology to the fibrils from single peptides. Additionally, gels from these mixed self-assemblies presented modular mechanical properties depending on the peptide content and displayed lower stiffening but significant increase in cell growth compared to mixtures of separated assembled fibrils. Overall, this strategy of intermixing peptides is very attractive for the production of biomaterials with modular biological and mechanical properties from existing peptides. The groups of Liu and Yang also reported the formation of hydrogels from mixed peptide derivatives.[178] Using rheological, TEM and UV-Vis experiments, two-components gels were shown to form 3D elastic networks made of 20-40 nm fibers arising mainly from aromatic π-π stacking interactions. Importantly, using LC-MS measurements, gels showed good stabilities to both dilution and enzymatic digestion, which makes them good candidates for tissue engineering. Recently, Hamley and coworkers reported a fundamental study on the co-self-assembly of peptide amphiphiles into extended nanotapes made from hydrated and dehydrated bilayer structures as demonstrated by TEM and SAXS experiments.[179] The aggregation into extended tape structures could be tuned using an appropriate mixture composition due to the formation of extended β-sheet formation as demonstrated by FTIR and CD experiments.

All these examples of multicomponent self-assembly clearly highlight the potential of supramolecular chemistry for generating new smart materials with tunable properties depending on the content in each monomer.

---

[178] Li, D.; Liu, J.; Chu, L.; Liu, J. and Yang, Z. A novel mixed-component molecular hydrogel system with excellent stabilities. *Chem. Commun.* **2012**, *48*, 6175–6177.

[179] Hamley, I. W.; Dehsorkhi, A. and Castelletto, V. Coassembly in Binary Mixtures of Peptide Amphiphiles Containing Oppositely Charged Residues. *Langmuir* **2013**, *29*, 5050−5059.

# RESULTS

# Chapter 1: Synthesis of molecular targets

In the bibliographical part, we have shown the importance of bisurea and perylene-based supramolecular polymers to produce various nanostructures which can ultimately lead to functional materials. We have also highlighted the importance of multifunctional co-self-assemblies to build self-assembled materials with potential applications in biomedicine. However, most of this work remains very fundamental and is mostaly aimed at demonstrating the different self-sorting effects that can be observed upon mixing several components. Additionally, examples of multi-functional self-assemblies based on perylene bisimides (PBI) remain scarce.

The initial goal of this thesis was to build multifunctional co-self-assemblies based on two different kinds of supramolecular interactions, namely hydrogen-bonding or π-π stacking, and to study their molecular and supramolecular rearrangement upon mixing. Considering precedents from the literature on both bisurea and perylene supramolecular polymers, we chose these two cores to build up the self-assemblies (Figure 29).

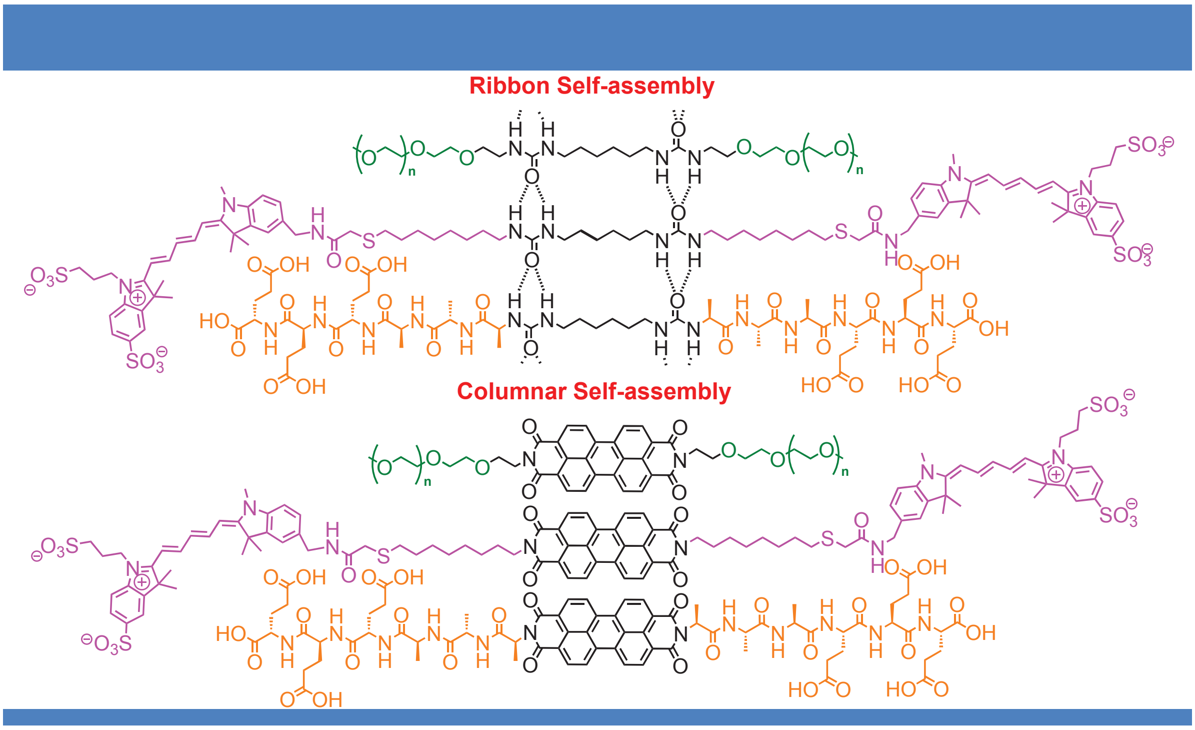

**Figure 29|** Molecular structures envisioned for the current project

Lateral side chains presenting structuring, fluorescence, or biorecognition properties were selected as functional units. In particular, PEG chains of different lengths were chosen as structuring units and cyanine dyes were selected as fluorescent moieties due to their high extinction coefficient and the possibility to perform fluorescence resonance energy transfer

(FRET, with the possibility ot give structural informations.[180] For the biorecognition unit, we chose the GluGluGluAlaAlaAla sequence which has already been reported to also induce the formation of β-sheets and as a model of bioactive peptide.[181] In the following sections, we will describe the synthesis of all the monomers studied during my PhD. The next chapters will be dedicated to the analyses of the supramolecular polymers made of a single monomer and of some co-self-assemblies with the bisurea monomers.

## 1. Retrosynthetic approach

The retrosynthetic approach to build the functional monomers described on Figure 29 is based on two building blocks: i) the central core, i.e. perylene-3,4,9,10-tetracarboxylic dianhydride (PTCDA) for PBI compounds or compound **30** for the bisurea compounds and ii) functional side chains terminated at one end by an amine group (Figure 30).

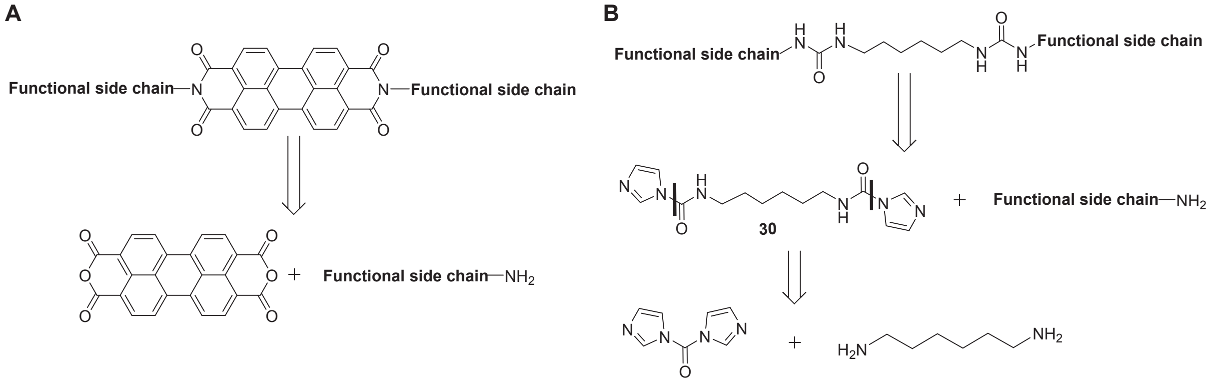

**Figure 30|** Retrosynthetic approaches envisioned for **a)** PBI compounds and **b)** bisurea compounds

The synthetic strategy to build bisurea compounds is original compared to synthetic routes described in the literature which rest on the use of bis-isocyanate molecules. Compound **30** should be obtained in one step from commercially available 1,1'-Carbonyldiimidazole (CDI) and 1,6-diaminohexane. One advantage of this approach is the possibility to access bisurea molecules from any diamino compound. As mentioned in the introduction of this chapter, the functional side chains will be divided in three categories: i) structuring units such as poly(ethylene glycol) methyl ether (hydroxyl)amines, ii) biorecognition units such as hexa- or hepta-peptides and iii) fluorescent units such as cyanine dyes (Figure 31).

---

[180] Ernst, L. A.; Gupta, R. K.; Mujumdar, R. B. and Waggoner, A. S. Cyanine dye labeling reagents for sulfhydryl groups. *Cytometry* **1989**, *10*, 3–10.

[181] Pashuck, E. T. and Stupp, S. I. Direct Observation of Morphological Transformation from Twisted Ribbons into Helical Ribbons. *J. Am. Chem. Soc.* **2010**, *132*, 8819-8821.

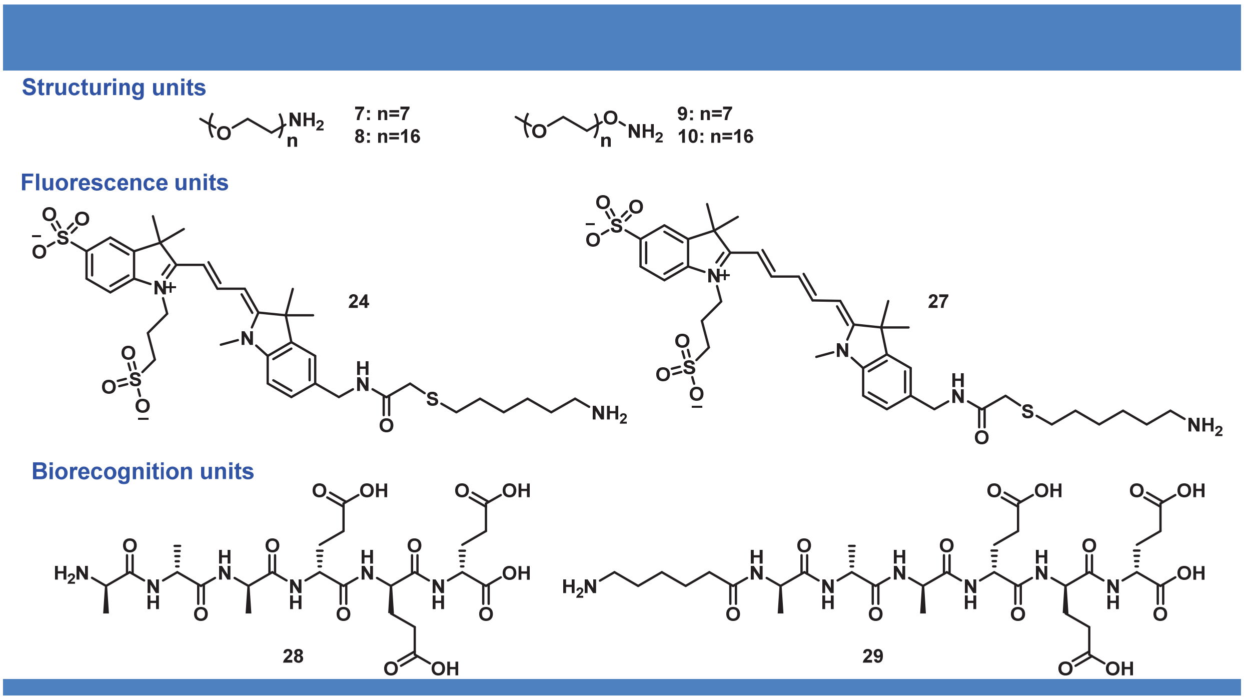

**Figure 31 |** Structures of the functional units planned in this thesis.

Compounds **7-10** will be synthesized in few steps from poly(ethylene glycol) monomethyl ether (compounds **7** and **8** could also be purchased). Peptidic units **28** and **29** will be synthesized by a stepwise approach on solid support. Fluorescent units **24** and **27** will be more challenging to synthesize as multi-step synthesis will be required following the retrochemical approach depicted on Figure 32.

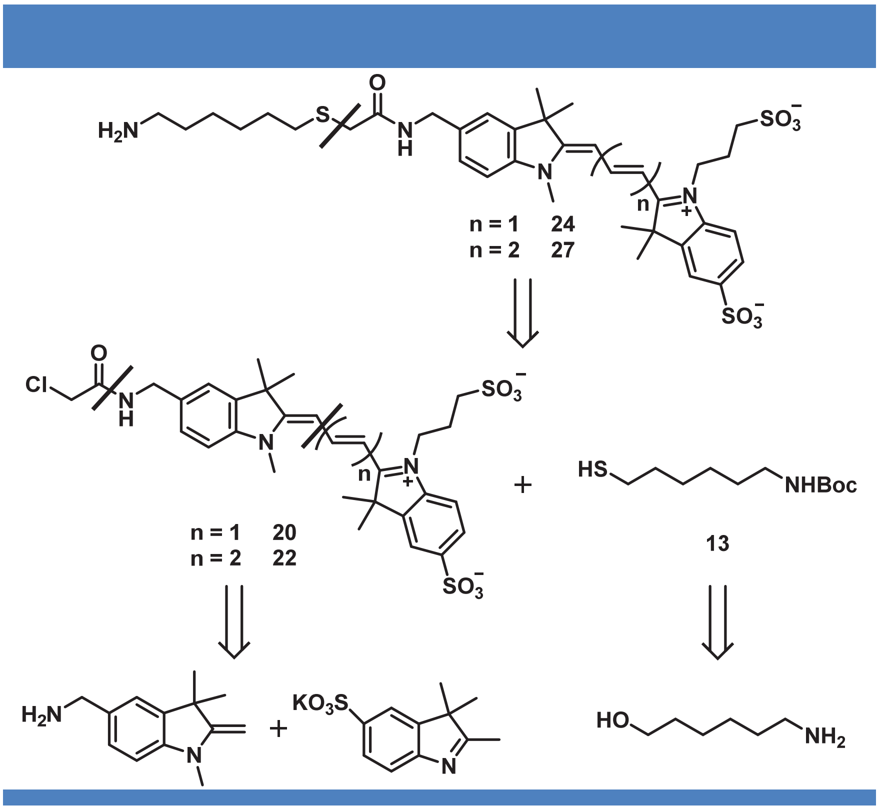

**Figure 32 |** Retrosynthetic analysis for cyanine derivatives **24** and **27**.

The synthesis of compounds **24** and **27**, which differ from the length of their conjugated backbone, is planned from cyanines **20** or **22** and compound **13** after nucleophilic substitution and deprotection of the terminal amine group. Compounds **20** and **22** will be built from commercially available following a convergent procedure described in the literature.[182] Finally, thiol **13** is planned from commercially available 6-aminohexan-1-ol.

## 2. Synthesis of the functional units

A first synthetic goal of my thesis was to build all the functional units necessary to produce the various functional monomers. In the following sections, we will describe the synthesis of these molecules. The corresponding protocols and characterization by $^1$H NMR, $^{13}$C NMR and MS are reported in the experimental section.

### a. Synthesis of polyethylene glycol amines ($PEG_nNH_2$, n = 7, 16) and hydroxylamines ($PEG_nONH_2$, n = 7, 16)

Poly(ethylene glycol) (PEG) is a well-known biocompatible and biodegradable polymer. For instance, PEG chains have been used widely used for biomedical applications in particular for drug delivery.[183] Some drug delivery systems stabilized with PEG chains have even received regulatory approvals.

The synthesis of the flexible PEG functional units is established on a procedure developed in our laboratory (Scheme 1).[69] Commercially available polydisperse monomethylether polyethylene glycol (Mw = 350 (n = 7) or 700 (n = 16)) is first tosylated using tosyl chloride in pyridine in good yiels. Tosylated PEG **1** and **2** then serve as common intermediates for the synthesis of both amine and hydroxylamines PEG units. PEG amine **7** and **8** are then obtained in two steps from compounds **1** and **2** after nucleophilic substitution with phtalimide followed by deprotection of the phtalimide unit using hydrazine in THF. A similar sequence is followed to obtain PEG hydroxylamine **9** and **10** using N-hydroxyphtalimide instead of phtalimide.

---

[182] a) Mujumdar, R. B.; Ernst, L. A.; Mujumdaar, S. R.; Lewis, C. J. and Waggoner, A. S. Cyanine Dye Labeling Reagents: Sulfoindocyanine Succinimidyl Esters. *Bioconjugate Chem.* **1993**, *4*, 105-111; b) Illy, H. and Funderburk, L. Fisher Indole Synthesis, Direction of Cyclization of Isopropylmethyl Ketone Phenylhydrazone, *J. Org. Chem.* **1968**, *33*, 4283-4285.

[183] a) Knop, K.; Hoogenboom, R.; Fischer, D. and Schubert, U. S. Poly(ethylene glycol) in Drug Delivery: Pros and Cons as Well as Potential Alternatives. *Angew. Chem. Int. Ed.* **2010**, *49*, 6288–6308. b)Webster, R.; Didier, E.; Harris, P.; Siegel, N.; Stadler, J.; Tilbury, L. and Smith, D. Pegylated Proteins: Evaluation of Their Safety in the Absence of Definitive Metabolism Studies. *Drug Metab. Dispos.* **2007**, *35*, 9-16.

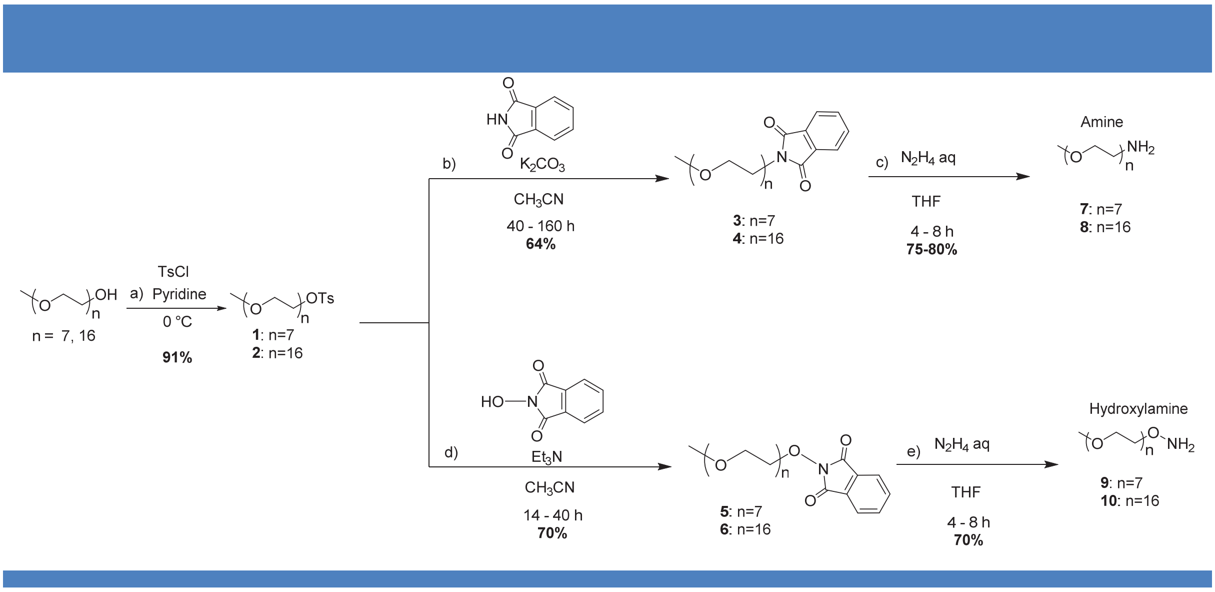

**Scheme 1 |** Synthesis of PEG$_n$NH$_2$ (**7**, **8**) and PEG$_n$ONH$_2$ (**9**, **10**)

*Reaction conditions used for* ***Scheme 1****: (a) monomethylether polyethylene glycol (1.0 equiv.), tosyl chloride (1.2 equiv.), pyridine, 0°C, 8 h, 91%; (b)* ***1*** *or* ***2*** *(1.0 equiv.), phthalimide (1.2 - 2.0 equiv.),* $K_2CO_3$ *(1.2 - 3.0 equiv.), acetonitrile, reflux, 40 h, 64%; (c)* ***3*** *or* ***4*** *(1.0 equiv.), aqueous hydrazine (40 equiv.), THF, r. t., 4 h, 75-80%; (d)* ***1*** *or* ***2*** *(1.0 equiv.), N-hydroxyphthalimide (1.2 equiv.), triethylamine (1.2 equiv.), acetonitrile, reflux, 40 h, 70%; (e)* ***5*** *or* ***6*** *(1.0 equiv.), aqueous hydrazine (40 equiv.), THF, r. t., 4 h, 70%.*

## b. Synthesis of peptidic residues

### *i. Introduction on solid-phase peptide synthesis*

Solid phase peptide synthesis (SPPS) is an approach to chemically synthesize polypeptides which was developed in 1963 by Merrifield who was awarded the Nobel Prize in 1984 "***for his development of methodology for chemical synthesis on a solid matrix***".[184] This technique involves the sequential attachment of protected amino acids to a growing peptide chain covalently bound to a solid polymeric resin particle (Figure 33). Initially, the technique developed by Merrifield was performed on PAM (hydroxymethylphenylacetamidomethyl) resin using Boc-protected amino acids. Although large peptides and small proteins could be efficiently synthesized using this approach, the need to use highly toxic HF for releasing the peptide from the resin has led to the development of milder approaches. The most used one is the Fmoc/*t*Bu method which is mostly performed on Wang Resin using amino acids protected by fluorenylmethoxycarbonyl (Fmoc) group.[185] Compared to Merrifield SPPS, this approach is typically performed under much milder conditions for both Fmoc deprotection (under basic conditions) and release of the peptide from the resin and simultaneous cleavage of the side

---

[184] Merrifield, R. B. Solid Phase Peptide Synthesis. I. The Synthesis of a Tetrapeptide. *J. Am. Chem. Soc.* **1963**, *85*, 2149-2154.

[185] Fmoc Solid Phase Peptide Synthesis, A Practical Approach, (W. C. Chan, P. D. White Eds), Oxford University Press, 2000.

chain protecting groups (under acidic conditions). The advantages of SPPS over classical liquid phase synthesis are high yields, convenient work-up, ease of purification, versatility and ease of automation.

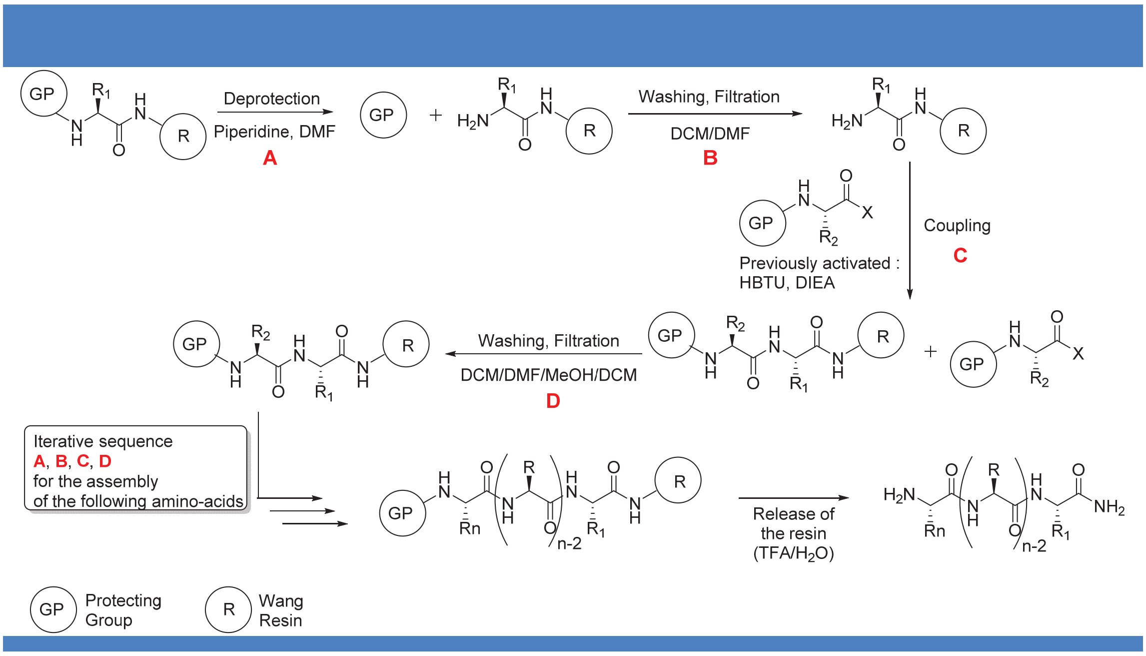

**Figure 33 |** General principle of solid phase peptide synthesis (SPPS) using the Fmoc/*t*Bu approach.

Typically, starting from a Wang resin already loaded with the first amino acid, solid phase peptide synthesis (SPPS) using the Fmoc/*t*Bu approach is performed as follows (Figure 33): i) deprotection of the Fmoc group followed by washing of the resin (**A, B**), ii) coupling with the next amino acid followed by washing of the free reagents from the resin (**C, D**). Iterative **A-D** sequences lead to the cformation of protected peptides attached to the resin. Final cleavage and deprotection of the peptide from the resin using TFA provide the desired peptide. Further precipitation and purification of the final peptide by reverse-phase HPLC are usually required to yield pure compounds. Since 1963, great progresses in chemistry (i.e., orthogonal protection strategy, coupling reagents, and solid supports) have improved the efficiency of SPPS.[186] More recently, application of microwave radiation to SPPS has been found to reduce reaction time and/or increase the initial purity of synthetic peptide products.[187]

### *ii. Synthesis of hexapeptide AAAEEE and heptapeptide EEEAAA-linker*

Among the major biocompatible and bioactive small molecules, peptides have been

---

[186] a) Albericio, F. Developments in peptide and amide synthesis *Curr. Opin. Chem. Biol.* **2004**, *8*, 211–221; b) Valeur, E. and Bradley, M. Amide bond formation: beyond the myth of coupling reagents. *Chem. Soc. Rev.* **2009**, *38*, 606-631.

[187] a) Murray, J. K.; Aral, J. and Miranda, L. P. Solid-phase peptide synthesis using microwave irradiation. *Methods Mol Biol.* **2011**, *716*, 73-88; b) Pedersen, S. L.; Tofteng, A. P.; Malika, L. and Jensen, K. J. Microwave heating in solid-phase peptide synthesis. *Chem. Soc. Rev.* **2012**, *41*, 1826-1844.

designed to self-assemble in a large variety of nanostructures such as vesicles, tubes, filaments and so on.[188] In particular, peptides appear as potential candidates for drug delivery and are know considered as new therapies in regenerative medicine.[189] The peptide sequence we chose is inspired by the work of Stupp, who reported the self-assembly of peptide amphiphiles based on the AAAEEE sequence into cylindrical nanofibers of nanometric diameters.[181,190] Hexa- and heptapeptides based on this sequence were synthesized using CEM Liberty 1 as a microwave peptide synthesizer following the sequence depicted on Scheme 2.

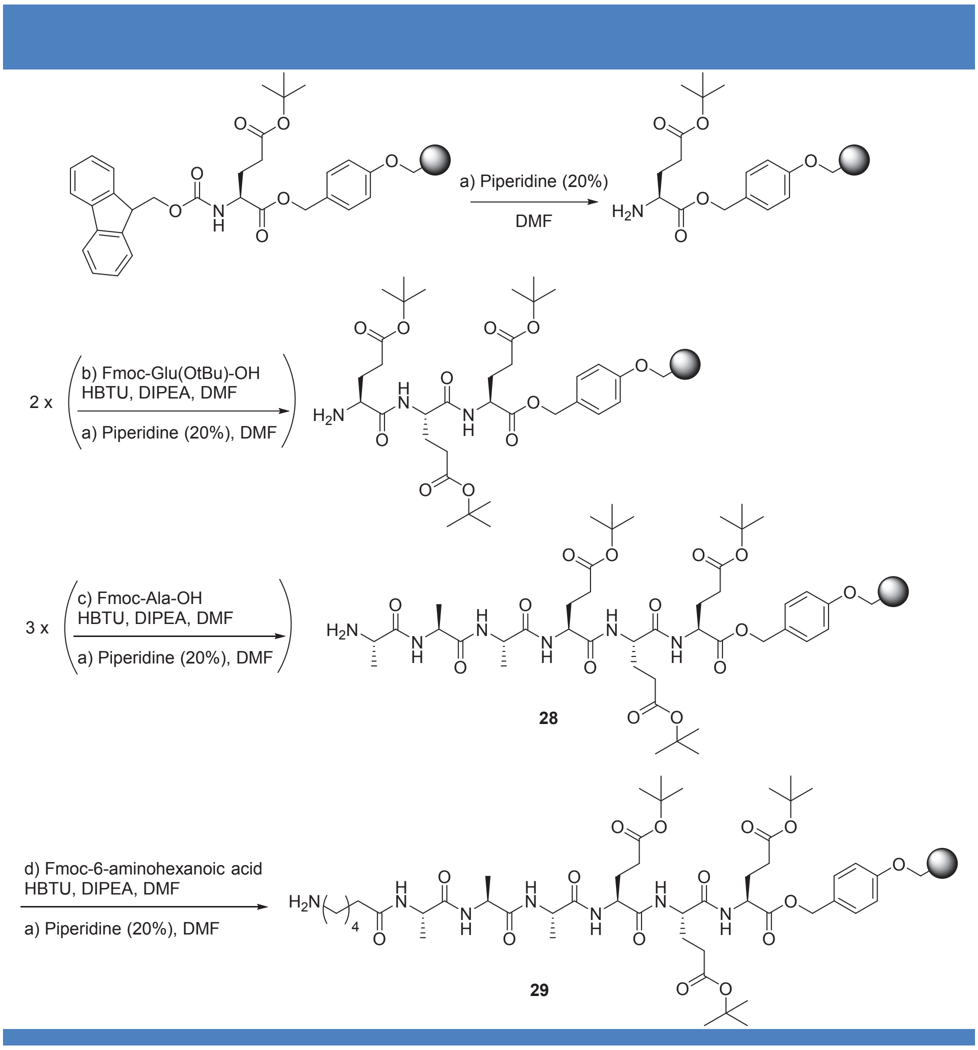

**Scheme 2 |** Synthesis of solid supported hexapeptide **28** and heptapeptide **29**

*Reaction conditions used for **Scheme 2**: a) Piperidine (20%) in DMF, 70°C, 55W, 2*3 min, b) Fmoc-L-Glu-OH (4 equiv.), HBTU (4 equiv.), DIPEA (8 equiv.), DMF, 70°C, 35W, 5 min, c) Fmoc-L-Ala-OH•$H_2O$ (4 equiv.), HBTU (4 equiv.), DIPEA (8 equiv.), DMF, 70°C, 35W, 5 min,*

---

[188] Panda, J. J. and Chauhan, V. S. Short Peptide Based Self-Assembled Nanostructures: Implication In Drug Delivery And Tissue Engineering. *Polym. Chem.* **2014**, *5*, DOI: 10.1039/C4PY00173G.

[189] Matsona, J. B. and Stupp, S. I. Self-assembling peptide scaffolds for regenerative medicine. *Chem. Commun.* **2012**, *48*, 26-33.

[190] Pashuck, E. T.; Cui, H. and Stupp, S. I. Tuning Supramolecular Rigidity of Peptide Fibers through Molecular Structure. *J. Am. Chem. Soc.* **2010**, *132*, 6041–6046.

*d) Fmoc-L-6-aminohexanoic acid (4 equiv.), HBTU (4 equiv.), DIPEA (8 equiv.), DMF, 70°C, 35W, 5 min.*

Typically, Fmoc-L-Glu-MPPA (wang)-Resin was used so that the sequence always starts with the deprotection of the Fmoc protecting group using piperidine (20%) in DMF. Iterative peptidic couplings using Fmoc-protected amino acids and HBTU as activating agent followed by Fmoc deprotection ultimately lead to expected hexapeptide **28** and heptapeptide **29** attached to Wang resin. The purity of the peptide on the resin was assessed by LC/MS and 1H NMR after releasing the peptide from the solid support using a mixture of TFA and TIPS in water.

### c. Synthesis of cyanine derivatives

Cyanine dyes $Cy_3$ and $Cy_5$ were first described by Waggoner and co-workers.[180] These dyes are bright and photostable, and can be used for cells labeling and imaging.[191] In particular, these molecules are known to produce fluorescence resonance energy transfer (FRET) over 50 Å. Recently, FRET between $Cy_3$ and $Cy_5$ dyes have been used to study the dynamic behavior of supramolecular polymers based on BTA building blocks upon binding with ssDNA.[192]

Here, we will describe first the synthesis of the bifunctional linker **13** and cyanine derivatives **20** and **22** as described in Figure 32.[182] We will then describe their coupling to produce functional dyes **24** and **27**.

#### *i. Synthesis of bifunctional linker **13***

6-aminohexan-1-ol was selectively protected on the amine moiety using $Boc_2O$ to give alcohol **11** (Scheme 3).[193] This compound was then reacted with thioacetic acid in a Mitsunobu reaction to produce compound **12**.[194] The acetate protecting group was then removed using sodium thiomethoxide in methanol and THF to give thiol compound **13**, which could not be stored due to its high propensity to form disulfide and had therefore to be directly coupled with compounds **20** or **22**.c[195]

---

[191] (a) Kraynov, V. S.; Chamberlain, C. E.; Bokoch, G. M.; Schwartz, M. A.; Slabaugh, S. and Hahn, K. M. Localized Rac activation Dynamics Visualized in Living Cells. *Science* **2000**, *290*, 333-337; (b) Kenworthy, A. K. Imaging Protein-protein Interactions Using Fluorescence Resonance Energy Transfer Microscopy. *Methods* **2001**, *24*, 289-296.

[192] Albertazzi, L.; Martinez-Veracoechea, F. J.; Leenders, C. M. A.; Voerts, I. K.; Frenkel, D. and Meijer, E. W. Spatiotemporal control and superselectivity in supramolecular polymers using multivalency. *Proc. Nat. Acad. Sci. USA* **2013**, *110*, 12203-12208.

[193] Lee, A. H. F. and Kool. E. T. Exploring the Limits of DNA Size:  Naphtho-Homologated DNA Bases and Pairs. *J. Am. Chem. Soc.* **2006**, *128*, 9219–9230.

[194] Moutevelis-Minakakis, P.; Neokosmidi, A.; Filippakou, M.; Stephens, D.; Dennis, E. A. and Kokotos, G. Synthesis of lipophilic 2-oxoamides based on γ-aminobutyric and δ-aminovaleric analogues and their activity against phospholipase A2. *J. Peptide Sci.* **2007**, *13*, 634–641.

[195] Tauk, L.; Schröder, A.; Decher, G. and Giuseppone, N. Hierarchical Functional Gradients of pH-responsive Self-assembled Monolayers using Dynamic Covalent Chemistry on Surfaces. *Nature Chem.* **2009**, *1*, 649-656.

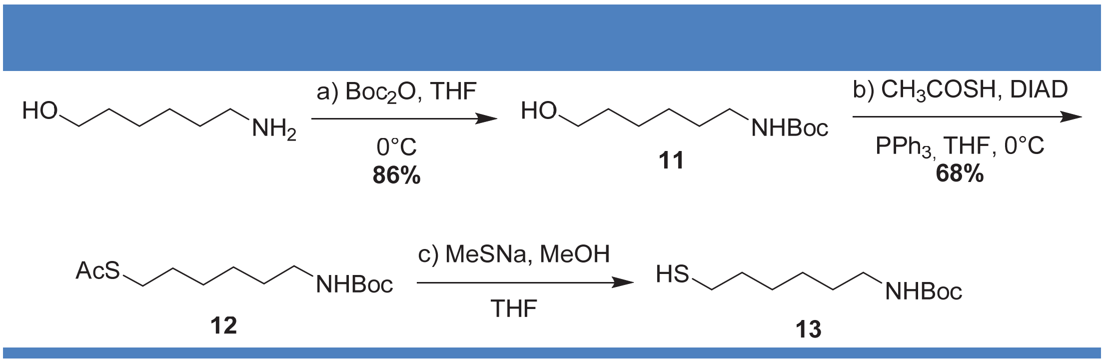

**Scheme 3 |** Synthesis of bifunctional linker **13**

*Reaction conditions used for* ***Scheme 3****: (a) Di-tert-butyl-dicarbonate (1.0 equiv.), 6-amino-1-hexanol (1.0 equiv.), THF, 0 °C, o. n., 86%; (b)* ***11*** *(1.0 equiv.), triphenylphosphine (1.1 equiv.), Diisopropylazodicarboxylate (DIAD, 1.1 equiv.), thioacetic acid (1.1 equiv.), THF, 0 °C, o. n., 68%; (c)* ***12*** *(1.0 equiv.), sodium thiomethoxide (1.0 equiv.),* $CH_3OH$*, THF, 0 °C, 1.5 h.*

### *ii. Synthesis of Cy$_3$ derivative*

One key intermediate for the synthesis of both Cy$_3$ and Cy$_5$ derivatives is chloroacetamide **17** (Scheme 4).

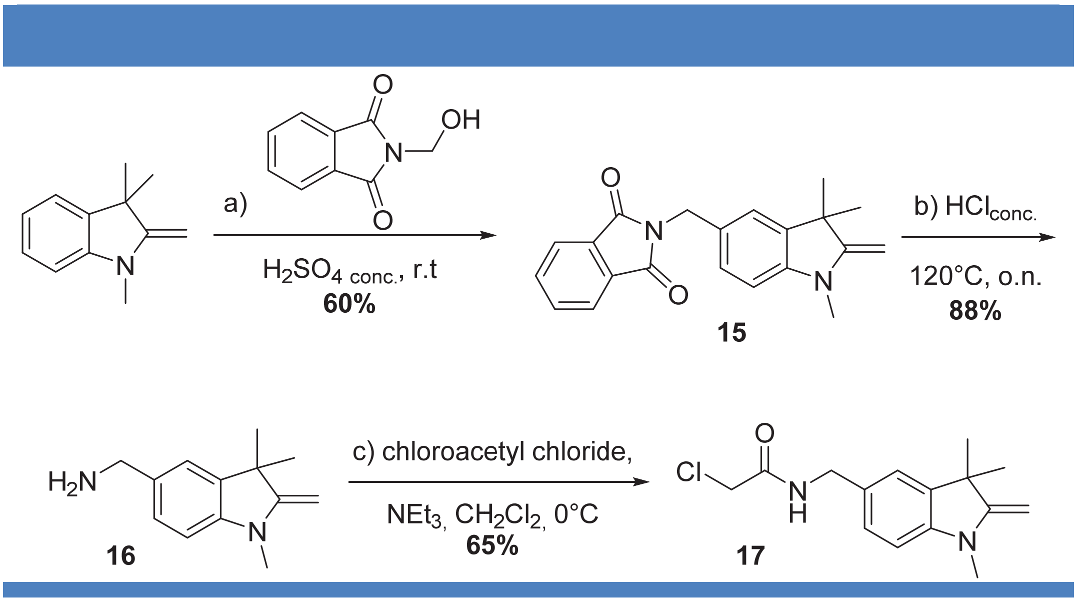

**Scheme 4 |** Synthesis of compound **17**

*Reaction conditions used for* ***Scheme 4****: (a) N-hydroxymethylphthalimide (1.0 equiv.), Fischer's base (1.0 equiv.), concentrated* $H_2SO_4$*, r. t., 70 h, 60%; (b)* ***15****, concentrated hydrochloric acid, reflux, o. n., 88%; (c)* ***16*** *(1.0 equiv.), triethylamine (1.0 equiv.), chloroacetyl chloride (1.0 equiv.),* $CH_2Cl_2$*, 0°C, 3 h, 65%.*

The first step consists in the condensation of Fischer's base with *N*-hydroxymethylphtalimide in concentrated sulfuric acid to yield compound **15**. Cristallisation of the reaction mixture allows the separation of the two isomers (at 5 or 6 position) obtained during this reaction, affording compound **15** as a single compound. This product is then deprotected at reflux in chlorhydric acid to yield amine **16**, which is further reacted with chloroacetyl chloride to yield **17** in 65% yield.[196]

For the second indole moiety, potassium 2,3,3-trimethyl-3H-indole-5-sulfonate was available in large scale in the laboratory;[195] therefore the synthesis of cyanine **20** was started directly from this intermediate (Scheme 5).

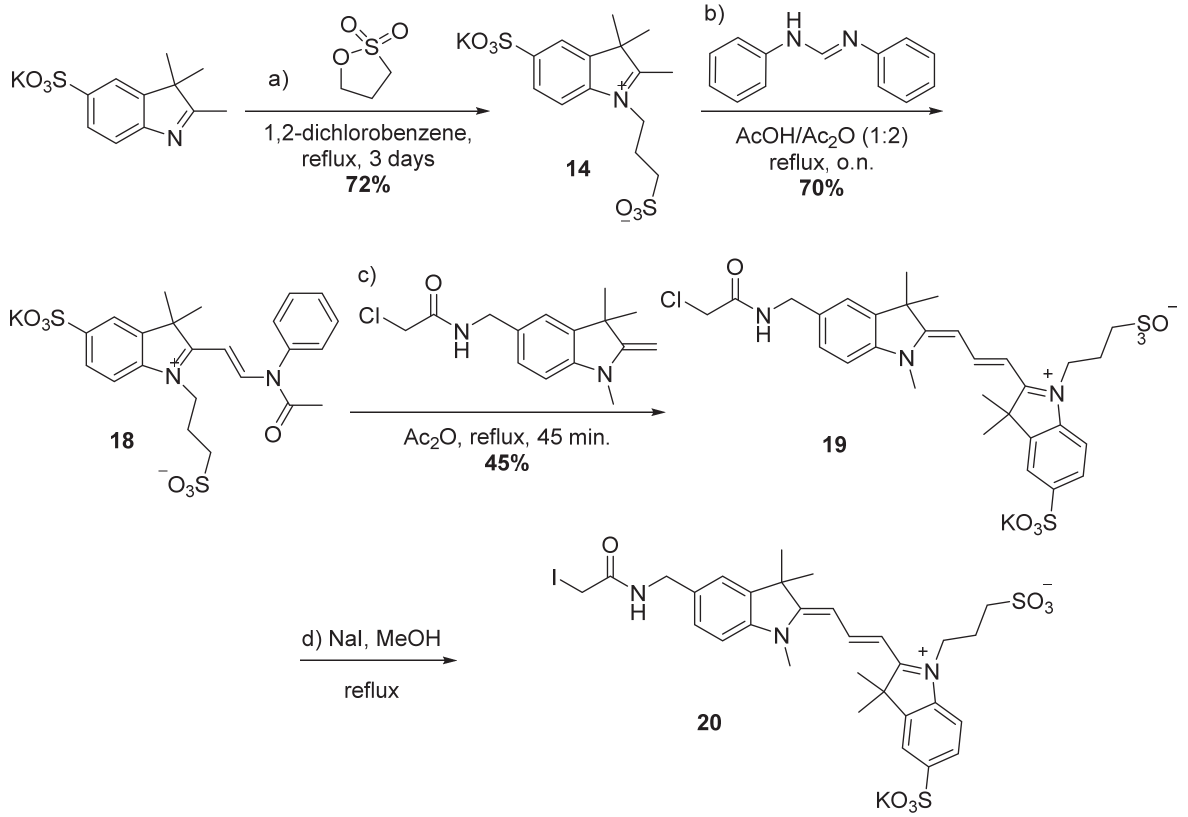

**Scheme 5 |** Synthesis of Iodo-$Cy_3$ **20**

*Reaction conditions used for* ***Scheme*** *5: (d) Potassium 2,3,3-trimethyl-3H-indole-5-sulfonate (1.0 equiv.), 1,3-propane sultone (2.1 equiv.), 1,2-dichlorobenzene, reflux, 3 days, 72%; (e)* ***14*** *(1.0 equiv.), N,N-diphenylformamidine (4.6 equiv.), acetic acid/acetic anhydride (1:2), reflux, o. n., 70%; (f)* ***17*** *(1.0 equiv.),* ***18*** *(1.0 equiv.), acetic anhydride, reflux, 45 min, 45%; (g)* ***19*** *(1.0 equiv.), NaI (1.0 equiv.), $CH_3OH$, reflux, 3 h.*

Propane sultone was reacted with potassium 2,3,3-trimethyl-3H-indole-5-sulfonate in 1,2-dichlorobenzene during three days to yield indoleninium bis-sulfonate **14** in 72% yield. This compound was then submitted to a condensation reaction with *N,N*-diphenylformamidine

---

[196] Gale, D. J.; Lin, J. and Wilshire, J .F. K. The Amidomethylation and Bromination of Fischer's Base. The Preparation of Some New Polymethine Dyes. *Aust. J. Chem.* **1977**, *30*, 689-694.

in a mixture of acetic acid and acetic anhydride at reflux for one night. Resulting compound **18** was obtained after filtration as a yellow solid in 70% yield. The poor stability of this compound forced us to use it as soon as possible in the condensation reaction with **17** to yield compound **19** after 45 min of reaction in acetic anhydride at reflux. One great asset of this synthesis resides on the possibility to yield various unsymmetric cyanine derivatives by modulating the structure of compound **18** *(vide infra)*. The moderate yield (45%) observed for compound **19** can be explained by the formation of homocoupling products. Finally, compound **20** was obtained after halogen exchange using sodium iodide in methanol at reflux.[197] This advanced cyanine intermediate **20** was then coupled in a nucleophilic substitution reaction with thiol **13** using potassium carbonate as a base in DMF (Scheme 6).

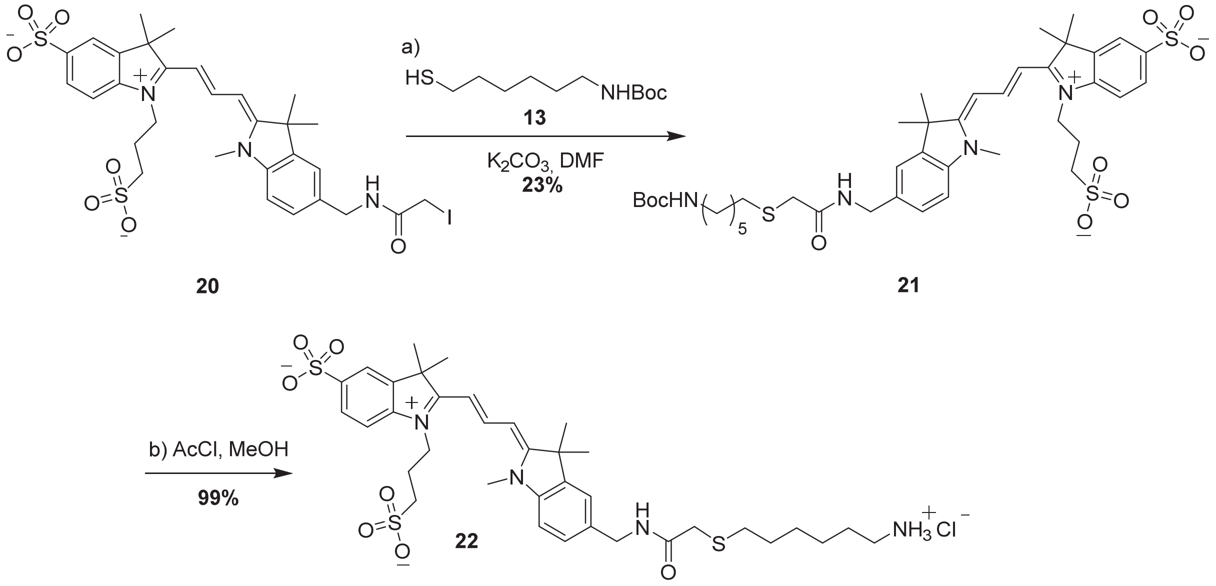

**Scheme 6 |** Synthesis of Cy$_3$-amine **22**

*Reaction conditions used for **Scheme 6**: (a) **20** (1.0 equiv.), **13** (2.0 equiv.), potassium carbonate (3.0 equiv.), DMF, r. t., o. n., 23%; (b) **21**, acetyl chloride/methanol (1:1), 0 °C, 30 min, 99%.*

Compared to the synthesis developed previously in the laboratory,[195] we chose Boc protecting group for the terminal amine as removal of the phtalimide protecting group using hydrazine was sometimes problematic due to the sensitivity of the conjugated backbone. The yield of the reaction leading to **21** is quite low but can be explained by its high purity after purification by reverse-phase preparative HPLC and the possible dimerization of compound

---

[197] Toutchkine, A.; Nalbant, P.; Hahn, K. M. Facile Synthesis of Thiol-Reactive Cy$_3$ and Cy$_5$ Derivatives with Enhanced Water Solubility. *Bioconjugate Chem.* **2002**, *13*, 387-391.

**13**. Finally, Boc protecting group was removed using mild acidic conditions to afford compound **22** as the hydrochloride salt.[198]

### iii. *Synthesis of Cy$_5$ derivative*

Similarly to Cy3, cyanine 5 derivative **27** was obtained from compounds **14** and **17**, whose synthesis has been previously described. Indoleninium bis-sulfonate **14** was reacted in a condensation reaction with malonaldehyde dianilide in a mixture of acetic acid and acetic anhydride at reflux for two hours (Scheme 7). Considering the compatibility of the reaction conditions, the resulting product, which is particularly unstable, was reacted in situ with indole **17** for additional 20 minutes at reflux, leading to pure compound **24** after reverse-phase preparative HPLC. Finally, following a nucleophilic substitution mechanism, compound **25** was obtained from **24** after halogen exchange using sodium iodide in methanol at reflux.

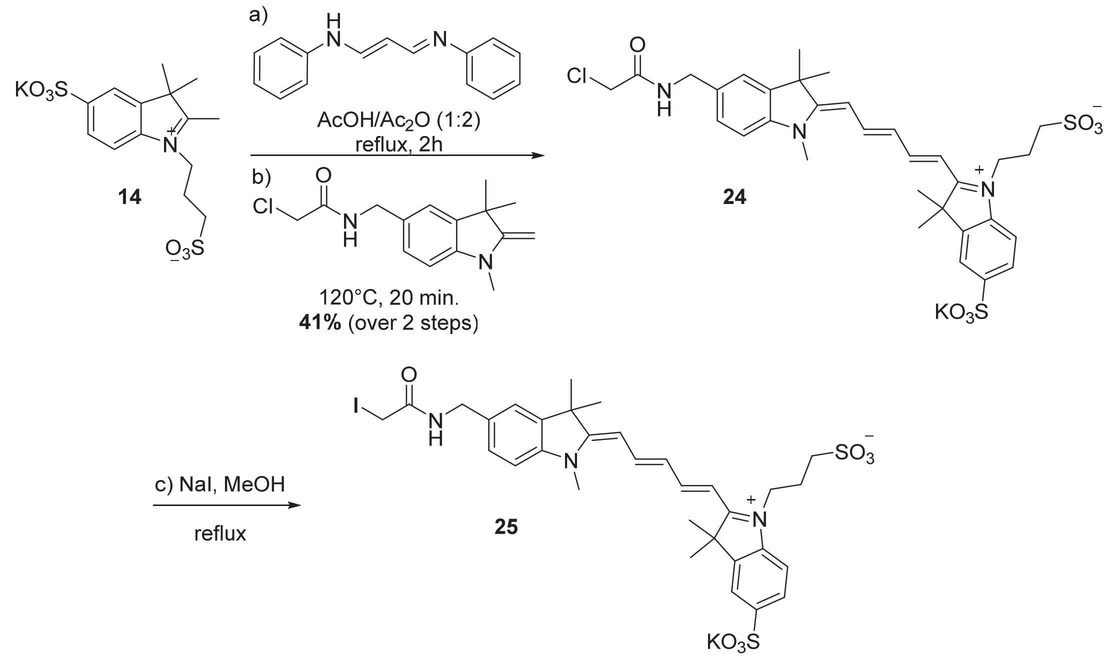

**Scheme 7** | Synthesis of iodo-Cy$_5$ **25**

*Reaction conditions used for* ***Scheme*** *7: (a)* ***14*** *(2.2 equiv.), malonaldehyde dianilide hydrochloride (1.0 equiv.), acetic acid-acetic anhydride (1:2) , reflux, 2 h; (b)* ***17*** *(1.0 equiv.), reflux, 20 min, 41% (over 2 steps); (b)* ***24*** *(1.0 equiv.), NaI (9.0 equiv.), $CH_3OH$, reflux, 3 h.*

Advanced cyanine intermediate **25** was then coupled in a nucleophilic substitution reaction with thiol **13** using potassium carbonate as a base in DMF (Scheme 8). As for compound **21**, the low yield of the reaction leading to **26** can be explained by its high purity

---

[198] Nudelman, A.; Bechor, Y.; Falb, E.; Fischer, B.; Wexler, B. A. and Nudelman, A. Acetyl Chloride-Methanol as a Convenient Reagent for: A) Quantitative Formation of Amine Hydrochlorides B) Carboxylate Ester Formation C) Mild Removal of N-t-Boc-Protective Group. *Synth. Commun.* **1998**, *28*,471-474.

after purification by reverse-phase preparative HPLC and the possible dimerization of compound **13**. Finally, Boc protecting group was removed using mild acidic conditions to afford compound **27** as the hydrochloride salt.

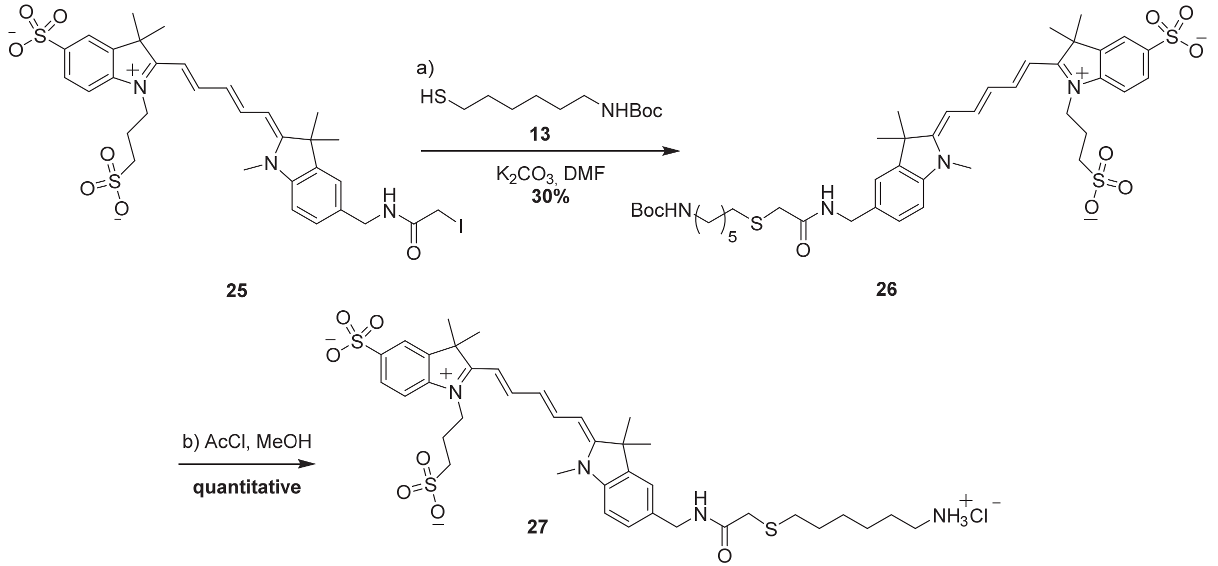

**Scheme 8 |** Synthesis of Cy$_5$-amine **27**

*Reaction conditions used for* ***Scheme 8****: (a)* ***25*** *(1.0 equiv.),* ***13*** *(2.0 equiv.), potassium carbonate (3.0 equiv.), DMF, r. t., o. n., 30%; (b)* ***26****, acetyl chloride/methanol (1:1), 0 °C, 30 min, quantitative.*

## 3. Synthesis of bisurea derivatives

### a. Synthesis of the structuring bisurea core

As mentioned in the first section, the most common strategy to build bis-urea compounds is achieved from bis-isocyanate molecules. Here, we decided to develop a strategy that could be extended to any diamine substrates. In the present work, we started from 1,6-diaminohexane to produce compound **30** after reaction with *N,N'*-carbonyldiimidazole (Scheme 9).

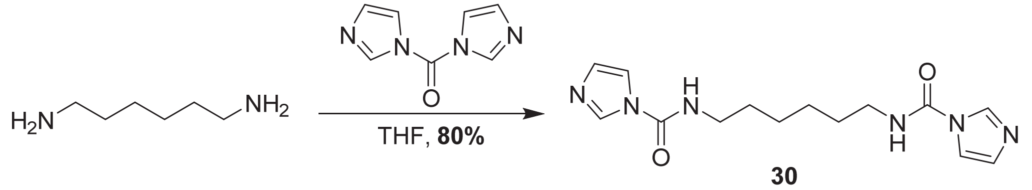

**Scheme 9 |** Synthesis of *N,N'*-1,6-hexanediylbis-1H-Imidazole-1-carboxamide (**30**)

*Reaction conditions used for* ***Scheme 9****: 1,6-diaminohexane (1.0 equiv.), N,N'-carbonyldiimidazole (2.1 equiv.), THF, r. t., 21 h, 80%.*

Importantly, this reaction can be performed on several grams and the resulting compound can be stored for several years without degradation.

### b. Synthesis of bisurea-polyethylene glycol derivatives (PEG$_n$NH$_2$, n=7, 16)

Bisurea-PEG derivatives were synthesized by reacting compound **30** with the previously synthesized PEG derivatives **7** and **8** (section 2.a) in dichloromethane at 40°C for 48 h (Scheme 10).[199]

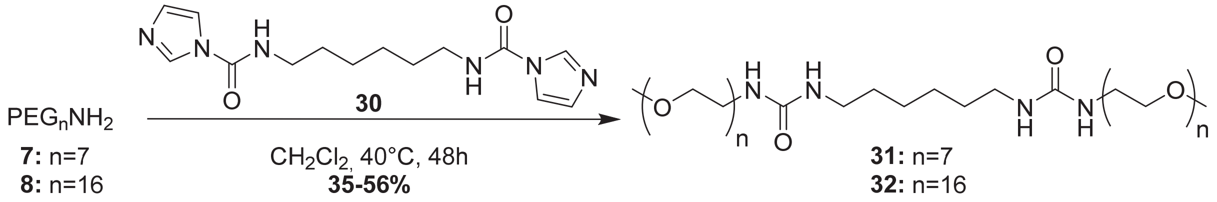

**Scheme 10 |** Synthesis of bisurea-PEG$_7$ **(31)** and bisurea-PEG$_{16}$ **(32)**.

*Reaction conditions used for* ***Scheme 10****:* ***7*** *or* ***8*** *(2.5 equiv.),* ***30*** *(1.0 equiv.),* $CH_2Cl_2$*, 40 °C, 2 days, 35-56%.*

After purification by reverse-phase preparative HPLC, good quantities of compounds **31** and **32** could be obtained (> 200 mg). Importantly, all attempts to couple PEG-hydroxylamine derivatives with compound **30** did not produce the expected compounds.

### c. Synthesis of bisurea–peptides derivatives

Initially, bisurea-peptides were synthesized in solution from compound **30** and the hexa- or heptapeptide released from the resin. Although this reaction proceeded well but only at quite high temperature for a reaction with a peptidic backbone (DIPEA (2 equiv.), **30** (1 equiv.), peptide (2 equiv.), DMF, 80°C under microwave (dynamic mode, power: 200 W), 24 h), its purification by preparative HPLC was difficult. Therefore, we envisioned the synthesis of these bisurea-peptides directly from the supported peptides **28** and **29** and expected that the work-up and the purification would be much easier as all the reagents would be removed by a simple filtration. The synthetic route followed to synthesize bisurea-6AA **35** and bisurea-7AA

---

[199] De Greef, T. F. A.; Nieuwenhuizen, M. M. L.; Stals, P. J. M.; Fitié, C. F. C.; Palmans, A. R. A.; Sijbesma, R. P. and Meijer, E. W. The Influence of Ethylene Glycol Chains on the Thermodynamics of Hydrogen-bonded Supramolecular Assemblies in Apolar Solvents. *Chem. Commun.* **2008**, 4306-4308.

**36** is depicted on Scheme 11.

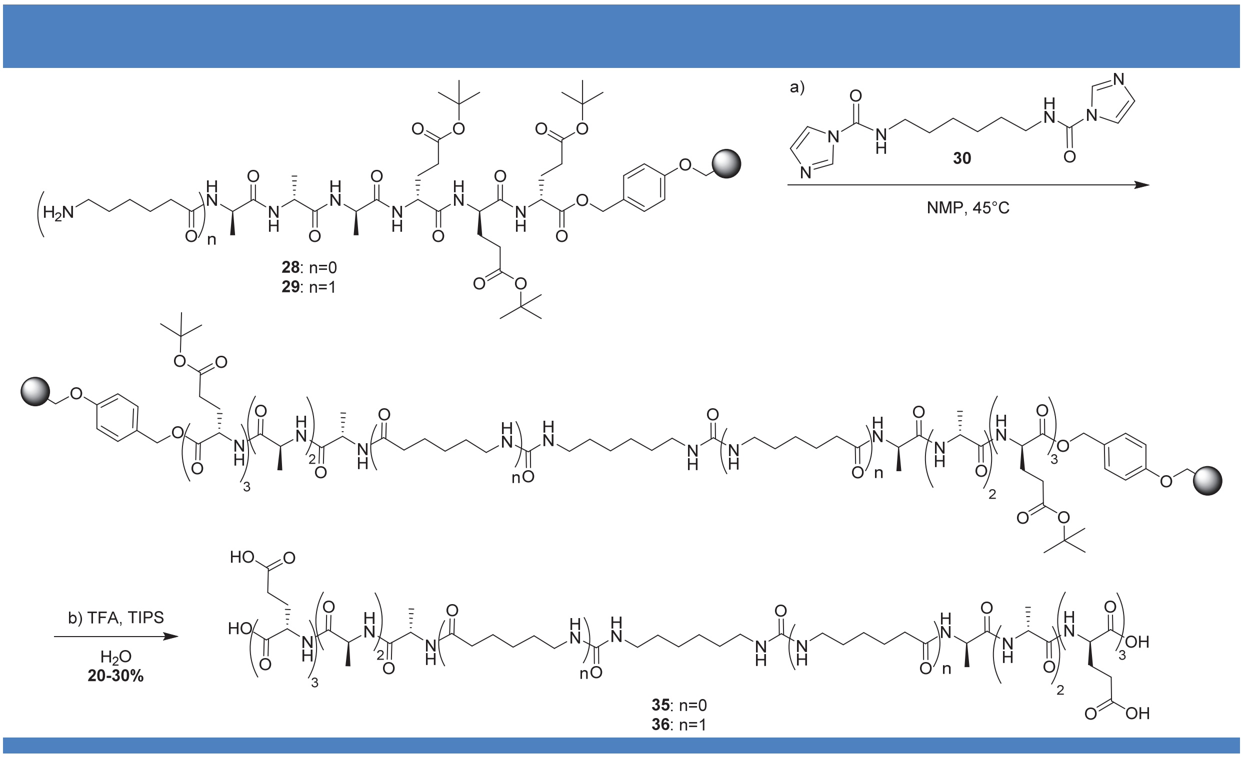

**Scheme 11 |** Synthesis of bisurea-6AA **(35)** and bisurea-7AA **(36)**.

*Reaction conditions used for* ***Scheme 11****: (a)* ***28*** *or* ***29*** *(2.1 equiv.),* ***30*** *(1.0 equiv.), NMP, 45 °C, 24-48 h; (b) TFA/$H_2O$/TIPS (9.5: 0.25:0.25), r. t., 2*1 h, 20-30% (over the whole peptidic sequence).*

Supported hexapeptide **28** and heptapeptide **29** were reacted individually with compound **30** at 45 °C in N-methylpyrrolidone (NMP) to produce supported bisurea-6AA and bisurea-7AA, respectively. The reaction was monitored by LC/MS after cleaving some beads of resin. Compounds **35** and **36** were then released from the solid support using a mixture of TFA/$H_2O$/TIPS (95:2.5:2.5) after concomitant removal of the tert-butyl protecting groups.

### d. Synthesis of bisurea–cyanine derivatives

Bisurea-cyanine derivatives **33** and **34** were synthesized following a strategy similar to the one used for bisurea-PEG compounds (Scheme 12). The main difference was the use of DMF instead of dichloromethane due to the poor solubility of compounds **22** and **27** in the latter solvent. Additionally, N-ethyldiisopropylamine was used to deprotonate their amine group. This base was chosen for its pKa value compared to the aliphatic amine and its poor nucleophilicity to avoid any degradation of the conjugated backbone of the cyanine cores. Both compounds (**33** and **34**) were obtained in sufficient quantities (20-30 mg) for the study of their self-assembly in water and their co-self-assemblies with other bis-urea derivatives (see Results - Chapter 2).

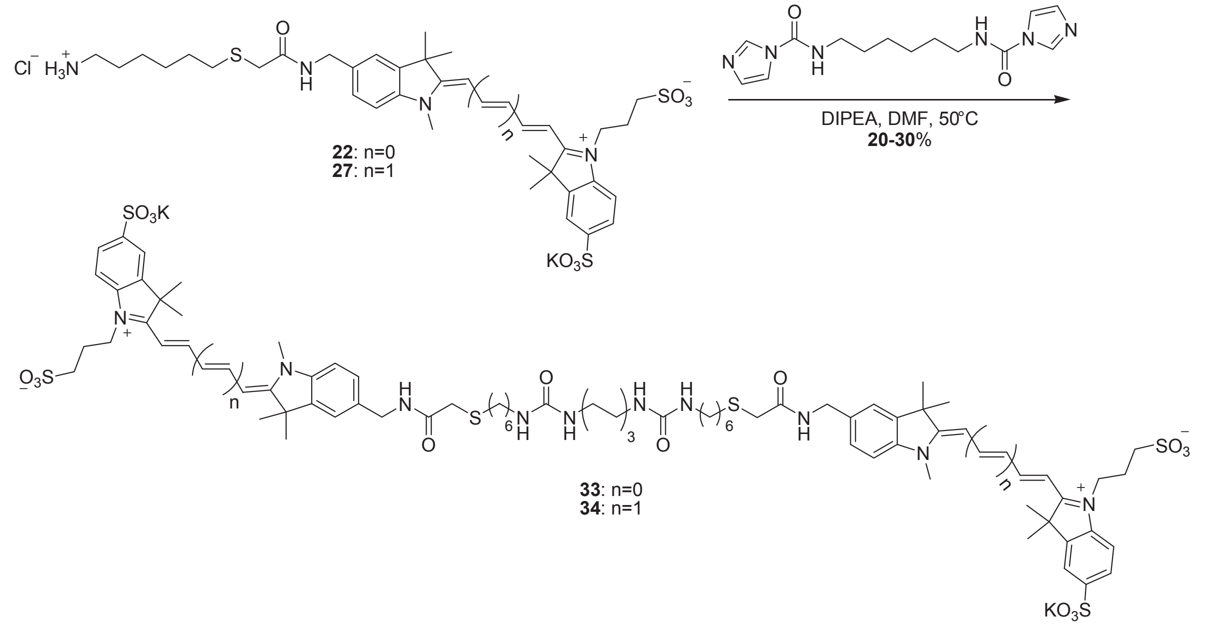

**Scheme 12 |** Synthesis of bisurea-Cy$_3$ **33** and bisurea-Cy$_5$ **34**.

*Reaction conditions used for* ***Scheme 12: 22*** *or* ***27*** *(2.0 equiv.),* ***30*** *(1.0 equiv.), N-ethyldiisopropylamine (4.0 equiv.), DMF, 50 °C, 32 h, 20-30%.*

## 4. Synthesis of perylene bisimide derivatives

All perylene bisimide (PBI) derivatives were synthesized from commercially available 3,4,9,10-perylenetetracarboxylic dianhydride (PTCDA) following different strategies that are well-known in the lilterature[130] and which will be detailed in the next sections.

### a. Synthesis of PBI-polyethylene glycol derivatives (PEG$_n$NH$_2$ and PEG$_n$ONH$_2$, n=7, 16)

PEG derivatives **7**, **8**, **9** and **10** were reacted with PTCDA in pyridine at reflux to produce PBI-PEG derivatives **37**, **38**, **39** and **40**, respectively.[200] Importantly, whereas some PBI-polyethylene glycol compounds have already been reported in the literature (see Bibliography, Chapter 3. a.), the synthesis of PBI molecules from hydroxylamine derivatives has never been reported so far.

---

[200] Cormier, R. A. and Gregg, B. A. Synthesis and Characterization of Liquid Crystalline Perylene Diimides. *Chem. Mater.* **1998**, *10*, 1309-1319.

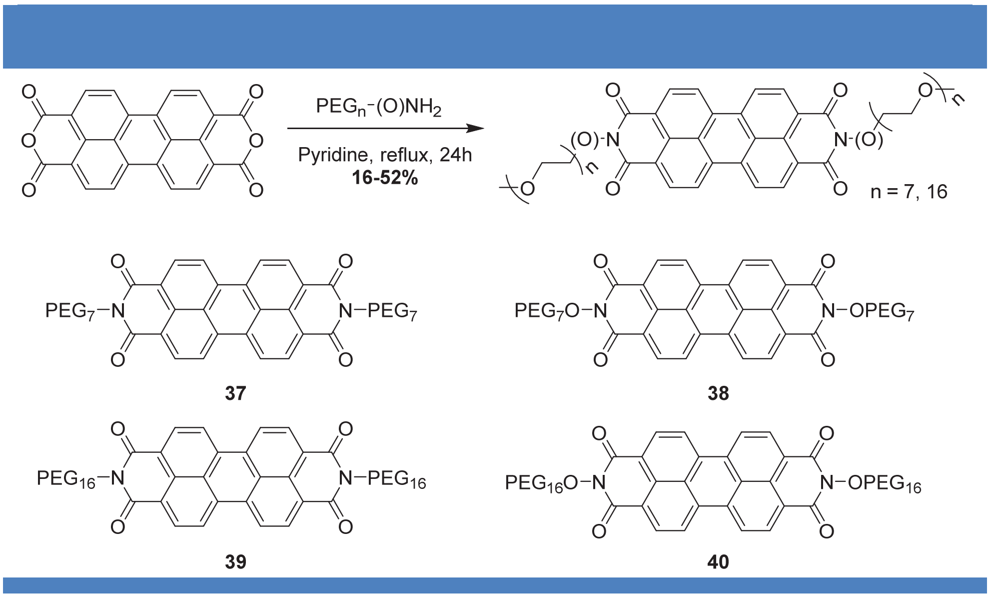

**Scheme 13 |** Synthesis of perylene derivatives PBI-PEG$_7$ (**37**), PBI-OPEG$_7$ (**38**), PBI-PEG$_{16}$ (**39**) and PBI-OPEG$_{16}$ (**40**)

*Reaction conditions used for **Scheme 13**: 7, **8**, **9** or **10** (1.0 equiv.), PTCDA (1.0 equiv.), pyridine, reflux, 24 h, 16-52%.*

## b. Synthesis of PBI-peptides derivatives

Inspired by previous work in the literature[144,145] and following our successful approach on bisurea-peptide derivatives, PBI-peptides **43** and **44** were directly synthesized from supported peptides **28** and **29** (Scheme 14).

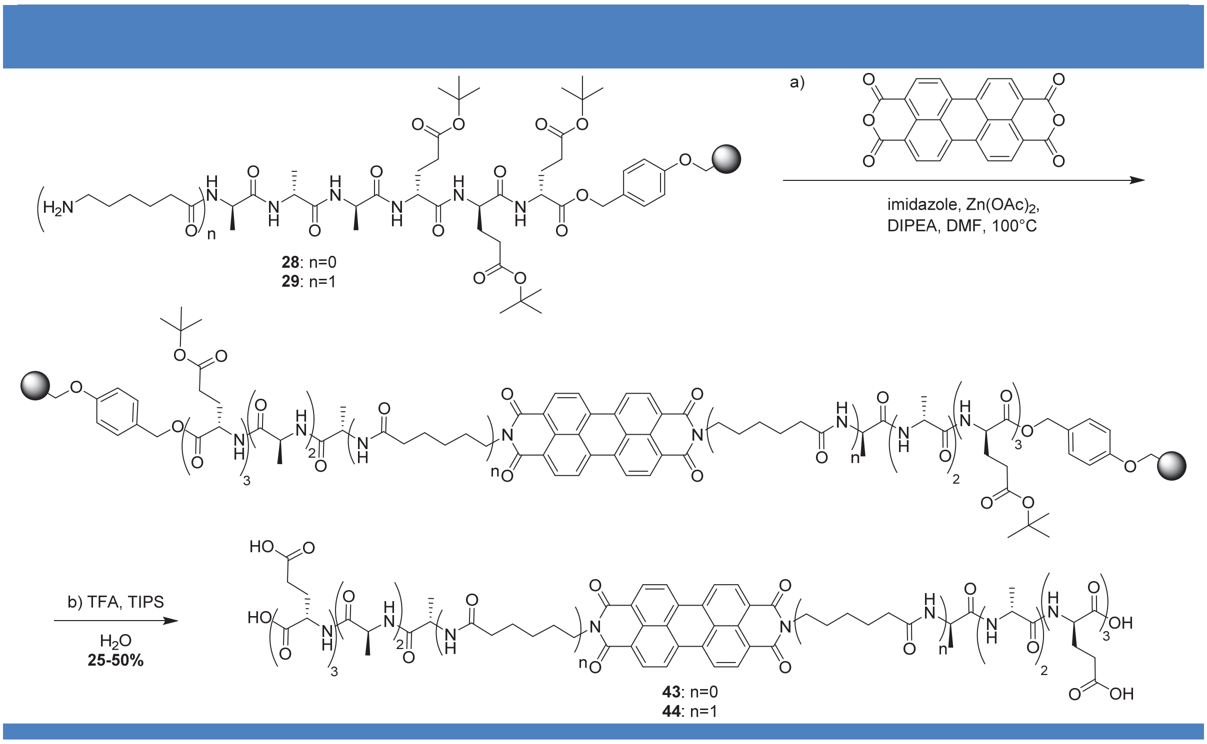

**Scheme 14 |** Synthesis of perylene derivatives PBI-6AA (**43**) and PBI-7AA (**44**)

*Reaction conditions used for* ***Scheme 14****: (a)* ***28*** *or* ***29*** *(2.1 equiv.), PTCDA (1.0 equiv.), imidazole (20 equiv), DIPEA (2.1 equiv), zinc acetate dehydrate (0.3 equiv), DMF, 100 °C, 2-3 days; (b) TFA/$H_2O$/TIPS (9.5: 0.25:0.25), r. t., 2*1 h, 25-50% (over the whole peptidic sequence).*

Identically to bisurea-peptide derivatives, compounds **43** and **44** were released from the solid support after reaction with a 95:2.5:2.5 miwture of TFA/TIPS/$H_2O$. Although the PBI core is highly hydrophobic, PBI-peptides derivatives display good solubility in water and could be purified by reverse-phase preparative HPLC.

### c. Synthesis of PBI–$Cy_3$ derivative

The most challenging synthetic work of this thesis was the synthesis of PBI-cyanine derivatives. Several synthetic procedures have been screened to reach molecule **41** and are detailed in the following table.

**Table 1|** Conditions screened for the synthesis of compound **41** from PTCDA and compound **22** in a 1:2 ratio.

| *Conditions* | *LC/MS analysis* |
|---|---|
| $CH_3COOH$, DMF, 100 ºC, 2 days | No product |
| DMF, 120 ºC, 24 h | No product; $Cy_3$ is stable |
| DMF, $Zn(OAc)_2$, 120 ºC, 24 h | Degradation of $Cy_3$ |
| TEA, $Zn(OAc)_2$, DMAc, 150 ºC, 10 h | No product; Degradation of $Cy_3$ |
| DIPEA, $Zn(OAc)_2$, DMAc, 110 ºC, 10 h | No product; Degradation of $Cy_3$ |
| DIPEA, imidazole, $Zn(OAc)_2$, DMF, 120 ºC, 12 h | Degradation of $Cy_3$ |
| DIPEA, imidazole, $Zn(OAc)_2$, pyridine, 120 ºC, 10 h | Degradation of $Cy_3$ |
| Pyridine, reflux, 24 h | No product; Poor solubility |
| Pyridine, DMF, reflux, 24 h | No product; Degradation of $Cy_3$ |
| Pyridine, microwave, 120 ºC, 24 h | No product, no degradation |
| Pyridine, $H_2O$, microwave, 110 ºC, 24 h | **Product** |

One main problem associated with this reaction was the degradation of cyanine 3 in most of the conditions screened. Although compound **22** was stable in DMF at 120°C for 24 h, no product was obtained by just reacting PTCDA with **22** under these conditions. All attempts performed using zinc acetate led to the degradation of the cyanine derivative. Finally, considering the conditions that were used for PBI-PEG derivatives, we envisioned the used of pyridine as solvent but compound **22** was poorly soluble. The only conditions screened that led to the isolation of compound **41** without significant degradation of the cyanine moiety were the combined use of pyridine and water at 110°C by microwave heating (Scheme 15). Importantly, water was mandatory to provide compound **41** due to the lowest solubility of compound **22** in pyridine. Interestingly, despite the strong hydrophobicity of the PBI core, compound **41** was very soluble in water and purification of the reaction mixture by reverse phase HPLC provided compound **41** with an excellent purity (see Results - Chapter 3.3.).

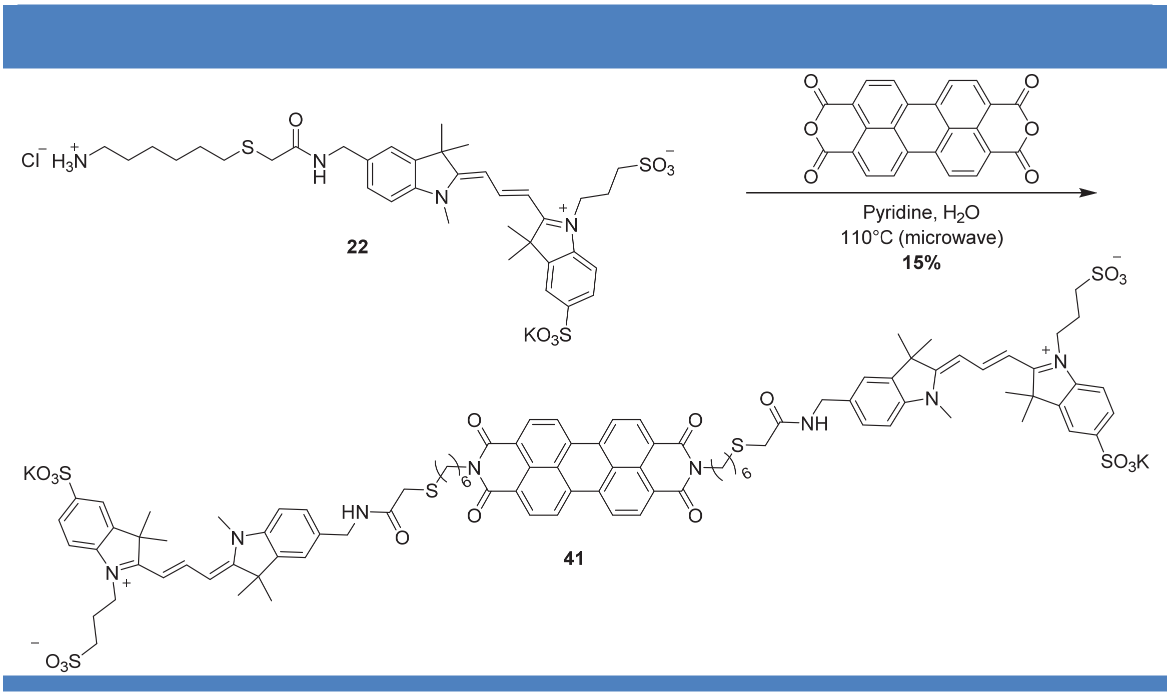

**Scheme 15 |** Synthesis of perylene derivative PBI-Cy$_3$ (**41**).

*Reaction conditions used for* ***Scheme 15****:* ***22*** *(2.0 equiv.), PTCDA (1.0 equiv), pyridine / $H_2O$ (1:1), sonicate, 110 °C (CEM microwave oven, Power: 200 W), 15%.*

All PBI compounds (**37-41** and **43-44**) were obtained in sufficient quantities (min. 20 mg) which allowed the study of their self-assembly in water (see Results - Chapter 3.3.). Due to a lack of time, their co-self-assemblies have only been studied recently by scattering experiments and therefore will not be described in this manuscript.

# Chapter 2: Supramolecular polymers based on bisurea motifs

## 1. Bisurea-polyethylene glycol supramolecular polymers

The possible self-assembly of bisurea-PEG monomers have been studied in various solvents ranging from non-polar, typically toluene, up to methanol or even water. Inspired by the work of Bouteiller,[104] we were wondering if the absence of hydrophobic units between the urea moieties and the solubilizing PEG chains would hinder the self-assembly due to the absence of hydrophobic effects and in more polar solvents as a consequence of the solvatation of the hydrogen bonding units. We have also studied the influence of the length of the PEG chain on the self-assembly process.

### a. Supramolecular polymers with $PEG_7$ side chains

#### i. $^1$H NMR spectra of bisurea-$PEG_7$ in various solvents

Bisurea-$PEG_7$ was initially characterized by $^1$H NMR in water (Figure 34). The spectra displays the expected set of signals and integration of the signals corresponding to the PEG chains is in accordance with the expected number of protons, considering that polydisperse PEG units have been used.

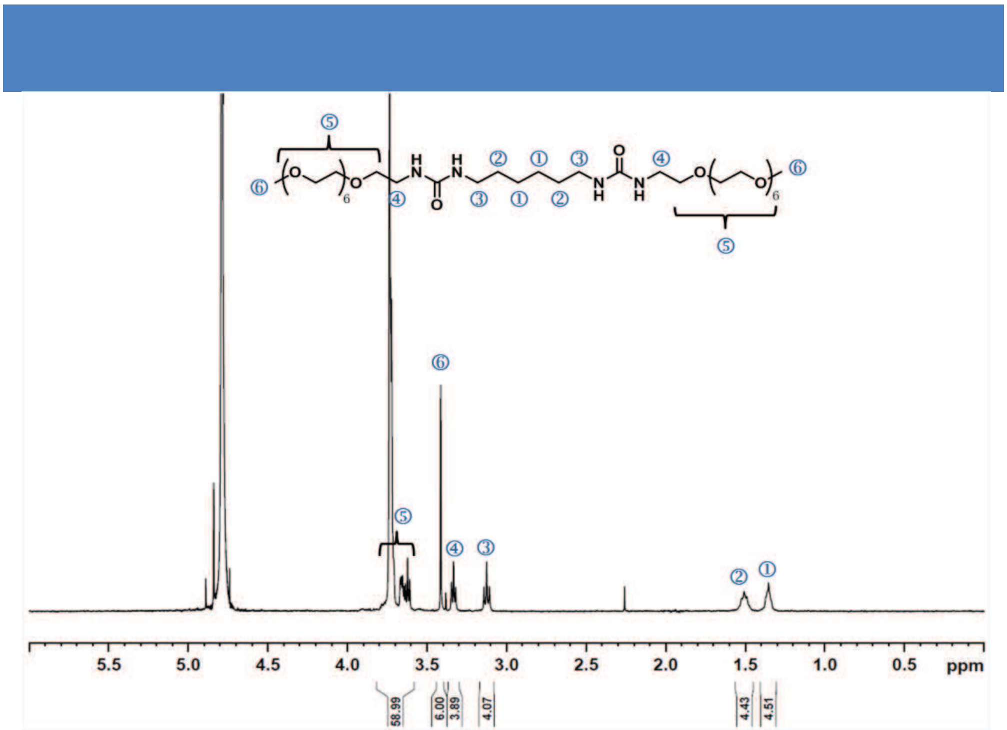

**Figure 34 |** $^1$H NMR spectra of bisurea-$PEG_7$ at $10^{-3}$ M in $D_2O$.

It should be noted that N-H protons from the urea motif are not observed and that all chemical shifts are not affected over the whole range of concentration analyzed by $^1$H NMR ($10^{-2}$ M down to 5 x $10^{-4}$ M). This molecule was then studied in various solvents covering a wide range of polarity, namely toluene, chloroform, acetonitrile, methanol and water (classified according to their polarity). In all solvents, bisurea-PEG$_7$ displayed good solubility up to $10^{-2}$ M (~8.5 mg/cm$^3$) and the corresponding $^1$H NMR spectra are reported in Figure 35.

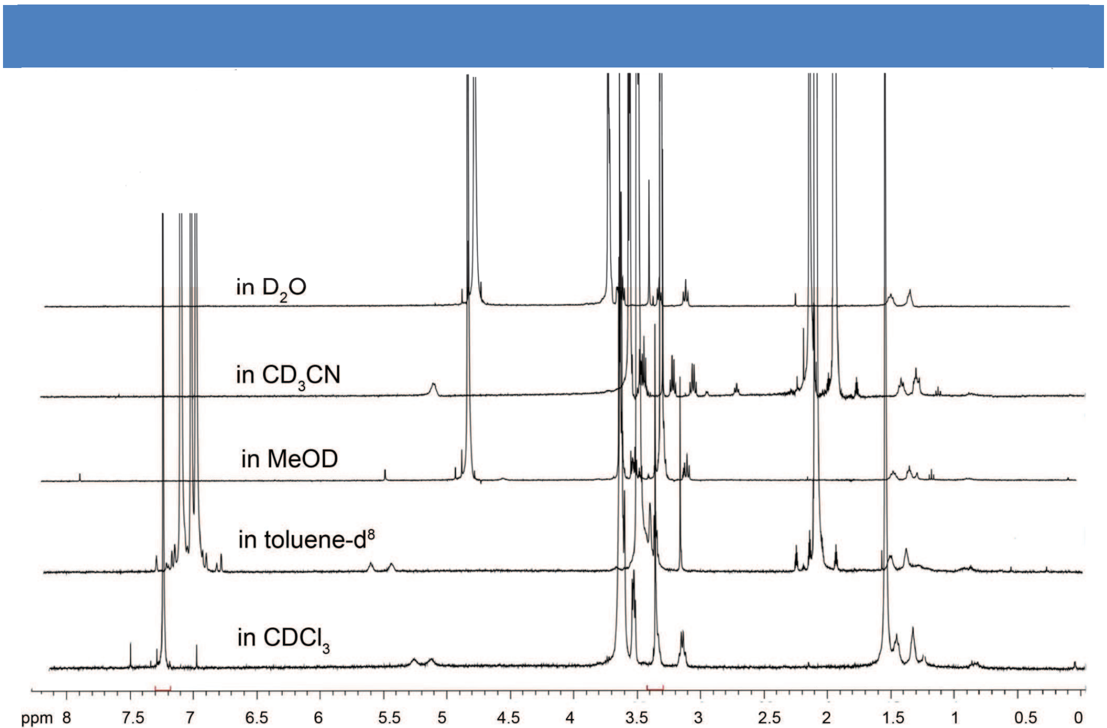

**Figure 35 |** $^1$H NMR spectra of bisurea-PEG$_7$ in CDCl$_3$, toluene-d$^8$, MeOD, CD$_3$CN and D$_2$O at $10^{-3}$ M.

Very similar NMR spectra were observed in all solvents. The major difference was observed for toluene-d$^8$ where peaks corresponding to ③ and ④ were shifted downfield compared to other solvents. Additionally, in this solvent, chemical shifts of the N-H protons from the urea motif were shifted up field by Δδ~0.2 ppm upon decreasing the concentration from $10^{-2}$ to $10^{-3}$ M. In other solvents, no concentration-dependant behavior was observed.

### *ii. FT-IR of bisurea-PEG$_7$ from various solvents*

In order to determine if some supramolecular interactions such as hydrogen bonds are involved in a possible self-assembly of this biurea-PEG$_7$ compound, FTIR experiments were performed by drop-casting a $10^{-3}$ M solution on an ATR diamond probe (Figure 36). Interestingly, very similar FT-IR spectra were obtained in all studied solvents.

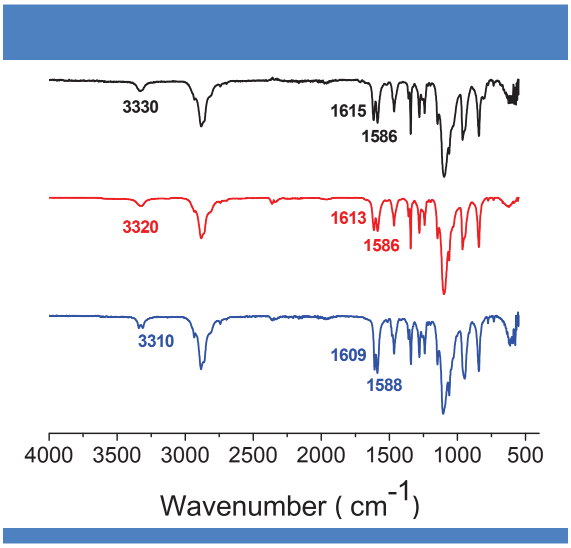

**Figure 36 |** FT-IR spectra of bisurea-PEG$_7$ from $CDCl_3$ (black), $D_2O$ (red) and toluene-d$^8$ (blue).

In particular, the presence of bands located at 3330, 3320 and 3310 cm$^{-1}$ from $CDCl_3$, $D_2O$ and toluene-d$^8$ respectively is indicative of the presence of strong H-bonded N-H stretching vibrations. Additionally, the sharpening of these bands along with their decreasing vibrational frequencies might indicate the formation of more ordered H-bonding structures in toluene compared to chloroform and water. Furthermore, the doublet observed at 3310 cm$^{-1}$ in toluene is most probably attributed to the in-phase and out-of-phase N-H stretching vibrations of the two N-H groups of the ordered urea groups.[201] No free N-H groups were observed in any of these solvents (no band at around 3450 cm$^{-1}$). In the carbonyl region, two sharp bands are observed at 1615 - 1609 cm$^{-1}$ and around 1586 cm$^{-1}$ for the amide I and amide II bands, respectively. These frequencies confirmed that bisurea-PEG$_7$ molecules are connected through strong and ordered hydrogen bonds.[202]

### *iii. SANS spectra of bisurea-PEG$_7$ in different solvents*

Having qualitative information on the possible self-assembly of bisurea-PEG$_7$ in various solvents, we then examined the shape and the size of the objects using small angle neutron scattering (SANS) experiments (Figure 37). Although these experiments require further analyses to extract the dimensions of the self-assemblies, qualitative informations can be obtained from the scattering curves recorded in three representative solvents (chloroform, acetonitrile and water).

---

[201] Coleman, M. M.; Sobkowiak, M.; Pehlert, G. J.; Painter, P. C. and Iqbal, T. Infrared temperature studies of a simple polyurea. *Macromol. Chem. Phys.* **1997**, *198*,117-134.

[202] Yilgor, E.; Burgaz, E.; Yurtsever, E. and Yilgör, I. Polymer, Comparison of Hydrogen Bonding in Polydimethylsiloxane and Polyether Based Urethane and Urea Copolymers. *Polymer* **2000**, *41*, 849-857.

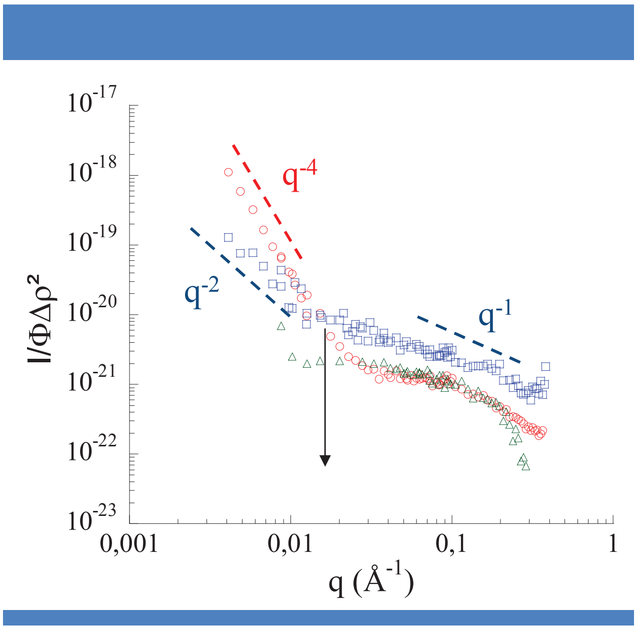

**Figure 37** | SANS spectra of bisurea-PEG$_7$ in $CDCl_3$ (blue squares), $CD_3CN$ (green triangles), and $D_2O$ (red circles) at $10^{-2}$ M.

In acetonitrile, at low q, a plateau analoguous to a Guinier regime and giving the size and the mass of the monomer unit is observed suggesting that no self-assembly is formed. In water, the scattering curve exhibits the following behavior: a) a $q^{-4}$ domain for q values lower than 0.8 Å$^{-1}$ that is characteristic of dense and large aggregates with a sharp interface, and b) a Guinier regime at the upper q-range corresponding to the cross-section of the self-assemblies. This behavior is very similar to the one observed for perylene-PEG compounds which have been characterized as dense globular self-assemblies (see Results - Chapter 3.1.). In chloroform, a different behavior is observed: a) a low-q regime in which the q-dependence of the data can be described by a power law with the exponent close to -2, such as in Gaussian coils; b) a $q^{-1}$ domain at intermediate q values that is characteristic of rigid rod-like behavior. This sequence is similar to that of semiflexible worm-like self-assemblies with a persistence length $L_p = 1/q^* \simeq 100$ Å, where q* corresponds to the cross-over between $q^{-2}$ and $q^{-1}$ characteristic regimes. Although mainly quantitative, these SANS experiments demonstrate that the solvent induce the formation of different assemblies from a same molecular building block. Further fiting of the curves with a form factor characteristic of the scattered objects should provide us with the characteristic dimensions of the assemblies.

TEM imaging of these self-assemblies in various solvents have been performed. Whereas polydisperse globular objects could be observed from the water solution (Figure 120 in Annexes), no morphologies were noticed for the other solvents.

## b. Supramolecular polymers with $PEG_{16}$ side chains

### *i. $^1H$ NMR spectra of bisurea-$PEG_{16}$ in different solvents*

Similarly to bisurea-$PEG_7$, bisurea-$PEG_{16}$ was initially characterized by $^1H$ NMR in water (Figure 38). The spectra displays the expected set of signals and integration of the signals corresponding to the PEG chains is in accordance with the expected number of protons, considering that polydisperse PEG units have been used. In $D_2O$, it should be noted that N-H protons from the urea motif are not observed and that all chemical shifts are not affected over the whole range of concentration analyzed by $^1H$ NMR ($10^{-2}$ M down to 5 x $10^{-4}$ M).

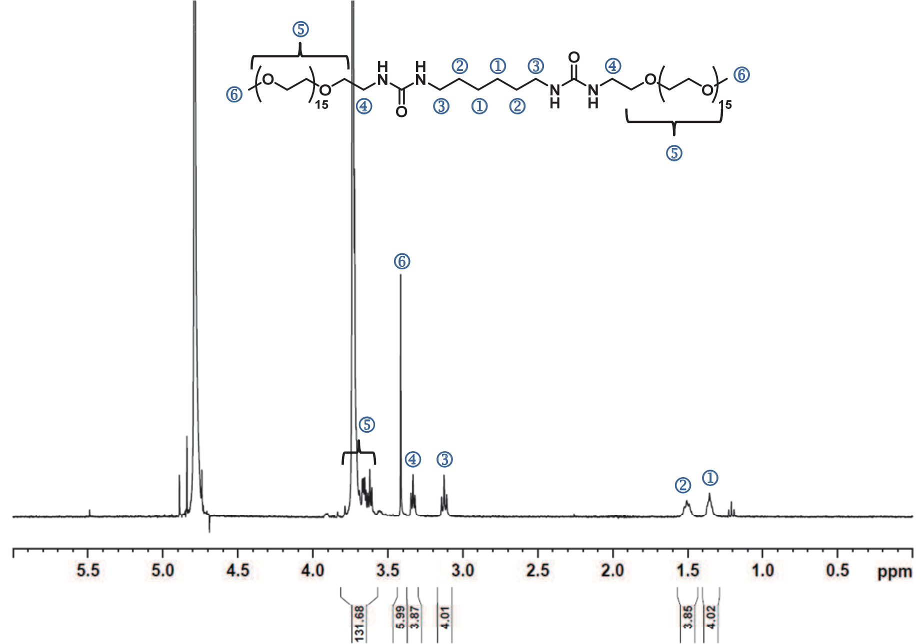

**Figure 38 |** $^1H$ NMR spectra of bisurea-$PEG_{16}$ at $10^{-3}$ M in $D_2O$.

This molecule was then studied in the same solvents as previously used for bisurea-$PEG_7$. In all solvents, bisurea-$PEG_{16}$ displayed good solubility up to 5 x $10^{-3}$ M (~8.2 mg/$cm^3$) and the corresponding $^1H$ NMR spectra are reported on Figure 39.

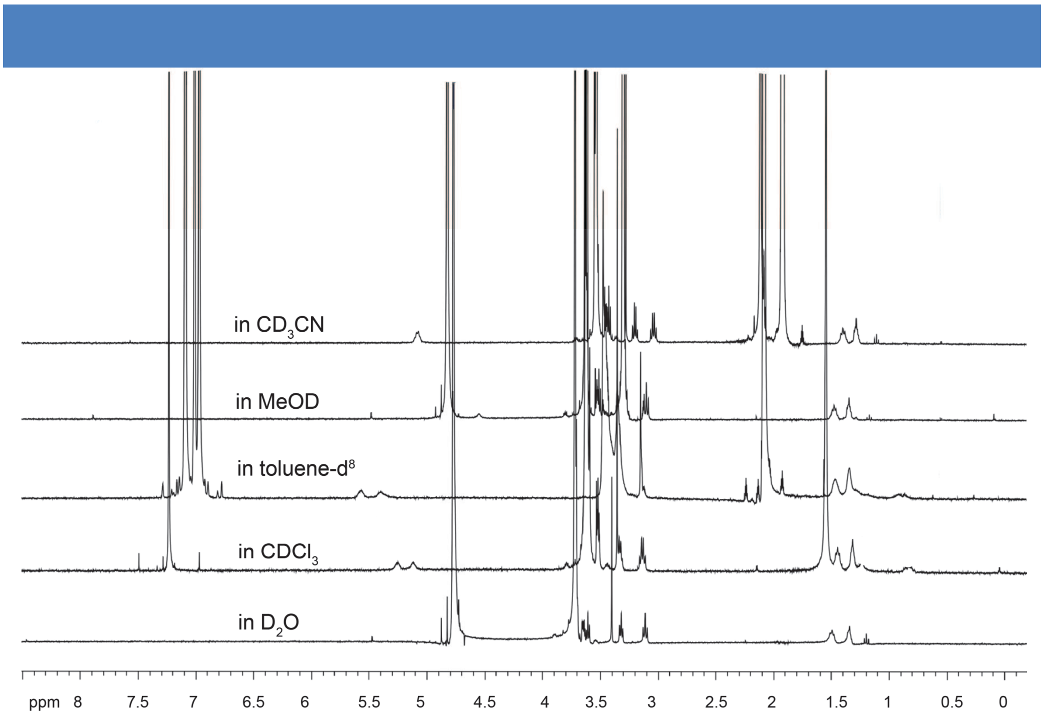

**Figure 39 |** $^1$H NMR spectra of bisurea-PEG$_{16}$ in CDCl$_3$, toluene-d$^8$, MeOD, CD$_3$CN and D$_2$O at $10^{-3}$ M.

Very similar NMR spectra were observed in all solvents with almost identical chemical shifts observed in chloroform, methanol and acetonitrile. The major difference was observed for toluene-d$^8$ where peaks corresponding to ③ and ④ were shifted downfield compared to other solvents. Additionally, in this solvent, chemical shifts of the N-H protons from the urea motif were shifted up field by $\Delta\delta$~0.2 ppm upon decreasing the concentration from 5 x $10^{-3}$ to $10^{-3}$ M. In other solvents, no concentration-dependant behavior was observed.

### *ii. FT-IR of bisurea-PEG$_{16}$ from various solvents*

We then performed FTIR experiments by drop-casting a $10^{-3}$ M solution on an ATR diamond probe in order to determine some of the important supramolecular interactions possibly involved in a self-assembly process (Figure 40). Interestingly, very similar FT-IR spectra were obtained in all studied solvents and presented almost identical bands compared to bisurea-PEG$_7$.

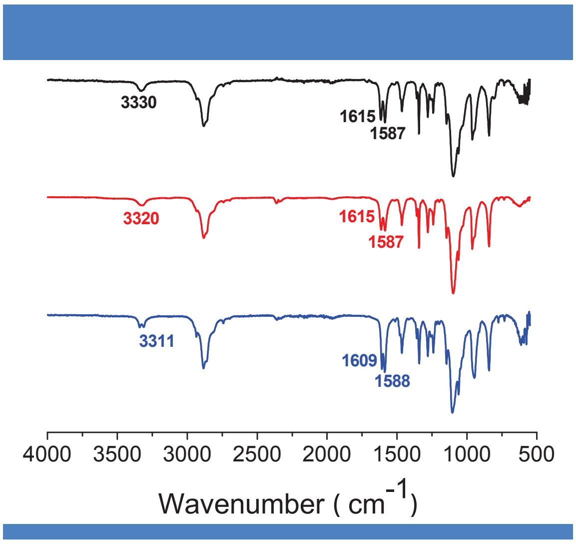

**Figure 40 |** FT-IR spectra of bisurea-PEG$_{16}$ from $CDCl_3$ (black), $D_2O$ (red) and toluene-d$^8$ (blue).

In particular, the presence of bands located between 3330 and 3311 cm$^{-1}$ from $CDCl_3$, $D_2O$, and toluene-d$^8$ indicates the presence of strong H-bonded N-H stretching vibrations. Additionally, in toluene, the sharpening of these bands along with their decreasing vibrational frequencies suggests the formation of more ordered H-bonding structures compared to chloroform and water. No free N-H groups were observed in any of these solvents (no band at around 3450 cm$^{-1}$). In the carbonyl region, two sharp bands are observed at 1615 - 1609 cm$^{-1}$ and around 1587 cm$^{-1}$ for the amide I and amide II bands respectively, confirming that bisurea-PEG$_{16}$ molecules are connected through strong and ordered hydrogen bonds.

We also studied the behavior of bisurea-PEG$_{16}$ compound in chloroform at various concentrations (Figure 41).

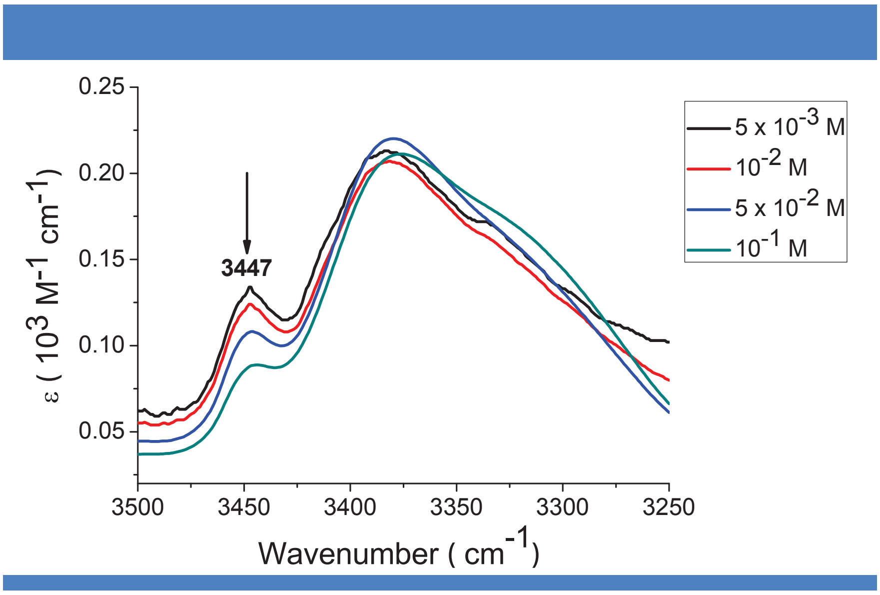

**Figure 41 |** Normalized FT-IR spectra of solutions of bisurea-PEG$_{16}$ in $CDCl_3$ with concentrations ranging from 5 × 10$^{-3}$ (black) up to 10$^{-1}$ M (green). The arrow indicates the increase in concentration

Two bands can be observed: one at ~3370 cm$^{-1}$, which remains stable at all concentrations and one at 3447 cm$^{-1}$, which decreases with increasing the concentration. Compared to the work of Bouteiller,[64] who reported the observation of four bands, only two bands are observed in our case as the urea is substituted on both side by aliphatic chains. The higher frequency band is typical for a free N-H vibration whereas the lower one is typical for a hydrogen bonded N-H vibration. This experiment shows that, in chloroform, a small percentage of monomeric bisurea-PEG$_{16}$ is always concomitantly found in the presence of self-assemblies. However, these data are not satisfactory to quantitatively analyze the mechanism of self-assembly of bisurea-PEG$_{16}$ due to the continuous presence of the hydrogen-bonded N-H peak even at the lowest concentration accessible by FTIR. Therefore, we have started some ITC experiments to determine the mechanism of self-assembly in the various solvents. The preliminary results in $CDCl_3$ and $D_2O$ are presented in section v.

### *iii. SANS spectra of bisurea-PEG$_{16}$ in different solvents*

Similarly to bisurea-PEG$_7$, having qualitative information on the possible self-assembly of bisurea-PEG$_{16}$ in various solvents, we then examined the shape and the size of the objects using SANS experiments (Figure 42). Qualitative informations almost identical to bisurea-PEG$_7$ could be obtained from the scattering curves in three representative solvents (chloroform, acetonitrile and water).

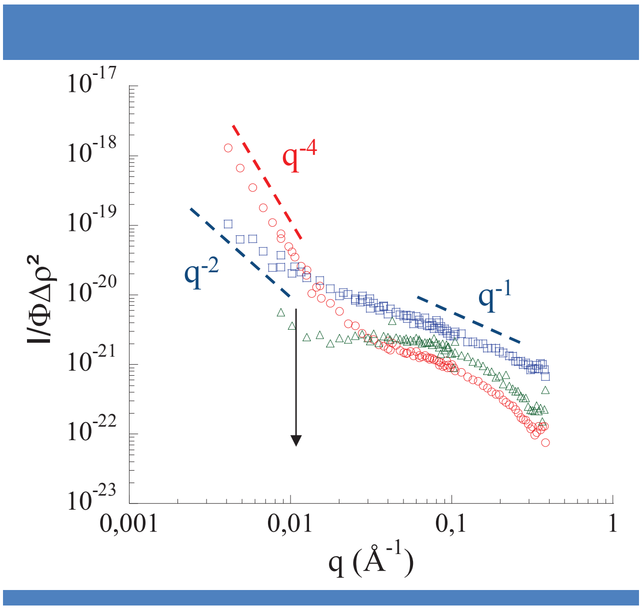

**Figure 42** | SANS spectra of bisurea-PEG$_{16}$ in $CDCl_3$ (blue squares), $CD_3CN$ (green triangles), and $D_2O$ (red circles) at $10^{-2}$ M.

In acetonitrile, at low q, a plateau analoguous to a Guinier regime and giving the size and the mass of the monomer unit is observed suggesting that no self-assembly is formed. In water, the scattering curve exhibits the following behavior: a) a $q^{-4}$ domain for q values lower than

0.8 Å$^{-1}$ that is characteristic of dense and large aggregates with a sharp interface, and b) a Guinier regime at the upper q-range corresponding to the cross-section of the self-assemblies. Here again, this behavior is very similar to the one observed for perylene-PEG compounds which have been characterized as dense globular self-assemblies (see Results - Chapter 3). In chloroform, compared to the two other solvents, a different behavior is observed: a) a low-q regime in which the q-dependence of the data can be described by a power law with the exponent close to -2, such as in Gaussian coils; b) a $q^{-1}$ domain at intermediate q values that is characteristic of rigid rod-like behavior. Here also, this sequence is similar to that of semiflexible worm-like self-assemblies with a persistence length $L_p \simeq 100$ Å. Although mainly quantitative, these SANS experiments demonstrate that the solvent induce the formation of different assemblies from a same molecular building block. Further fiting of the curves with a form factor characteristic of the scattered objects should provide us with the characteristic dimensions of the assemblies.

TEM imaging of these self-assemblies in various solvents have been performed. No evident morphologies were noticed in any solvents. Further imaging using Cryo-TEM, as reported by Sijbesma on similar products,[103] would be necessary to evidence the different morphologies observed by scattering experiments.

### iv. ITC experiments on bisurea-PEG$_{16}$ in $CDCl_3$ and $D_2O$

In order to understand the possible mechanism of self-assembly in the different solvents, we have recently started some isothermal titration calorimetry (ITC) experiments on this molecule in chloroform and water (Figure 43). As mentioned in the bibliography chapter, ITC experiments are used to provide thermodynamic informations on molecular reversible associations. In 2004, the group of Bouteiller reported the use of ITC to characterize the self-assembly mechanism of supramolecular polymers.[203] Typically, aliquots of a solution containing the supramolecular polymer is injected into pure solvent, placed in a calorimetric cell. The heat flow measured corresponds to the partial dissociation of the polymer and correlates with the self-assembly process.

---

[203] Arnaud, A. and Bouteiller, L. Isothermal Titration Calorimetry of Supramolecular Polymers. *Langmuir* **2004**, *20*, 6858-6863.

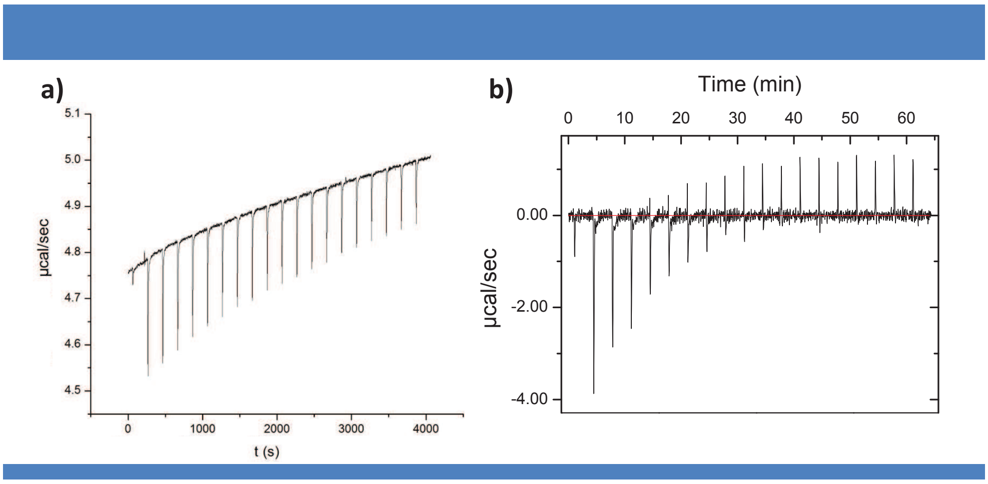

**Figure 43** | ITC of bisurea-PEG$_{16}$ in (a) $D_2O$ and (b) $CDCl_3$ at ~5 mM.

Whereas in-depth fitting of the experimental results would be necessary to access thermodynamic parameters such as dimerization/oligomerization constants or enthalphies of dimerization/oligomerization, qualitative experiments can already be extracted from these first experiments. In both solvents, the heat exchange process is fast as demonstrated by the quick return to the baseline after each injection. This observation proves that the self-assembly process is dynamic, as already suggested by the fact that self-assembly occurs readily in solvents without sonication or heating steps. Additionally, the sign of the heat exchanged provides information on the main driving force for the self-assembly process. In water, the negative sign for the dilution experiment shows that the dissociation generates heat ($\Delta H_{(dissociation)} < 0$ and consequently $\Delta H_{(association)} > 0$). Considering that $\Delta G = \Delta H - T\Delta S$, the association process is entropy driven ($\Delta S_{(association)} > 0$) and therefore favored by hydrophobic interactions. Additional experiments involving the use of protected urea moieties would be helpful to understand the role of hydrogen bonding in the self-assembly process in water. In chloroform, the process seems to be more complicated. Indeed, at the beginning of the experiment, the sign of the heat exchanged suggests also that the association process is entropy driven ($\Delta H_{(dissociation)} < 0$) and therefore directed by solvophobic interactions. However, the inversion of the sign of the heat exchanged after 8 injections suggest that a second association process takes place which is enthalpy driven ($\Delta H_{(association)} < 0$). This event suggests that hydrogen bonding plays an important role in the supramolecular polymerization. In chloroform, although further analyses of the ITC data are required to better understand the self-assembly process, a mechanism involving sequentially two supramolecular interactions can be envisioned.

By using a combination of NMR, scattering and ITC experiments, we have shown that simple bisurea-PEG monomers can give rise to different morphologies in solvents with a wide range of polarity. Additionally, the length of the PEG chain does not seem to influence the self-assembly process as scattering curves of $PEG_7$ and $PEG_{16}$ monomers display almost identical behavior. Further work will consist in understanding the mechanism of self-assembly in the different solvent as already suggested by the first ITC measurements.

## 2. Bisurea-based supramolecular polymer with peptidic residues

The possible self-assembly of bisurea-peptide monomers have been studied only in water, due to the lack of solubility in other solvents. The presence of a hydrophobic linker between the urea moieties and the hexapeptidic chain (bisurea-7AA) was expected to induce different self-assemblies compared to bisurea-6AA due to additional hydrophobic effects in water.

### a. Supramolecular polymers with hexapeptidic side chains

#### *i. $^1$H NMR spectra of bisurea-6AA in $D_2O$*

Bisurea-6AA was initially characterized by $^1$H NMR in water (Figure 44). The spectrum displays the expected set of signals which were determined thanks to 2D-COSY NMR.

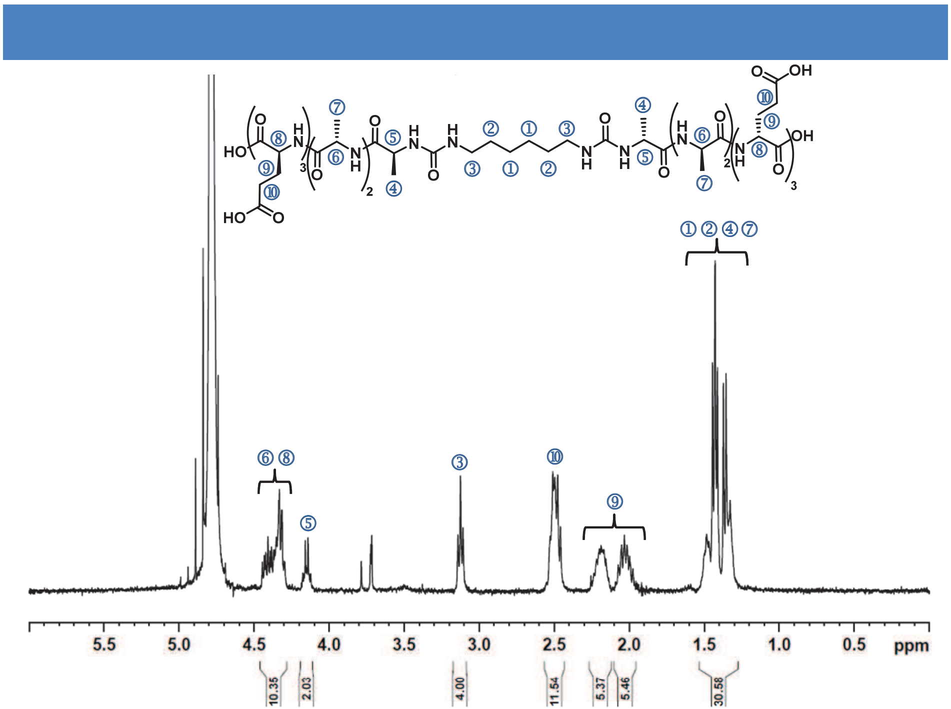

**Figure 44 |** $^1$H NMR spectra of bisurea-6AA at $10^{-3}$ M in $D_2O$.

This compound displays a good solubility in water up to $10^{-2}$ M, where a broadening of all the NMR signals is observed without affecting the chemical shifts. At $10^{-1}$ M, a gel is formed (see section *vi*).

#### *ii. Viscosity experiments on bisurea-6AA in $D_2O$*

Capillary viscosimetry experiments were then performed to qualitatively monitor the propensity of bisurea-6AA monomer to self-assemble into high molar mass assemblies (Figure 45).

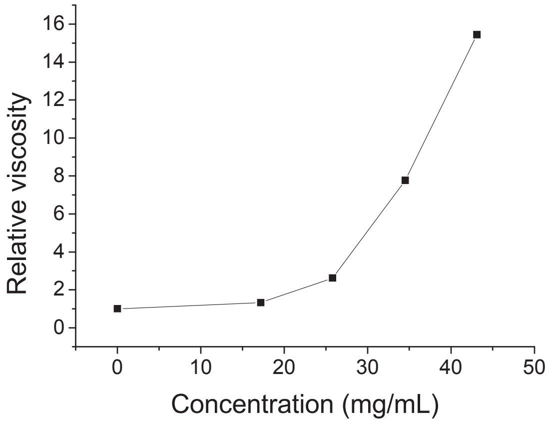

**Figure 45 |** Relative viscosity of bisurea-6AA in $D_2O$ at 25°C.

These measurements were performed using an Ubbelohde type viscometer on freshly prepared samples obtained by simply dissolving the monomer in water at room temperature. A very sharp increase in viscosity was observed at concentrations above 25 mg/mL, i.e. 17 mM. This strong non-linear viscosity increase with concentration at high concentration is probably due to the formation of large aggregates above a critical concentration which is (somehow) lower than the critical gel concentration determined using the inverted tube experiment (see section *vi*).

### *iii. FT-IR of bisurea-6AA from $D_2O$*

We then performed FTIR experiments by drop-casting a $10^{-3}$ M solution on an ATR diamond probe in order to qualitatively determine the interactions involved in the formation of aggregates as determined by viscosimetry experiments (Figure 46). Compared to bisurea-PEG compounds, more intense peaks were observed both in the 3200-3600 $cm^{-1}$ and 1400-1700 $cm^{-1}$ regions, which corresponds to both N-H and C=O vibrational frequencies.

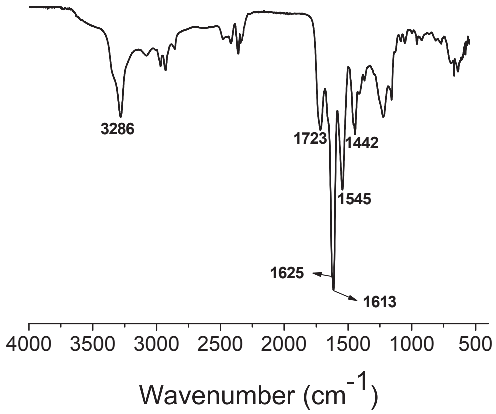

**Figure 46 |** FT-IR spectra of bisurea-6AA from $D_2O$.

These peaks correspond clearly to the signature of the peptidic side chains. Indeed, the sharp band at 3286 cm$^{-1}$ is typical for the N-H stretch of peptide amides. The strong bands at 1613 cm$^{-1}$ and 1545 cm$^{-1}$ also indicates the presence of amide I (C=O stretch of the amide) and amide II (N-H in-plane bend and C-H stretch of peptide amide).[204] Additionally, the broadening of the band at 1613 cm$^{-1}$ towards higher frequencies can be assigned to the formation of β-sheet secondary structures.[205] For this molecule, the formation of hydrogen-bond interactions between the urea motifs is hindered by the bands corresponding to the peptide moieties. However, the shoulder observed at around 3349 cm$^{-1}$ probably suggests the presence of H-bonds between urea motifs. Additionally, the large broad shoulder around 3587 cm$^{-1}$ along with the peak at 1723 cm$^{-1}$ confirms the presence of glutamic acid residues in the hexapeptide. Overall, this FTIR experiment on bisurea-6AA strongly suggests the formation of aggregates through hydrogen-bonding interactions.

### *iv. LS and SANS experiments on bisurea-6AA in $D_2O$*

The formation of organized self-assemblies was confirmed by complementary SANS and SLS experiments on bisurea-6AA at $10^{-3}$ M in $D_2O$ which provided information on the structure of the self-assembly (Figure 47).

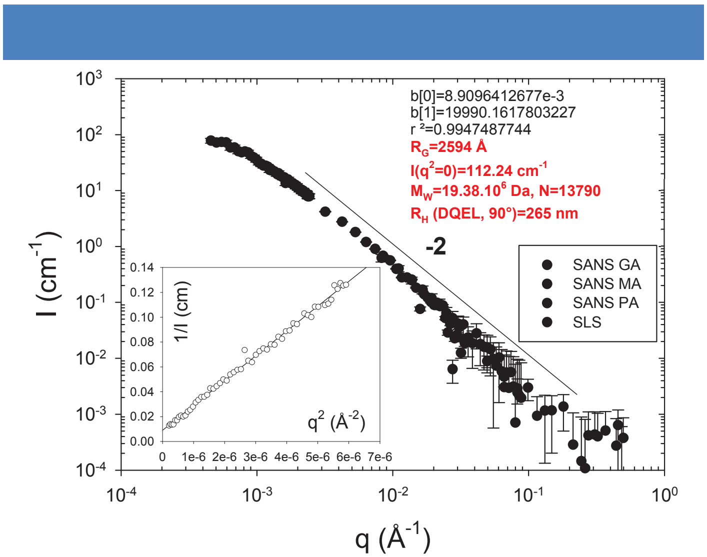

**Figure 47 |** SLS and SANS spectra of bisurea-6AA in $D_2O$ at 1.43*$10^{-3}$ g/L.

Qualitatively, the scattering curve exhibits the following behavior: a) a smooth variation analogous to a Guinier regime at very low q values and associated with the finite size and mass of the objects, and b) a $q^{-2}$ domain for q values between $10^{-3}$ and $10^{-1}$ Å$^{-1}$ that is

---

[204] Jiang, H.; Guler, M. O. and Stupp, S. I. The internal structure of self-assembled peptide amphiphiles nanofibers. *Soft Matter* **2007**, *3*, 454-462.

[205] Pashuck, E. T. and Stupp, S. I. Direct observation of morphologial transformation from twisted ribbons into helical ribbons. *J. Am. Chem. Soc.* **2010**, *132*, 8819-8821.

characteristic of smooth two-dimensional objects. At low q, in the Guinier regime, the plot of $1/I$ as a function of $q^2$ provide us with the apparent gyration radius ($R_{g,\ app}$) determined from the slope of the plot and the apparent molecular weight ($M_{w,\ app}$) of the aggregates obtained from the intercept of the plot at $q^2=0$. For bisurea-6AA in $D_2O$, $R_{g,\ app}$ was determined to be 259 nm and $M_{w,\ app}$ was calculated to be as high as $19.38 \times 10^6$ Da, which corresponds to an aggregation number $N_{agg}$ of 13790, i.e. the number of monomers involved in a supramolecular aggregate. Additional DLS measurements showed a monoexponential auto-correlation function, which provided an apparent hydrodynamic radius $R_{H,\ app}$ of 265 nm after applying cumulant analysis to our data. Importantly, $R_g/R_H$ ratio is almost equal to 1, which could correspond to the formation of two-dimensional sheets of polymers.[206] For instance, for rectangular plates, as $R_g^2 = 1/12\ (a^2 + b^2)$ and hypothesizing that a = b, we can determine that a = 634 nm from our $R_g$ value. This could correspond to the aggregation of several sheets in two dimensions but not stacked one on top of each other.

### v. *AFM and TEM imaging of bisurea-6AA*

The formation of such objects was clearly evidenced by both AFM and TEM imaging of $D_2O$ solutions of bisurea-6AA (Figure 48).

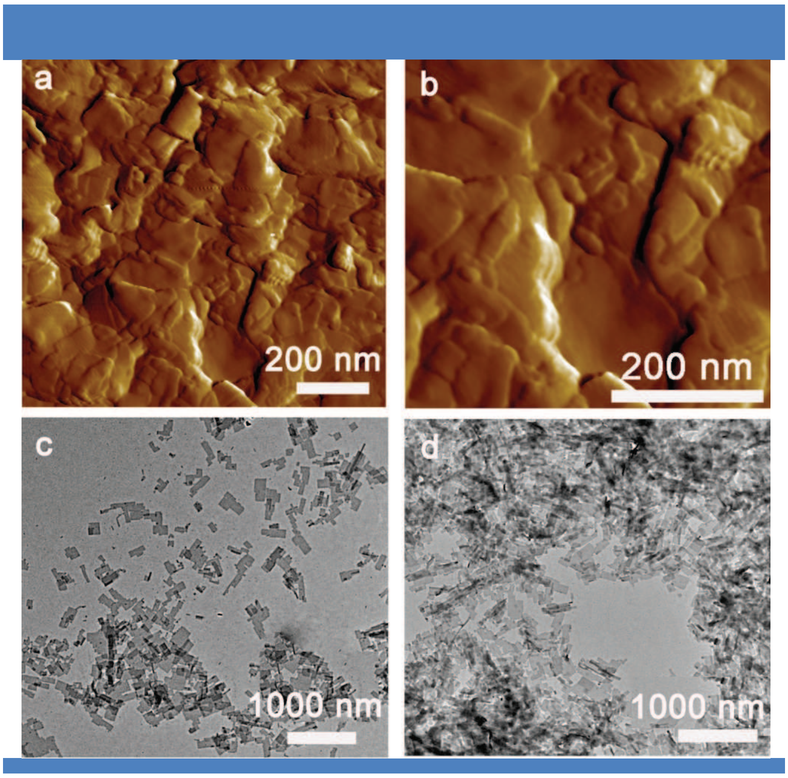

**Figure 48 |** AFM (a, b) and TEM (c, d) images from $D_2O$ solutions of bisurea-6AA ($10^{-4}$ M).

---

[206] Knauert, S. T.; Douglas, J. F. and Starr, F. W. Morphology and Transport Properties of Two-Dimensional Sheet Polymers. *Macromolecules* **2010**, *43*, 3438–3445.

AFM images also show the formation of superimposed sheet-like structures, which could result from additional supramolecular interactions between sheets.

### *vi. Hydrogelation properties of bisurea-6AA*

During the course of the previous experiments, we noticed that bisurea-6AA displays a gel-like behavior at relatively high concentration ($\geq 10^{-2}$ M). Therefore, we decided to evaluate the hydrogelation properties of this compound by performing the inverted tube experiment (Figure 49).

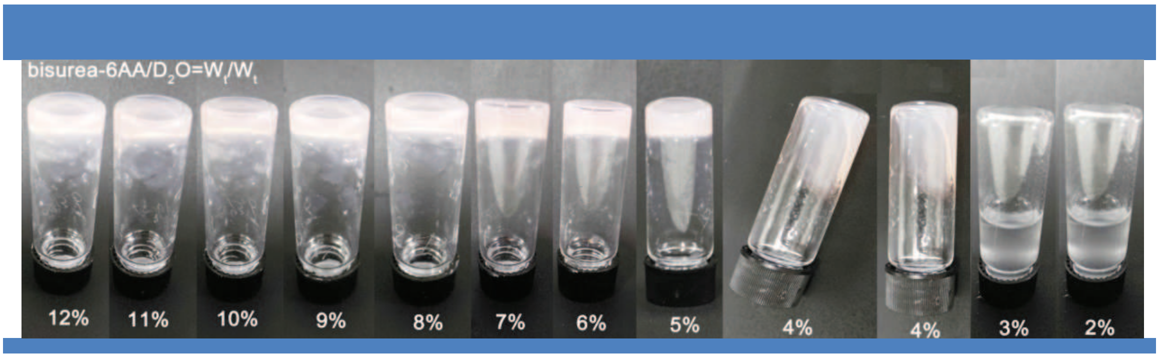

**Figure 49 |** Inverted tube experiment on bisurea-6AA solutions in $D_2O$ at various concentrations (w/w).

Concentrations ranging from 2 to 12% w/w in $D_2O$ were evaluated. Above 5% w/w, gel-like behaviors were observed with no slipping of the gel over 24 hours. However, whereas the 4 $w_t$% gel was shown to slowly slide down along the walls of the vial, samples with concentration over 3% resulted in solutions.

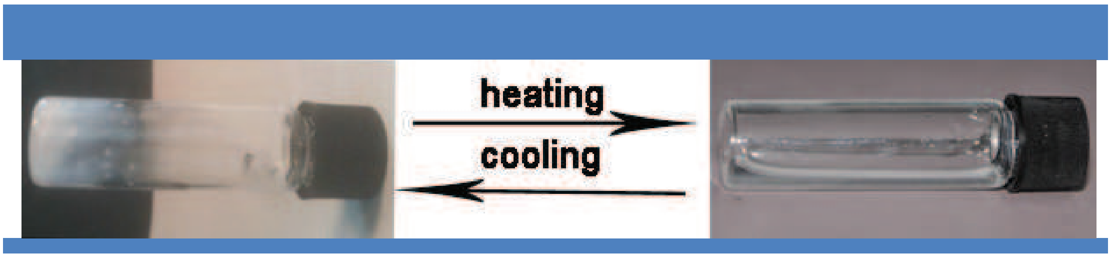

**Figure 50 |** Thermo-reversible experiments on a solution of 5 % bisurea-6AA in $D_2O$.

We also studied qualitatively the influence of the temperature on the 5 % gel (Figure 50). Upon heating up to 70 °C, the gel transformed to a solution which could reversibly turn back to a stable gel upon decreasing the temperature to room temperature. Further DSC experiments are currently performed in the laboratory to evaluate precisely the melting ($T_m$) and gel formation ($T_g$) temperatures of this molecule. This gel was also studied by TEM using a replica of a freeze-fractured sample (Figure 51). Similarly to AFM images obtained from a drop-casted solution, sheet-like structures were observed with a precise parallel alignment of fibers-like structure within a single sheet (frame on Figure 51b).

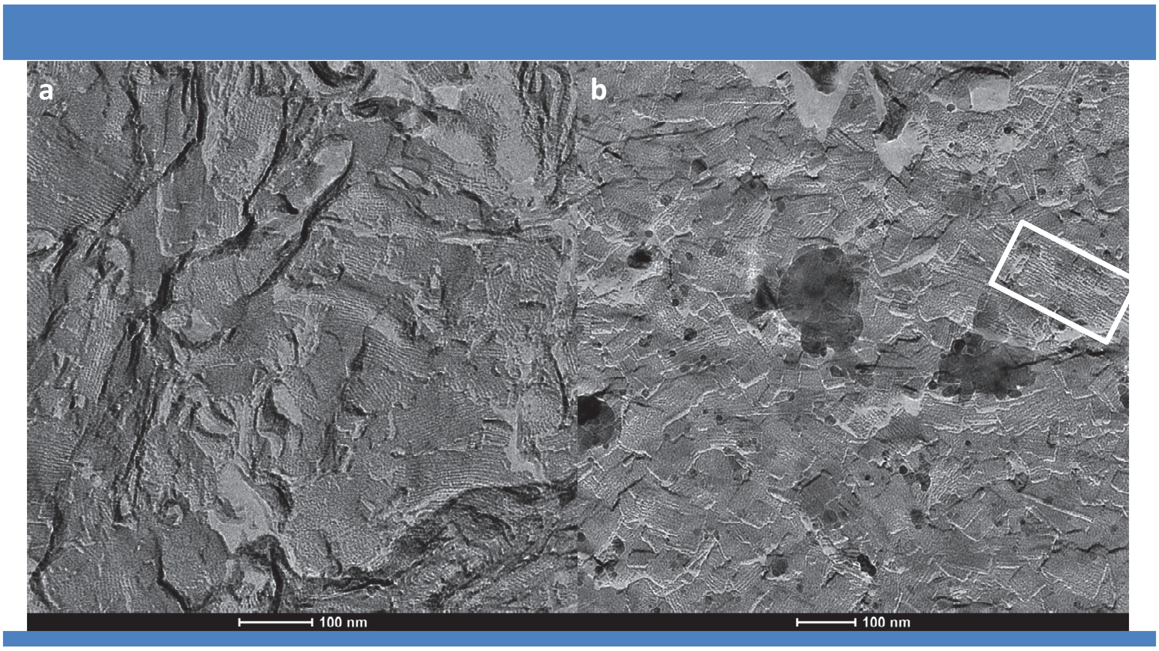

**Figure 51 |** Freeze-fracture TEM images of a hydrogel made of bisurea-6AA gel.

These fiber-like structures could potentially arise from the hydrogen-bonding framework induced by the urea moieties and the β-sheet arrangement of the peptidic side chains. Further X-ray studies of this gel could support this assumption by providing information on the molecular arrangement within the nanostructures, particularly regarding the formation of β-sheet structures.

## b. Supramolecular polymers with heptapeptidic side chains

### i. $^1$H NMR spectra of bisurea-7AA in $D_2O$

Bisurea-7AA was initially characterized by $^1$H NMR in water (Figure 52). The spectrum displays the expected set of signals which were determined thanks to 2D-COSY NMR.

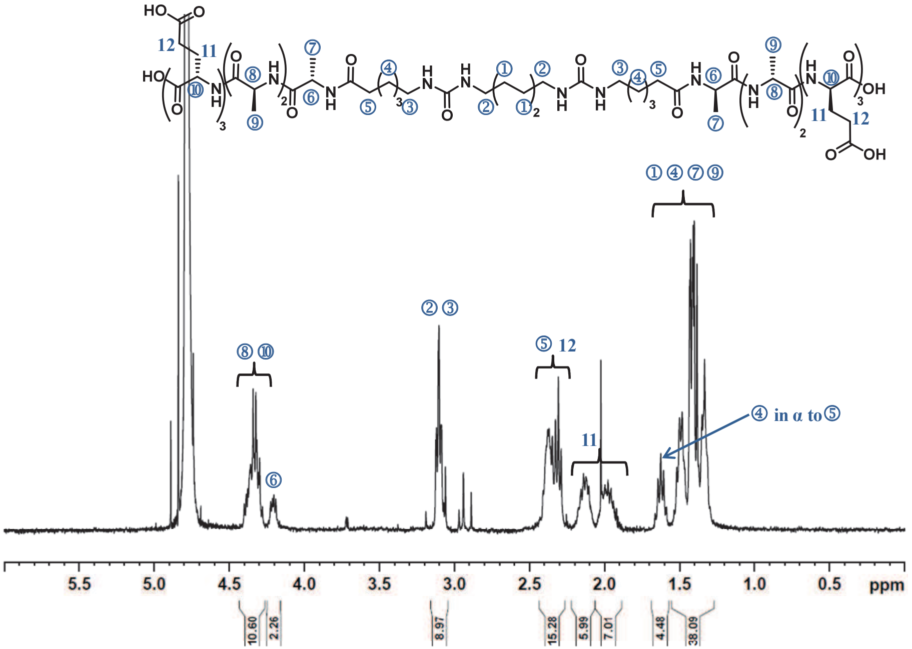

**Figure 52 |** $^1$H NMR spectra of bisurea-7AA at $10^{-3}$ M in $D_2O$.

This compound displays a good solubility in water up to $10^{-2}$ M and none of the chemical shifts were affected over the whole range of concentration analyzed by $^1$H NMR ($10^{-2}$ M down to 5 x $10^{-4}$ M). However, compared to bisurea-6AA, no formation of gel was observed at higher concentrations. This simple observation demonstrates that the introduction of a hydrophobic spacer between the urea moieties and the hexapeptidic side chains clearly influences the behavior of the molecule in water.

### ii. Viscosity experiments on bisurea-7AA in $D_2O$

Similarly to bisurea-6AA, capillary viscosimetry experiments were performed to qualitatively monitor the propensity of bisurea-7AA monomer to self-assemble into high molar mass assemblies (Figure 53).

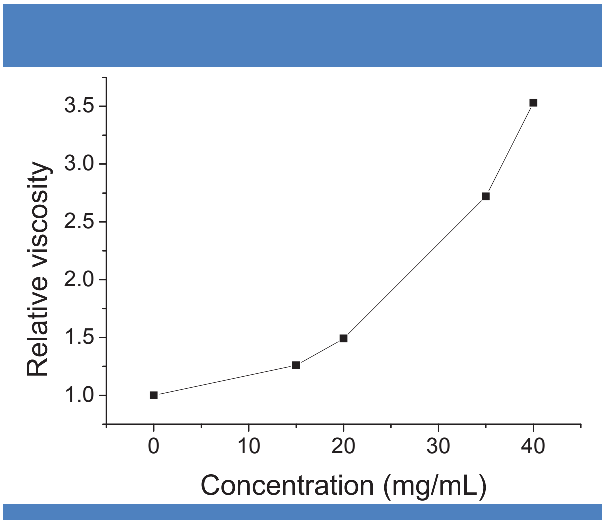

**Figure 53 |** Relative viscosity of bisurea-7AA in $D_2O$ at 25°C.

Compared with the relative viscosity of bisurea-6AA (Figure 45), a much lower viscosity is observed, confirming the influence of the flexible linker on the self-assembly of bisurea-peptide monomer. However, the recorded viscosity of aqueous solutions of bisurea-7AA is non negligible (compared with ref 104) and might anyhow indicate the formation of large aggregates.

### *iii. FT-IR of bisurea-7AA from $D_2O$*

As for bisurea-6AA, we then performed FTIR experiments by drop-casting a $10^{-3}$ M solution on an ATR diamond probe to establish if similar interactions are involved in the formation of aggregates (Figure 54). Compared with bisurea-6AA, similar peaks were observed in the 3200-3600 $cm^{-1}$ and 1400-1700 $cm^{-1}$ regions with different intensities.

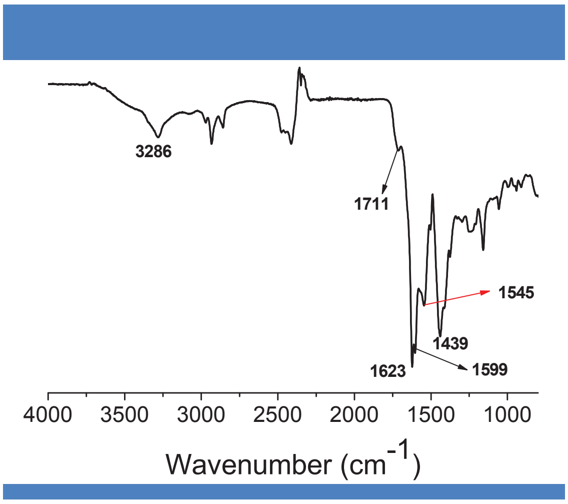

**Figure 54 |** FT-IR spectra of bisurea-7AA from $D_2O$.

For instance, the band at 3286 $cm^{-1}$ which is typical for the N-H stretch of peptide amides has a lower intensity compared to symmetric and asymmetric stretches of $CH_2$ groups in the

2950-2800 cm$^{-1}$ region, due to the presence of the aliphatic linker. Intense bands are still observed in the 1720-1500 cm$^{-1}$ region which corresponds to the presence of amide and carbonyl groups. Importantly, the presence of a band at 1623 cm$^{-1}$ also indicates the formation of β-sheet secondary structures. Here again, the formation of hydrogen-bond interactions between the urea motifs is hindered by the bands corresponding to the peptide moieties, but observations similar to bisurea-6AA can be made. Additionally, the strong band at 1439 cm$^{-1}$ compared to the quite weak peak at 1711 cm$^{-1}$ comes probably from the presence of deprotonated glutamic acid residues in the hexapeptide. Overall, although differences are observed between FTIR spectra of bisurea-6AA and bisurea-7AA, similar vibrational frequencies are observed, which suggests the formation of aggregates through identical interactions.

### *iv. LS and SANS experiments on bisurea-7AA in $D_2O$*

The formation of organized self-assemblies was confirmed by SANS and SLS experiments on bisurea-7AA at 10$^{-3}$ M in $D_2O$ which provided information on the structure of the self-assembly (Figure 55). Compared with bisurea-6AA, the shape and the slope of the scattering curve were different, confirming that the flexible linker has a non-negligible effect on the packing of the monomers.

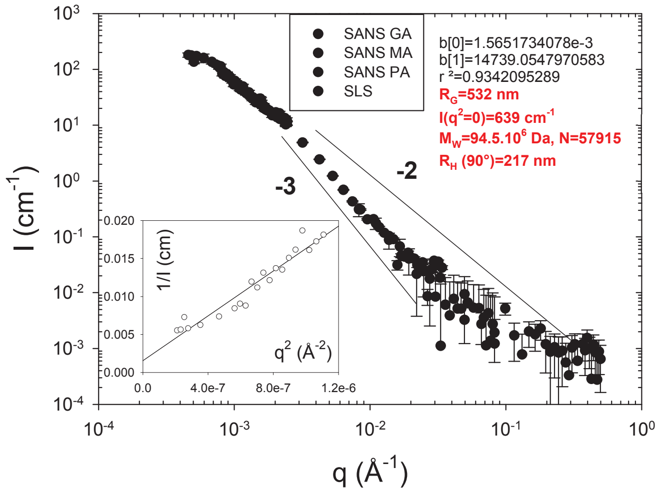

**Figure 55 |** SLS and SANS spectra of bisurea-7AA in $D_2O$ at 1.6*10$^{-3}$ g/L.

Qualitatively, the scattering curve exhibits the following behavior: a) the onset of a smooth variation analogous to a Guinier regime at very low q values and associated with the finite size and mass of the objects, and b) an intermediate q regime in which the q-dependence of the data can be described by a power law with the exponent between -2 and -3, which could be characteristic of branched Gaussian chains as also shown by microscopy (*vide infra*). At low q, in the Guinier regime, the plot of $1/I$ as a function of $q^2$ provide us with $R_{g,\,app} = 532$ nm and $M_{w,\,app} = 94.5 \times 10^6$ Da, which corresponds to an aggregation number $N_{agg}$ of 57915, i.e. the number of monomers involved in a supramolecular aggregate. Additional DLS measurements showed a monofunctional auto-correlation function, which provided an apparent hydrodynamic radius $R_{H,\,app}$ of 217 nm after cumulant analysis. Importantly, $R_g/R_H$ ratio is greater than 2, which could correspond to the formation of an extended structure, as confirmed by microscopy techniques.

### v. AFM and TEM imaging of bisurea-7AA

AFM imaging of diluted $D_2O$ solutions revealed the formation of branched and long micrometric fibers with a width of ~ 5 nm (Figure 56). This structure was confirmed by TEM experiments which show the presence of long fibers with polydisperse widths.

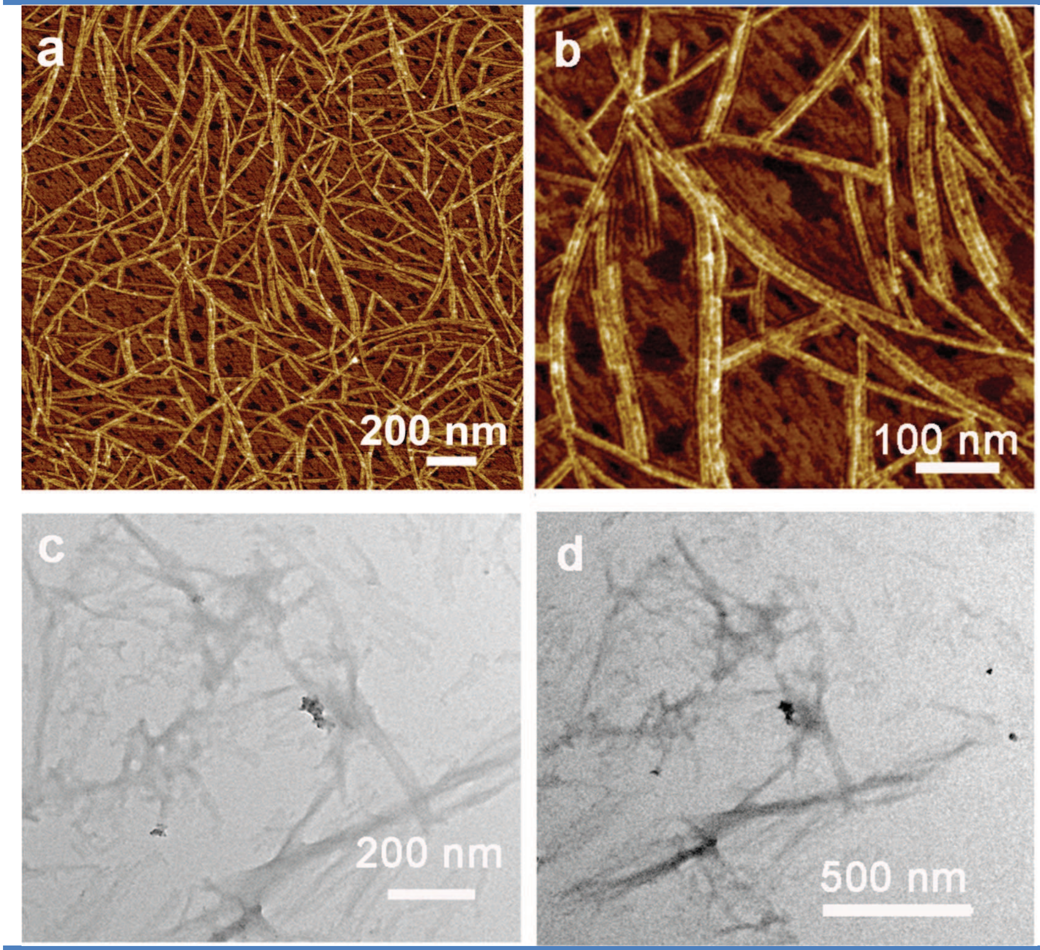

**Figure 56 |** AFM (a, b) and TEM (c, d) images from a $D_2O$ solution of bisurea-7AA ($10^{-4}$ mol/L).

These images clearly point out the differences with the self-assembled structures obtained from bisurea-6AA and corroborate the differences observed by other analytical tools, namely viscosimetry, FT-IR and scattering experiments. All these studies reveal that the flexible aliphatic linker between the peptide and the urea group plays an important role in the structuring of the self-assembled fibers.

Overall, using a combination of analytical, scattering and imaging techniques, we have shown that bisurea-6AA and bisurea-7AA molecules give rise to different self-assemblies in water. By comparing both systems, we can deduce that the self-assembly of bisurea-7AA is not only directed by hydrogen-bonding interactions but also by hydrophobic interactions owing to the presence of the aliphatic linker. Additionally, these differences in morphologies and molecular arrangements led to different macroscopic properties. Further experiments to characterize the hydrogelation properties of bisurea-6AA remain to be performed.

# 3. Bisurea-based supramolecular polymer with fluorescent residues

## a. Supramolecular polymers with Cy$_3$ side chains

### i. $^1$H NMR spectra of bisurea-Cy$_3$ in CD$_3$OD

Bisurea-Cy$_3$ was initially characterized by $^1$H NMR in methanol (Figure 57). The spectrum displays the expected set of signals which were determined thanks to 2D-COSY NMR.

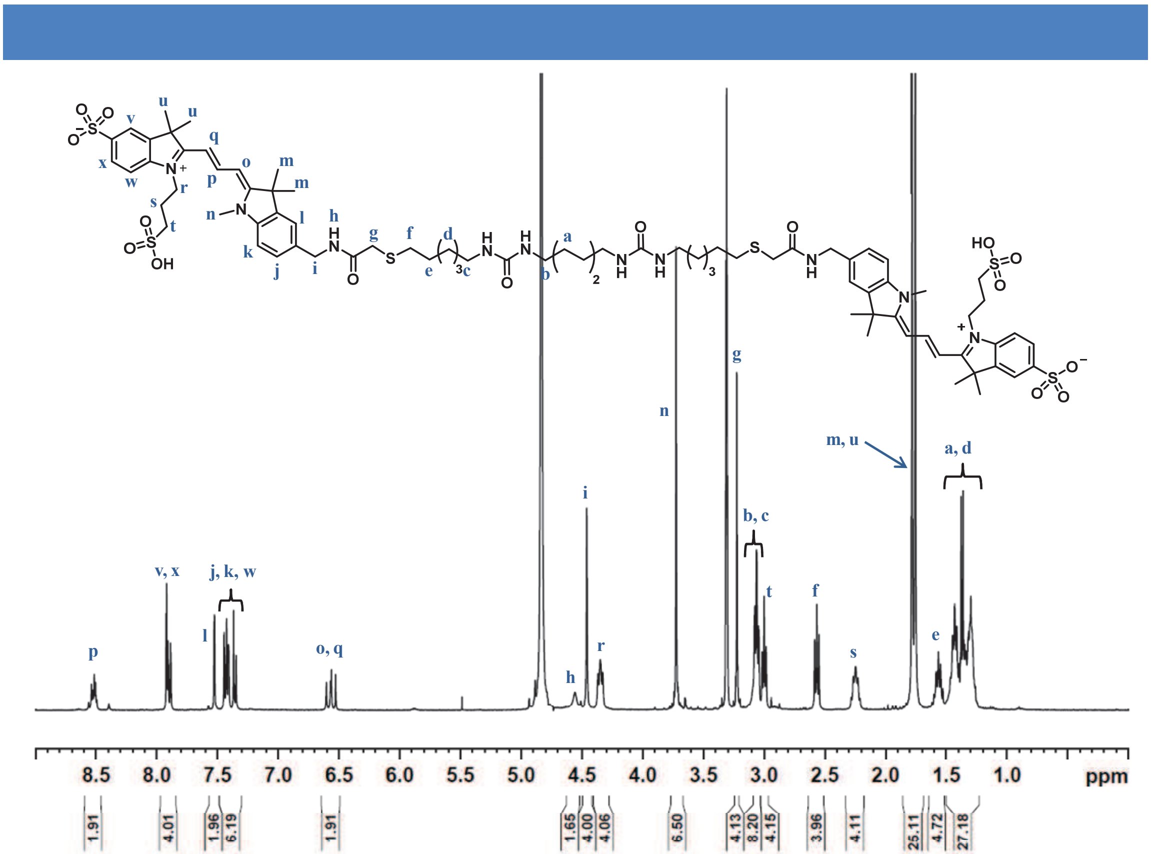

**Figure 57 |** $^1$H NMR spectra of bisurea-Cy$_3$ in CD$_3$OD.

This compound was also soluble in water and the corresponding NMR spectrum is described in the experimental section. However, as analyses by spectroscopic and scattering techniques in methanol did not demonstrate the formation of self-assembled structures, all the following experiments are reported in water.

### ii. Viscosity experiments on bisurea-Cy$_3$ in D$_2$O

Similarly to bisurea-based supramolecular polymers with peptidic residues, capillary viscosimetry experiments were performed to qualitatively monitor the propensity of bisurea-Cy$_3$ monomer to self-assemble into high molar mass assemblies (Figure 58).

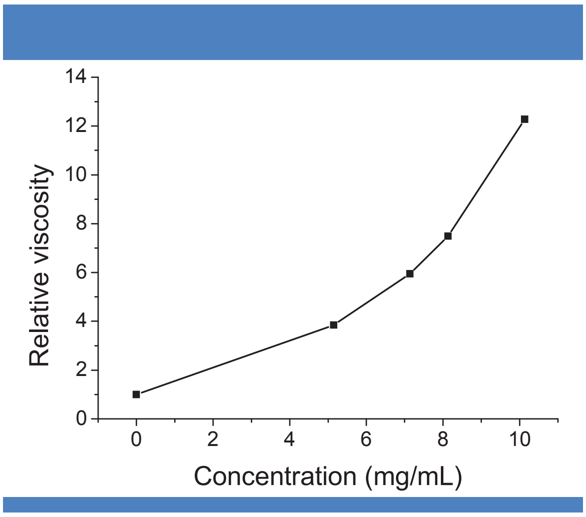

**Figure 58 |** Relative viscosity of bisurea-Cy$_3$ in $D_2O$ at 25°C.

These measurements were performed following the same protocol as for bisurea-6AA. A continuous increase in viscosity was observed along with increasing concentrations. However, measurements at concentration higher than 10 mg/mL were not performed due to the high viscosity of the corresponding solutions. Importantly, the strong viscosity increase with concentration even at 5 mg/mL is comparable in terms of relative viscosity with the values obtained for bisurea-6AA and indicates the formation of large aggregates. Compared with bisurea-7AA, this result demonstrates that the aliphatic linker between the cyanine moiety and the bisurea motif is not detrimental to the self-assembly process.

### *iii. FT-IR of bisurea-Cy$_3$ in $D_2O$*

Compared with other bisurea derivatives, bisurea-Cy$_3$ compound was studied in solution ($D_2O$) at various concentrations in the 3700-3000 cm$^{-1}$ and 1700-1400 cm$^{-1}$ regions, which are characteristic of N-H, C=O and aromatic vibrational frequencies (Figure 59).

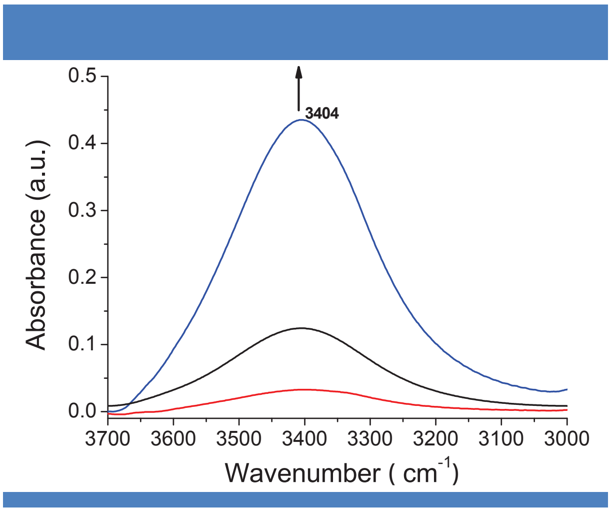

**Figure 59 |** FT-IR spectra of solutions of bisurea-Cy$_3$ in $D_2O$ for concentrations ranging from 3 × 10$^{-5}$ (red) up to 2 x 10$^{-3}$ M (blue).

Only one band can be observed at ~3404 $cm^{-1}$, which increases with increasing concentrations. Such a frequency for an N-H stretching band is typically too high for a hydrogen bonded urea and too low for a free hydrogen bonding unit.[201] Therefore, this band probably results from the overlap of the hydrogen-bonded N-H stretching band corresponding to the urea motif and the free N-H stretching band corresponding to the amide moiety on the cyanine core.

### iv. UV-Vis experiments on bisurea-$Cy_3$

Considering the optical properties of cyanine derivatives, we compared the absorption spectra of bisurea-$Cy_3$ in water with the one recorded in methanol and performed concentration-dependent UV-Vis experiments in $D_2O$ (Figure 60).

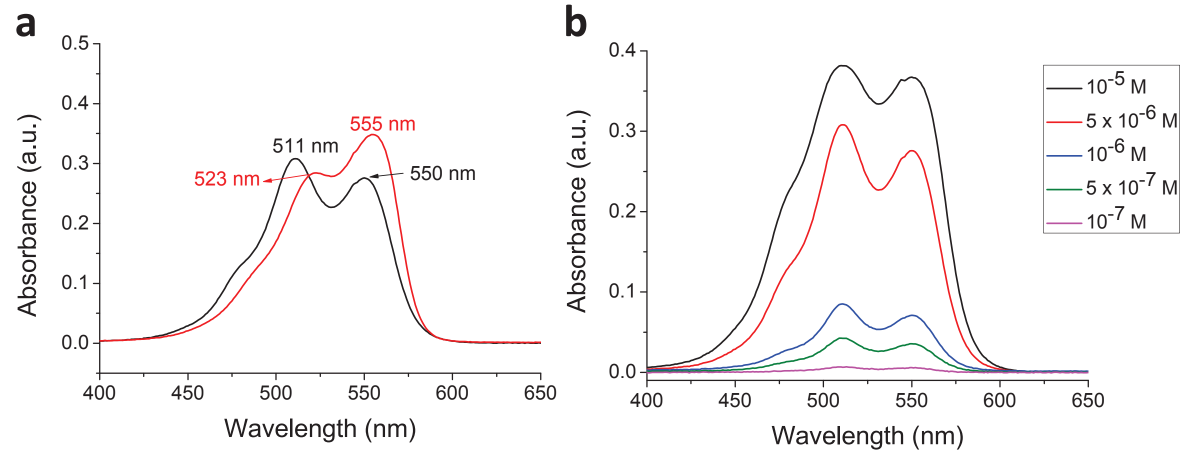

**Figure 60 |** a) Comparison of the UV-Vis spectra of a 5 × $10^{-6}$ M solution of bisurea-$Cy_3$ in $D_2O$ (black) and in $CD_3OD$ (red); b) UV-Vis spectra of a $D_2O$ solution of bisurea-$Cy_3$ in $D_2O$ for concentrations ranging from $10^{-7}$ (pink) up to $10^{-5}$ mol/L (black).

In $CD_3OD$, a maximum absorption is observed at 555 nm with a shoulder at 523 nm, in agreement with the UV-Vis spectra reported for cyanine derivative **20**.[197] Interestingly, in water, the maximum of absorption is observed at 511 nm with another clear peak at 550 nm. This shift of the absorption bands to lower wavelengths denotes the formation of H-aggregates whereas cyanine dyes have been mainly reported to produce J-aggregates.[207] This result suggests that the H-aggregation of the cyanine dyes is probably induced by the supramolecular polymerization of the bis-urea units. Importantly, concentration-dependent UV-Vis experiments show that the formation of these H-aggregates is observed for concentration as low as 5 × $10^{-7}$ mol/L, suggesting that, even at so low concentration, the

---

[207] Würthner, F.; Kaiser, T. E. and Saha-Möller, C. R. J-Aggregates: From Serendipitous Discovery to Supramolecular Engineering of Functional Dye Materials. *Angew. Chem. Int. Ed.* **2011**, *50*, 3376-3410.

bisurea-based supramolecular polymer is already formed.

### v. *Fluorescent experiment on bisurea-$Cy_3$ in $D_2O$*

Considering the fluorescent properties of cyanine derivatives, we then studied the fluorescent behavior of bisurea-$Cy_3$ at various concentrations in $D_2O$ (Figure 61).

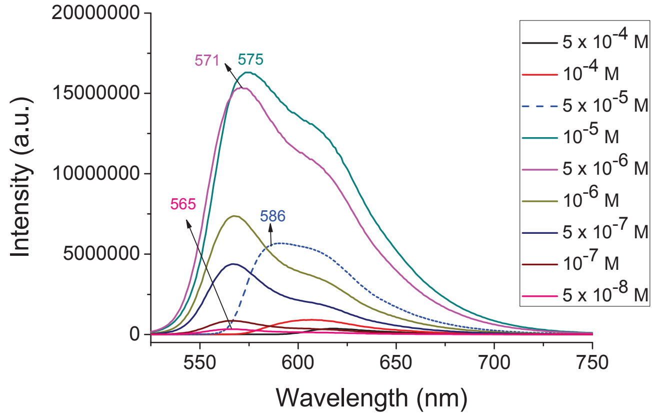

**Figure 61** | Fluorescent spectra of bisurea-$Cy_3$ in $D_2O$ for concentrations ranging from $5 \times 10^{-8}$ up to $5 \times 10^{-4}$ mol/L, $\lambda_{ex} = 511$ nm.

For most of the concentrations (up to $10^{-5}$ mol/L), upon excitation at 511 nm, the maximum emission is observed at ~567 nm with a shoulder at 608 nm and the emission intensity of both bands is increasing with the concentration. Noteworthily, the emission band at 567 nm is red-shifted from 565 nm to 575 nm upon increasing the concentration. However, above $5 \times 10^{-5}$ mol/L, both emission bands started decreasing with only the 608 nm band remaining at $5 \times 10^{-4}$ M. These results suggest that the emission band at 567 nm correspond to the monomer whereas the emission band at 608 nm could arise from the formation of oligomeric species. Although the absence of fluorescence quenching is in contradiction with the formation of H-aggregates,[208] further analyses of these experiments remains to be done in order to better understand the photophysical behavior of the supramolecular polymer.

### vi. *LS and SANS experiments on bisurea-$Cy_3$ in $D_2O$*

The formation of aggregates was confirmed by SANS and SLS experiments on bisurea-$Cy_3$ at $10^{-3}$ M in $D_2O$ which provided information on the structure of the self-assembly (Figure 62).

---

[208] Rösch, U.; Yao, S.; Wortmann, R. and Würthner, F. Fluorescent H-aggregates of merocyanine dyes. *Angew. Chem. Int. Ed.* **2006**, *45*, 7026-7030.

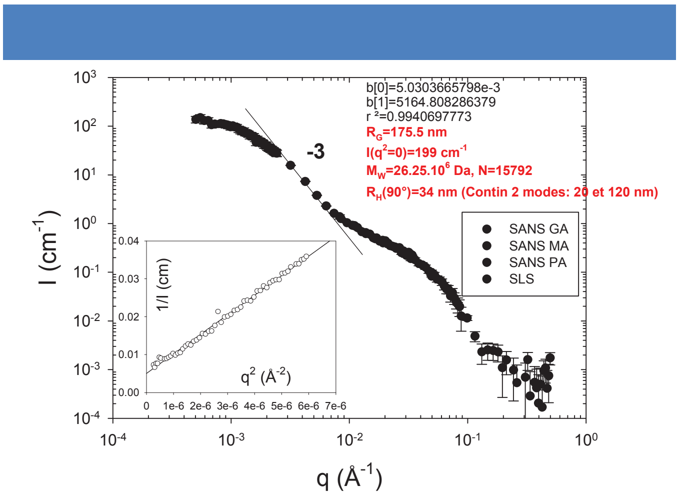

**Figure 62 |** LS and SANS spectra of bisurea-Cy$_3$ in $D_2O$ at 1.66*10$^{-3}$ g/L.

Qualitatively, the scattering curve exhibits the following behavior: a) a smooth variation analogous to a Guinier regime at very low q values and associated with the finite size and mass of the objects; b) a low-q regime in which the q-dependence of the data can be described by a power law with the exponent close to -3, such as in collapsed polymer coils; c) a $q^{-1}$ domain at intermediate q values that is characteristic of rigid-rod-like behavior followed by d) another Guinier regime associated with the cross-section of the polymers. Above 2 x $10^{-1}$ Å$^{-1}$, some oscillations might be observed. This sequence is characteristic of the formation of large unidirectional objects such as twisted ribbons, as suggested by microscopy techniques (*vide infra*). At low q, in the Guinier regime, the plot of $1/I$ as a function of $q^2$ provide us with an apparent gyration radius ($R_{G, app}$) of 175 nm and an apparent molecular weight ($M_{w, app}$) of the aggregates of 26.25 × $10^6$ Da, which corresponds to an aggregation number $N_{agg}$ of 15792.

Additional DLS measurements at θ=90° show a bimodal auto-correlation function characteristic of two populations with apparent hydrodynamic radii $R_{H, app}$ of 20 and 120 nm (obtained by applying the CONTIN method to our data). Importantly, $R_g/R_H$ ratio is much larger than 1, which suggests the formation of an extended structure. Further analysis should provide us with the dimensions of the cross-section of the twisted ribbons, which will be compared with the size obtained by microscopy images.

### *vii. AFM and TEM imaging of bisurea-Cy$_3$*

AFM imaging of diluted $D_2O$ solutions revealed the formation of branched and long micrometric twisted ribbons with a width of ~12 nm (Figure 63). TEM experiments show the presence of long fibers but could not confirm the formation of twisted ribbons. Importanly, at low concentrations, isolated ribbons could be observed by AFM whereas, at higher concentrations, interpenetrated ones were observed. These observations are in agreement with the scattering data which suggest the formation of long hollows cylinder made from twisted ribbons.

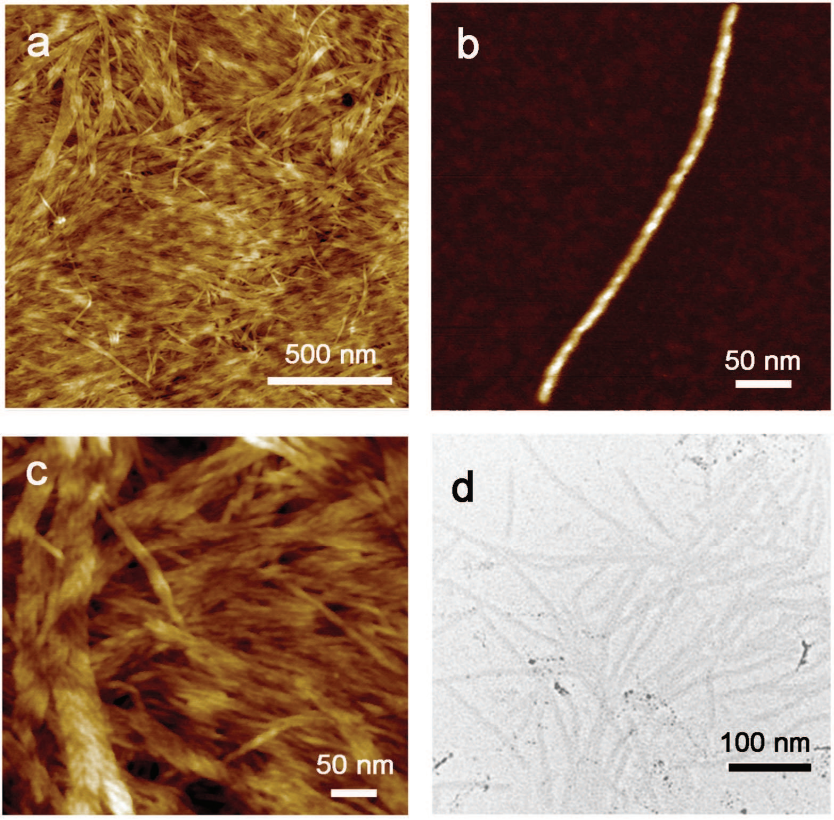

**Figure 63 |** AFM (a, b, c) and TEM (d) images of bisurea-$Cy_3$ from $D_2O$ solutions.

### *viii. Hydrogelation properties of bisurea-$Cy_3$*

During the course of the previous experiments, we noticed that bisurea-$Cy_3$ displays a gel-like behavior at relatively high concentration ($\geq 10^{-2}$ M). Therefore, we decided to evaluate the hydrogelation properties of this compound by performing the inverted tube experiment (Figure 64).

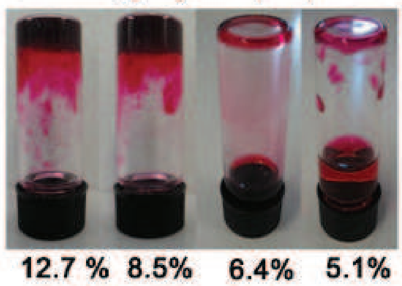

**Figure 64 |** Inverted tube experiment on bisurea-$Cy_3$ solutions in $D_2O$ at various concentrations (w/w)..

Concentrations ranging from 5 to 13% w/w in $D_2O$ were evaluated. Above 8% w/w, gel-like behaviors were observed with no slipping of the gel over 24 hours. However, all samples below 6.5 $w_t$% resulted in solutions.

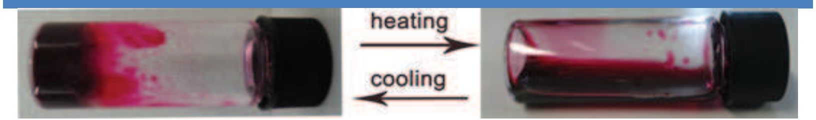

**Figure 65 |** Thermo-reversible experiments on a solution of 8.5% bisurea-$Cy_3$ in $D_2O$.

We also studied qualitatively the influence of the temperature on the 8.5% gel (Figure 65). Interestingly, upon heating up to 60 °C, the gel transformed to a solution which could reversibly turn back to a stable gel upon decreasing the temperature to room temperature. Further DSC experiments are currently performed in the laboratory to evaluate precisely the melting ($T_m$) and gel formation ($T_g$) temperatures of this molecule.

## b. Supramolecular polymers with $Cy_5$ side chains

### *i. $^1H$ NMR spectra of bisurea-$Cy_5$*

Bisurea-$Cy_5$ was initially characterized by $^1H$ NMR in methanol (Figure 66). The spectrum displays the expected set of signals which were determined thanks to 2D-COSY NMR.

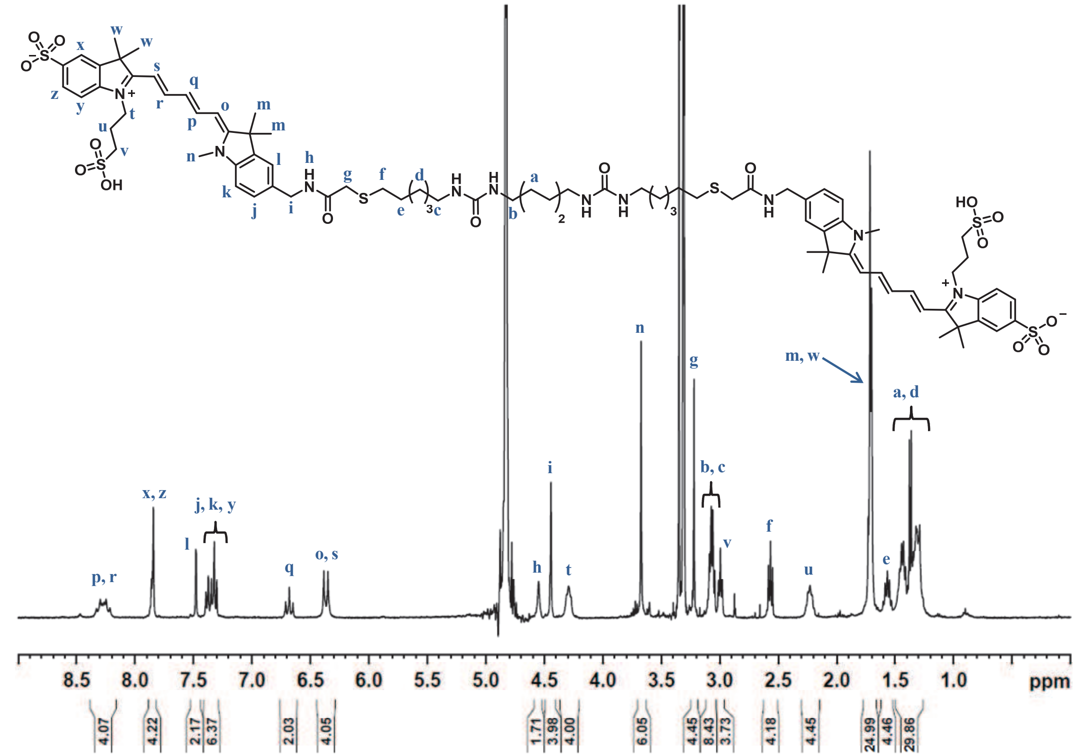

**Figure 66 |** $^1H$ NMR spectra of bisurea-$Cy_5$ in $CD_3OD$ at $5*10^{-3}$ M.

This compound was also soluble in water but no suitable NMR spectrum could be recorded probably due to the formation of aggregates. Considering that spectroscopic and scattering experiments in methanol did not demonstrate the formation of self-assembled structures, all the following experiments are reported in water.

### *ii. UV-Vis experiment on bisurea-Cy$_5$*

Similarly to bisurea-Cy$_3$, we compared the absorption spectra of bisurea-Cy$_5$ in water with the one recorded in methanol and performed concentration-dependent UV-Vis experiments in $D_2O$ (Figure 67).

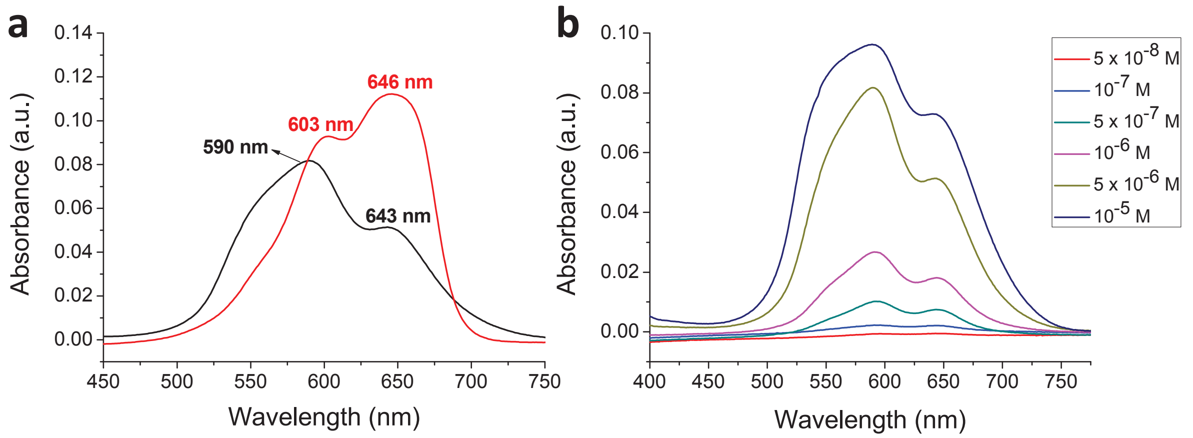

**Figure 67 |** a) Comparison of the UV-Vis spectra of a 5 × $10^{-6}$ M solution of bisurea-Cy$_5$ in $D_2O$ (black) and in $CD_3OD$ (red); b) UV-Vis spectra of a $D_2O$ solution of bisurea-Cy$_5$ in $D_2O$ with concentrations ranging from 5 x $10^{-8}$ (red) up to $10^{-5}$ mol/L (dark blue).

In $CD_3OD$, a maximum absorption is observed at 646 nm with a define shoulder at 603 nm, in agreement with the UV-Vis spectra reported for cyanine derivative **25**.[197] Interestingly, in water, the maximum of absorption is observed at 590 nm as a broad peak with a shoulder at 643 nm. As for bisurea-Cy$_3$, this shift of the absorption bands to lower wavelengths denotes the formation of H-aggregates. This result suggests that the H-aggregation of the cyanine dyes is probably induced by the supramolecular polymerization of the bis-urea units. Importantly, concentration-dependent UV-Vis experiments show that the formation of these H-aggregates is observed for concentration as low as 5 × $10^{-8}$ mol/L, suggesting that, even at so low concentration, the bisurea-based supramolecular polymer is already formed.

### *iii. Fluorescence experiment on bisurea-Cy$_5$ in $D_2O$*

Identically to bisurea-Cy$_3$, we then studied the fluorescent behavior of bisurea-Cy$_5$ at various concentrations in $D_2O$ (Figure 68).

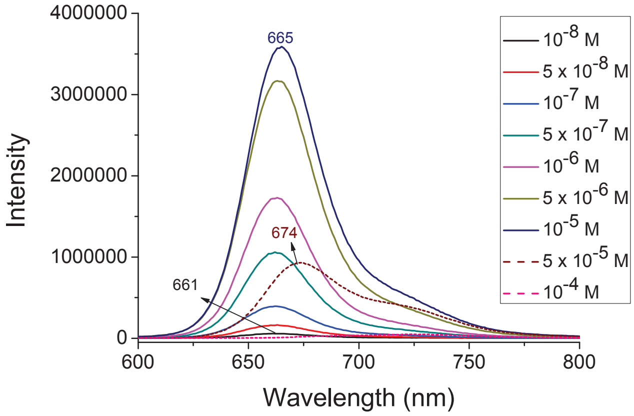

**Figure 68** | Fluorescent spectra of bisurea-$Cy_5$ in $D_2O$ for concentration ranging from $10^{-8}$ up to $10^{-4}$ mol/L, $\lambda_{ex} = 588$ nm.

For most of the concentrations (up to $10^{-5}$ mol/L), upon excitation at 588 nm, the maximum emission is observed at ~663 nm and the emission intensity is increasing with the concentration. In this case, the emission band at 663 nm is only slightly red-shifted from 661 nm to 665 nm upon increasing the concentration. However, above $5 \times 10^{-5}$ mol/L, the emission band at 663 nm starts to decrease with a red-shift to 674 nm whereas a shoulder band appears at ~716 nm. These results suggest that the emission band at 663 nm correspond to the monomer (this value is in agreement with the reported maximum emission for cyanine derivative **25**.[197]) whereas the emission band at 716 nm could arise from the formation of oligomeric species. Importantly, above $10^{-4}$ mol/L, complete quenching of the fluorescence occurs. Although the absence of fluorescence quenching even at low concentration is in contradiction with the formation of H-aggregates, further analyses of these experiments remains to be done in order to better understand the photophysical behavior of the supramolecular polymer.

### *iv. TEM imaging of bisurea-$Cy_5$*

The formation of aggregates was initially evaluated by scattering experiments on bisurea-$Cy_5$ at $10^{-3}$ M in $D_2O$. However, although SANS experiments remain to be analyzed, LS experiments could not be performed due to the absorption of the laser beam ($\lambda = 632.8$ nm) by the sample. In order to have an indication on the morphology of the aggregates, we performed TEM experiments by drop-casting a solution of bisurea-$Cy_5$ on a copper grid. TEM images of this solution show the presence of long fibers with a homogenous diameter distribution of ~7 nm (Figure 69).

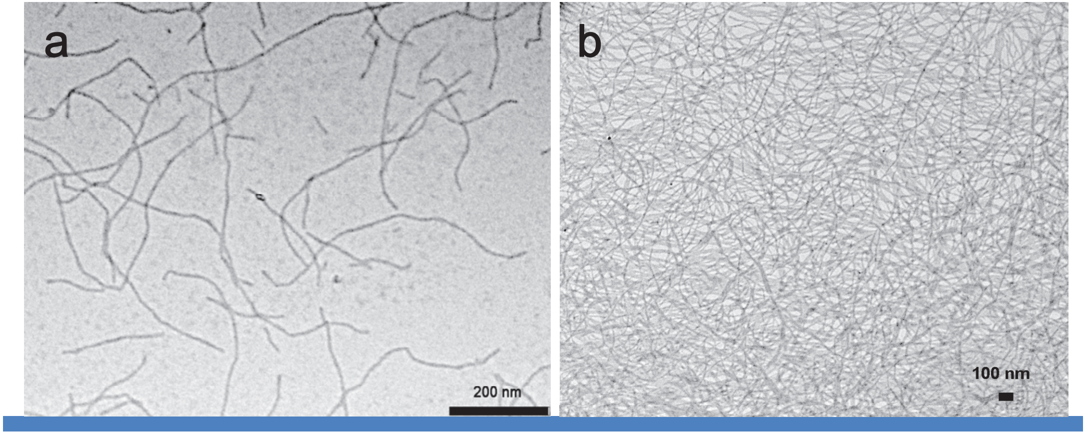

**Figure 69 |** TEM images of bisurea-$Cy_5$ from $D_2O$ solutions.

Importantly, although almost individual fibers could be imaged, large networks of these fibers could be observed with monodisperse diameters. This dense network probably accounts for the hydrogelation properties observed for bisurea-$Cy_5$.

### *v. Thermo-reversible hydrogel based on bisurea-Cy₅*

Similarly to bisurea-$Cy_3$, we noticed that bisurea-$Cy_5$ displays a gel-like behavior in $D_2O$ at relatively high concentration ($\geq 4 \times 10^{-2}$ M). We studied qualitatively the influence of the temperature on the 6.8% gel (Figure 70). Interestingly, upon heating up to 70 °C, the gel transformed to a solution which could reversibly turn back to a stable gel upon decreasing the temperature to room temperature.

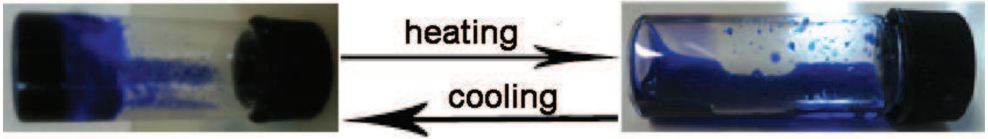

**Figure 70 |** Thermo-reversible experiments on a solution of 6.8% bisurea-$Cy_5$ in $D_2O$.

Further DSC experiments are currently performed in the laboratory to evaluate precisely the melting ($T_m$) and gel formation ($T_g$) temperatures of this molecule.

Overall, using a combination of optical spectroscopies, scattering and/or imaging techniques, we have shown that both bisurea-$Cy_3$ and bisurea-$Cy_5$ molecules give rise to fibrillar self-assemblies in water. Further in-depth analyses of the scattering data and additional experiments to characterize the hydrogelation properties of both molecules remain to be performed.

# 4. Co-self-assemblies of bisurea-based supramolecular polymers with peptidic and fluorescent residues

## a. Co-self-assemblies of bisurea-peptides monomers with bisurea-$Cy_3$

### *i. UV-Vis experiments*

As shown by the characterization of the monomers, the aggregation of bisurea-cyanine monomers can be easily monitored by absorption and fluorescence spectroscopies. Therefore, we have started to study co-self-assemblies based on these fluorescent monomers using optical spectroscopies. We have first studied the co-self-assembly of bisurea-$Cy_3$ monomer with either bisurea-6AA or bisurea-7AA using UV-Vis experiments (Figure 71).

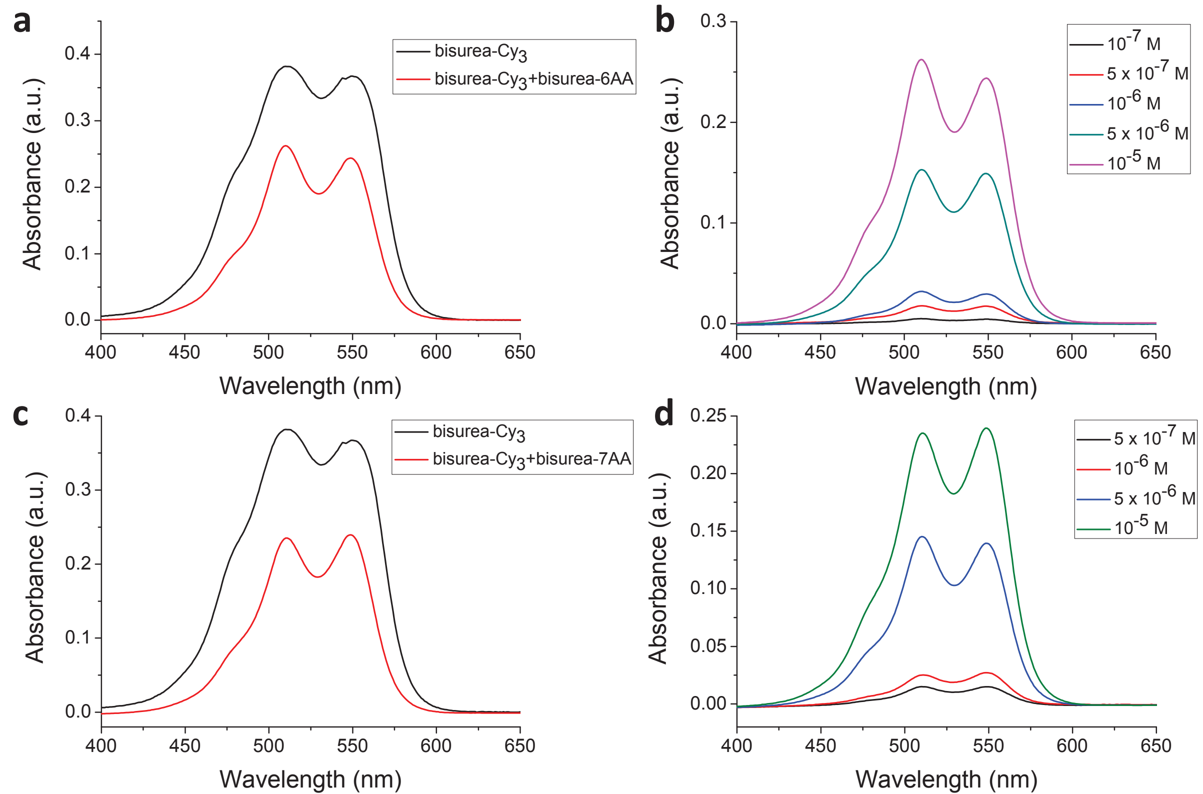

**Figure 71 |** a) Comparison of the UV-Vis spectra of a $10^{-5}$ M solution of bisurea-$Cy_3$ (black) and of a 1:1 mixture of bisurea-$Cy_3$/bisurea-6AA (red) in $D_2O$; b) UV-Vis spectra of a $D_2O$ solution of bisurea-$Cy_3$/bisurea-6AA in $D_2O$ for concentrations ranging from $10^{-7}$ (black) up to $10^{-5}$ mol/L (pink); c) Comparison of the UV-Vis spectra of a $10^{-5}$ M solution of bisurea-$Cy_3$ (black) and of a 1:1 mixture of bisurea-$Cy_3$/bisurea-7AA (red) in $D_2O$; d) UV-Vis spectra of a $D_2O$ solution of bisurea-$Cy_3$/bisurea-7AA in $D_2O$ for concentrations ranging from $5 \times 10^{-7}$ (black) up to $10^{-5}$ mol/L (green).

As demonstrated by the comparison with the UV-Vis spectrum of bisurea-$Cy_3$ (Figure 71a and c, black), UV-Vis spectra of its mixture with either bisurea-6AA (Figure 71a, red) or bisurea-7AA (Figure 71c, red) display almost identical absorption bands with a maximum absorption at ~510 nm in both cases. We can notice that the second absorption band at 549 nm is more intense (and almost at the same intensity than the 510 nm band) for the mixture with bisurea-7AA compared to the other mixture. Additionally, difference in intensities between bisurea-Cy$_3$ and the mixtures are attributed to the lower concentration of dyes in the mixtures for a same total concentration ($10^{-5}$ M). Similarly to bisurea-Cy$_3$ monomer, the shift of the absorption bands to lower wavelengths compared to the monomer itself and the appearance of a shoulder peak at 497 nm suggests the formation of H-aggregates. Concentration-dependent UV-Vis experiments on both mixtures show that the formation of these H-aggregates is observed for concentration as low as $5 \times 10^{-7}$ mol/L (Figure 71b and d), suggesting that, even at so low concentration, a bisurea-based supramolecular polymer is already formed.

### *ii. Fluorescence experiments*

In order to better understand how bisurea-peptides monomers are packed with bisurea-Cy$_3$ monomers, we studied the mixtures by fluorescence spectroscopy at different concentrations (Figure 72).

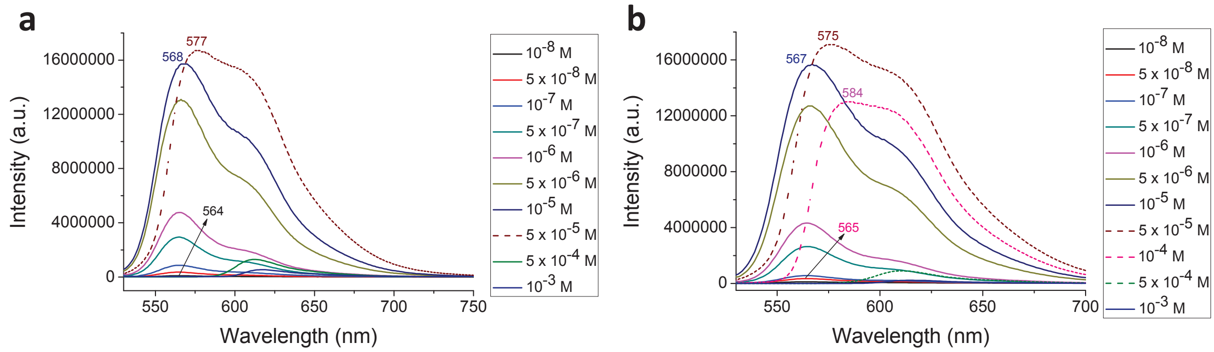

**Figure 72 |** a) Fluorescence spectra of a 1:1 mixture of bisurea-Cy$_3$/bisurea-6AA for concentrations ranging from $10^{-8}$ up to $10^{-3}$ mol/L in $D_2O$, $\lambda_{ex}$=511 nm; b) Fluorescence spectra of a 1:1 mixture of bisurea-Cy$_3$/bisurea-7AA for concentrations ranging from $10^{-8}$ up to $10^{-3}$ mol/L in $D_2O$, $\lambda_{ex}$=511 nm.

Compared with the fluorescence spectra of bisurea-Cy$_3$ at various concentrations (Figure 61), similar behaviors were observed for both mixtures. Namely, for the lowest concentrations (up to $10^{-5}$ mol/L), upon excitation at 511 nm, the maximum emission is observed at ~565 nm with a shoulder at 607 nm and the emission intensity of both bands is increasing with the concentration. Noteworthily, the emission band at 567 nm is only slightly red-shifted (2-4 nm) upon increasing the concentration up to $10^{-5}$ mol/L. Above $5 \times 10^{-5}$ mol/L, both emission bands started to merge in a single band at ~607 nm, which remained visible up to $10^{-3}$ mol/L but decreases which suggests some quenching.

We also compared the fluorescence spectra of the mixtures with the one of the single dye at selected concentrations (Figure 73).

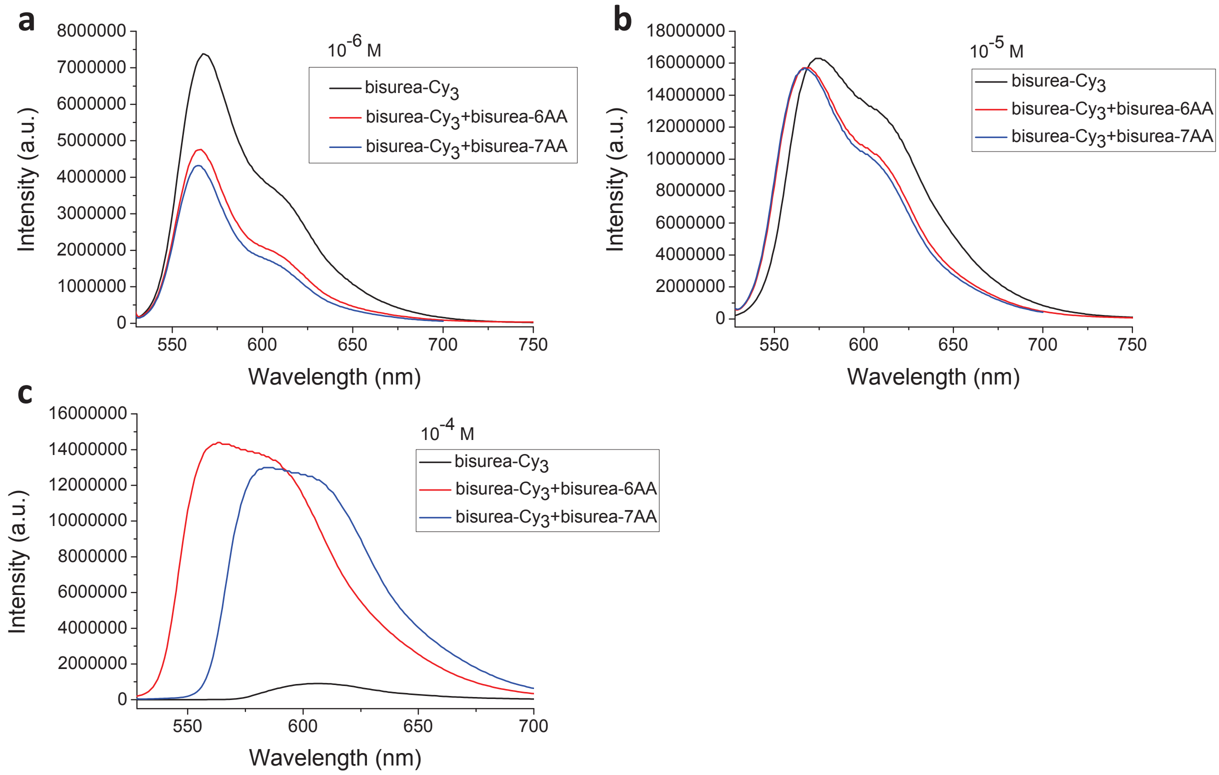

**Figure 73** | Comparison of the fluorescence spectra of a solution of bisurea-$Cy_3$ (black), of a 1:1 mixture of bisurea-$Cy_3$/bisurea-6AA (red) and of a 1:1 mixture of bisurea-$Cy_3$/bisurea-7AA (blue) at a) $10^{-6}$ M in $D_2O$, b) at $10^{-5}$ M in $D_2O$ and c) at $10^{-4}$ M in $D_2O$.

At $10^{-6}$ and $10^{-5}$ M, the fluorescence spectra of the mixtures are almost identical to the spectrum of bisurea-$Cy_3$. However, at $10^{-6}$ M, its intensity is almost twice lower for the mixtures compared to bisurea-$Cy_3$. At $10^{-5}$ M, the intensities of all spectra are almost identical but the absorption maximum is slightly blue-shifted for the mixtures compared to bisurea-$Cy_3$. Finally, at $10^{-4}$ M, the fluorescence of the mixtures remains as a broad band with a high intensity whereas the fluorescence of bisurea-$Cy_3$ is almost completely quenched. This absence of fluorescence quenching for the mixtures suggests that the bisurea-peptide monomers probably intercalate within the assembly formed by bisurea-$Cy_3$. Overall, this observation suggests that mixing peptidic and fluorescent monomers leads to social self-sorting.

### *iii. SANS and LS experiments*

This observation of social self-sorting was confirmed by SANS and LS experiments on

1:1 mixtures of bisurea-6AA with bisurea-$Cy_3$ and bisurea-7AA with bisurea-$Cy_3$ (Figure 74).

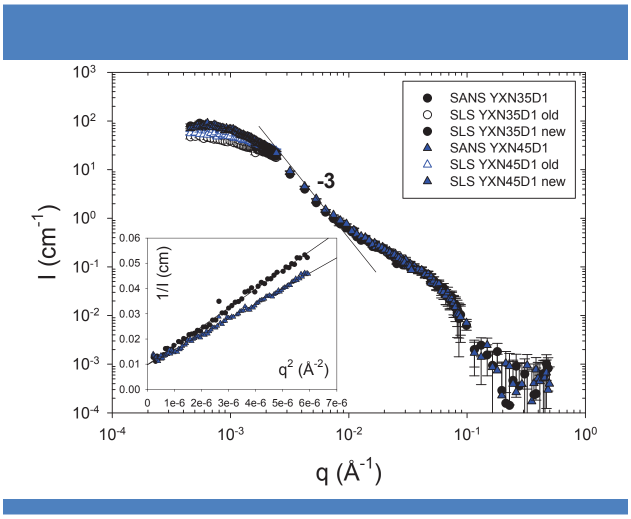

**Figure 74 |** SANS and LS spectra of 1:1 mixtures of bisurea-$Cy_3$/bisurea-6AA (YXN35D1) and bisurea-$Cy_3$/bisurea-7AA in $D_2O$ at $10^{-3}$ M (YXN35D1). “Old” and “new” refers to solutions which have been prepared for several weeks and 2-3 days, respectively.

Indeed, qualitatively, the scattering curve of both mixtures exhibits a global behavior that is almost identical to the one observed for bisurea-$Cy_3$ (Figure 62): a) the onset of a smooth variation analogous to a Guinier regime at very low q values and associated with the finite size and mass of the objects; b) a low-q regime in which the q-dependence of the data can be described by a power law with the exponent between -2 and -3, such as in collapsed polymer coils; c) a $q^{-1}$ domain at intermediate q values that is characteristic of rigid-rod-like behavior followed by d) another Guinier regime associated with the cross-section of the polymers. At low q, in the Guinier regime, the plot of $1/I$ as a function of $q^2$ provide us with an apparent gyration radius ($R_{g,\,app}$) of 151 nm and an apparent molecular weight ($M_{w,\,app}$) of the aggregates of $15.27 \times 10^6$ Da, which corresponds to an aggregation number $N_{agg}$ of 9956 for the 1:1 mixture of bisurea-$Cy_3$/bisurea-6AA. For the 1:1 mixture of bisurea-$Cy_3$/bisurea-7AA in $D_2O$, $R_{g,\,app}$ was determined to be 137 nm and $M_{w,\,app}$ was calculated to be as high as $14.25 \times 10^6$ Da, which corresponds to an aggregation number $N_{agg}$ of 8652. Additional DLS measurements at θ=90° provided an apparent hydrodynamic radius $R_{H,\,app}$ of 52 and 58 nm after cumulant analysis for the 1:1 mixtures of bisurea-$Cy_3$/bisurea-6AA and bisurea-$Cy_3$/bisurea-7AA, respectively. Importantly, $R_g/R_H$ ratio is almost equal to 3, which suggests the formation of extended structures. We can also clearly see from these spectra that the shape of the self-assemblies is dictated by the cyanine monomer. Compared to bisurea-$Cy_3$ derivative, the global scattering spectrum is very similar and the characteristic sizes $R_g$ and $R_H$ are slightly lower, which result in a lower degree of polymerization.

### *iv. AFM imaging*

For both mixtures, AFM imaging of diluted $D_2O$ solutions revealed the formation of branched and long micrometric fibers (Figure 75).

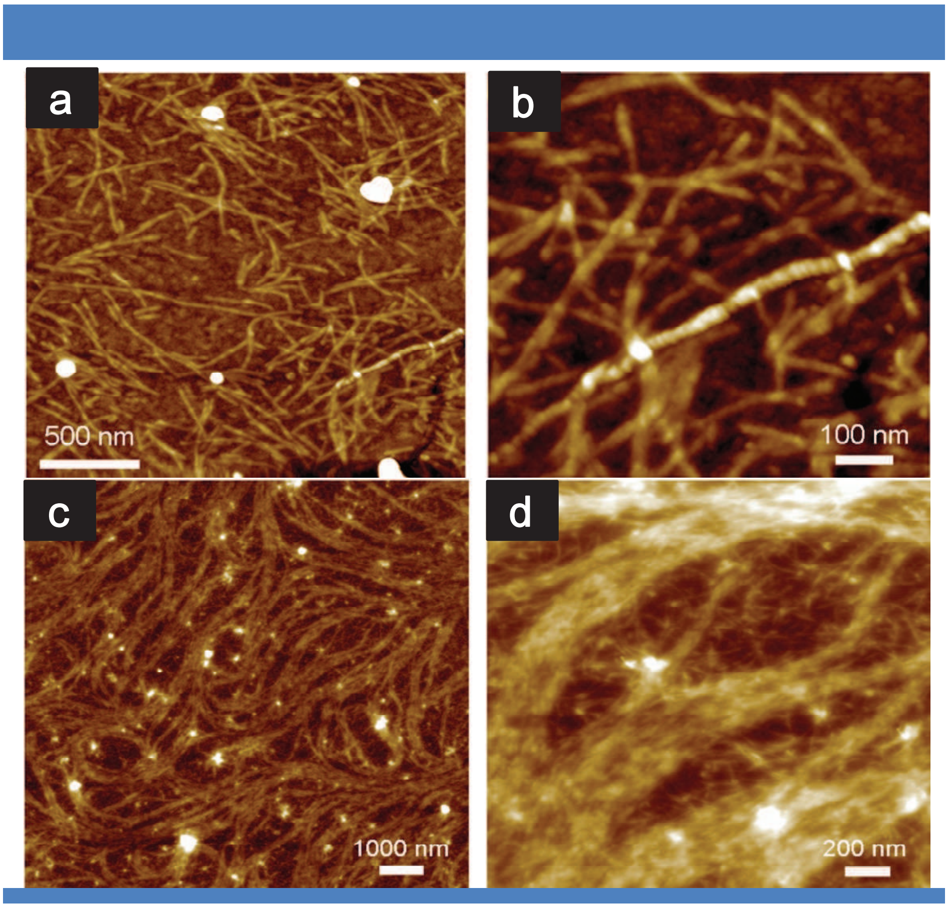

**Figure 75** | AFM images of 1:1 mixtures of bisurea-$Cy_3$/bisurea-6AA (a, b) and bisurea-$Cy_3$/bisurea-7AA (c, d) from $D_2O$ solutions.

Compared to the AFM image of bisurea-6AA, complete disappearance of the sheet-like structures was observed for the 1:1 mixture of bisurea-$Cy_3$/bisurea-6AA and the resulting morphology is very similar to the one observed for bisurea-$Cy_3$ (Figure 75a and b). In particular, the width of a single fiber (~15 nm) is almost identical for both samples (Figure 75b and Figure 63b). For the 1:1 mixture of bisurea-$Cy_3$/bisurea-7AA, less rigid fibers are observed, compared to the AFM image of bisurea-7AA (Figure 75a and b). However, for this sample, based only on the imaging technique, it is difficult to reach a conclusion regarding the preferential morphology of the co-self-assemblies. When all characterizations are considered, both co-self-assemblies induce multicomponent supramolecular polymers arising from a social self-sorting between different monomers. This social self- sorting implies breaking the bisurea-peptide self-assemblies, i.e. breaking β-sheets structures, which suggests that entropy plays an important role in this process.

## b. Co-self-assemblies of bisurea-peptides monomers with bisurea-Cy$_5$

### i. UV-Vis experiments

Similarly to the previous section, we have also studied the co-self-assembly of bisurea-Cy$_5$ monomer with either bisurea-6AA or bisurea-7AA using UV-Vis experiments (Figure 76).

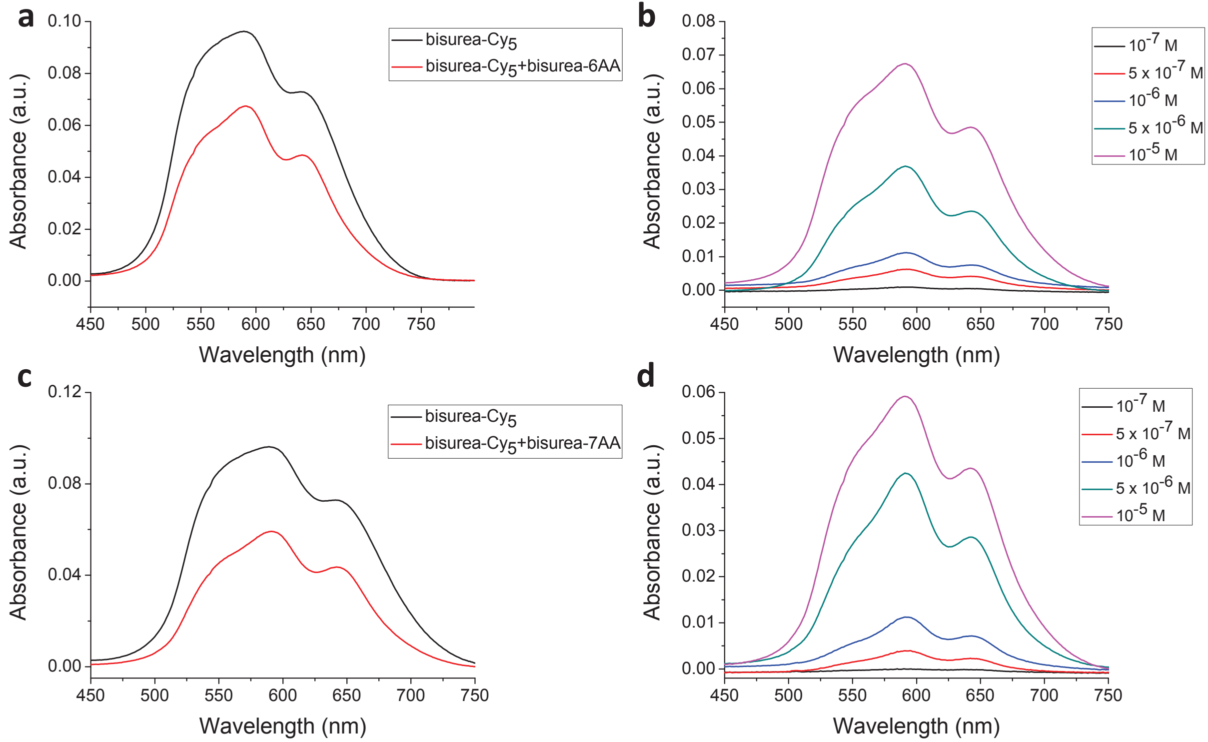

**Figure 76 |** a) Comparison of the UV-Vis spectra of a $10^{-5}$ M solution of bisurea-Cy$_5$ (black) and of a 1:1 mixture of bisurea-Cy$_5$/bisurea-6AA (red) in $D_2O$; b) UV-Vis spectra of a $D_2O$ solution of bisurea-Cy$_5$/bisurea-6AA in $D_2O$ for concentrations ranging from $10^{-7}$ (black) up to $10^{-5}$ mol/L (pink); c) Comparison of the UV-Vis spectra of a $10^{-5}$ M solution of bisurea-Cy$_5$ (black) and of a 1:1 mixture of bisurea-Cy$_5$/bisurea-7AA (red) in $D_2O$; d) UV-Vis spectra of a $D_2O$ solution of bisurea-Cy$_5$/bisurea-7AA in $D_2O$ for concentrations ranging from $10^{-7}$ (black) up to $10^{-5}$ mol/L (pink).

As demonstrated by the comparison with the UV-Vis spectrum of bisurea-Cy$_5$ (Figure 76a and c, black), UV-Vis spectra of its mixture with either bisurea-6AA (Figure 76a, red) or bisurea-7AA (Figure 76c, red) display almost identical absorption bands with a maximum absorption at 591 nm in both cases. For both mixtures, additional peaks at 551 (shoulder) and 642 nm are observed. Additionally, difference in intensities between bisurea-Cy$_5$ and the mixtures are attributed to the lower concentration of dyes in the mixtures for a same total concentration ($10^{-5}$ M). Similarly to bisurea-Cy$_5$ monomer, the shift of the absorption bands to lower wavelengths compared to the monomer itself and the appearance of a shoulder peak at 551 nm suggests the formation of H-aggregates. Concentration-dependent UV-Vis experiments on both mixtures show that the formation of these H-aggregates is observed for concentration as low as $5 \times 10^{-7}$ mol/L (Figure 76b and d), suggesting that, even at so low concentration, a bisurea-based supramolecular polymer is already formed.

### *ii. Fluorescence experiments*

In order to better understand how bisurea-peptides monomers are packed with bisurea-Cy3 monomers, we studied the mixtures by fluorescence spectroscopy at different concentrations (Figure 77).

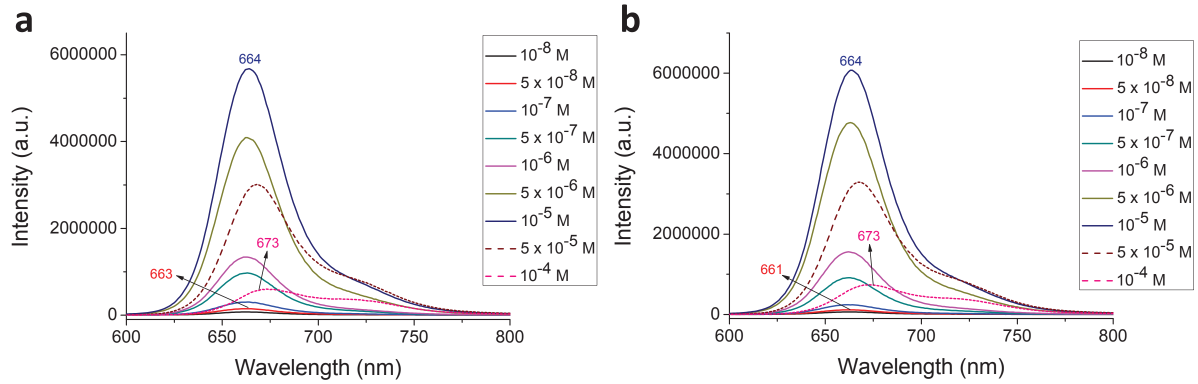

**Figure 77** | a) Fluorescence spectra of a 1:1 mixture of bisurea-$Cy_5$/bisurea-6AA for concentrations ranging from $10^{-8}$ up to $10^{-4}$ mol/L in $D_2O$, $\lambda_{ex}$=588 nm; b) Fluorescence spectra of a 1:1 mixture of bisurea-$Cy_5$/bisurea-7AA for concentrations ranging from $10^{-8}$ up to $10^{-4}$ mol/L in $D_2O$, $\lambda_{ex}$=588 nm.

Compared with the fluorescence spectra of bisurea-$Cy_5$ at various concentrations (Figure 68), similar behaviors were observed for both mixtures. Namely, for the lowest concentrations (up to $10^{-5}$ mol/L), upon excitation at 588 nm, the maximum emission is observed at ~662 nm with a shoulder appearing at 722 nm for concentrations above $10^{-6}$ M and the emission intensity of both bands is increasing with the concentration. Noteworthily, the emission band at 663 nm is almost not red-shifted (< 3 nm) upon increasing the concentration. Above $10^{-5}$ mol/L, the 663 nm emission band starts to decrease and to merge into a single broad band from 640 to 770 nm but with much lower intensity. Above $10^{-4}$ M, complete quenching of the fluorescence occurs.

We also compared the fluorescence spectra of the mixtures with the one of the single dye at selected concentrations (Figure 78).

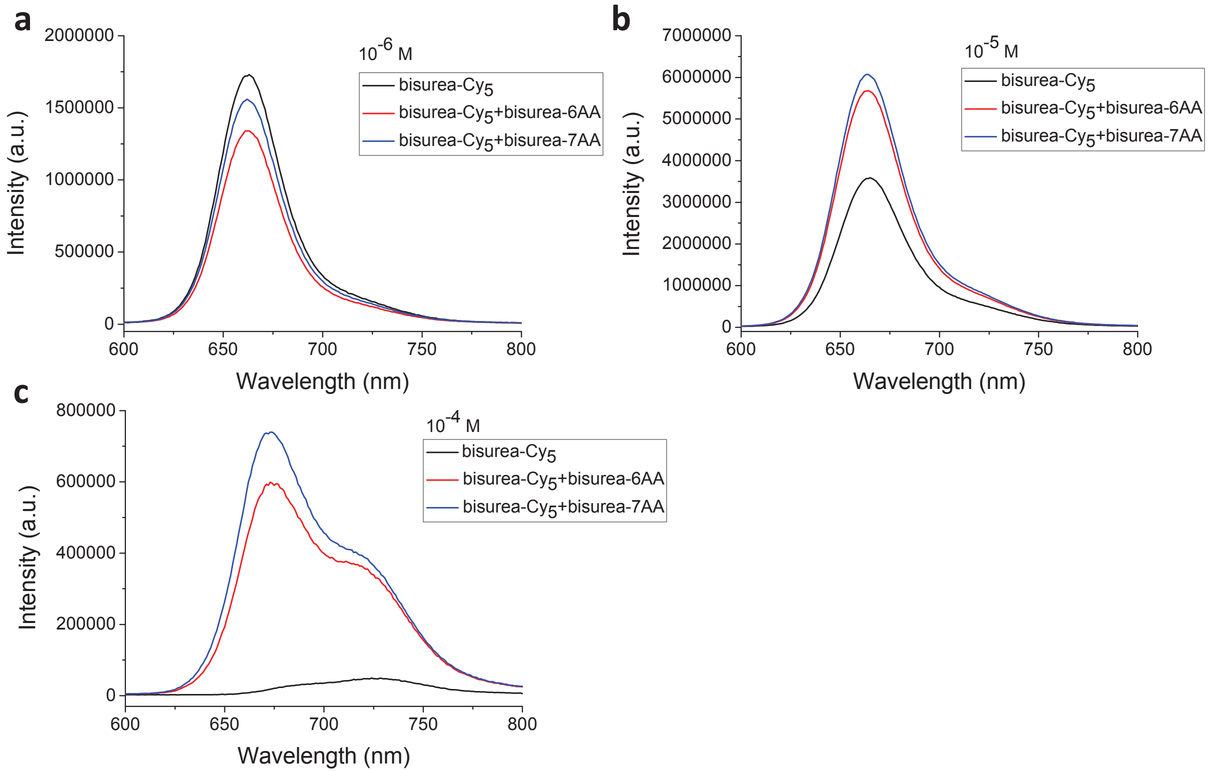

**Figure 78 |** Comparison of the fluorescence spectra of a solution of bisurea-$Cy_3$ (black), of a 1:1 mixture of bisurea-$Cy_3$/bisurea-6AA (red) and of a 1:1 mixture of bisurea-$Cy_3$/bisurea-7AA (blue) at a) $10^{-6}$ M in $D_2O$, b) at $10^{-5}$ M in $D_2O$ and c) at $10^{-4}$ M in $D_2O$.

At $10^{-6}$ and $10^{-5}$ M, the fluorescence spectra of the mixtures are almost identical to the spectrum of bisurea-$Cy_5$. However, at $10^{-6}$ M, its intensity is slightly lower for the mixtures compared to bisurea-$Cy_5$, whereas, at $10^{-5}$ M, the intensities of the mixtures are almost twice higher than the intensity of bisurea-$Cy_5$. This behavior is different from what was observed at the same concentrations for the mixtures with bisurea-$Cy_3$ (see section 4. a. ii.) This enhancement of the fluorescence suggests that the bisurea-peptide monomers probably intercalate within the assembly formed by bisurea-$Cy_5$ already at $10^{-5}$ M. At $10^{-4}$ M, a similar behavior was observed compared to bisurea-$Cy_3$ as the fluorescence of the mixtures remains whereas the fluorescence of bisurea-$Cy_5$ is almost completely quenched. This absence of fluorescence quenching for the mixtures suggests that the bisurea-peptide monomers probably intercalate within the assembly formed by bisurea-$Cy_5$. Similarly to the previous mixtures studied, these observations suggest that mixing peptidic and fluorescent monomers leads to social self-sorting.

Recently, we have attempted SANS and LS experiments in order to evaluate the morphology of these two mixtures. However, although SANS experiments remain to be analyzed, LS experiments could not be performed due to the absorption of the laser beam (λ =

632.8 nm) by the sample.

### c. Co-self-assembly of bisurea-based supramolecular polymers with a mixture of fluorescent residues

Förster resonance energy transfer (FRET) is a powerful tool to probe monomer roximity on the molecular scale.[209] In order to understand the arrangement of our multicomponent supramolecular polymers at this scale, we thought that the use of the FRET pair $Cy_3/Cy_5$, which displays a Förster radius of 50 Ǻ, would be a valuable tool.[210] Before envisioning three-component mixtures, we have first studied the fluorescent properties of mixtures of bisurea-$Cy_3$/bisurea-$Cy_5$ (Figure 79).

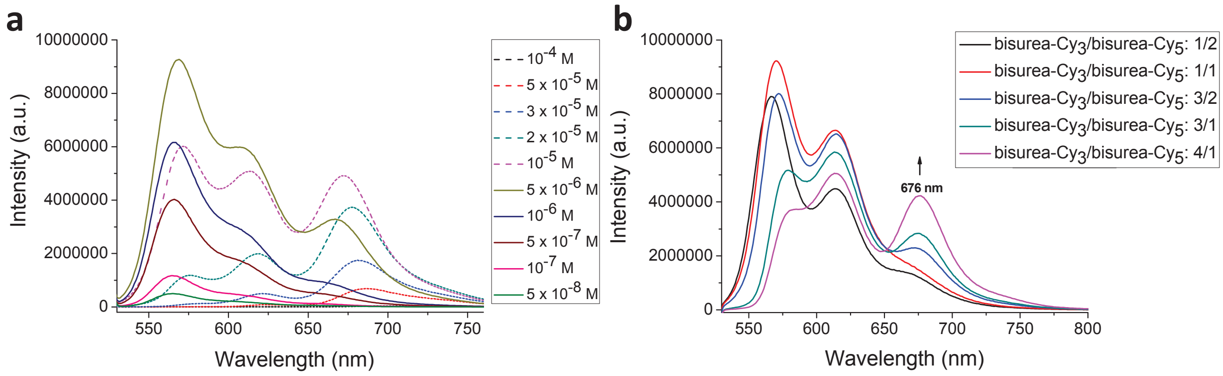

**Figure 79 |** a) Fluorescence spectra of a 1:1 mixture of bisurea-$Cy_3$/bisurea-$Cy_5$ for concentrations ranging from $5 \times 10^{-8}$ up to $10^{-4}$ mol/L in $D_2O$, $\lambda_{ex}$=511 nm; b) Fluorescence spectra of various mixtures of bisurea-$Cy_3$/bisurea-$Cy_5$ at $10^{-5}$ M in $D_2O$, $\lambda_{ex}$=511 nm. Ratio of bisurea-$Cy_3$/bisurea-$Cy_5$ varies from 1:2 (black), 1:1 (red), 3:2 (blue), 3:1 (green) to 4:1 (pink). All spectra have been substracted from the fluorescence spectrum of bisurea-$Cy_5$ at $10^{-5}$ M in $D_2O$.

For concentrations up to $10^{-6}$ mol/L, upon excitation at 511 nm, the maximum emission is observed at ~566 nm with a shoulder at 609 nm, which demonstrates that only bisurea-$Cy_3$ monomers fluoresce. At 5 x $10^{-6}$ mol/L, a strong emission band appears at 666 nm along with fluorescence at 566 and 609 nm, which means that energy transfer occurs from bisurea-$Cy_3$ to bisurea-$Cy_5$. This observation suggests that the supramolecular polymer is being formed with the intercalation of bisurea-$Cy_5$ within a supramolecular polymer made of bisurea-$Cy_3$. Above this concentration, the fluorescence of bisurea-$Cy_3$ starts decreasing until complete quenching while the fluorescence of bisurea-$Cy_5$ remains. Noteworthily, upon increasing the concentration, the emission band at 666 nm is red-shifted from 672 nm to 686 nm until complete quenching at high concentration ($10^{-4}$ mol/L). From 5 x $10^{-6}$ mol/L, this

---

[209] a) Stryer, L. Fluorescence energy-transfer as a spectroscopic ruler. *Annu. Rev. Biochem.* **1978**, *47*, 819-846; Stennett, E. M. S.; Ciuba, M. A. and Levitus, M. Photophysical processes in single molecule organic fluorescent probes. *Chem. Soc. Rev.* **2014**, *43*, 1057-1075.

[210] Albertazzi, L.; Martinez-Veracoechea, F. J.; Leenders, C. M. A.; Voerts, I. K.; Frenkel, D. and Meijer, E. W. Spatiotemporal control and superselectivity in supramolecular polymers using multivalency. *Proc. Nat. Acad. Sci. USA* **2013**, *110*, 12203-12208.

concentration-dependant fluorescence suggests the formation of a supramolecular polymer until complete social self-sorting of the monomers at $10^{-4}$ mol/L.

We also monitored the fluorescent spectra of various mixtures of bisurea-$Cy_3$/bisurea-$Cy_5$ at $10^{-5}$ M (Figure 79b). Interestingly, the intensity of the emission band at 676 nm is increasing with the content of bisurea-$Cy_3$ in the mixture whereas the emission at 566 nm is decreasing and red-shifting. This increase in FRET between bisurea-$Cy_3$ and bisurea-$Cy_5$ provides evidence that intercalation of bisurea-$Cy_5$ occurs within a supramolecular polymer made of bisurea-$Cy_3$. Although all these experiments remain preliminary and require further analyses, they demonstrate that the use of our bisurea-fluorescent probes could be a valuable tool to evaluate the molecular arrangement and sef-sorting properties of our multifunctional co-self-assemblies.

Overall, we have shown that organized self-assemblies can be obtained by mixing bisurea-based monomers with different side chains and these lateral chains dictate the preferential organization of the supramolecular polymer. Additionally, social self-sorting occurs within well-defined structures, which give rise to multifunctional supramolecular copolymers.

# Chapter 3: Supramolecular polymers based on perylene bisimides (PBI)

## 1. Perylene bisimide-polyethylene glycol supramolecular polymer

As already mentioned in the bibliography section, most examples of perylene bisimide-polyethylene glycol supramolecular polymers have been studied in organic solvents, whereas only few studies have been performed in water or aqueous solutions. Additionally, the decoration of PBI units with simple polyethylene glycol monomethylether chains has not been reported to the best of our knowledge. In this work, we have studied such PBI-PEG molecules in various solvents and analysed the supramolecular behavior in water. We have also studied the influence of the length of the PEG chain and of the insertion of a hydroxylamine function instead of an amine one at the PBI core on the self-assembly process. However, most of our analyses showed that this variation of the PEG chain length and/or the use of PEG-hydroxylamine derivatives did not produce any major change in the supramolecular architecture (see section *a. v.*). Therefore, in the following parts of this chapter, we will focus on the PBI-PEG$_7$ molecules (**37**). $^1$H NMR, UV-Vis and fluorescence analyses for compounds **38**, **39** and **40** are reported in the Annexes section.

### a. Supramolecular polymers with PEG$_7$ side chains in D$_2$O and CD$_3$CN

#### *iv. $^1$H NMR spectra of PBI-PEG$_7$ in different solvents*

PBI-PEG$_7$ was initially characterized by $^1$H NMR in chloroform (Figure 80). The spectrum displays the expected set of signals which are well resolved, accounting probably for the absence of self-assembly. Accordingly, it should be noted that, in chloroform, chemical shifts corresponding to ① and ② are only slighty affected ($\Delta\delta \sim 0.1$ ppm) and not broadened over the whole range of concentration analyzed by $^1$H NMR ($10^{-2}$ M down to $5 \times 10^{-5}$ M). Integration of the NMR signals corresponding to the PEG chains is in accordance with the expected number of protons, considering that polydisperse PEG units have been used.

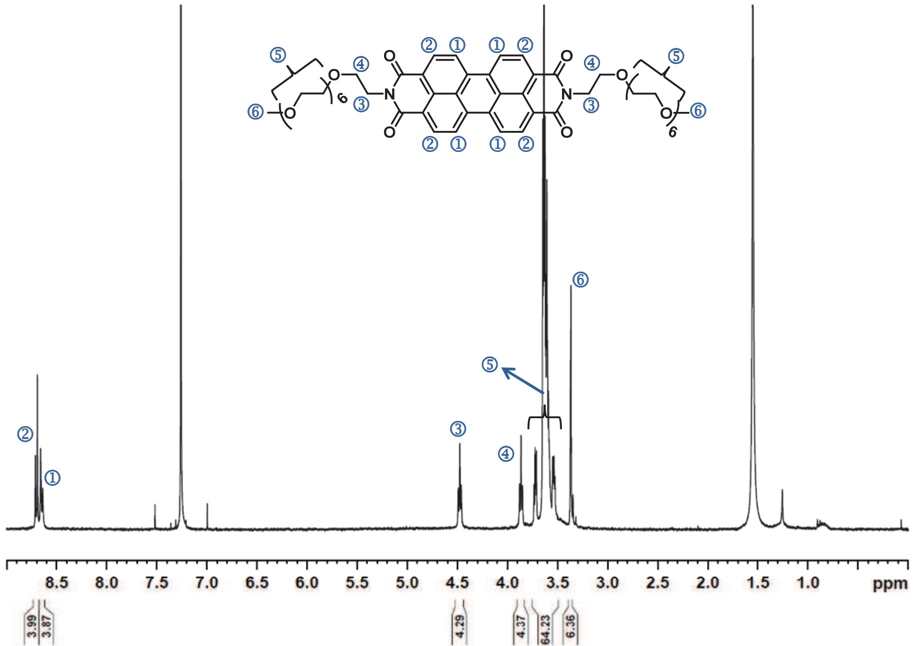

**Figure 80 |** $^1$H NMR spectra of PBI-PEG$_7$ at $10^{-3}$ M in CDCl$_3$.

This molecule was then studied in various solvents including chloroform, acetonitrile, methanol and water. In all solvents, PBI-PEG$_7$ displayed good solubility up to $10^{-2}$ M (~10.4 mg/cm$^3$) and the corresponding $^1$H NMR spectra are reported on Figure 81.

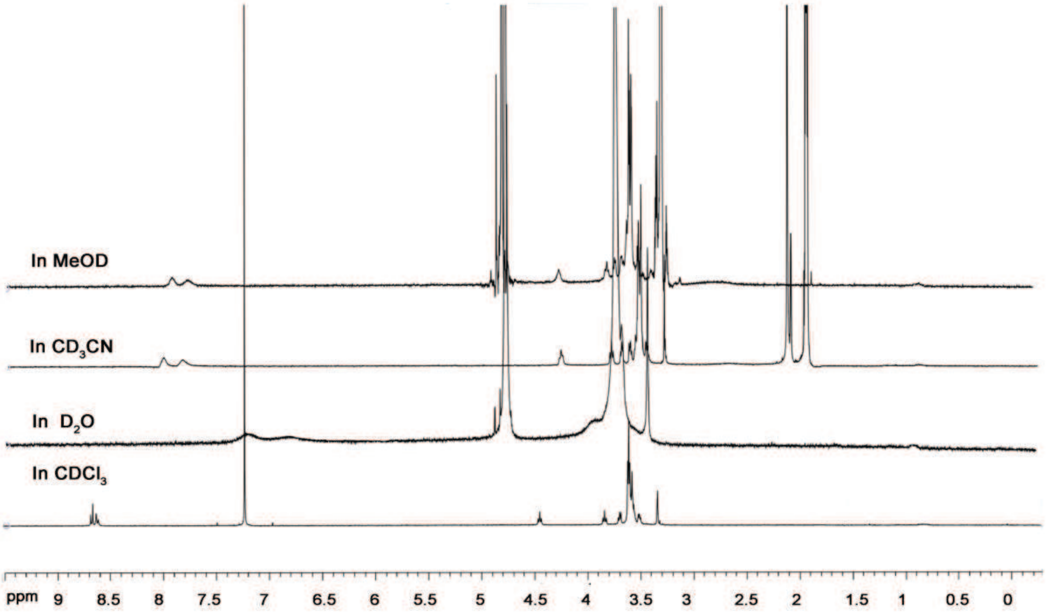

**Figure 81 |** $^1$H NMR spectra of PBI-PEG$_7$ in CDCl$_3$, MeOD, CD$_3$CN and D$_2$O at $10^{-3}$ M.

In all solvents except chloroform, signals corresponding to the protons of the PBI core along with proton ③ on the PEG chain are shifted high-field and become broad. In D$_2$O, protons ① and ② are particularly affected ($\Delta\delta > 1.5$ ppm) and all the signals corresponding to the PEG chains become broad. These observations clearly suggest the formation of supramolecular aggregagtes in acetonitrile, methanol and water. Whereas, in water, chemical shifts were not affected by concentration (they are broad all over the concentration range), chemical shifts of protons ①, ②, ③ and ④ showed high-field shifting with increasing concentration in $CD_3CN$ (Figure 82).

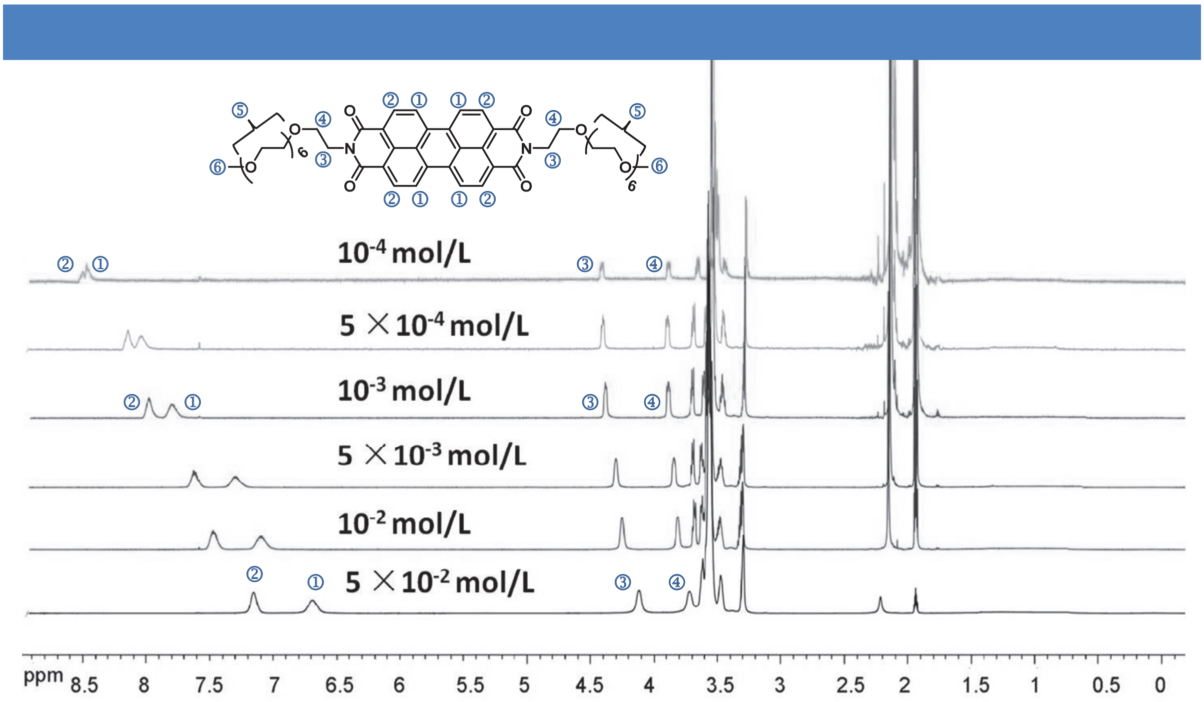

**Figure 82 |** $^1H$ NMR spectra of PBI-PEG$_7$ at different concentration ($10^{-4}$ to $5 \times 10^{-2}$ mol/L) in $CD_3CN$.

The chemical shift of proton ① is slightly more affected by concentration than the one of proton ②. This observation suggests that perylene cores are aggregated by π-π stacking interactions centered on the center of the perylene unit. Additionally, shifts of protons ③ and ④ to low-field with decreasing concentration indicate that PEG chains also participate in the aggregation of PBI-PEG units in acetonitrile. A similar behavior was also observed in methanol. Considering that aggregation processes of PBI molecules can be monitored by optical spectroscopies,[83] we performed UV-Vis and fluorescence experiments on this PBI-PEG$_7$ derivative in both acetonitrile and water.

### *v. UV-Vis experiments on PBI-PEG$_7$ in $CD_3CN$ and $D_2O$*

Suprinsingly, in acetonitrile, the UV-Vis spectral patern of PBI-PEG$_7$ showed the presence of non-aggregated monomeric units up to $10^{-5}$ mol/L (Figure 83a). Similar behaviors were also observed in methanol and chloroform.

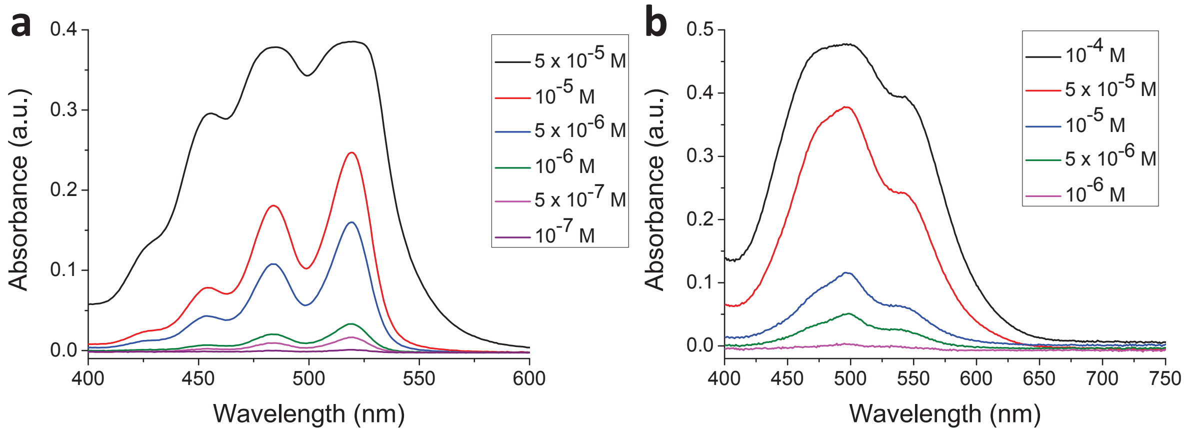

**Figure 83 |** a) UV-Vis spectra of a $CD_3CN$ solution of PBI-PEG$_7$ with concentrations ranging from $10^{-7}$ (purple) up to 5 × $10^{-5}$ mol/L (black); a) UV-Vis spectra of a $D_2O$ solution of PBI-PEG$_7$ with concentrations ranging from $10^{-6}$ (pink) up to $10^{-4}$ mol/L (black).

Indeed, for non-aggregated PBI molecules, UV-Vis spectra are characterized by three main absorption bands which correspond to the electronic transitions: $S_{0\text{–}0}$ at λ = 515-525 nm, $S_{0\text{–}1}$ at λ = 470-480 nm and $S_{0\text{–}2}$ at λ = 440-460 nm. Typically, their intensities follow the order $S_{0\text{–}0} > S_{0\text{–}1} > S_{0\text{–}2}$.[129] In acetonitrile, up to $10^{-6}$ M, the UV-Vis absorption spectrum of PBI-PEG$_7$ diplays the 3 main transitions at 454, 484 and 519 nm, the latter being the most intense. These observations suggest that self-assembly does not occur in acetonitrile up to $10^{-6}$ M. Additional experiments at higher concentration have been performed but result in a saturation of the detector as already observed at 5 × $10^{-5}$ mol/L (Figure 83a, black curve). In order to confirm the self-assembly of this molecule at higher concentration as it was suggested by $^1$H NMR experiments, measurements should be performed with cuvettes with lower path lengths (less than 5 mm). This work still requires to be performed.

In water, UV-Vis absorption spectra displayed very different absorption profiles over the whole range of concentration screened (Figure 83b) and the non-aggregated absorption pattern was not observed even at low concentration (down to $10^{-6}$ M). Three main absorbance bands can be seen at 470 (shoulder peak), 498 and 545 nm and the absorption band at 498 nm, which corresponds to the $S_{0\text{–}1}$ electronic transition, was the most intense over the whole range of concentration recorded. This shift of the maximum of absorption to lower wavelengths compared to the monomers denotes the formation of H-aggregates. Compared to acetonitrile, the aggregation of PBI-PEG$_7$ in water occurs at very low concentration ($10^{-6}$ M). Here again, experiments at higher concentration (>$10^{-4}$ mol/L) should be performed in cuvettes with lower path lengths in order to determine if PBI-PEG$_7$ aggregation occurs through a single or multiple type of stacking depending on the concentration. Such behavior was recently reported by Islam and Sundararajan on amphiphilic PBI molecules.[142]

### *vi. Fluorescence experiments on PBI-PEG$_7$ in CD$_3$CN and D$_2$O*

Similarly to UV-Vis experiments, we also recorded the fluorescence spectra of PBI-PEG7 as a function of concentration in either acetonitrile or water (Figure 84).

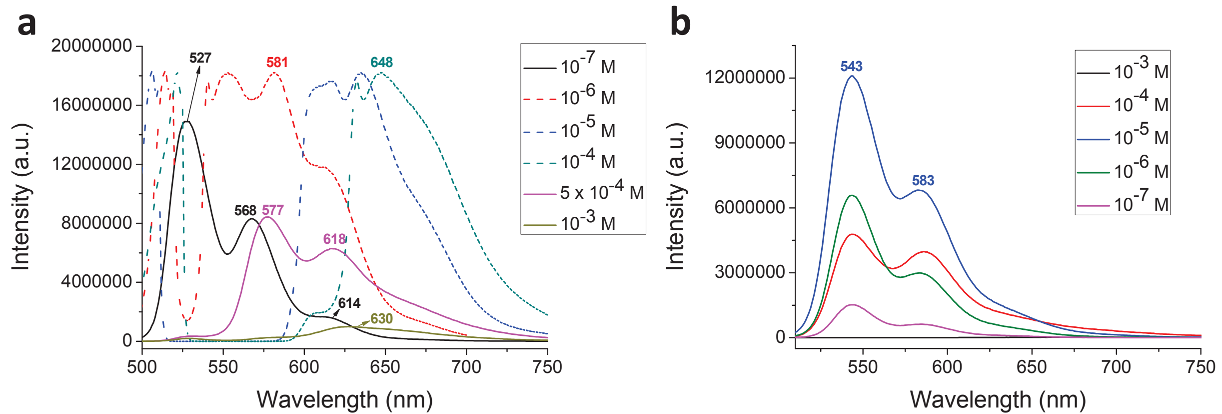

**Figure 84 |** a) Fluorescent spectra of PBI-PEG$_7$ in CD$_3$CN for concentrations ranging from 10$^{-7}$ mol/L (black) up to 10$^{-3}$ mol/L (green yellow), $\lambda_{ex}$=483 nm; b) Fluorescent spectra of PBI-PEG$_7$ in D$_2$O for concentrations ranging from 10$^{-7}$ mol/L (pink) up to 10$^{-3}$ mol/L (black), $\lambda_{ex}$=498 nm.

In acetonitrile, upon excitation at 483 nm, three emission bands at 527, 568 and 614 nm are recorded for the sample at 10$^{-7}$ M. Interestingly, in the concentration range between 10$^{-6}$ and 10$^{-4}$ M, a broadening of the fluorescence spectrum along with a large bathochromic shift of the maximum of emission ($\Delta\lambda_{max}$ > 120 nm between 10$^{-7}$ and 10$^{-4}$ M) is observed with increasing concentration. Although this behavior is unexpected and was observed for several perylene derivatives (*vide infra*), it has been reported to be the signature of the 0→3 transition and could arise from the formation of oligomers as reported by Li and coworkers.[211] However, at 5 × 10$^{-4}$ M, the emission is blue-shift and strongly decreased compared to the emission at 10$^{-4}$ M with two maximum emission observed to 577 and 618 nm. In that case, the maximum of absorption at 577 nm suggests a 0→2 transition and the decrease in intensity probably indicates the aggregation of the PBI units in polymers. At 10$^{-3}$ M, the spectrum becomes broad with a shapeless emission band from ~600 to 720 nm and reduced fluorescence intensity. These observations support the formation of aggregates through π-π stacking at high concentration in acetonitrile as already demonstrated by $^1$H NMR. Additionally, the various changes in emission probably indicate the formation of several kinds of self-assembly as a function of the concentration. Further work will be dedicated to elucidate the possible

---

[211] a) Wang, W.; Li, L.-S.; Helms, G.; Zhou, H.-H.and Li, A. D. Q. To Fold or to Assemble? *J. Am. Chem. Soc.* **2003**, *125*, 1120-1121; b) Li, A. D. Q.; Wang, W. and Wang L.-Q. Folding versus Self-Assembling. *Chem. Eur. J.* **2003**, *9*, 4594-4601.

structural rearrangement as a function of the concentration.

In water, a different behavior was observed. Upon excitation at 498 nm, for concentration ranging from $10^{-7}$ to $10^{-4}$ mol/L, two emission bands at 544 nm and 585 nm can be identified (Figure 84b). At $10^{-4}$ mol/L, a broadening of the spectra is observed at higher wavelength (620 to 750 nm) and the band at 544 nm decreases faster than the one at 585 nm. At $10^{-3}$ mol/L, the fluorescence is almost quenched over the whole spectral range with a small band with low intensity remaining at high wavelength (674 nm). This enhancement of the fluorescence at higher wavelength upon increasing concentration was recently ascribed to the formation of H-type aggregates.[142] Spectroscopic differences observed for PBI-PEG$_7$ in acetonitrile and water suggest that two different kinds of aggregates are formed.

Whereas PBI-PEG$_7$ has been fully characterized in water using scattering techniques (*vide infra*), its characterization in acetonitrile was more challenging as, for light scattering, we encountered some problems due to the absorption of the laser beam ($\lambda$ = 632.8 nm) by the sample at $10^{-3}$ M. SANS experiments have been performed recently and remain to be analyzed. Briefly, the overall behavior shows a) a low-q regime ($q < 10^{-2}$ Å$^{-1}$) in which the q-dependence of the data can be described by a power law with the exponent close to -3; b) a Guinier regime at intermediate q and c) a $q^{-2}$ domain at high q values. Further imaging of PBI-PEG$_7$ in acetonitrile is also on going.

## b. PBI-PEG$_7$ supramolecular polymers in aqueous solutions

### *i. $^1$H NMR spectra of PBI-PEG$_7$ in various aqueous solutions*

Inspired by the work of Wurthner,[137] we then studied the self-assembly of PBI-PEG$_7$ in aqueous solutions containing various percentage of either THF, methanol or acetonitrile. Initially, this self-assembly was studied by $^1$H NMR at 40% water (Figure 85). In all solvent systems, signals corresponding to protons ① and ② of the PBI core become broader and are down-shifted compared to the solution in $D_2O$, suggesting that the association of PBI cores is weaker in aqueous solutions than in pure $D_2O$. In MeOD and $CD_3CN$ mixtures, chemical shifts of these protons are slightly high-field shifted compared to the corresponding pure organic solvents. In THF, these signals merge into a broad single one at ~8.3 ppm. At 40% water, these observations suggest that $\pi$-$\pi$ stacking that induces the formation of supramolecular aggregates is stronger in the methanol mixture compared to the acetonitrile one, the weaker one being the THF mixture.

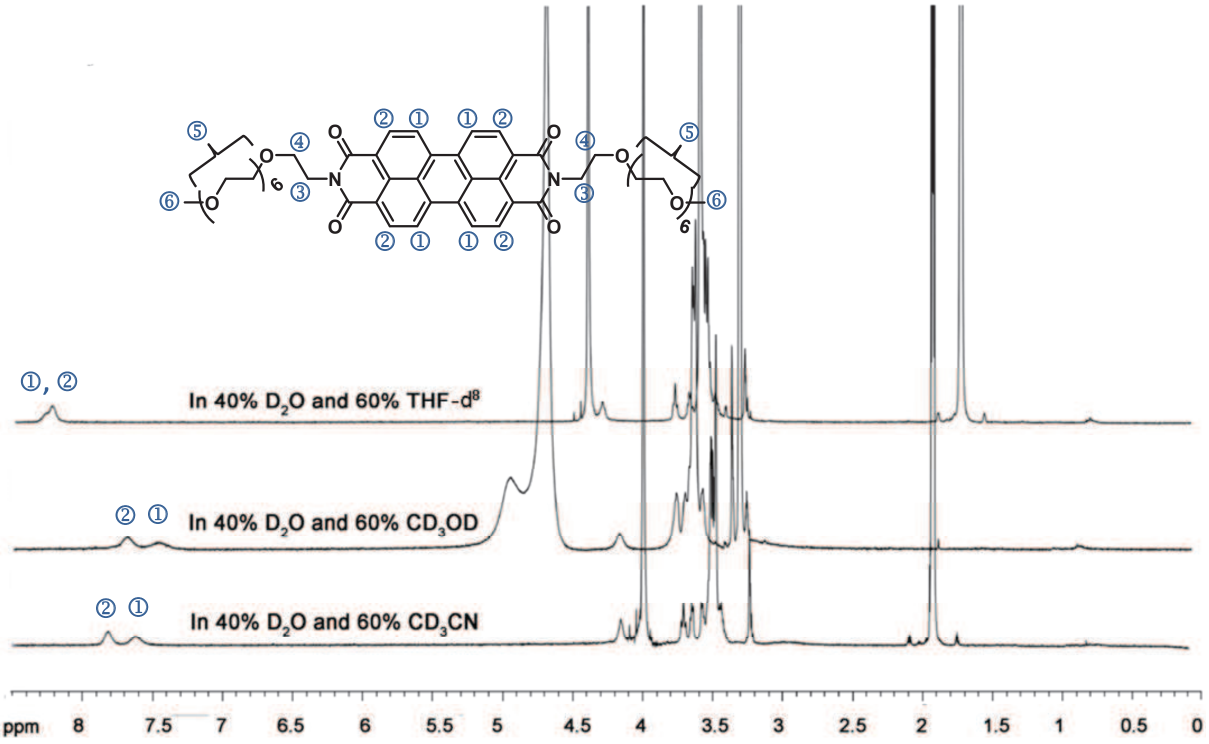

**Figure 85 |** $^1$H NMR spectra of PBI-PEG$_7$ at $10^{-3}$ M in three solvent mixtures containing 40% $D_2O$ ($D_2O$/THF-d$^8$, $D_2O$/MeOD and $D_2O/CD_3CN$).

### ii. UV-Vis experiments on PBI-PEG$_7$ in $H_2O$/THF mixtures

We further studied this self-assembly in mixtures of solvents using various UV-Vis experiments (Figure 86). We particularly focused on water/THF mixtures but the same approach can be applied to water/methanol and water/acetonitrile mixtures (*vide infra*).

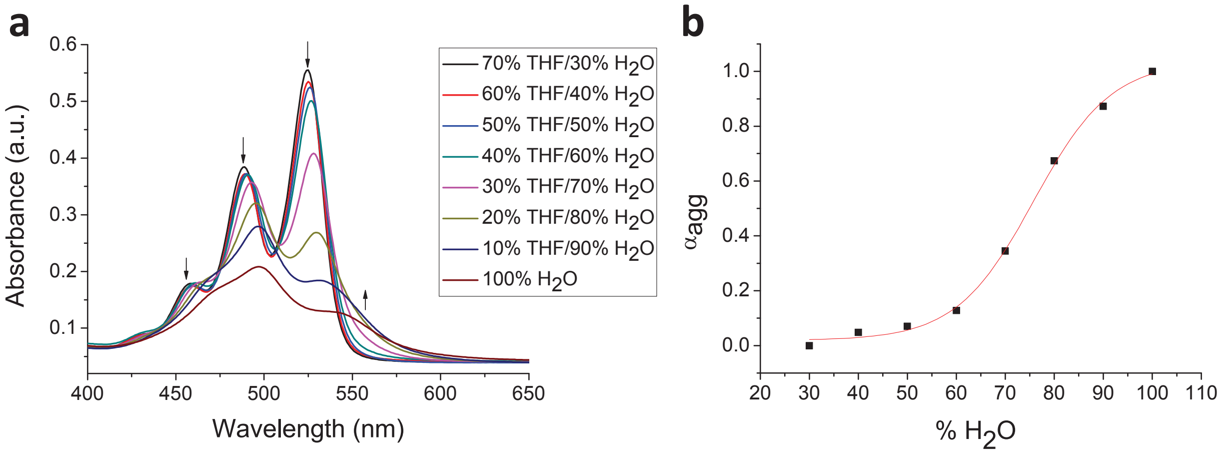

**Figure 86 |** a) Solvent-dependent UV-Vis absorption spectra of PBI-PEG$_7$ in various $H_2O$/THF mixtures ranging from 70% THF/30% $H_2O$ to 100% $H_2O$ at $10^{-5}$ M and room temperature. Arrows indicate the spectral changes upon increasing the amount of $H_2O$ (from 30% to 100%); b) Plot of $\alpha_{agg}$ as a function of solvent composition ($H_2O$/THF) for PBI-PEG$_7$. The sigmoidal fit for the data points were obtained by using the Boltzmann function.

The self-assembly of PBI-PEG$_7$ in different water/THF mixtures was examined by UV-Vis spectroscopy and the corresponding absorption spectra are reported on Figure 86a. As THF is known to be a good solvent for the $\pi$ system of PBI dyes,[137] the dyes did not form aggregates for high THF contents at $10^{-5}$ M. Indeed, for a 70:30 THF/$H_2O$ ratio, a well-resolved vibronic structure ranging from 440 to 570 nm and characteristic of isolated PBI chromophores is observed. In contrast, at high volume ratios of $H_2O$ in THF, the loss of a fine vibronic structure suggest that aggregation occurs, confirming that $H_2O$ is a bad solvent for the $\pi$ system of PBI. The most prominent spectral changes concern a reduction in the peak intensity along with a significant blue-shift of the absorption maximum and the appearance of a new peak at 550 nm with a non-negligible intensity. At 80% $H_2O$ in THF, the absorption band corresponding to the $S_{0-1}$ transition (488 nm) becomes more intense than the one at 525 nm. This intensity reversal along with the hypsochromic evolution of the maximum absorption suggests the enhanced formation of face-to-face $\pi$ stacks, i.e. H-aggregates of PBI chromophores.

In order to quantify the propensity for $\pi$-stack formation of PBI-PEG$_7$ in $H_2O$/THF mixtures, we have estimated the mole fraction of aggregated dyes ($\alpha_{agg}$) at different $H_2O$ contents from the solvent-dependent UV-Vis studies by the following equation:

$$\alpha_{agg} \approx \frac{A_{mix}-A_{mon}}{A_{agg}-A_{mon}} \qquad \text{(eqn 5)}$$

with $A_{mix}$ corresponding to the absorbance at 525 nm in a given solvent mixture, and $A_{mon}$ and $A_{agg}$ denoting the absorbance at 525 nm at the lowest (30%) and highest (100%) $H_2O$ content in THF, respectively. The calculated $\alpha_{agg}$ values for PBI-PEG$_7$ were then plotted as a function of the solvent composition (Figure 86b). The critical solvent composition for which the mole fraction of aggregate corresponds to 0.5 ($\alpha_{50}$) was estimated at 74% water in THF.

We then probed the self-assembly of PBI-PEG$_7$ as a function of temperature in a 20:80 THF/$H_2O$ solvent mixture. For this solvent composition, at 283 K (10 °C), a mostly self-assembled structure is observed and the evolution of the absorption spectra as a function of temperature was recorded (Figure 87a).

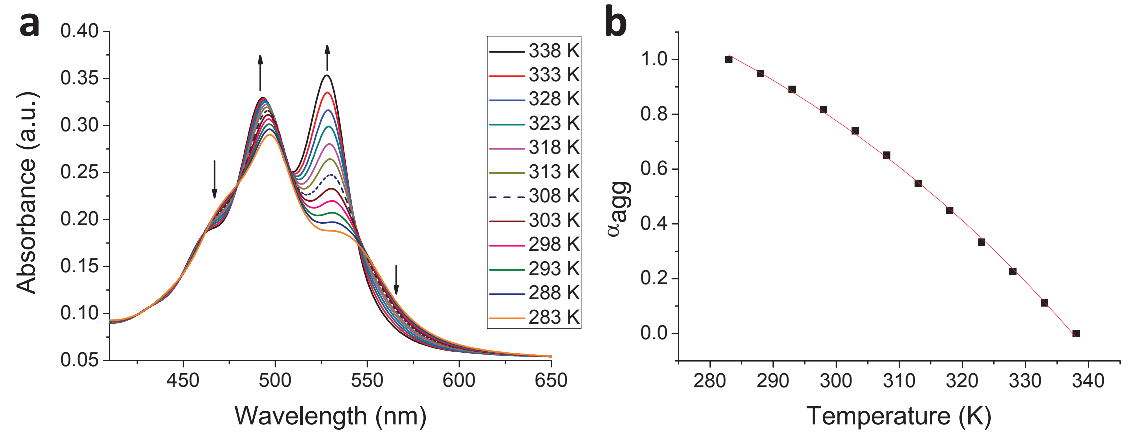

**Figure 87 |** a) Temperature-dependent UV-visible absorption spectra of PBI-PEG$_7$ in $H_2O$/THF mixture (80:20) at a concentration of 1 × $10^{-5}$ M. Arrows indicate the spectral changes with an increasing temperature from 283 K up to 338 K; b) Plot shows the mole fraction of aggregate ($\alpha_{agg}(T)$) as a function of temperature.

With increasing temperature, the absorption above 550 nm gradually decreases. At elevated temperature, the broad band becomes structured with resolved peaks at 492 and 528 nm and the absorbance intensity reversal ($A_{528} > A_{492}$) happens at 328 K (55 °C). All these observations suggest conversion of the aggregated structure to the monomeric dye above 55°C. Additionally, solutions of PBI-PEG$_7$ in 20:80 THF/$H_2O$ were slowly cooled down from 338 to 283 K to ensure that self-assembly took place under thermodynamic control. For this cooling rate no hysteresis in the absorption was observed when heating the solution again to 338 K, which indicated that the self-assembly process was reversible. Temperature-dependent UV/Vis spectral data were then used to determine the self-assembly mechanism of PBI-PEG$_7$ in the 80:20 $H_2O$/THF mixture (Figure 87b). We first considered the simplest self-assembling model, namely the isodesmic or equal-K model, which is often used for perylene self-assembly.[16,83] This model assumes that all equilibrium constants or Gibbs free energy changes are equal for every binding event. The mole fraction of aggregate at each temperature ($\alpha_{agg}(T)$) was estimated according to the following equation:

$$\alpha_{agg}(T) \approx \frac{A\,(T)-A_{mon}}{A_{agg}-A_{mon}} \qquad \text{(eqn 6)}$$

in which $A(T)$, $A_{mon}$, and $A_{agg}$ are the absorbance at 528 nm for the solution at temperature T, the monomer (i.e. at T = 338 K), and the pure aggregate solutions (i.e. at T = 283 K), respectively. The $\alpha_{agg}$ (T) values were plotted as a function of temperature. Applying the isodesmic model to our temperature-dependent experiments, the fraction of aggregated species ($\alpha_{agg}$) can by expressed by equation (22) in which $\Delta H$ is the enthalpy release, $R$ is the ideal gas constant and $T_m$ is the melting temperature, that is, the temperature for $\alpha_{agg}(T)=0.5$.[212]

$$\alpha_{agg}(T) \approx \frac{1}{1+e^{-0.908\Delta H\frac{T-T_m}{RT_m^2}}} \qquad \text{(eqn 7)}$$

By applying equation (7) to the spectral changes of PBI-PEG$_7$, we noticed that the data points corresponding to $\alpha_{agg}$ as a function of temperature at $10^{-5}$ M could not be fitted satisfactorily, indicating that the self-assembly process does not follow the isodesmic model. Therefore we considered a cooperative process also described as the nucleation-elongation mechanism (see Bibliography – Chapter 1). For the analysis of cooperativity, we have used the nucleation-elongation model developed by Meijer and Schenning.[212a] In the elongation regime, the fraction of aggregated species ($\alpha_{agg}$) can be defined by equation (8) in which $\Delta H_e$ is the enthalpy corresponding to the aggregation (elongation) process, $T$ the absolute temperature, $T_e$ the elongation temperature, $R$ the ideal gas constant and $\alpha_{SAT}$ is a parameter introduced to ensure that $\alpha_{agg}/\alpha_{SAT}$ does not exceed unity.

$$\alpha_{agg}(T) = \alpha_{SAT}\left(1 - exp\left[\frac{-\Delta H_e}{RT_e^2}(T - T_e)\right]\right) \qquad \text{(eqn 8)}$$

By using equation 8, we could accurately fit the experimental data to the elongation regime (Figure 87b) with an $R^2=0.99907$. At the given concentration of $10^{-5}$ M, the enthalpy release during the self-assembly of PBI-PEG$_7$ in the elongation process ($\Delta H_e$) and the elongation temperature ($T_e$) were calculated to be -13.18 kJ.mol$^{-1}$ and 337.46 K, respectively (see Table 2).

**Table 2 |** Thermodynamic parameters $T_e$, $\Delta H_e$ and $\alpha_{SAT}$ obtained from the temperature-dependent UV/Vis experiments of PBI-PEG$_7$ in THF/H$_2$O (20:80) on the basis of the modified nucleation-growth model.

| | C [mol/L] | $\alpha_{SAT}$ | $T_e$ [K] | $\Delta H_e$ [kJmol$^{-1}$] |
|---|---|---|---|---|
| PBI-PEG$_7$ | $10^{-5}$ | 1.91009 | 337.46 | -13.18 |

However, in the range of temperature screened during this experiment, we could not observe the nucleation regime and therefore, we could not determine the dimensionless equilibrium constant K$_a$ of the activation step at the elongation temperature nor the number-averaged degree of polymerization $\langle N_n \rangle$ of the elongation regime which depends on K$_a$.

---

[212] a) Smulders, M. M.; Nieuwenhuizen, M. M. L.; De Greef, T. F. A.; Van der Schoot, P.; Schenning, A. P. H. J.; Meijer, E. W. How to Distinguish Isodesmic from Cooperative Supramolecular Polymerisation *Chem. Eur. J.* **2010**, *16*, 362–367; b) Fernández, G.; Stolte, M.; Stepanenko, V. and Würthner, F. Cooperative Supramolecular Polymerization comparison of different models applied to the self-assembly of Bis(merocyanine) dyes. *Chem. Eur. J.* **2013**, *19*, 206–217

### *iii. UV-Vis experiments on PBI-PEG$_7$ in $H_2O/CH_3CN$ and $H_2O/CH_3OH$ mixtures*

We also studied the self-assembly of PBI-PEG$_7$ in different water/acetonitrile and water/methanol mixtures by UV-Vis spectroscopy and the corresponding absorption spectra are reported on Figure 88a and c. Both solvent mixtures display very similar patterns upon increasing the water content.

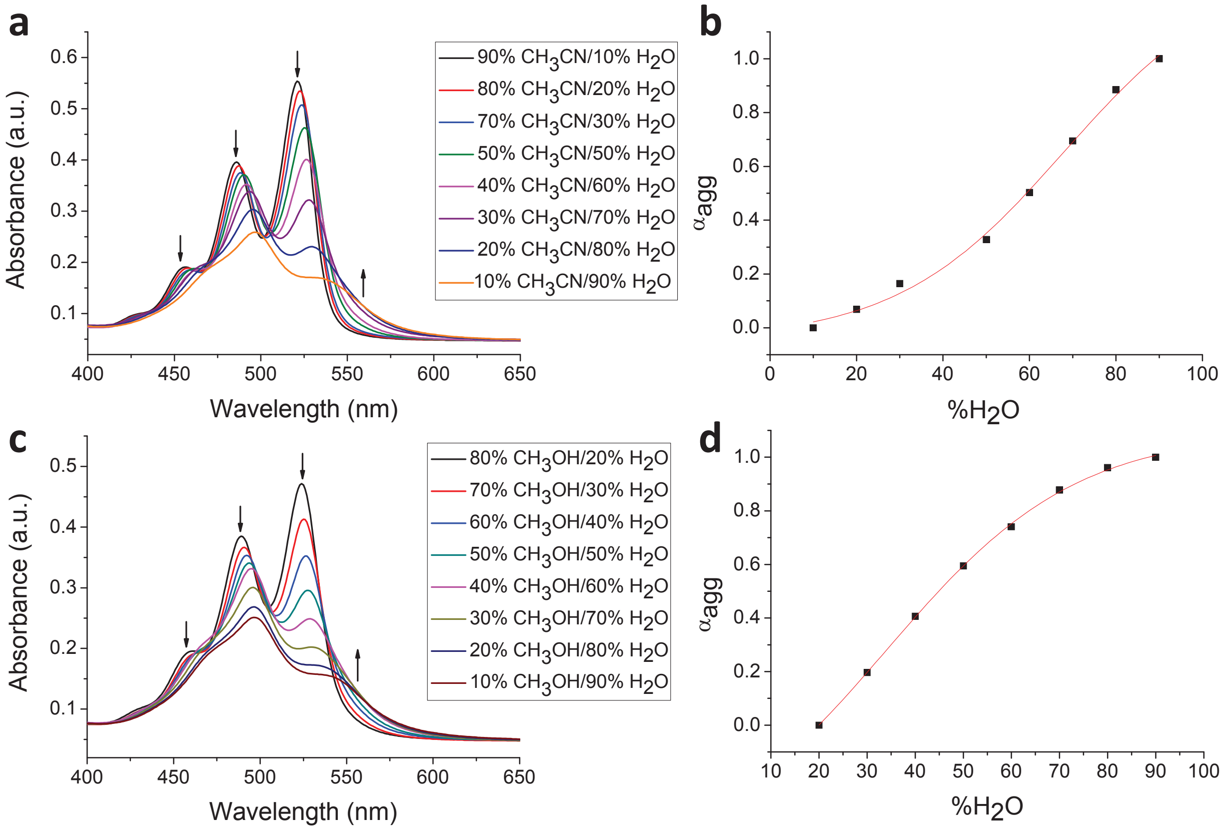

**Figure 88 |** a) UV-Vis spectra of PBI-PEG$_7$ ($10^{-5}$ M) in $CH_3CN/H_2O$ at different $H_2O$ ratio; b) Plot of $\alpha_{agg}$ as a function of solvent composition ($H_2O/CH_3CN$) for PBI-PEG$_7$. The sigmoidal fit for the data points were got by using the Boltzmann function. c) UV-Vis spectra of PBI-PEG$_7$ ($10^{-5}$ M) in $CH_3OH/H_2O$ at different $H_2O$ ratio; d) Plot of $\alpha_{agg}$ as a function of solvent composition ($H_2O/CH_3OH$) for PBI-PEG$_7$. The sigmoidal fit for the data points were gained by adopting the Boltzmann function.

For high $CH_3CN$ or $CH_3OH$ contents at $10^{-5}$ M, the dyes did not form aggregates confirming that $CH_3CN$ or $CH_3OH$ are good solvents for the π system of PBI dyes. Indeed, for a 90:10 $CH_3CN/H_2O$ ratio, a well-resolved vibronic structure going from 440 to 570 nm and characteristic of isolated PBI chromophores is observed. A similar observation was made for a 80:20 $CH_3OH/H_2O$ ratio. In contrast, at high volume ratios of $H_2O$ in either $CH_3CN$ or $CH_3OH$, the loss of a fine vibronic structure suggests that aggregation occurs, confirming that $H_2O$ is a bad solvent for the π system of PBI. For both solvent mixtures, the most prominent spectral changes concern a reduction in the peak intensity along with a significant blue-shift of the absorption maximum and the appearance of a new peak appeared at 550 nm with a non-negligible intensity. At 70% $H_2O$ in $CH_3CN$, the absorption band corresponding to the $S_{0\text{-}1}$ transition (486 nm) becomes more intense than the one at 521 nm. For 40% $H_2O$ in $CH_3OH$, a similar intensity reveal occurs. In both solvent mixtures, intensity reversal along with hypsochromic evolution of the maximum absorption suggests the enhanced formation of H-aggregates of PBI-$PEG_7$ molecules.

Using equation (5), we also quantified the propensity for π-stack formation of PBI-$PEG_7$ in $H_2O/CH_3CN$ and $H_2O/CH_3OH$ mixtures (Figure 88b and d). The critical solvent composition for which the mole fraction of aggregate corresponds to 0.5 ($\alpha_{50}$) was estimated at 60% water in $CH_3CN$ and 44% water in $CH_3CN$ (Table 3).

**Table 3 |** The $\alpha_{50}$ (% of $H_2O$ in mixture solvent at which the $\alpha_{agg}$ value is 0.5) of PBI-$PEG_7$ in THF/$H_2O$, $CH_3OH/H_2O$ and $CH_3CN/H_2O$ (with different ratio) respectively.

| | in THF/ $H_2O$ | in $CH_3CN/H_2O$ | in $CH_3OH/H_2O$ |
|---|---|---|---|
| $\alpha_{50}$ (% of $H_2O$) | 74 | 60 | 44 |

These UV-Vis experiments support the $^1H$ NMR observations that, at 40% water, aggregation is stronger in the methanol mixture compared to the acetonitrile and the THF one, the latter being the weaker.

### *iv. Fluorescence experiments onPBI-PEG$_7$ in $H_2O$/THF mixtures*

We also monitored the fluorescence of solutions of PBI-$PEG_7$ in various $H_2O$/THF mixtures (Figure 89).

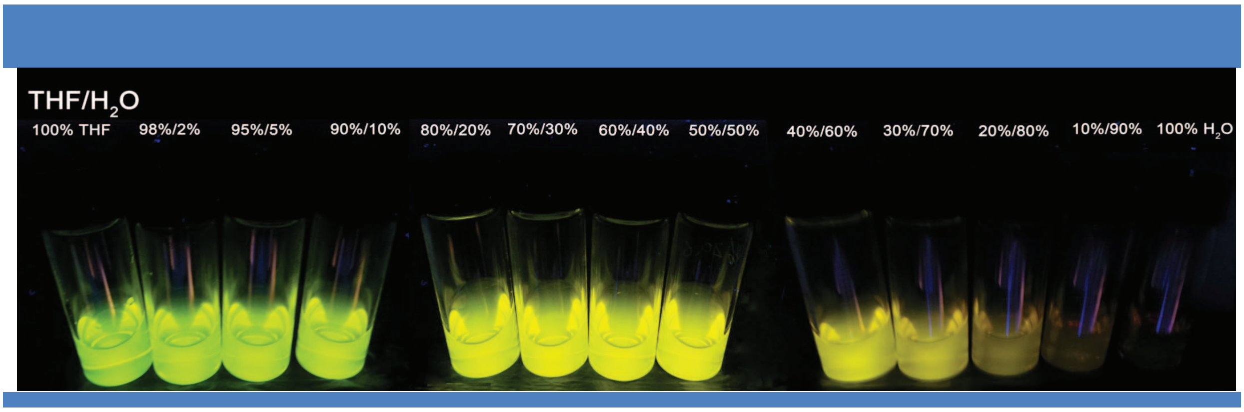

**Figure 89 |** Fluorescent picture of PBI-$PEG_7$ in $H_2O$/THF mixture solvents for different percentage of $H_2O$ (from 0%to 100%).

Qualitatively, from a simple excitation experiments using a UV lamp ($\lambda_{ex}$ = 363 nm), we could observe that these solutions change from green, to yellow and red with increasing of the water content of THF. This experiment provides evidence that PBI-$PEG_7$ gradually self-assembles with increasing ratio of water in $H_2O$/THF mixture. This also supports the previous UV-Vis experiments. We also monitored the fluorescence spectra of these solutions at different ratios of $H_2O$ in THF using the spectrofluorimeter (Figure 90).

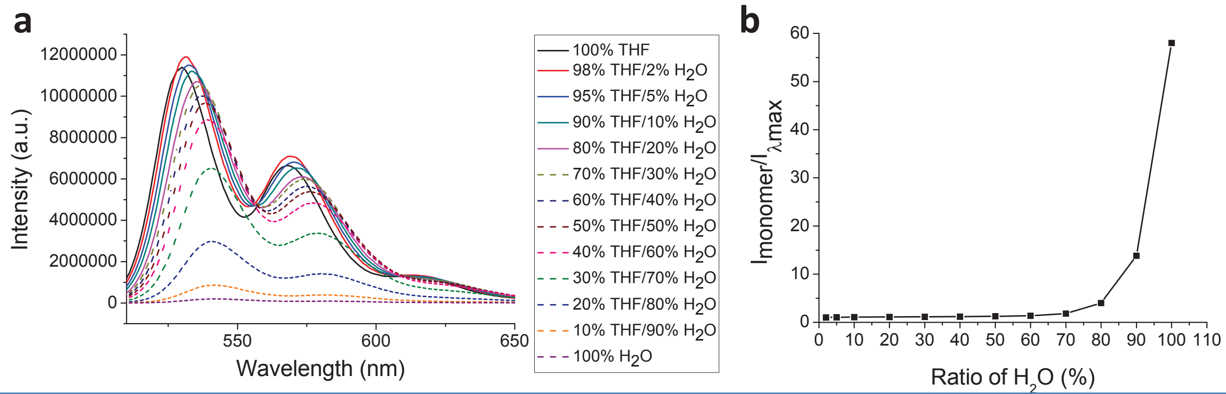

**Figure 90 |** a) Fluorescence spectra of PBI-PEG$_7$ ($10^{-5}$ M) for different ratio of $H_2O$ in THF (from 0% $H_2O$ to 100% $H_2O$); b) Change in fluorescence intensity with increasing $H_2O$ contents.

With increasing water contents, the fluorescent spectra of PBI-PEG$_7$ is bathrochomically shifted and reduction of fluorescent intensity occurs at water content higher than 80%. The reduction of fluorescence intensity is due to the formation of aggregates via strong π–π interaction and the quenching at higher concentration can be explained as photo-induced electron transfer within the aggregates of higher order.[213] Additionally, the ratio between the maximum intensity of the monomer (i.e. for 100% THF) and the intensity at $\lambda_{max}$ at different water contents provide qualitative information on the propensity of self-assembly as a function of the ratio of water (Figure 90b). This plot indicates that aggregation becomes stronger for water content above 70%, which is in good agreement with the $\alpha_{50}$ value calculated previously.

We also performed these fluorescence experiments on PBI-PEG$_7$ in $CH_3OH/H_2O$ and $CH_3CN/H_2O$ mixtures and similar behaviors were observed (Figure 91a and b). Namely, bathochromic evolution of the fluorescence was observed with increasing water contents along with reduction of fluorescence intensity. These observations can be supported by the same arguments as proposed for the self-assembly in THF. The evolution of $I_{monomer}/I_{\lambda max}$ as a function of ratio of water in organic solvent was also monitored. Similarly to THF/$H_2O$ mixtures, good correlations could be established with $\alpha_{50}$ values calculated in either $CH_3OH/H_2O$ or $CH_3CN/H_2O$ mixtures. Comparison of the three plots confirm the trend

---

[213] (a) He, X.; Liu, H.; Li, Y.; Liu, Y.; Lu, F.; Li, Y. and Zhu, D. A New Copolymer Containing Perylene Bisimide and Porphyrin Moieties: Synthesis and Characterization. *Macromol.Chem. Phys.* **2005**, *206*, 2199–2205; (b) Balakrishnan, K.; Datar, A.; Naddo, T.; Huang, J.; Oitker, R.; Yen, M.; Zhao, J. and Zang, L. Effect of Side-Chain Substituents on Self-Assembly of Perylene Diimide Molecules:□ Morphology Control. *J. Am. Chem. Soc.* **2006**, *128*, 7390–7398.

observed using the $\alpha_{50}$ value, i.e. the aggregation is stronger in $CH_3OH/H_2O$ than in $CH_3CN/H_2O$ and in $THF/H_2O$ mixture for a given water content. This plot $I_{monomer}/I_{\lambda max}$ (%$H_2O$), which does not require any mathematical treatment, provide a good approximation of $\alpha_{50}$ values for our system. It could possibly be extended to other supramolecular fluorescent aggregates.

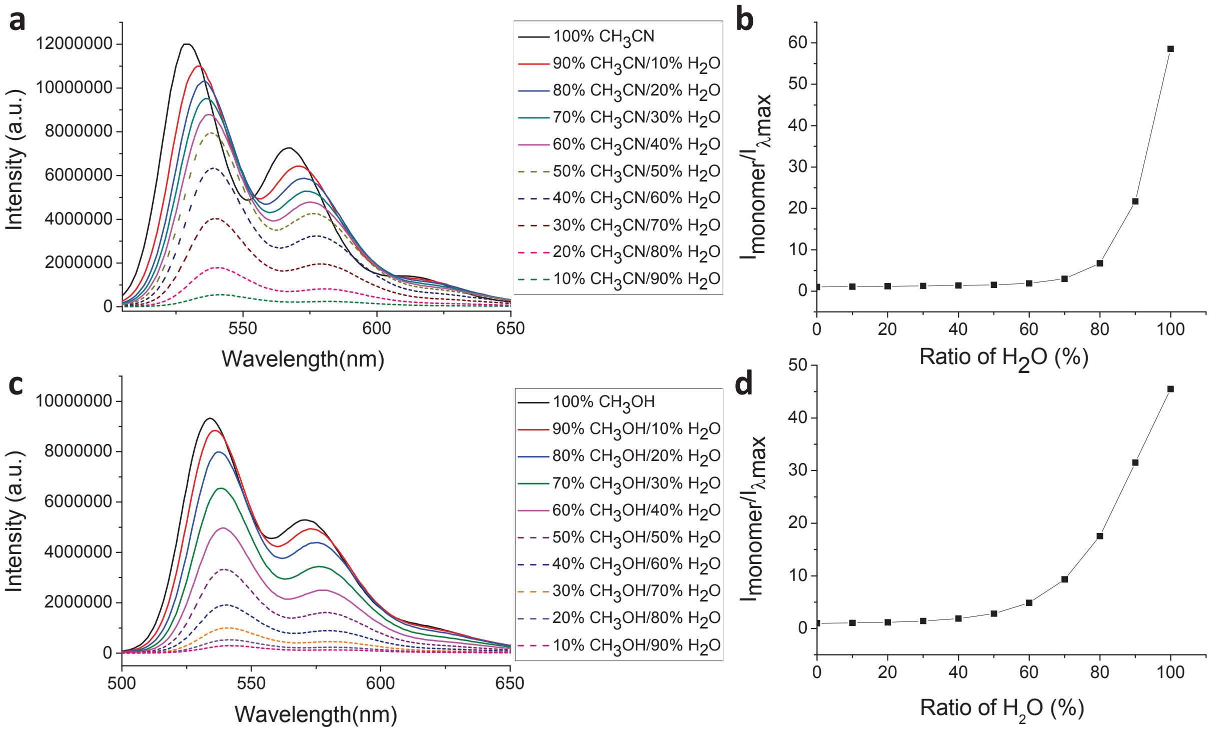

**Figure 91 |** a) Fluorescence spectra of PBI-PEG$_7$ ($10^{-5}$ M) for different $H_2O$ ratio in $CH_3CN$ (from 0% $H_2O$, to 100% $H_2O$); a) Fluorescence spectra of PBI-PEG$_7$ ($10^{-5}$ M) for different $H_2O$ ratio in $CH_3OH$ (from 0% $H_2O$, to 100% $H_2O$); c) Change in fluorescence intensity of PBI-PEG$_7$ ($10^{-5}$ M) in $H_2O/CH_3CN$ mixtures with increasing $H_2O$ contents; d) Change in fluorescence intensity of PBI-PEG$_7$ ($10^{-5}$ M) in $H_2O/CH_3OH$ mixtures with increasing $H_2O$ contents.

Overall, using a combination of optical spectroscopies, we have demonstrated that, in polar media made of water and polar organic solvents, PBI-PEG$_7$ self-assembles in H-aggregates, which are characterized by their weak fluorescence. This self-assembly follows a cooperative mechanism but our experiments did not permit the observation of the nucleation step and therefore precluded the calculation of the number-averaged degree of polymerization. Additional experiments at higher temperature should be performed in order to possibly oberve this nucleation regime.

## c. Structural study of PBI-PEG$_7$ and PBI-OPEG$_{16}$ supramolecular polymers in D$_2$O

### *i. Molecular conformation of PBI-PEG self-assemblies*

First, we focused on the structural properties of dilute aqueous solutions of amphiphilic perylene diimides PBI-PEG compounds which readily solubilized in water. First, we checked if the presence of an oxygen atom between the perylene core and the grafted PEG had an influence on the structural behavior of the self-assemblies, by comparing compound **37** with **38** and compound **39** with **40** (Figure 92). It can be seen from this figure that there is almost no difference in SANS scattering for PBI compounds with identical PEG chain length. Therefore, in the following sections, we will only focus on compounds **37** and **40**.

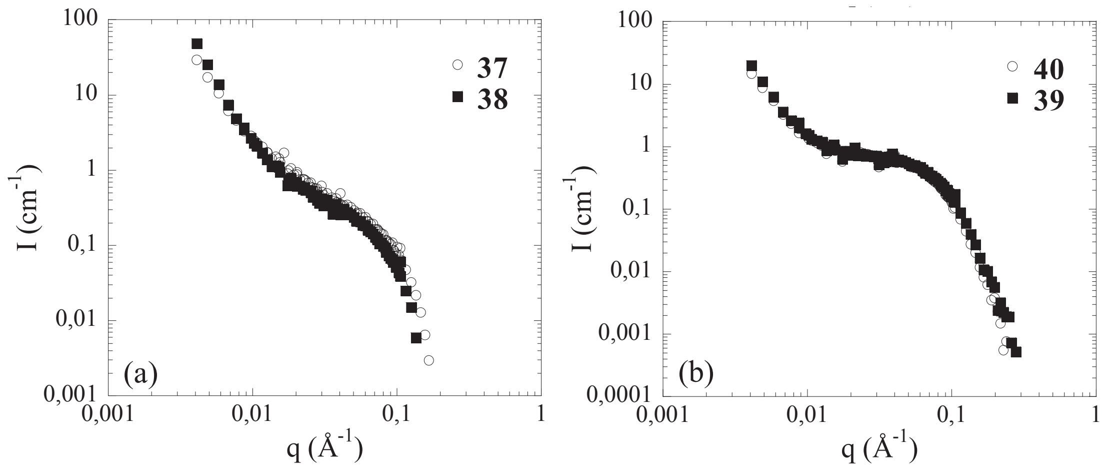

**Figure 92 |** SANS Scattering intensity as a function of q for compounds **37** and **38** (a) and **39** and **40** (b) at C=10 mM and T=21°C.

### ***Overall Molecular Conformation***

After solubilization of **37** and **40**, both systems appear as monophasic, non-viscous, slightly red-colored, and limpid solutions over the whole investigated concentration range (from $10^{-4}$ g/cm$^3$ to $5 \times 10^{-2}$ g/cm$^3$). In this concentration domain, the normalized field autocorrelation function, $g^{(1)}(q,t)$, can be described by a single exponential relaxation for both systems. Variations of $1/\tau q^2$ with $q^2$ show clearly that the single mode is a diffusive mode with a characteristic relaxation time $\tau$ inversely proportional to $q^2$. The slight increase of $1/\tau q^2$ with $q^2$ observed for some samples depends on the polydispersity and the structure of the scattered objects.[214] The extrapolation of $(\langle\tau\rangle q^2)^{-1}$ to $q^2=0$ gives the apparent diffusion coefficient, $D_{app}$,

---

[214] Sedlàk, M. and Amis, E. J. Dynamics of moderately concentrated salt-free polyelectrolyte solutions: Molecular weight dependence. *J. Chem. Phys.* **1992**, *96*, 817-825.

leading to the apparent hydrodynamic radius, $R_{H,app}$ using the Stokes-Einstein relation (see Bibliography – Chapter 1). The concentration evolution of $R_{H,app}$ for both PEG-PDI **1** and **2** systems can be visualized in Figure 93a. The normalized distribution of the scattered intensity as a function of size obtained by applying the Contin method to our data at $10^{-2}$ g/cm$^3$, which suggests a single size distribution for both systems (Figure 93b). These results clearly demonstrate that **37** and **40** spontaneously self-assemble in aqueous solution to form large structures of 100-250 nm of hydrodynamic radii, those ones increasing when the overall concentration decreases. In addition, large self-assemblies were observed even at very low concentration (<$10^{-4}$ g.cm$^{-3}$) where one would expect a large population of unimers by referring to literature in the case of slightly shorter PEG chains.[215] This result shows that the critical aggregation concentration (CAC) is becoming very low for sufficiently long PEG chains.

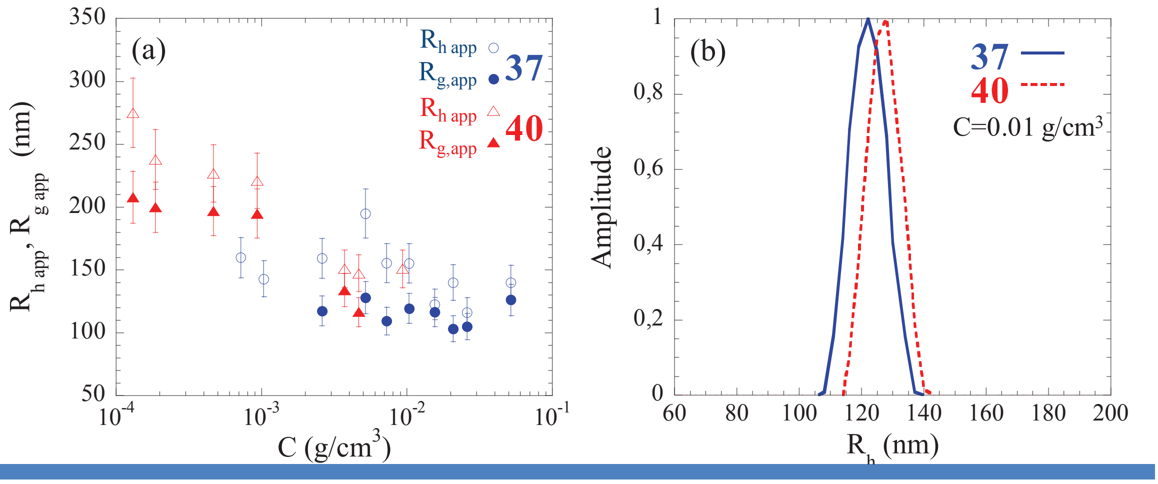

**Figure 93 |** a) Variation with concentration at T=21°C of the apparent hydrodynamic radius (empty symbols) and of the apparent radius of gyration (full symbols) for compounds **37** (blue circles) and **40** (red triangles). For high concentrations of **40**, as the samples are strongly colored, the laser beam was too attenuated and measurements were not possible. (b) Size distributions obtained by applying the Contin analysis to our data at C=0.01g/cm$^3$ for **37** (blue continuous line) and **40** (red dashed line) at a scattering angle θ of 90°.

We then recorded SLS scattering patterns for compound **37** in aqueous solution at various concentrations (Figure 94a). For the sake of clarity, the representation I(q)/C was displayed by shifting the curves with respect to one another.

---

[215] Arnaud, A.; Belleney, J.; Boué, F.; Bouteiller, L.; Carrot, G. and Wintgens, V. Aqueous Supramolecular Polymer Formed from an Amphiphilic Perylene Derivative. *Angew. Chem. Int. Ed.* **2004**, *43*, 1718–1721.

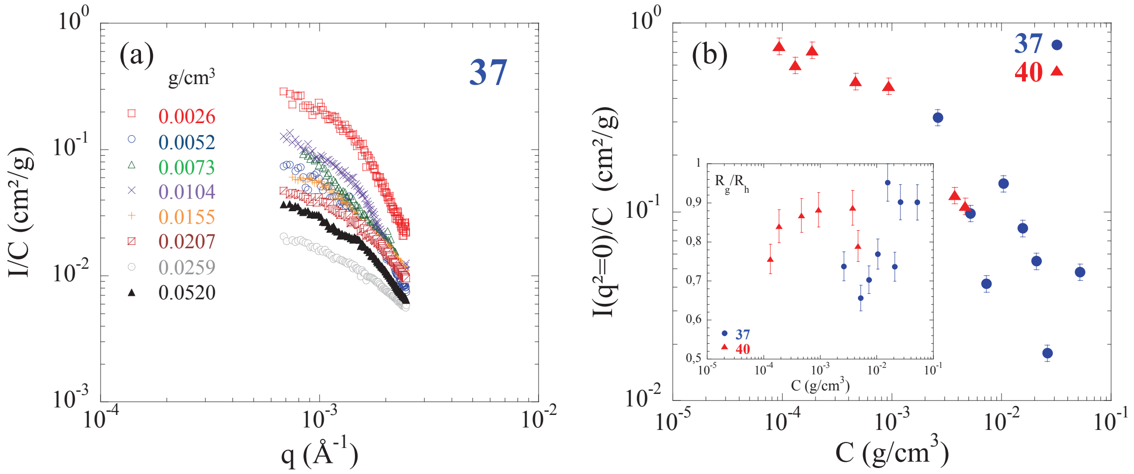

**Figure 94 |** a) Variation of the ratio I(q)/C with q obtained using SLS experiments for dilute solutions of compound **37**. (b) Concentration dependence of the ratio I(q²=0)/C for **37** (blue circles) and **40** (red triangles). The insert shows the evolution of $R_g/R_h$ for **37** and **10**. Note that for high concentrations of **40** (>$5.10^{-3}$ g/cm$^3$) the laser beam is too attenuated and the static measurements are thus not possible.

All the scattering curves exhibit the same behavior characterized by a Guinier regime in the low q range associated with a finite size of the self-assemblies. The low SLS q data have been fitted by the classical Guinier expression ($I(q)=I_0\exp(-q^2R_g^2/3)$), which provides the average radius of gyration $R_g$ (plotted in full symbols in Fig. 1a) and the zero-wave vector scattered intensity, I(q=0).

We also calculated the concentration dependence of the ratio I(q=0)/C of the low q scattered intensity over the whole concentration range for both systems (Figure 94b). This ratio is associated to the finite molecular weight of the assemblies. The variation of I(q=0)/C at T=21°C exhibits a smooth decrease, whereas the apparent radius of gyration, $R_{g,app}$, is independent on the concentration, with $R_{g,app}$ being larger for **40** than for **37**. Important indications on the self-assemblies' topology (structure and degree of compactness) can be provided by the ratio $R_g/R_h$ (see insert of Figure 94b). The value of the ratio $R_g/R_h$ is lower than 1 in the whole concentration range and close to 0.775 for low concentrations, a value calculated for homogeneous hard spheres and suggesting the formation of dense globular aggregates.

From the values of the structural parameters, some important features on the global structure of the self-assemblies can be emphasized. *i*) The hydrodynamic radii $R_h$ of both **37** and **40** are slightly decreasing with increasing the concentration, with values being higher for **40** at low C. *ii*) At the same time, the radii of gyration are almost constant. *iii*) Neglecting the virial effects, the concentration dependence of I(q²=0)/C combined with that of $R_g/R_h$ suggest that the degree of compactness and the weight-average molecular weight $M_W$ of the aggregates decrease with increasing concentration. Thus **37** and **40** self-assemble in solution to form aggregates with inverse concentration dependence, and according to the length of the grafted PEGs.

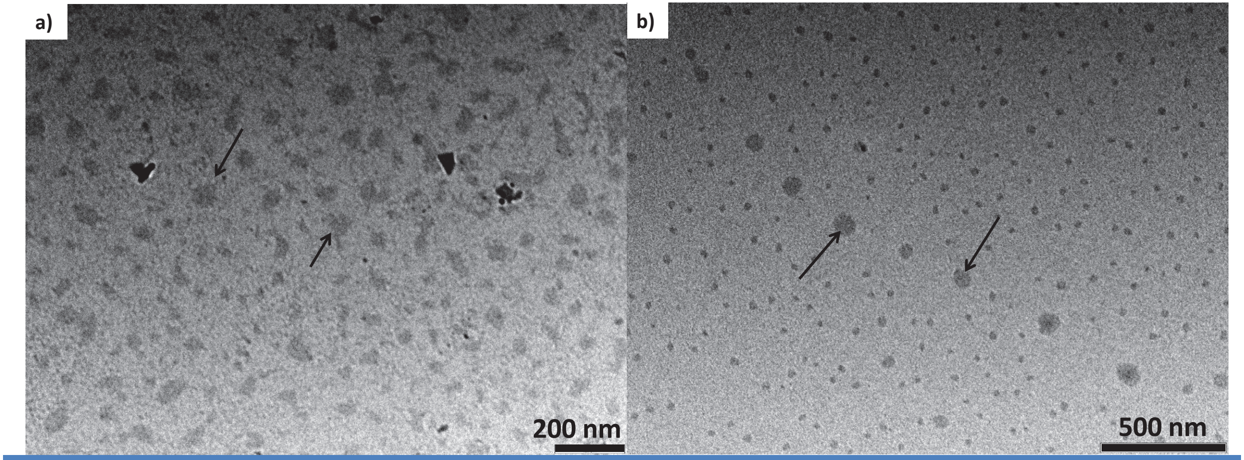

**Figure 95** | TEM images for (a) **37** at $C=1\times10^{-4}$ g $cm^{-3}$ (scale bar: 200 nm) and (b) **40** at $C = 2.7\times10^{-3}$ g $cm^{-3}$ (scale bar: 500 nm) solutions.

To gain insight into the arrangement of the supramolecular self-assemblies, combined TEM experiments were performed on solutions of **37** at $C=1.10^{-4}$ g/cm$^3$ and **40** at $C=2.7.10^{-3}$ g/cm$^3$ at room temperature (Figure 95). TEM observations are in good agreement with the results obtained from light scattering measurements. Indeed, a common observation in all these micrographs confirm that PBI-PEG **37** and **40** systems do not form elongated or single columnar assemblies but rather polydisperse non-elongated and globular self-assemblies, as seen by the broad size distribution obtained by the Contin analysis (Figure 93b). The larger aggregates indicated by the black arrows dominate the light scattering signal.

### *ii. Local structure and molecular packing of PBI-PEG self-assemblies*

To gain insight into the local structure, we turned to SAXS measurements. Due to the high electronic density of the perylene, the SAXS signal is dominated by the scattering of the aromatic core as shown in Figure 96 representing the calculated contrast terms $\Delta\rho^2=(\rho-\rho_{solvent})^2$ of the perylene core and the grafted PEGs. This figure shows that the PEG chains $\Delta\rho^2$ value is very close to that of the solvent (i.e. the scattering length density (SLD) ρ of PEG is very similar to that of the solvent), meaning that SAXS signal is not sensitive to these grafted PEGs. On the contrary, perylene core exhibits a very high contrast (i.e. high $\Delta\rho^2$) with solvent and thus is predominant in the SAXS scattering.

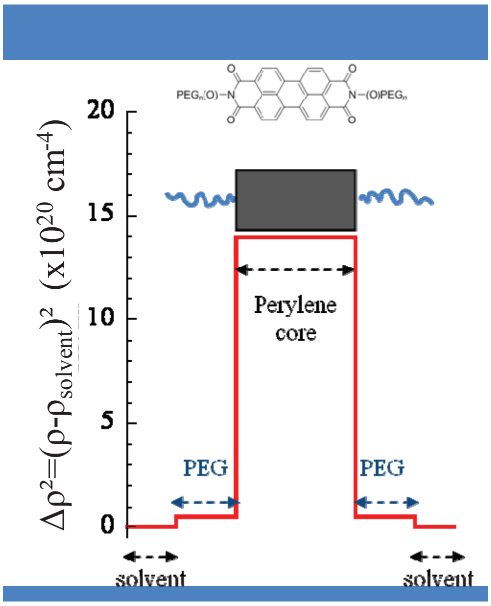

**Figure 96 |** Contrast terms $\Delta\rho^2=(\rho-\rho_{solvent})^2$ for PEG$_n$-PDI molecule. The calculation is made with $\rho_{PEG\ chain}=10\times10^{10}$ cm$^{-2}$ (with density d=1.13 g/cm$^3$), $\rho_{perylene\ core}=13.74\times10^{10}$ cm$^{-2}$ (with d=1.597 g/cm$^3$) and $\rho_{solvent}=9.31\times10^{10}$ cm$^{-2}$.

SAXS experiments wer performed for compound **37** at three different concentrations (C=0.052, 0.016, and 0.0073 g/cm$^3$) and for monomer **40** at C=0.019 g/cm$^3$ (Figure 97).

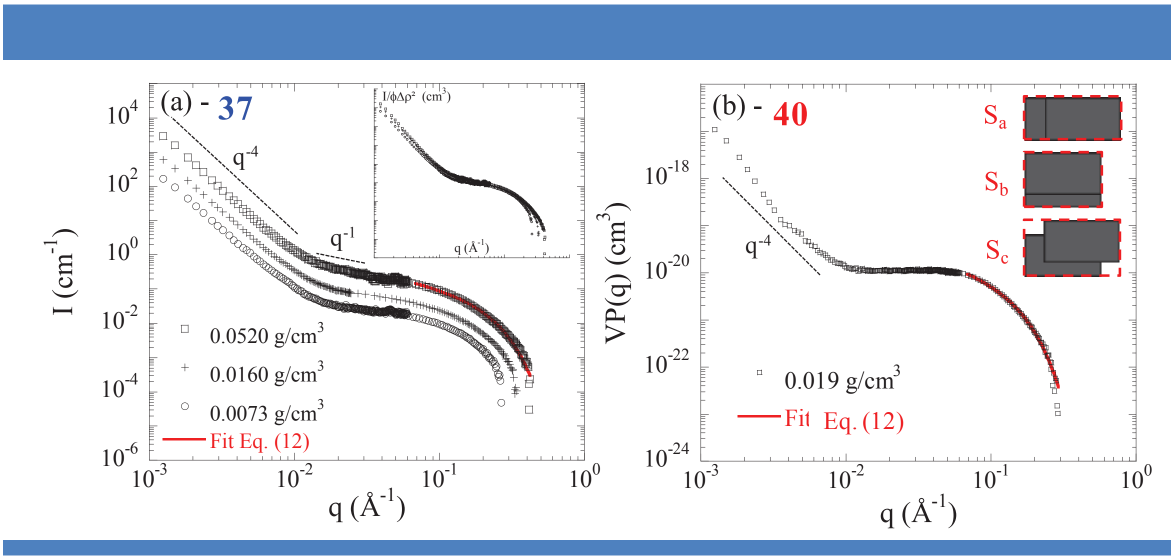

**Figure 97 |** a) SAXS profiles collected at three different concentrations for **37**: 0.052 (squares), 0.016 (cross) and 0.0073 (circles) g/cm$^3$. The insert shows the data normalized by the volume fraction Φ and the contrast term $\Delta\rho^2=(\rho-\rho_{solvent})^2$. b) Variation of the SAXS signal $I/\phi\Delta\rho^2=VP(q)$ with q for unimer **40** at 0.019 g/cm$^3$. The red line corresponds to the fit of the high-q data by a Guinier expression for the form factor of the section (eq. 12). The inset shows the molecular packing possibilities of perylene cores (represented by a black rectangle). S$_a$: longitudinal shift, S$_b$: transverse shift, S$_c$: shift in both direction.[129]

The curves can be described as follows. Each scattering profile exhibits: *i*) a sharp increase of scattering intensity at low q, which scales as q$^{-4}$; *ii*) an intermediate regime for **37** (0.015 Å$^{-1}$<q<0.05 Å$^{-1}$) in which the q dependence of the scattered intensity can be described by a power law with an exponent close to -1; and *iii*) a Guinier regime at the upper q-range corresponding to the cross-section of the perylene core assemblies. For compound **40**, the $q^{-4}$ law, which is characteristic of dense and large aggregates with a sharp interface, is directly followed by the cross-section Guinier regime.

For **37**, in the intermediate $q^{-1}$ regime, the scattering curves can be fitted satisfactorily by means of the form factor derived for rigid rod particles given by:

$$P(q) = \frac{\pi}{qL} \qquad \text{(eqn 9)}$$

where L is the contour length of the rod. By fitting the equation above to the experimental data, the linear mass density $M_L=M_w/L$ (mass per unit length) can be determined as $M_L=108\pm5$ g/mol/Å. This value is independent on the concentration as seen by the superimposition of the normalized data in the inset of Figure 97a representing the variations of $I/\phi\Delta\rho^2$ with q. To explain such a value for $M_L$, one could invoke a π-π stacking of the perylene aromatic rings, as observed in chemically similar systems forming columnar mesophases.[18] In the present case, the local structure can be seen as a single 1D-columnar assembly of perylene aromatic cores involving π-π stacking as the structure-directing factor with a linear mass density of $M_{L\ \mathrm{theoretical}}=390/3.4=114.7$ g/mol/Å, (with 390 g/mol being the molecular weight of the core and 3.4 Å being the intermolecular distance between two perylene cores). The physical dimension of this model, $M_{L,\mathrm{theoretical}}$, is in very good agreement with what was determined experimentally using SAXS. Also from the extrapolation of the scattered intensity at q=0 of the $q^{-1}$ part of the spectra, one can deduce an average molecular weight for the 1D-columnar elementary assembly of 20770 g/mol (corresponding approximately to a stacking aggregation number $N_{agg}$ of 53+/-5 perylene cores in the rod assembly, in good agreement with small rod-like self-assemblies previously observed with other similar systems[137]), and a contour length $L=M_w/M_L$ of 19.2 nm. Assuming that the radius of gyration of rod-like objects is given by $R_g^2=L^2/12$, we can determine a radius of $R_g=5.5$ nm, i.e. a hydrodynamic radius $R_h$ of 3.7 nm (if one assumes that $R_g/R_h=1.5$).[216]

Conversely, no $q^{-1}$ variations (characteristic of rod-like behavior) were observed for compound **40** (Figure 97b). The SAXS profile exhibits a plateau in the intermediate q-range indicating that the internal structure is quite different to **37** in this spatial scale. This plateau provides an average molecular weight of 9000 g/mol giving a PDI stacking aggregation number, $N_{agg}$, of 23, that is lower than for **37**.

Then, the high q data can be fitted by a Guinier expression for the form factor of the section:

---

[216] K. S. Schmitz, An introduction to dynamic light scattering by macromolecules, Academic Press, London, 1990.

$$VP(q) = \left(\frac{\pi S}{q}\right) exp\left(\frac{-q^2 R_g^2}{2}\right) \qquad \text{(eqn 10)}$$

Where S and $R_g$ are respectively the area and the radius of gyration of the cross section. From the fits of Figure 97, we obtain $S_1$=198 Å² and $R_{g,\mathbf{37}}$=7.14 Å for **37** and $S_2$=264 Å² and $R_{g,\mathbf{40}}$=10.10 Å for **40.** From these values some speculations on the molecular packing can be made. Using a theoretical value of 103 Å² for the cross-section of the core perylene 1D-assembly, the ribbon side lengths should be a=11.2 Å and b=9.2 Å.[217] The experimental values that are slightly greater than the predicted ones are however in good agreement with molecular parameters if we consider longitudinal or transverse shifts of the PDIs in the elementary columnar assembly as already shown by Würthner *et al.* [129] (see insert in Figure 97b). The radius of gyration of the cross-section of such a ribbon is given by:

$$R_c^2 = \frac{1}{12}(a^2 + b^2) \qquad \text{(eqn 11)}$$

Using the experimental values of a=S/b and b=S/a, we obtain $R_c$=6.75 Å for **37** and 8.7 Å for **40** (if b is fixed to 9.2 Å, see $S_a$ in Figure 97b), $R_c$=6 Å for **37** and 7.5 Å for **40** if a is fixed to 11.2 Å (see $S_b$, in Figure 97b), which are values somewhat smaller than the experimental values of ~7 and 10 Å, respectively. These differences might be due to shifts from both directions that certainly occur at the same time (see $S_c$, in Figure 97b). $S_2$ is also greater than $S_1$ suggesting that the stacking distortion is more pronounced due to higher steric hindrance for the long PEG chains system. It should be notes that the local behavior described above is independent of the concentration as seen by the superimposition of $I/\Phi\Delta\rho^2$ in the whole q-range (see insert in Figure 97a) for both **37** and **40**.

Finally the structural investigation on amphiphilic PEG-PDI systems in aqueous solution can be summarized as follows. Compounds **37** and **40** spontaneously polymerize in small primary stacks composed of few molecules thanks to hydrophobic effects and π-π interaction of the perylene cores. The aggregation number $N_{agg}$ of the primary stacks (elementary 1D assembly) depends on the PEG length and is larger for shorter PEG chains. The stronger steric hindrance of grafted $PEG_{16}$ which avoid perfect 1D molecular stacking increases the twist between perylene cores and distorts the 1D packing. Conversely, decreasing the steric effect by decreasing the PEG length promotes the stacking (as observed for **37**) with increasing $N_{agg}$ and decreasing S. Thus, we consider these primary stacks as the smallest stable objects in solution, which hierarchically self-assemble in larger aggregates responsible for the $q^{-4}$ behavior at low q. These quantitative results are also in good agreement

---

[217] Liu, S.-G.; Sui, G.; Cormier, R.A.; Leblanc, R. M. and Gregg, B.A. Self-Organizing Liquid Crystal Perylene Diimide Thin Films: Spectroscopy, Crystallinity, and Molecular Orientation. *J. Phys. Chem. B* **2002**, *106*, 1307-1315.

with the red color of the assemblies which is indeed related to the local ordering adopted by the unimers and thus to the nature of the π-π perylene interaction.[217,218] Indeed highly ordered stacks in single columns on surface with slight shift optimize the π-orbitals overlap leading to black or green phases. On the contrary red color is the signature of quite disordered phases and is consistent with our structural analysis showing the association in 1D stack with a moderate degree of order.

### *iii. Dynamic properties of the self-assemblies*

The unusual behavior of the 3D aggregates, related to the decrease of the size and degree of compactness with increasing concentration, led us to conduct further studies including the evolution with time of the dynamic properties.

#### ***Evolution with the time of the system***

When dispersed in the solvent, monomers are rapidly solubilized to give rise to monophasic slightly red colored limpid systems. Surprisingly, in the considered systems, we observed that the scattered electric field autocorrelation function $g^{(1)}$ (q,t) evolves slowly over very long periods of times (up to months), especially for solutions of **37**. Figure 98 shows the correlation function obtained for **37** at C=0.0104 g/cm$^3$ and T=21°C just after dispersion and solubilization of the sample, i.e. initial state (blue triangles) and at rest after several months (red circles).

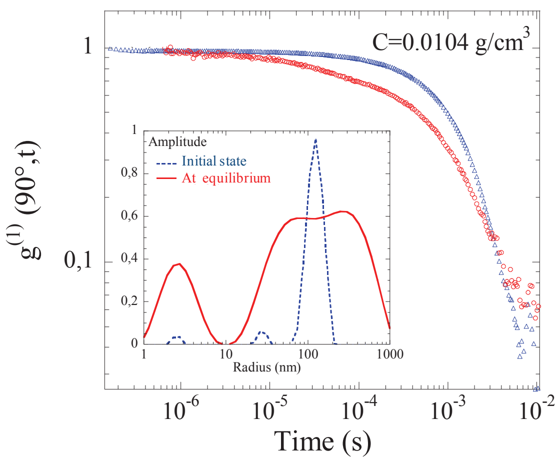

**Figure 98 |** Evolution with time of the scattered electric field auto-correlation function $g^{(1)}$ (q,t) for **37** at C=0.0104 g/cm$^3$ (initial state : blue triangles; infinite time: red circles) and at 90°. The insert shows the size distributions obtained by applying the Contin analysis to our data at 90°.

In the initial state, the autocorrelation function is well described by a single slow

---

[218] Kazmaier, P.M. and Hoffmann, R. A Theoretical Study of Crystallochromy. Quantum Interference Effects in the Spectra of Perylene Pigments. *J. Am. Chem. Soc.* **1994**, *116*, 9684-9691.

diffusive relaxation analyzed by the Cumulant procedure giving, after extrapolation of the data to $q^2=0$, an apparent hydrodynamic radius for the self-assemblies $R_{h\ app}$ of 155 nm. The results obtained by applying the Contin procedure to our data confirms this trend with the presence of a single peak appearing in the normalized size distribution function (see insert). Fast modes of very small amplitude without physical meaning are also observed. When the same sample was left in the scattering cell for seven months, the correlation function clearly became bimodal and can be described by the sum of two relaxations widely separated in time:

$$g^{(1)}(q,t) = A_{fast}(q)\exp\left(-\frac{t}{\tau_{fast}}\right) + A_{slow}(q)\exp\left(-\frac{t}{\tau_{slow}}\right) \qquad \text{(eqn 12)}$$

With $g^{(1)}(q,0)=A_{fast}+A_{slow}=1$.

The inspection of Figure 99a, representing the evolution of $\tau_{fast}$ and $\tau_{slow}$ with q, shows clearly that fast and slow modes are diffusive modes with characteristic times $\tau_{fast}$ and $\tau_{slow}$ varying as $q^{-2}$. The extrapolation to $q^2=0$ of $1/\tau_{fast}q^2$ and $1/\tau_{slow}q^2$ gives respectively the fast diffusion coefficient, $D_{fast}$, and the slow diffusion coefficient, $D_{slow}$, leading respectively to $R_{h,app\ fast}=3.5$ nm and $R_{h,app\ slow}=116$ nm. In the insert of Figure 98 showing the results obtained by applying the Contin method to our data, one also clearly observes the two modes. As the elapsed time increases, the relative amplitude of the fast mode increases whereas that of the slow mode decreases. After seven months, no further time evolution is observed and the systems can be considered at equilibrium. Similar results are obtained in the whole investigated concentration range.

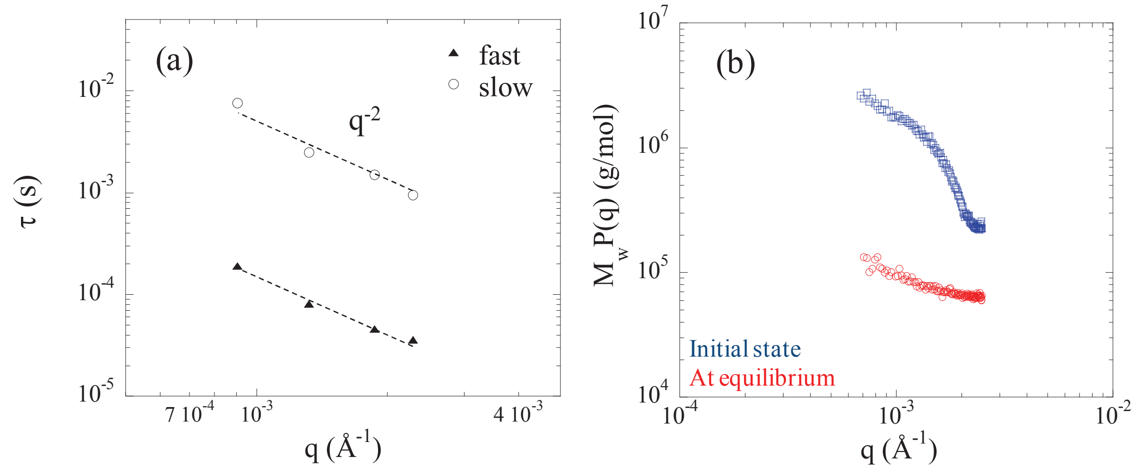

**Figure 99** | a) Variation of $\tau_{fast}$ (plain triangles) and of $\tau_{slow}$ (circles) with q; b) SLS measurements giving $M_wP(q)$ as a function of q at the initial state (blue squares) and at infinite time (red circles). Initial state corresponds to the time at which the samples were prepared and solubilized. Infinite time corresponds to the equilibrium at rest after several months.

Figure 99b shows $M_wP(q)$ obtained by SLS for **37** at $C=0.0104 g/cm^3$ at time-zero (initial state, blue squares) and at infinite time (equilibrium, red circles). After solubilization of the sample (time-zero or initial state), the variation of the scattering intensity displays a Guinier regime associated to the finite size and mass of the self-assemblies. We found a radius of gyration $R_g$ of 119.5 nm (see structural analysis in the first part) and an average molecular weight of 2.92 x $10^6$ g/mol, i.e. an aggregation number $N_{agg}$ of 2822 ($N_{agg}$ is the total number of unimers in an aggregate). At infinite time (equilibrium), the scattering intensity is much lower in the whole q-range and its variation with q presents a plateau at large q giving an average molecular weight of 66.1 x $10^3$ g/mol, i.e. an aggregation number of 64 unimers. The slight increase at very low q is due to larger aggregates still present in solution.

The fast relaxation mechanism is associated with the diffusion of the primary stacks described previously, whereas the slower relaxation indicates the presence of large self-assemblies. Indeed, values obtained for $R_{h,fast}$ and $N_{agg}$ at infinite time are very close to those determined by SAXS ($R_{h,primary\ stack}$=3.7 nm and $N_{agg,primary\ stack}$=53). Both the ratio of the amplitudes of the two modes, $A_{slow}/A_{fast}$, and the scattered intensity drop with time. These results suggest that the aggregates dissociate slowly to form primary stacks whose proportion increases with time. This behavior is confirmed by TEM (Figure 100) where large aggregates (white arrow) are clearly in coexistence with an important proportion of small primary stacks (black arrows). The white arrow points to a 150 nm self-assembly composed of many aggregated primary stacks (indicated by black arrows).

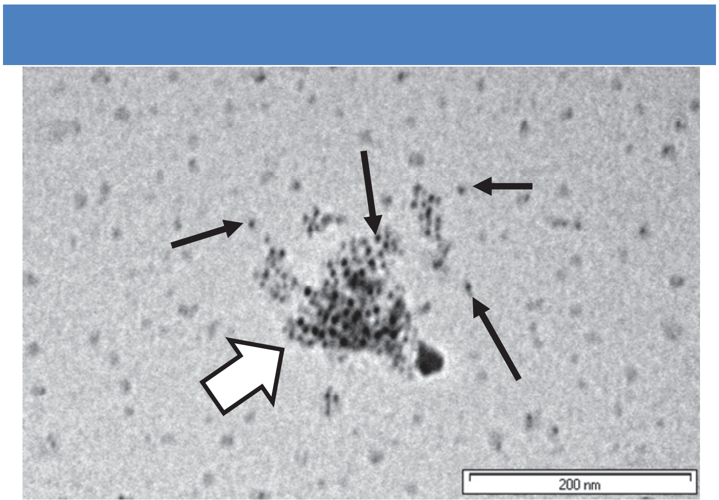

**Figure 100 |** TEM image of **40** at C=$10^{-3}$g/cm$^3$ illustrating the dissociation of large aggregates (white arrow) into small primary stacks (black arrows). The scale bar is 200nm.

### *Influence of unimer concentration*

In the previous parts, we have shown that the degree of compactness of the aggregates decreases with the concentration at initial time (after solubilization) and with the aging of the solution as shown by the release of free primary stacks from the self-assemblies. We also probed if the same effects are produced by an increase of concentration at equilibrium; i.e., at infinite time. Figure 101a shows the correlation functions $g^{(1)}(q, t)$, which are clearly bimodal, at different concentrations and at infinite time (7 months) for solutions of **37** at T=21°C. The insert of Figure 101a presents the normalized scattered intensity distribution as a function of the size obtained by applying the Contin procedure to our data at 90°. The amplitude of the fast mode increases with concentration while the amplitude of the slow mode decreases.

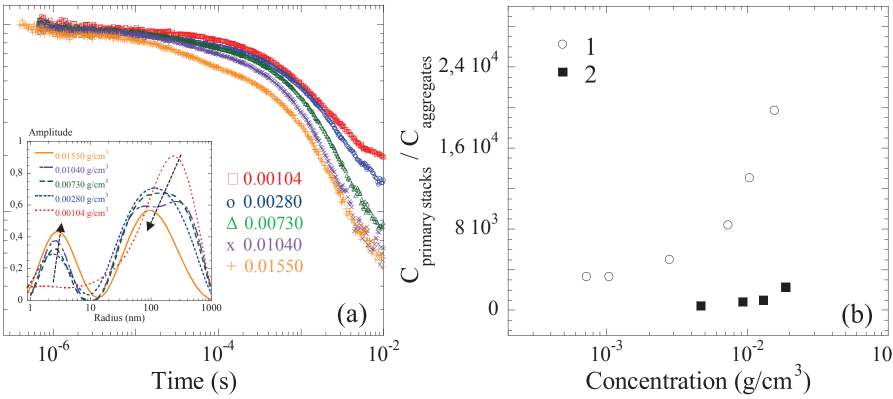

**Figure 101** | a) Evolution with concentration of $g^{(1)}$ (q,t) at equilibrium for **37** solutions at θ=90° and T=21°C. The inset shows the size distribution obtained using the Contin method. The black arrows show the peak evolution when increasing concentration. (b) Variation of the ratio $C_{primary\ stacks}/C_{aggregates}$ with C.

The relative amplitudes $A_{fast}$ and $A_{slow}$ measured by DLS can be used to evaluate the ratio between the concentration of free primary stacks and aggregates.[219] The sum of the amplitudes is equal to 1:

$$A_{fast}(q) + A_{slow}(q) = 1 \qquad \text{(eqn 13)}$$

Defining $I_{primary\ stacks}$ and $I_{aggregates}$ as the time-average absolute intensities associated with the fluctuations of PBI-PEG$_n$ monomer concentration with respectively short and long relaxation times and neglecting the virial effects, we obtain:

$$\left(\frac{A_{slow}}{A_{fast}}\right)_{q\to 0} = \left(\frac{I_{aggregates}}{I_{primary\ stacks}}\right)_{q\to 0} = \frac{KC_{aggregates}M_{W,aggregates}}{KC_{primary\ stacks}M_{W,primary\ stacks}} \approx \frac{C_{aggregates}}{C_{primary\ stacks}}\left(\frac{R_{H,aggregates}}{R_{H,primary\ stacks}}\right)^3 \qquad \text{(eqn 14)}$$

Where $K=(4\pi^2 n_0^2)/(N_a\lambda^4).(dn/dc)^2$ is the scattering constant. The value of the total absolute intensity, I(q), can be deduced from the SLS measurements.

---

[219] Esquenet, C.and Buhler, E. Aggregation Behavior in Semidilute Rigid and Semirigid Polysaccharide Solutions. *Macromolecules* **2002**, *35*, 3708–3716.

$$I(q) = I(q)_{primary\,stacks} + I(q)_{aggreagates} \qquad \text{(eqn 15)}$$

$C_{aggregates}$ and $C_{primary\ stacks}$ represent respectively the concentrations, in g/cm$^3$, of unimers in aggregates and of unimers in free primary stacks, the total concentration of the solution being equal to the sum of these concentrations:

$$C = C_{primary\,stacks} + C_{aggreagates} \qquad \text{(eqn 16)}$$

The variation of $C_{primary\ stacks}/C_{aggregates}$ with the total concentration deduced from the $A_{fast}/A_{slow}$ ratio can be observed in Figure 101b (circles for **37** and plain squares for **40**). For both systems, the proportion of free primary stacks clearly increases with the total concentration of the solution. This result supports the fact that primary stacks are the elementary bricks of the aggregates and are thus in equilibrium with them. For **40**, the ratio $C_{primary\ stacks}/C_{aggregates}$ obtained at a given concentration is lower than that obtained for **37**, but follows the same trend. Thus, the behavior at equilibrium (infinite time) is different for systems (**37**) and (**40**). As the ratio between the hydrodynamic radii of aggregates and free primary stacks is large (~30), calculated $C_{primary\ stacks}$ is pretty high in the whole range of concentration for **37**. The contribution of few large aggregates to the DLS signal is significant as shown by the height of the peak corresponding to the slow relaxation process obtained by applying the Contin analysis (see Figure 101a). For solutions of component **37** at infinite time (equilibrium), free primary stacks represent the main population.

Importantly, for **40**, the hydrodynamic radius associated to the slow mode is lower ($R_{H,slow}$=75 nm for C=0.019 g/cm$^3$, see Table 1), suggesting that the assemblies of **40** are more dense. For shorter PEG side chain systems (**37**), the effects of solution aging are particularly important as shown by the release of a very large number of free primary stacks.

**Table 4|** Hydrodynamic radii $R_h$ associated to the fast (free primary stacks) and slow mode (self-assemblies) for **37** and **40** solutions at T=21°C and C=0.019g/cm$^3$. Oppositely to $R_{h,fast}$, $R_{h,slow}$ is time and concentration dependent.

| $R_h$ | 37 | 40 |
|---|---|---|
| **$R_{h\ fast}$ (nm)** | 3.5 | 3.5 |
| **$R_{h\ slow}$ (nm)** | 113 | 75 |

### *Effect of temperature*

We also monitored the temperature dependence of the ratio $C_{primary\ stacks}/C_{aggregates}$ and of the apparent hydrodynamic radii $R_h$ associated with the fast and the slow modes obtained for solutions of component **37** and **40** at C=0.01 g/cm$^3$ (Figure 102).

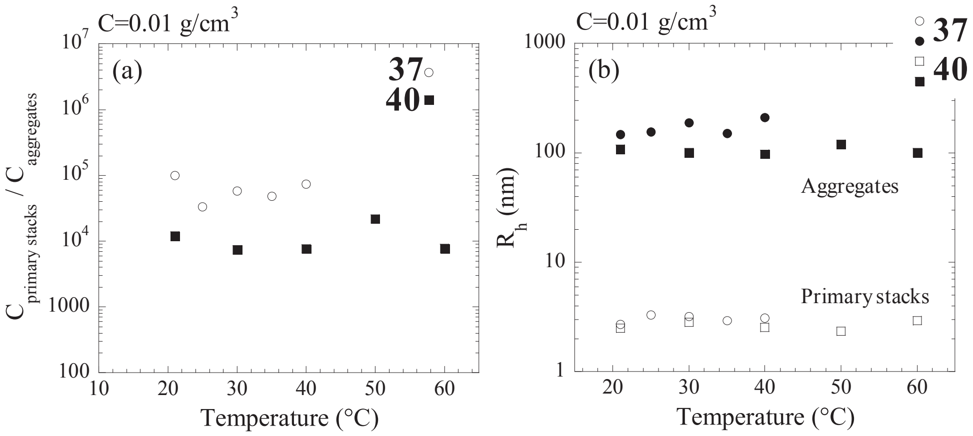

**Figure 102 |** Temperature dependence of (a) the ratio $C_{primary\ stacks}/C_{aggregates}$ and of (b) the hydrodynamic radii $R_h$ associated with fast (free primary stacks) and slow (aggregates) modes obtained for solutions of component **37** (circles) and **40** (squares) at C=0.01 g/cm$^3$.

For both molecules, the concentrations of free primary stacks and aggregates as well as the corresponding hydrodynamic radii remain constant with temperature. This is consistent with previous studies showing no effect of temperature on PEG solutions below 60°C.[220] The same behavior is observed in the whole investigated concentration range.

### *Influence of shaking*

Notably, an interesting shaking effect was observed for these PBI-PEG systems as depiscted on Figure 103a, which shows the evolution with time after a vigorous shaking of the autocorrelation function of the scattered electric field, $g^{(1)}$ (90°,t), for a solution of **37** at C=0.016g/cm$^3$. The behavior is similar for all concentrations of **37** and, for C=0.016g/cm$^3$ solutions, we observe two distinct relaxation modes for times higher than 100 hours and a single slow relaxation for times lower than 100 hours. From the ratio of the amplitudes of the slow and the fast components respectively, the fraction of free primary stacks can be estimated. The evolution with time of this fraction, $C_{primary\ stacks}/C_{aggregates}$, as well as that of the hydrodynamic radius associated to the aggregates, $R_{H,aggregates}$, is represented in Figure 103b. At time zero, i.e. just after the vigorous shaking, $R_{H\ aggregates}$ increases strongly, whereas $C_{primary\ stacks}$ is close to zero. Then both the size and the proportion of aggregates drop with time, indicating that the latter dissociate progressively into free primary stacks. The system recovers its equilibrium state after several months. In this limit the concentration of free primary stacks is extremely important and $R_{H\ aggregates}$ tends to ~120 nm. For the system

---

[220] Polik, W. F. and Burchard, W. Static light scattering from aqueous poly(ethylene oxide) solutions in the temperature range 20-90°C. *Macromolecules* **1983**, *16*, 978–982.

involving **40**, the shaking effect is less pronounced indicating that the aggregated self-assemblies composed of long PEG grafts are stronger and therefore more stable.

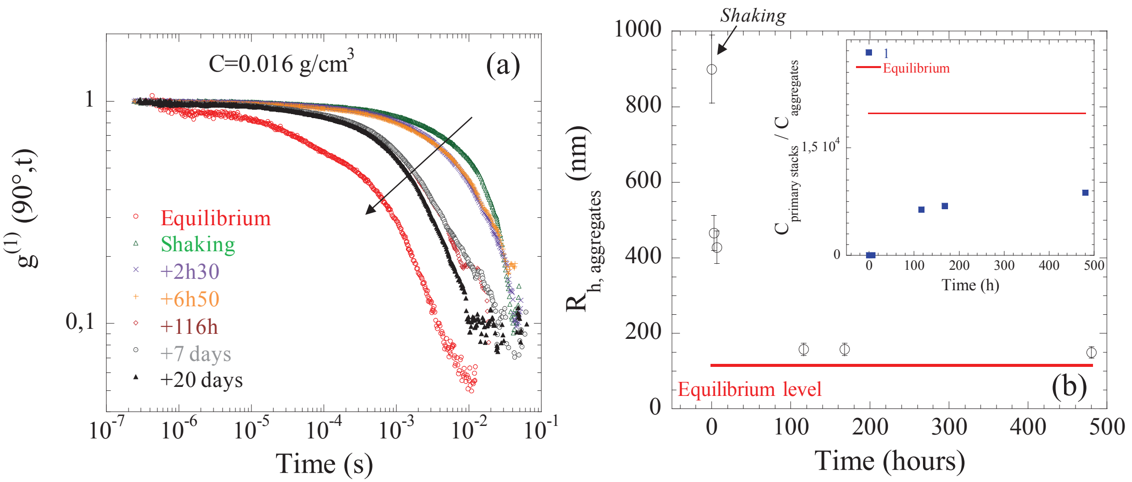

**Figure 103** | a) Evolution with time of $g^{(1)}(q,t)$ for a solution of **37** at θ=90°, C=0.016 g/cm$^3$ and T=21°C. The black arrow indicates the evolution of the correlation functions with time. Time-zero correspond to the time at which the sample was vigorously shaked. (b) Time evolution of the hydrodynamic radius associated with the slow mode, $R_{h,aggregates}$. The insert shows the variation of the ratio $C_{primary\ stacks}/C_{aggregates}$ with time.

Overall, these scattering experiments reveal a multistep self-assembly process. When dispersed in solvent, PBI-PEG molecules (Figure 104a) spontaneously self-assemble in primary stacks composed of a few number of molecules (Figure 104b). These primary stacks are thermodynamically the most stable objects in solution, which then self-assemble into dense aggregates via PEG chain interpenetration (Figure 104c). This PEG aggregation is due to the combined effects of *i*) the increase of local polymer concentration within the primary stacks and *ii*) the stretching conformation of PEG chains in aggregates, which finally increase the hydrophobic attractive interaction between the $CH_2$ groups of the PEG grafts. This hydrophobic interaction is more important for long PEG chains and one expects more stable aggregates for the PBI-$PEG_{16}$ system than for the PBI-$PEG_7$ one. This effect has been previously observed in PEG solutions under turbulent flow leading to the formation of aggregates.[53] Then, at rest, the former nano-aggregates dissociate slowly with time in free primary stacks together with less dense aggregates still present in solution (Figure 104d). This dissociation process is driven by the slow and progressive re-solubilization of PEG chains by water, which “releases” the primary stacks.

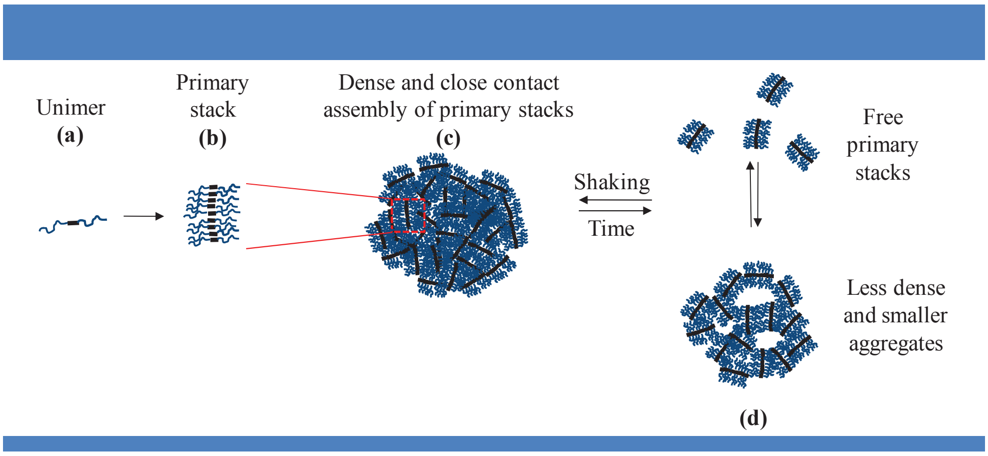

**Figure 104** | Schematic diagram depicting the effect of time (or equivalently of concentration) and of shaking on the structure of the PEG–PBI system

This phenomenon is concentration and time dependent: the degree of compactness as well as the mass of the aggregates decrease with time and/or the increase of the total concentration due to the release of free primary stacks in solution from aggregates as shown in Figure 101. The proportion of free primary stacks at equilibrium is particularly important for the PBI-PEG$_7$ system for which the PEG-PEG hydrophobic intra-aggregates interaction is less important and shows the key role played by the PEG length in the kinetic of dissociation. As the total concentration increases, the PEG interaction between neighboring clusters become more important and induce a swelling of the aggregates and consequently a more consistent release of free primary stacks in solution. At infinite time, aggregates are then loosely packed. We also attribute the size increase under shaking to the incorporation by mechanical effect of the free primary stacks into the aggregates thanks to PEG-PEG interactions.[221] Indeed, Duval *et al.* observed the formation of PEG aggregates under turbulent flow and a progressive dissociation into isolated chains with time: the molecular weight of the aggregates $M_{w,aggregates}$ and the radius of gyration $R_{g,aggregates}$ decrease respectively by a factor 3 and 1.33 in three months. Overall, this study shows that it is possible to control the dissociation speed and the quantity of released primary stacks by playing on the initial concentration, and/or the PEG length, and/or the mechanical stirring. These changes in structural and dynamic state in aqueous solution make PBI-PEG compounds systems of potential interest for controlled drug delivery.

---

[221] Duval**,** M. and Boué**,** F. Dilute Poly (ethylene oxide) Aqueous Solutions in a Turbulent Flow. *Macromolecules* **2007**, *40*, 8384–8388.

## 2. PBI-based supramolecular polymer with peptidic residues

### a. Supramolecular polymers with hexapeptidic side chains

#### i. $^1$H NMR spectra of PBI-6AA in $D_2O$

Similarly to PBI-PEG$_7$, PBI-6AA was initially characterized by $^1$H NMR in water (Figure 105) and displayed good solubility up to $10^{-2}$ mol/L.

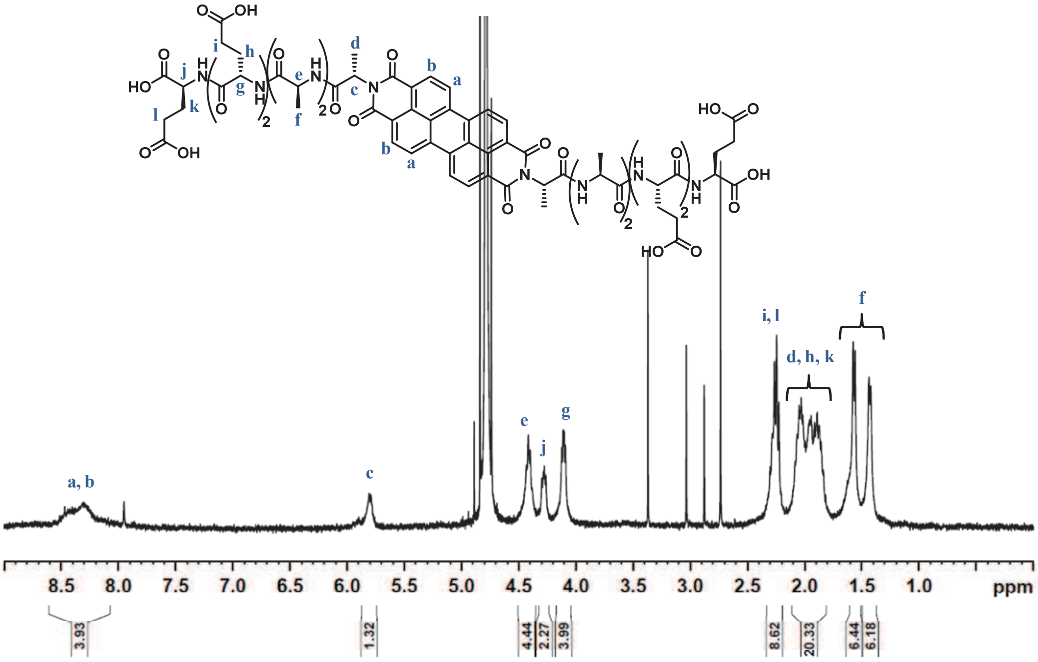

**Figure 105 |** $^1$H NMR spectra of PBI-6AA in $D_2O$ at $10^{-3}$ M.

The spectrum displays the expected set of signals which appear broaden at $10^{-3}$ M, therefore the integration does not exactly match the expected number of protons. This broadening of the signals already suggests the formation of supramolecular polymers in water. In particular, signals corresponding to protons "**a**" and "**b**" are very broad and could almost not be distinguished from the baseline. However, none of the chemical shifts were affected over the whole range of concentration analyzed by $^1$H NMR ($10^{-2}$ M down to $10^{-4}$ M).

#### ii. UV-Vis experiments on PBI-6AA in $D_2O$

In order to confirm the possible self-assembly of PBI-6AA in water, we studied its optical properties by both UV-Vis and fluorescence experiments (Figure 106 and 107). As mentioned in the previous chapter, monomeric perylene are characterized by vibronic transition bands.

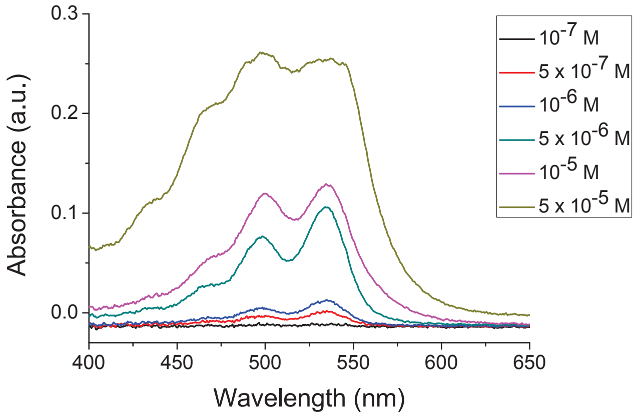

**Figure 106 |** UV-Vis spectra of a $D_2O$ solution of PBI-6AA for concentrations ranging from $10^{-7}$ (black) up to $5 \times 10^{-5}$ mol/L (light brown).

Up to $10^{-5}$ M, the UV-Vis absorption spectrum of PBI-6AA diplays these 3 main transitions at 468, 499 and 535 nm, the latter being the most intense. However, at $10^{-5}$ M, the emission band at 499 nm displays an intensity that is almost similar to the one at 535 nm. The partial loss of the vibronic structure suggests that self-assembly occur in water for concentrations above $10^{-5}$ M. Additional experiments at higher concentration have been performed but result in a saturation of the detector as already observed at $5 \times 10^{-5}$ mol/L (Figure 106, light brown curve). The appearance of a new band at 434 nm at $5 \times 10^{-5}$ mol/L might indicate the formation of H-aggregates. In order to confirm the H-aggregation of this molecule at concentration higher than $5 \times 10^{-5}$ M, measurements should be performed with cuvettes with lower path lengths (less than 5 mm). This work still requires to be performed.

### *iii. Circular dichroism on PBI-6AA in $H_2O$*

We also performed some circular dichroism (CD) experiments on PBI-6AA at different concentrations (Figure 107).

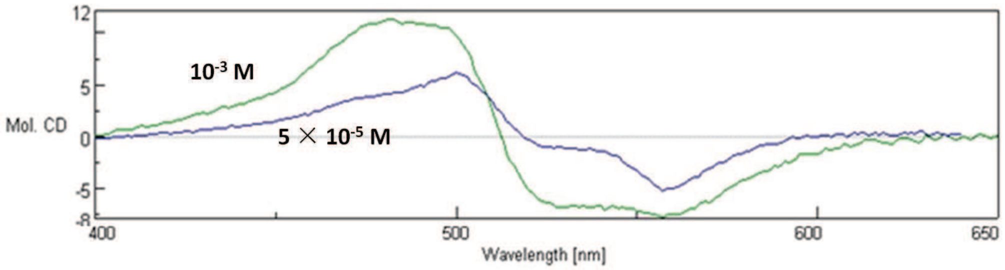

**Figure 107 |** Circular dichroism of PBI-6AA at $10^{-3}$ M (green) and $5 \times 10^{-5}$ M (blue) in $H_2O$.

At $5 \times 10^{-5}$ mol/L, the spectrum shows a CD exciton couplet with first a positive Cotton effect with a maximum at 498 nm and a shoulder peak at 475 nm followed by a negative

Cotton effect with a maximum at 558 nm. For the $10^{-3}$ M solution, the bands became broader which indicated the stronger stacking interaction between PBI-6AA molecules. This preliminary experiment shows that the chirality of the peptide chain induces chirality to the self-assembled structure. Further experiments at higher temperature should be performed in order to demonstrate that the observed Cotton effect is due to the chirality of the supramolecular aggregates.

### *iv. Fluorescence experiments on PBI-6AA in $D_2O$*

We also probed the possible self-assembly of PBI-6AA in water using fluorescence experiments at various concentrations (Figure 108).

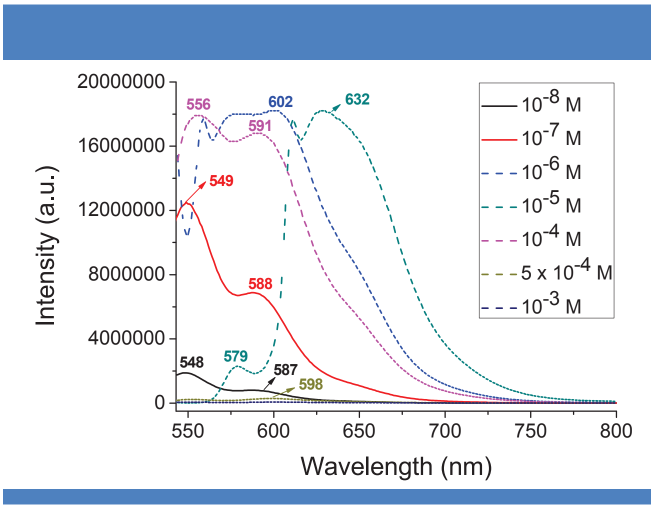

**Figure 108 |** Fluorescent spectra of PBI-6AA in $D_2O$ for concentrations going from $10^{-8}$ mol/L (black) up to $10^{-3}$ mol/L (black), $\lambda_{ex}$=534 nm.

Upon excitation at 534 nm, two emission bands at 548 and 587 nm are observed for a $10^{-7}$ M solution in $D_2O$. At $10^{-5}$ M, similarly to PBI-PEG$_7$ in acetonitrile, a large red-shift of the emission is observed ($\Delta\lambda$ ~80 nm) which suggests the formation of oligomers. At $10^{-4}$ M, the emission is blue-shifted to 556 and 591 nm and their intensity is still very high. Above this concentration, the fluorescence is almost completely quenched. The weakening of the emission band corresponding to the $S_{0\text{–}0}$ transition (~550 nm) is consistent with a self-assembly of PBI-6AA in water. Here again, the red-shift and further blue-shift of the emission maximum requires to be better understand, but the quench of fluorescence suggests the formation of supramolecular aggregates at concentrations higher than 5 x $10^{-4}$ M.

### *v. DLS experiments on PBI-6AA in $D_2O$*

Preliminary light scattering experiments were performed using Zetasizer NanoZS (Figure 109).

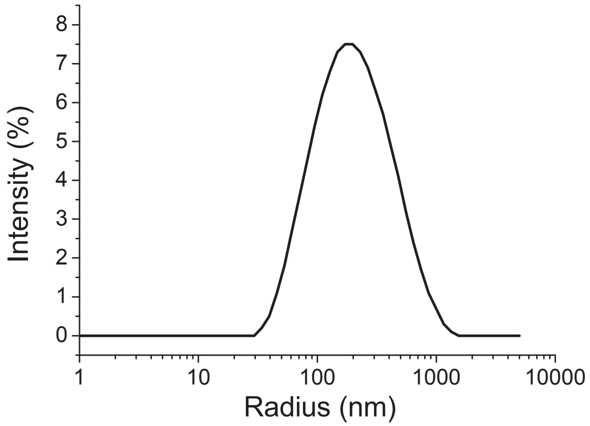

**Figure 109** | Hydrodynamic radius distribution observed for PBI-6AA ([PBI-6AA] = 1 mM in $D_2O$ at T=25°C and θ=173°).

Over three independent measurements, a single distribution of objects was observed with a mean hydrodynamic radius of ~126 nm. Further SLS and SANS experiments have been performed recently and will provide the shape and characteristic dimensions of the self-assembled objects. Additionally, AFM imaging of these structures is currently on going.

## b. Supramolecular polymers with heptapeptidic side chains

### i. $^1$H NMR spectra of PBI-7AA in $D_2O$

Similarly to PBI-6AA, PBI-7AA was characterized by $^1$H NMR in water (Figure 110) and also displayed good solubility up to $10^{-2}$ mol/L.

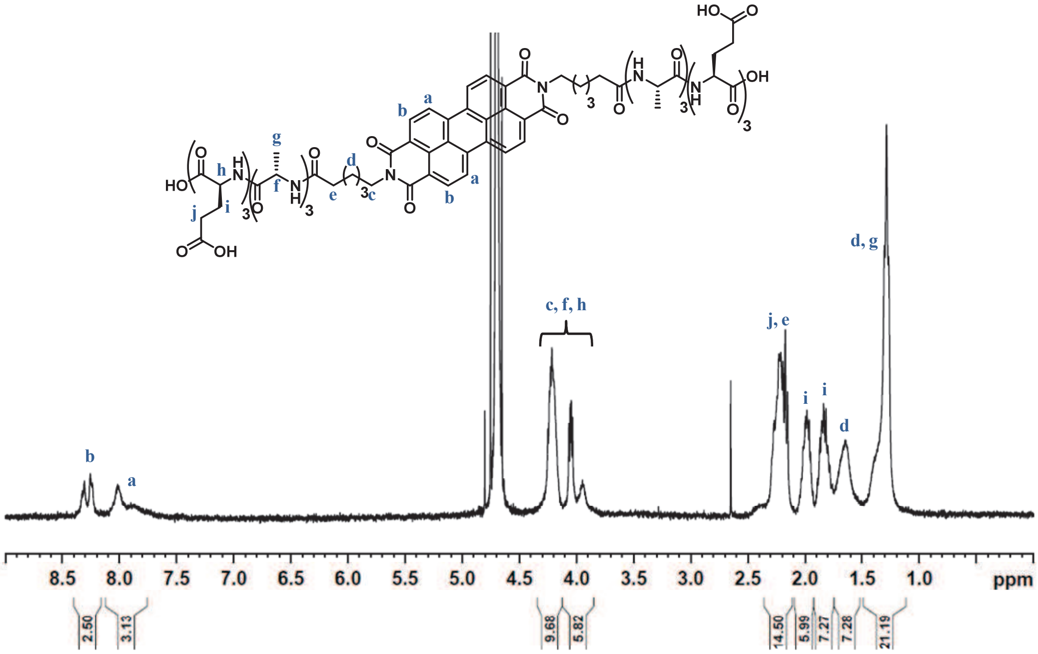

**Figure 110** | $^1$H NMR spectra of PBI-7AA in $D_2O$ at $10^{-3}$ M.

The spectrum displays the expected set of signals which appear partially broaden at $10^{-3}$ M, therefore the integration does not exactly match the expected number of protons. This broadening of the signals already suggests the formation of supramolecular polymers in water. Compared to PBI-6AA, the NMR signal corresponding to proton "**b**" is well-defined whereas the one corresponding to proton "**a**" is broadened. This observation suggests that perylene cores are aggregated by π-π stacking interactions centered on the center of the perylene unit. Additionally, none of the chemical shifts were affected over the whole range of concentration analyzed by $^1$H NMR ($10^{-2}$ M down to $10^{-4}$ M).

### *ii. UV-Vis experiments onPBI-7AA in $D_2O$*

We then studied the self-assembly of PBI-7AA in water by UV-Vis experiments (Figure 111).

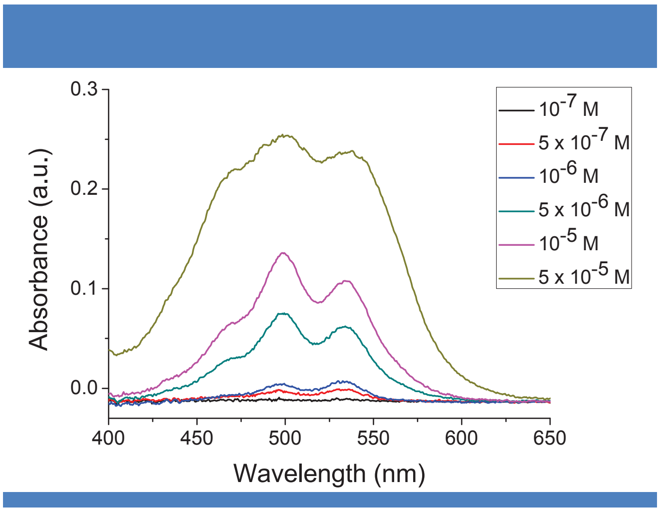

**Figure 111 |** UV-Vis spectra of a $D_2O$ solution of PBI-7AA for concentrations ranging from $10^{-7}$ (black) up to $5 \times 10^{-5}$ mol/L (light brown).

Up to $10^{-6}$ M, the UV-Vis absorption spectrum of PBI-7AA diplays 3 main peaks at 466 (shoulder peak), 498 and 533 nm, the latter being the most intense. At $5 \times 10^{-6}$ M, the emission band at 498 nm displays an intensity that is higher than the one at 533 nm. This reserval of intensity of the vibronic structure suggests that self-assembly occur in water from concentrations starting at $5 \times 10^{-6}$ M. A more pronounced effect is observed at $10^{-6}$ M. Additional experiments at higher concentration have been performed but result in a saturation of the detector as already observed at $5 \times 10^{-5}$ mol/L (Figure 111, light brown curve). The increase of the band at 466 nm at concentrations above $5 \times 10^{-6}$ mol/L compared to the band at 533 nm might indicate the formation of H-aggregates. Similarly to other studied PBI molecules, the H-aggregation of this molecule at concentration higher than $5 \times 10^{-5}$ mol/L should be confirmed by additional measurements with cuvettes with lower path lengths. We also performed some CD experiments on PBI-7AA at 5 x $10^{-5}$ M and $10^{-3}$ M in water. In both cases, no CD signals were observed, indicating that no chiral self-assembly or self-assemblies with both handedness are formed by this molecule. This experiment demonstrates that the introduction of the aliphatic linker between the perylene core and the peptidic side chain influences the self-assembly of the PBI-peptide molecules.

### *iii. Fluorescence experiments on PBI-7AA in $D_2O$*

We then investigated the concentration-dependant fluorescence of PBI-7AA in water (Figure 104).

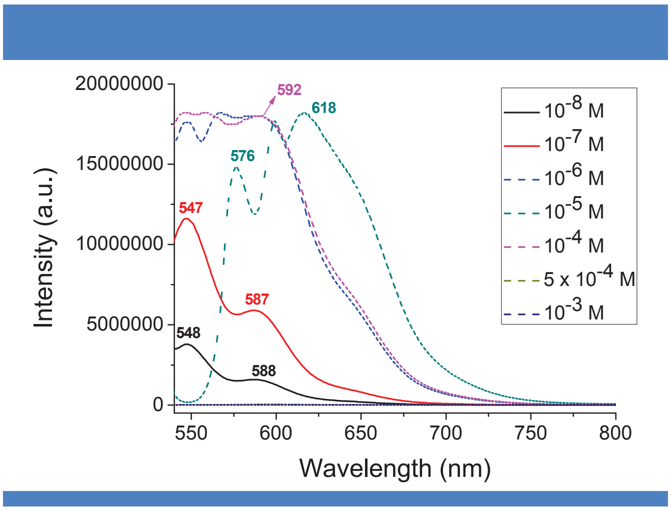

**Figure 112 |** Fluorescent spectra of PBI-7AA in $D_2O$ for concentrations ranging from $10^{-8}$ mol/L up to $10^{-3}$ mol/L, $\lambda_{ex}$=534 nm.

Similarly to PBI-6AA, upon excitation at 534 nm, two emission bands at 548 and 588 nm are observed for a $10^{-8}$ M solution in $D_2O$ and which intensity increases for concentration up to $10^{-6}$ M. At $10^{-5}$ M, similarly to PBI-6AA, a large red-shift of the emission is observed ($\Delta\lambda$ ~70 nm) which suggests the formation of oligomers. At $10^{-4}$ M, the emission is blue-shifted to a broad emission band that matches the one observed at $10^{-6}$ M. When the concentration is increased to 5 × $10^{-4}$ mol/L, the fluorescence is completely quenched. The weakening of the emission band corresponding to the $S_{0\text{–}0}$ transition (~550 nm) is consistent with a self-assembly of PBI-7AA in water at concentrations higher than 5 × $10^{-4}$ M. The differences in emission for concentrations going from $10^{-6}$ to $10^{-4}$ M remain difficult to be explained although the absence of self-assembly at $10^{-6}$ M could explain the increase of fluorescence, and the formation of oligomers at $10^{-5}$ M could induce the red-shift of the emission maximum. The reversal of absorption maximum is more difficult to explain but could come from different kinds of self-assemblies.

### iv. DLS experiments on PBI-7AA in $D_2O$

As for PBI-7AA, preliminary light scattering experiments were performed using Zetasizer NanoZS (Figure 113).

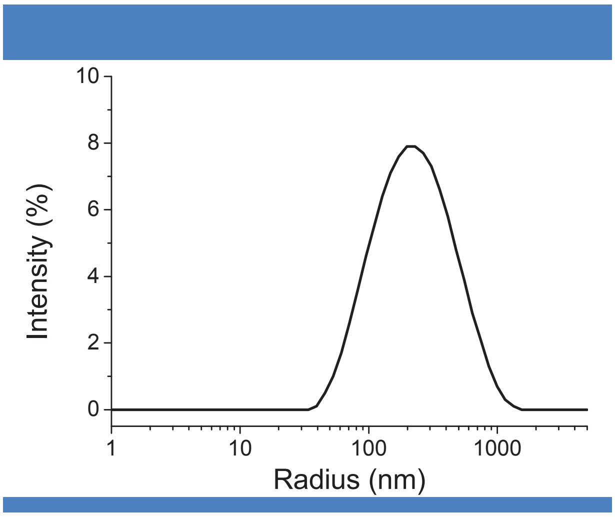

**Figure 113** | Hydrodynamic radius distribution observed for PBI-7AA ([PBI-7AA] = 1 mM in $D_2O$ at T=25°C and θ=173°).

Over three independent measurements, a single distribution of objects was observed with a mean hydrodynamic radius of ~137 nm, which is slightly larger than the one observed for PBI-6AA. Further SLS and SANS experiments have been performed recently and will provide the shape and characteristic dimensions of the self-assembled objects.

Whereas SANS and LS experiments on PBI-peptide molecules remain to be analyzed to elucidate the shape and characteristic dimensions of the self-assemblies and have to be correlated with AFM imaging, CD experiments have shown that the aliphatic linker introduced between the perylene core and the peptidic side chain influences the self-assembly of these molecules. This trend also seems to be indicated by UV-Vis experiments which display slightly different absorption patterns at low concentrations. However, additional optical spectroscopic measurements at high concentrations will have to be performed in order to fully understand the self-assembly process of these PBI-peptides molecules.

## 3. PBI-based supramolecular polymer with cyanine residues

### *i. HPLC-MS spectra of PBI-$Cy_3$*

For PBI-$Cy_3$ derivative, all recorded $^1H$ NMR of the purified compound resulted in the complete disappearance of all proton signals. This observation already suggests the strong association of these molecules into large anisotropic aggregates. The purity and structure confirmation of PBI-$Cy_3$ was therefore only determined thanks to HPLC-MS experiments (Figure 114).

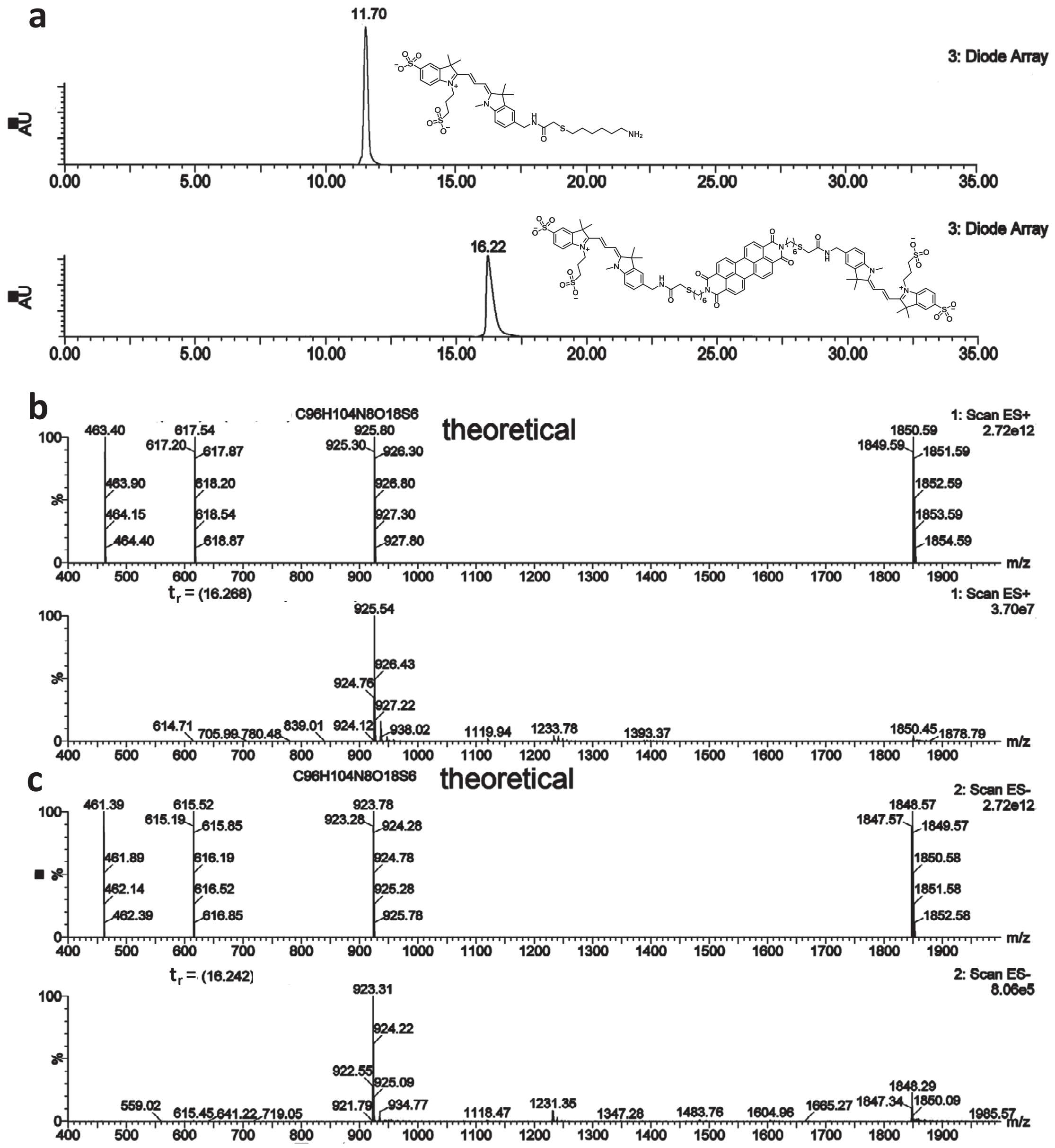

**Figure 114 |** a) HPLC chromatograms of (i) compound **22** (starting material for the synthesis of PBI-$Cy_3$) and (ii) PBI-$Cy_3$; b) Mass spectra corresponding to the peak at 16.22 min (positive ionization); c) Mass spectra corresponding to the peak at 16.22 min (negative ionization).

Indeed, after purification, the chromatogram corresponding to PBI-$Cy_3$ displays a single peak by UV (λ = 500 nm) and its retention time is greater than the one corresponding to compound **22**, the cyanine derivative used as starting material for the synthesis of PBI-$Cy_3$ (Figure 114a). This simple observation is in agreement with the presence of the perylene core on the cyanine derivative owing to the hydrophobic nature of the core. From the HPLC-MS setup, extraction of the mass that corresponds to the peak observed by UV confirmed the presence of PBI-$Cy_3$. In both positive and negative ionisation, the observed mass and its isotopic distribution are matching the calculated ones for PBI-$Cy_3$ (Figure 114b).

### *ii. UV-Vis experiments on PBI-$Cy_3$ in $H_2O$*

In order to confirm a possible self-assembly of PBI-$Cy_3$ in water, we studied its optical properties by both UV-Vis and fluorescence experiments (Figure 115, 116).

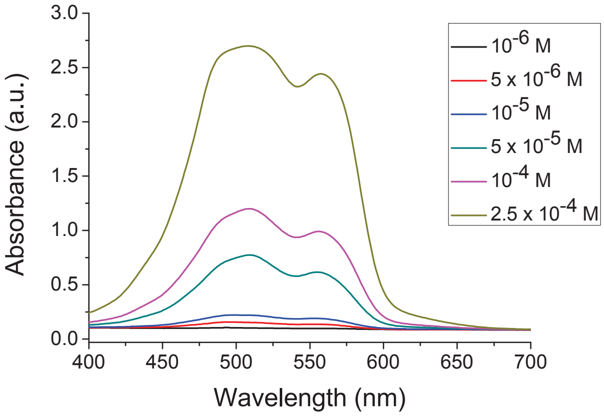

**Figure 115 |** UV-Vis spectra of a $H_2O$ solution of PBI-$Cy_3$ for concentrations ranging from $10^{-6}$ (black) up to $2.5 \times 10^{-4}$ mol/L (light brown). A 1 mm path length cuvette was used for this experiment.

From the lowest concentration recorded ($10^{-6}$ M), a structureless band ranging from ~450 to 600 nm is observed and broadens upon increasing the concentration. A maximum absorption can however be observed at 511 nm with a shoulder peak at 497 nm and an additional absorption band at 554 nm. Whereas the absorption bands at 511 and 554 nm suggest a contribution from the cyanine moiety (see Figure 60b, Results - Chapter 2), the shoulder at 497 nm is probably arising from the perylene core (see other perylene derivatives described previously). The presence of a structureless band over the whole range of concentration suggests the formation of supramolecular aggregates even at $10^{-6}$ M. Considering that precise contributions of both perylene and cyanine moieties remain to be determined, it is difficult to state on the type of aggregate obtained for this supramolecular polymer. Further work will be oriented towards this goal.

### iii. *Fluorescence experiment on PBI-Cy$_3$ in H$_2$O*

We then examined the fluorescent behavior of PBI-Cy$_3$ in water at different concentrations (Figure 116).

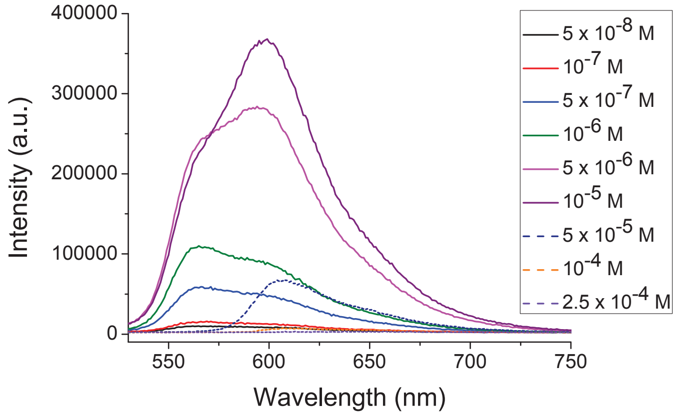

**Figure 116 |** Fluorescent spectra of PBI-Cy$_3$ in D$_2$O for concentrations ranging from 5 x 10$^{-8}$ mol/L up to 2.5 x 10$^{-4}$ mol/L, $\lambda_{ex}$=511 nm.

Upon excitation at 511 nm, two emission bands at 564 and 600 nm are observed for a 10$^{-6}$ M solution in D$_2$O, the latter being the less intense. When the concentration is increased to 5 x 10$^{-6}$ mol/L, the emission band at 600 nm becomes stronger than the one at 564 nm but both intensities continue to increase. At 10$^{-5}$ mol/L, a single emission band at 600 nm remains. When the concentration keeps on increasing, the fluorescence starts to be quenched until complete quenching at 2.5 x 10$^{-4}$ mol/L. The weakening of the emission band corresponding to the S$_{0\text{–}0}$ transition (~550 nm) is consistent with a self-assembly of PBI-7AA in water. This observation along with the bathochromic shift of the emission band corresponding to the S$_{0\text{–}1}$ transition (~590 nm) support the formation of H-aggregates as suggested by UV-Vis experiments.

### iv. *AFM and TEM imaging of PBI-Cy$_3$*

We have also performed some AFM and TEM imaging of the self-assembled structures obtained for PBI-Cy$_3$ in water (Figure 117). Both techniques show the formation of long fibrillar structures whose diameter has been estimated by AFM at 5-6 nm. Further molecular modeling should be performed to confirm that the diameter of the self-assembled structure corresponds to the size of the monomeric unit.

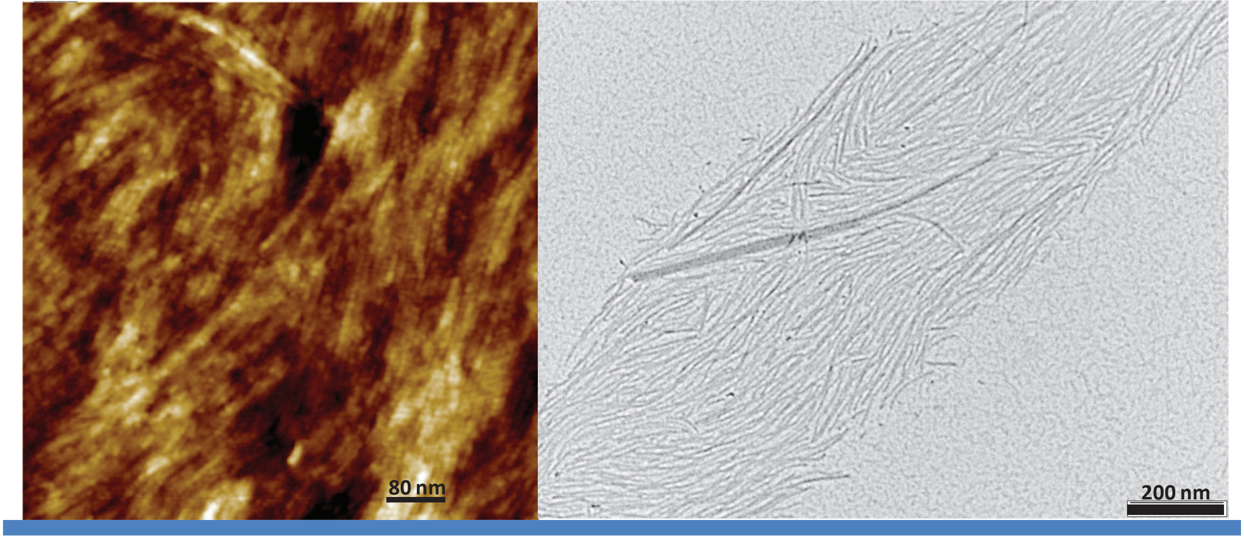

**Figure 117** | AFM and TEM images of PBI-$Cy_3$ from a $D_2O$ solution.

Overall, using a combination of optical spectroscopies and imaging techniques, we have shown that PBI-$Cy_3$ molecules give rise to fibrillar self-assemblies in water. Further analyses of the scattering data (SANS and SLS) which have been recorded recently and additional spectroscopic experiments to determine the contribution of the cyanine and the perylene core to the self-assembly remain to be performed.

# CONCLUSIONS AND PERSPECTIVES

First of all, this work relies on the successful synthesis of several molecules incorporating bisurea and perylene cores which serve as hydrogen-bonding or π-π stacking recognition units for their subsequent supramolecular polymerization. Noteworthily, bisurea- and perylene-peptide monomers have been fully synthesized on solid support which greatly facilitates their final purification. Additionally, a great challenge of this thesis was the synthesis of advanced organic molecules incorporating cyanine derivatives, which represent some of the most complex molecules built from these dyes so far.

We were then able to successfully polymerize all these molecular units in various solvents, and notably in water. To characterize them, we have followed a systematic approach using a combination of $^1$H NMR, UV-Vis, and fluorescence spectroscopies; small angle neutron scattering and light scattering techniques; AFM and TEM imaging. The structure and properties of most of these supramolecular polymers have been elucidated. In particular, molecules with a same core but different lateral chains have been shown to form various nanostructures going from twisted ribbons, to 2D plates, and to branched fibers. Additionally, bisurea-based supramolecular polymers decorated with a hexapeptide or a cyanine derivative (both $Cy_3$ and $Cy_5$) displayed thermoreversible hydrogelation properties, which remain to be fully characterized. The hierarchical self-assembly of perylene-PEG compounds was also elucidated by scattering techniques and UV-Vis experiments, demonstrating a cooperative self-assembly in water/THF mixtures. Alternatively, ITC has also been envisioned to monitor the polymerization mechanism of bisurea-PEG compounds. Although some experimental work remains to fully characterize these supramolecular polymers build from a single type of monomer, we have started studying the formation of multifunctional supramolecular copolymers incorporating biorecognition and fluorescence side chains. UV-Vis and fluorescence spectroscopies were used to demonstrate the social self-sorting process that occurs during the polymerization process where SANS, SLS, and AFM experiments confirmed the preferential formation of a single mixed nanostructure mostly dictated by one of the monomers. Interestingly, we have shown that the combined use of bisurea-$Cy_3$ and bisurea-$Cy_5$ derivatives represents a valuable tool to monitor self-sorting processes by energy transfer.

Overall, this work implements the recent research field on supramolecular co-self-assemblies and hold great promises for achieving complex multifunctional supramolecular copolymers because social self-sorting can be obtained even by using very different functional groups. After completing all the characterizations of polymers and gels described in this thesis, we envision to extend the current work to the combination of 3 or 4 monomers in a single polymer and to study the formation of such supramolecular copolymers from perylene monomers. Such achievements would bring new tools to simply build advanced purely organic materials with potential applications for targeted biorecognition. In addition, the gels produced during this work could be envisages as temperature-controlled sustained-release system, whereas the PBI-based self-assembly could also find potential applications in organic electronics.

# EXPERIMENTAL PART

# Synthesis and characterization of organic compounds

## 1. General Procedures

### a. Solvent and chemical reagents

All reagents and solvents were purchased at the highest commercial quality and used without further purification unless otherwise noted. Dry solvents were obtained using a double column SolvTech purification system. Water was deionized by using a milli-gradient system (Millipore, Molsheim, France). Microwave reactions were carried out with a single mode cavity Discover Microwave Synthesizer (CEM Corporation, NC, USA). Yields refer to spectroscopically purified ($^1$H NMR) homogeneous materials.

### b. Chromatographic methods

*Thin Layer Chromatographies* were performed using silica on TLC Al foils (silica gel matrix with fluorescent indicator 254 nm, thickness: 500 µm, Sigma-Aldrich). In most cases, irradiation using a *Bioblock VL-4C* UV-Lamp (6 W, 254 nm and/or 365 nm) as well as *p*-anisaldehyde, phosphomolybdic acid and Cerium ammonium molybdate stainings were used for visualization. *Preparative Adsorption Flash Column Chromatographies* were performed using silica gel (60 Å, 230 - 400 mesh, 40 - 63 µm, Sigma-Aldrich) or aluminium oxide 90 (standardized activity II, 70 - 230 mesh, Merck). *Preparative Ultra Performance Liquid Chromatographies* were performed using a *Waters AutoPurify* system equipped with a UV detector (set at 300 nm, 500 nm or 600 nm), a *3100* mass spectrometer, reverse phase columns (Waters, Sun Fire Prep $C_{18}$ 5.0 µm, 19 × 150 mm; Waters, XBridge Prep $C_{18}$ 5.0 µm, 19 × 150 mm) running with a water/methanol gradient as eluent, and the MassLynx 4.1 – XP software.

## c. Analytical methods and instruments

### i. Nuclear Magnetic Resonance (NMR)

*$^1$H NMR spectra* were recorded on a *Bruker Avance 400* spectrometer at 400 MHz and $^{13}$C NMR spectra at 100 MHz. The spectra were internally referenced to the residual proton solvent signal. Residual solvent peaks were taken as reference ($CDCl_3$: 7.26 ppm, $CD_3OD$: 3.31 ppm, $CD_3CN$: 1.94 ppm, DMSO-$d_6$: 2.50 ppm and $D_2O$: 4.80 ppm). For $^1$H NMR assignments, the chemical shifts are given in ppm. Coupling constants *J* are given in Hz. Peaks are described as singlet (s), doublet (d), triplet (t), quartet (q), multiplet (m) and broad (br).

### ii. Mass spectrometry

*Ultra Performance Liquid Chromatographies coupled to Mass Spectroscopy* (UPLC-MS) were carried out on a *Waters Acquity UPLC-SQD* apparatus equipped with a PDA detector (190–500 nm, 80Hz), using a reverse phase column (Waters, BEH $C_{18}$ 1.7 µm, 2.1 x 50 mm), the MassLynx 4.1 – XP software and a gradient (water-acetonitrile + 0.1% TFA) as eluent.

### iii. Optical Spectroscopies

*UV-VIS-NIR spectra* were recorded on a Varian Cary 5000 apparatus.

*Fluorescence experiments* were recorded on a FluoroMax-4 (Horiba Jobin-Yvon) spectrofluorometer with the following settings: slit width = 5 nm, inc = 1, integration time = 0.1 s.

*I.R. spectra* were recorded on a Fourier transform infrared spectrometer VERTEX 70 (Bruker).

### iv. Viscosimetry

Measurements were performed with a Ubbelohde type viscometer (**Schott AVS-360)** monitored with the Dilut4 / Schott software. At least, three consecutive measurements were performed and the mean value was reported.

### v. Isothermal titration calorimetry

*ITC experiments* were performed by Dr. Jeremy Brandel (ECPM) according to the following protocol. Heats of dissociation were measured using a MicroCal iTC200 titration microcalorimeter. The sample cell (200 μL) was filled with pure solvent. A solution of bisurea-PEG$_{16}$ in the same solvent was placed in a 40μL continuously stirred syringe. A first 0.4 μL aliquot was injected, without taking into account the observed heat, to remove the effect of solute diffusion across the syringe tip during the equilibration period. Aliquots of the solution (2 μL) were then automatically injected into the sample cell every 200 s, until the syringe was empty.

### vi. Small angle neutron scattering (SANS)

*SANS experiments* were performed on the PAXE and PACE spectrometers at the Laboratoire Leon Brillouin (LLB, CEA Saclay). On PACE, three configurations were used: the first with a distance sample to detector of 5 m, a wavelength of 13 Å and a collimation distance of 5.00 m, the second at 3 m and 7 Å and the last at 1 m and 7 Å with a collimation distance of 2.50 m, providing a large accessible q-range from 3 x $10^{-3}$ to 0.3 Å$^{-1}$. Data treatment has been done with a homemade program (Pasinet) following standard procedures.

### vii. Small angle X-ray scattering (SAXS)

*SAXS experiments* were performed at the ESRF (Grenoble, France) on the ID-02 instrument using the pinhole camera at an energy of 12.46 keV at two sample-to-detector distances (1 m and 8 m) corresponding to a q-range varying between 0.0011 Å$^{-1}$ and 0.57 Å$^{-1}$. The absolute units are obtained by normalization with respect to water (high *q*-range) or lupolen (low *q*-range) standard.

### viii. Dynamic and static light scattering (DLS and SLS)

*DLS and SLS spectra* were performed at the University Paris Diderot on the 3D DLS spectrometer (LS Instruments, Fribourg, Switzerland) equipped with a 25mW HeNe laser (JDS uniphase) operating at λ=632.8 nm, a two channel multiple tau correlator (1088 channels in autocorrelation), a variable-angle detection system, and a temperature-controlled index matching vat (LS Instruments). The scattering spectrum was measured using two single mode fibre detections and two high sensitivity APD detectors (Perkin Elmer, model SPCM-AQR-13-FC). Solutions were directly filtered through 0.22 μm Millipore filter into the scattering cell. Additional DLS experiments were performed using a ZetaSizer Nano ZS (Malvern Instruments, Worcestershire, U.K.).

- *Static light scattering (SLS)*

In SLS experiment, the scattering intensity $I(q)$ is measured as a function of scattering wave vector $q$ defined by:

$$q = \frac{4\pi}{\lambda} n_0 \sin\left(\frac{\theta}{2}\right) \qquad \text{(eqn 17)}$$

where $n_0$ is the refractive index of the solvent (1.33 for water at 20 °C), λ is the wavelength of light under vacuum and θ is the scattering angle, which has been varied from 30° to 140° providing a $q$-range from $7 \times 10^{-4}$ Å$^{-1}$ to $2.4 \times 10^{-3}$ Å$^{-1}$. Corrections to the absolute scattering intensities $I(q)$ (called also Rayleigh ratio R($q$)) were made using a toluene sample reference for which the excess Rayleigh ratio is well-known ($R_{toluene}=1.3522 \times 10^{-5}$ cm$^{-1}$ at $\lambda = 632.8$ nm) and R($q$) can thus be written as:

$$R(q) = \frac{I - I_0}{I_{toluene}} \left(\frac{n_0}{n_{toluene}}\right)^2 R_{toluene}(q) \qquad \text{(eqn 18)}$$

where $I$ is the scattering intensity of the solution sample, $I_0$ the scattering intensity of the solvent, and ntoluene is the refractive index of the toluene ($n_{toluene} = 1.49$ at 20 °C). The usual equation for absolute light scattering combines the form factor $P(q)$, the structure factor $S(q)$ and the weight average molecular weight $M_w$ of the scattered objects:

$$R(q) = \frac{4\pi^2 n_0^2}{N_a \lambda^4} \left(\frac{dn}{dc}\right)^2 C M_w P(q) S(q) \qquad \text{(eqn 19)}$$

where d$n$/d$c$ is the refractive index increment and $N$a is the Avogadro's number. The d$n$/d$c$ of the two amphiphilic perylene diimides (**37** and **40**) was measured using a Mettler Toledo Portable Lab refractometer at room temperature. Values of -0.082 cm$^3$ g$^{-1}$ for **37** and 0.066 cm$^3$ g$^{-1}$ for **40** were obtained.

- *Dynamic Light Scattering (DLS)*

In DLS experiments, the normalized time autocorrelation function of the scattered intensity is measured as a function of $q$:[222]

$$g^{(2)}(q,t) = \frac{\langle I(q,0) I(q,t) \rangle}{\langle I(q,0) \rangle^2} \qquad \text{(eqn 20)}$$

The latter can be expressed in terms of the field autocorrelation function or equivalently in terms of the autocorrelation function of the concentration fluctuations, $g^{(1)}(q,t)$, through:

---

[222] (a) Schmitz, K. S. An Introduction to Dynamic Light Scattering by Macromolecules. Academic Press, London, 1990; (b) Appell, J.; Porte, G. and Buhler, E. Self-Diffusion and Collective Diffusion of Charged Colloids Studied by Dynamic Light Scattering. *J. Phys. Chem. B* **2005**, *109*, 13186–13194.

$$g^{(2)}(q,t) - 1 = \alpha + \beta \left| g^{(1)}(q,t) \right|^2 \qquad \text{(eqn 21)}$$

where $\alpha$ is the baseline (varying between $1\times 10^{-4}$ and $2 \times 10^{-4}$ depending on the scattering angle and/or the system) and $\beta$ the coherence factor, which in our experiments is varying between 0.6 and 0.9, depending on the concentration, the samples and the setup geometry. The normalized dynamical correlation function, $g^{(1)}(q,t)$, of polymer concentration fluctuations is defined as:

$$g^{(1)}(q,t) = \frac{\left\langle \delta c(q,0)\delta c(q,t) \right\rangle}{\left\langle \delta c(q,0)^2 \right\rangle} \qquad \text{(eqn 22)}$$

where $\delta c(q,t)$ and $\delta c(q,0)$ represent fluctuations of the polymer concentration at time $t$ and zero, respectively.

For solutions characterized by a single relaxation mechanism, we have adopted the classical Cumulant analysis:[223]

$$\ln g^{(1)}(t) \approx k_0 - k_1 t + \frac{k_2}{2} t^2 + \ldots \qquad \text{(eqn 23)}$$

Where $k_1 = 1/<\tau>$ and $k_2/k_1^2$ is the polydispersity index (PDI).

For a diffusive process, with characteristic time inversely proportional to $q^2$, the extrapolation of $(<\tau>q^2)^{-1}$ to $q = 0$, where $<\tau>$ is the average relaxation time of $g^{(1)}(q,t)$, yields the mutual diffusion coefficient $D = 1/(<\tau>q^2)$. The latter is related to the average apparent hydrodynamic radius, $R_H$, of the supramolecular assemblies through the Stokes–Einstein relation:

$$D = \frac{k_B T}{6\pi\eta_0 R_h} = \left( \frac{1}{\tau q^2} \right)_{q^2=0} \qquad \text{(eqn 24)}$$

where $k_B$ is the Boltzmann constant, $\eta_0$ the solvent viscosity (1 mPa s for water at $T = 20$ °C), and $T$ the absolute temperature. For solutions characterized by two diffusive relaxation mechanisms, the autocorrelation function $g^{(1)}(q, t)$ was fitted with the sum of two exponentials:

$$g^{(1)}(q,t) = A_{fast}(q) \exp\left( -\frac{t}{\tau_{fast}} \right) + A_{slow}(q) \exp\left( -\frac{t}{\tau_{slow}} \right) \qquad \text{(eqn 25)}$$

where $\tau_{\text{fast}}$ and $\tau_{\text{slow}}$ represent two cooperative characteristic relaxation times, and $A_{\text{fast}}$ and $A_{\text{slow}}$ are their corresponding amplitudes. Using (eqn 17) we can access the hydrodynamic radius of both populations.

---

[223] Koppel, D. E. Analysis of Macromolecular Polydispersity in Intensity Correlation Spectroscopy: The Method of Cumulants. *J. Chem. Phys.* **1972**, *57*, 4814.

For solutions characterized by several relaxation mechanisms we also used the Contin method based on the inverse Laplace transform of $g^{(1)}(q,t)$:[224]

$$g^{(1)}(q,t) = \int_0^\infty G(\Gamma)\exp(-\Gamma t)d\Gamma \qquad \text{(eqn 26)}$$

where G(Γ) is the normalized decay constant distribution.

### ix. TEM

TEM was performed using a CM12 Philips microscope equipped with a MVIII (SoftImaging System) CCD camera. Samples were analyzed in Bright Field Mode with a $LaB_6$ cathode and 120 kV tension. Image treatments were performed by using analySIS (Soft Imaging System) software. Samples were prepared by dropping an aqueous solution of the perylene derivative on a carbon-coated copper grid. The drop was left to adsorb for 30 seconds on the grid and the remaining solution was absorbed with a filter paper.

Freeze Fracture Electron Microscopy (FFEM) was performed with the same microscope. The gel samples were placed between two copper holders and rapidly frozen in liquid nitrogen. The sample was kept frozen and transferred into a freeze-fracture apparatus (developed by J.-C. Homo) where the sample was cleaved. Pt was then evaporated onto the sample which was allowed to warm to room temperature afterwards. The replica was rinsed with chloroform and deposited on 400 mesh grids. This technique preserves the native structure of the supramolecular polymer as solvated in the gel state.

### x. AFM

Atomic force microscopy (AFM) images were obtained by scanning the samples using a Nanoscope 8 (Bruker) operated in Peak-Force tapping mode. Peak-Force AFM is based on Peak force tapping technology, during which the probe is oscillated in a similar fashion as it is in tapping mode, but at far below the resonance frequency. Each time the tip and the sample are brought together, a force curve is captured. These forces can be controlled at levels much lower than contact mode and even lower than tapping mode allowing operation on even the most delicate soft samples, as is the case here. Ultra-sharp silicon cantilevers were used. During AFM imaging, the force was reduced in order to avoid dragging of molecules by the tip. Integral gain was adjusted to give sharp images. All analyses of the images were conducted in integrated software.

---

[224] S.W. Provencher, *Makromol. Chem*. **1985**, *82*, 632.

## d. Preparation of solution samples

For concentration-dependent UV-Vis and fluorescence experiments, a precise amount of compound (Table 5) was dissolved in the selected solvent (3 mL) to get a $10^{-2}$ mol/L solution. Then 200 µL of this $10^{-2}$ mol/L solution was diluted into 1.8 mL of solvent to get the $10^{-3}$ mol/L solution. Following the same protocol, solutions at $10^{-4}$, $10^{-5}$, $10^{-6}$, $10^{-7}$ and $10^{-8}$ mol/L were obtained. For $5 \times 10^{-3}$ mol/L solutions, 1000 µL of a $10^{-2}$ mol/L solution was diluted into 2 mL of solvent. Solutions at $5 \times 10^{-4}$, $5 \times 10^{-5}$, $5 \times 10^{-6}$, $5 \times 10^{-7}$, and $5 \times 10^{-8}$ mol/L were obtained according to the same procedure.

**Table 5|** Quantities of compounds necessary to get 3 mL of a $10^{-2}$ M solution

| Molecule | Weight (mg) |
|---|---|
| **33** | 49.5 |
| **34** | 51.3 |
| **37** | 31.1 |
| **41** | 55.5 |
| **42** | 47.9 |
| **43** | 54.6 |

## 2. Synthetic procedures

### Compound 1

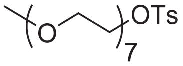

**1**

A solution of tosyl chloride (34.28 mmol, 6.5 g) in pyridine (10.3 mL) was added slowly over a solution of polyethylene glycol monomethylether 350 (28.57 mmol, 10.0 g) in pyridine (10 mL) at 0 °C. The mixture was stirred for 8 h at 0 °C and treated by adding ice with a 6N HCl solution (101.5 mL). The mixture was extracted three times with dichloromethane (100 mL) and the organic layer was washed with a 2N HCl solution (300 mL). The organic layer was dried over $Na_2SO_4$ and evaporated to provide pure tosylated compound **1** (13.1 g, 91%) as a clear yellow oil. $^1$H NMR ($CDCl_3$, 400 MHz, 25°C): $\delta$ = 7.76 (d, $^3J$=8.4 Hz, 2H), 7.31 (d, $^3J$=8.3 Hz, 2H), 4.12 (t, $^3J$=4.8 Hz, 2H), 3.66 (t, $^3J$=5.0 Hz, 2H), 3.62-3.48 (brm, 26H), 3.34 (s, 3H), 2.41 (s, 3H); $^{13}$C NMR ($CDCl_3$, 100 MHz, 25°C): $\delta$ = 144.66, 132.90, 129.70, 127.84, 71.80, 70.60, 70.47, 70.43, 70.37, 69.13, 68.54, 58.88, 21.50; ESI-MS: calcd for $C_{22}H_{38}O_{10}S$ 495.22 $[M+H]^+$, found: 495.45.

### Compound 2

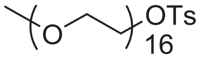

**2**

A solution of tosyl chloride (53.34 mmol, 10.2 g) in pyridine (16 mL) was added in two portions (30 min between each addition) over a solution of polyethylene glycol monomethylether 750 (26.67 mmol, 20.0 g) was dissolved in pyridine (20.0 mL) with a small amount of dichloromethane at 0 °C. The mixture was stirred for 8 h at 0 °C, and treated by adding ice with a 6N HCl solution (180 mL). The mixture was extracted three times with dichloromethane (120 mL) and the organic layer was washed with a 2N HCl solution (540 mL). The organic layer was dried over sodium sulfate and evaporated to provide pure tosylated compound **2** (21.9 g, 91%) as a clear yellow oil. $^1$H NMR (CDCl$_3$, 400 MHz, 25°C): δ = 7.79 (d, $^3J$=8.4 Hz, 2H), 7.33 (d, $^3J$=8.3 Hz, 2H), 4.14 (t, $^3J$=4.8 Hz, 2H), 3.67 (t, $^3J$=4.8 Hz, 2H), 3.65-3.64 (m, 6H), 3.63-3.61 (m, 44H), 3.60-3.59 (m, 4H), 3.57-3.56 (m, 4H), 3.54-3.53 (m, 2H), 3.37 (s, 3H), 2.44 (s, 3H); $^{13}$C NMR (CDCl$_3$, 100 MHz, 25°C): δ = 144.78, 133.05, 129.83, 127.99, 71.94, 70.75, 70.57, 70.51, 69.25, 68.69, 59.04, 21.66; ESI-MS: calcd for $C_{40}H_{74}O_{19}S$ 908.47 [M+H$_2$O]$^+$, found: 908.90.

### *Compound 3*

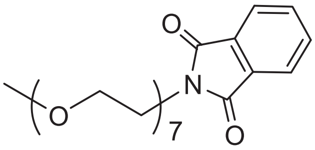

**3**

Phthalimide (5.31 mmol, 781 mg) was dissolved in acetonitrile (27.3 mL) and the solution was heated up to reflux. Potassium carbonate (5.31 mmol, 744 mg) was then added followed by compound **1** (4.42 mmol, 2.2 g). The mixture was stirred for 40 h at reflux. The solvent was then evaporated and water was added (50 mL). The aqueous mixture was extracted three times with dichloromethane (25 mL). The resulting organic phase was then washed with a pH 12 aqueous solution (50 mL), dried over sodium sulfate and further evaporation under reduced pressure afforded pure compound **3** (1.4 g, 64%) as a white solid. $^1$H NMR (CDCl$_3$, 400 MHz, 25°C): δ = 7.84-7.82 (m, 2H), 7.75-7.73 (m, 2H), 4.37 (t, $^3J$=5.6 Hz, 2H), 3.86 (t, $^3J$=6.0 Hz, 2H), 3.65-3.53 (m, 24H), 3.37 (s, 3H); $^{13}$C NMR (CDCl$_3$, 100 MHz, 25°C): δ = 163.41, 134.43, 128.99, 123.47, 77.19, 71.95, 70.79, 70.59, 70.57, 70.49, 70.47, 69.31, 59.02, 53.39. ESI-MS: calcd for $C_{23}H_{35}NO_9$ 487.23 [M+H$_2$O]$^+$, found:487.50.

### *Compound 4*

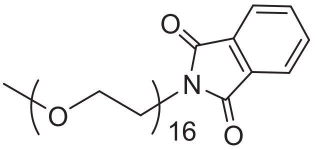

**4**

Phthalimide (10.05 mmol, 1.48 g) was dissolved in acetonitrile (44.4 mL) and the solution was heated up to reflux. Potassium carbonate (15.08 mmol, 2.08 g) was then added followed by compound **2** (5.03 mmol, 4.54 g). The mixture was stirred for 40 h at reflux. The solvent was then evaporated and water was added (90 mL). The aqueous mixture was extracted three times with dichloromethane (45 mL). The resulting organic phase was then washed with a pH 12 aqueous solution (90 mL), dried over sodium sulfate and further evaporation under reduced pressure afforded pure compound **4** (2.83 g, 64%) as a yellow solid. $^1$H NMR ($CDCl_3$, 400 MHz, 25°C): $\delta$ = 7.86-7.84 (m, 2H), 7.74-7.72 (m, 2H), 3.89 (t, $^3J$=5.8 Hz, 2H), 3.74 (t, $^3J$=5.8 Hz, 2H), 3.69-3.59 (m, 60H), 3.38 (s, 3H); $^{13}$C NMR ($CDCl_3$, 100 MHz, 25°C): $\delta$ = 168.24, 133.92, 132.15, 123.25, 71.95, 70.57, 70.09, 67.89, 59.03, 37.26; ESI-MS: calcd for $C_{41}H_{71}NO_{18}$ 883.48 $[M+H_2O]^+$, found: 883.88.

### Compound 5

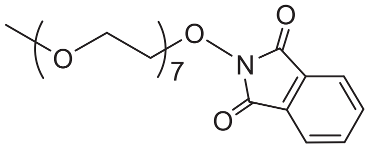

**5**

*N*-hydroxyphthalimide (7.14 mmol, 1.17 g) was dissolved in acetonitrile (23.3 mL) and the solution was heated up to reflux. Triethylamine (1.0 mL) was then added followed by compound **1** (5.95 mmol, 3.0 g). The mixture was stirred for 10 h at reflux. The solvent was then evaporated and water was added (80 mL). The aqueous mixture was extracted three times with dichloromethane (40 mL). The resulting organic phase was then washed with a pH 12 aqueous solution (80 mL), dried over sodium sulfate and further evaporation under reduced pressure afforded pure compound **5** (2.06 g, 70%) as a dark yellow oil. $^1$H NMR ($CDCl_3$, 400 MHz, 25°C): $\delta$ = 7.85-7.83 (m, 2H), 7.75-7.73 (m, 2H), 4.37 (t, $^3J$=4.4 Hz, 2H), 3.86 (t, $^3J$=4.4 Hz, 2H), 3.68-3.56 (m, 24H), 3.37 (s, 3H); $^{13}$C NMR ($CDCl_3$, 100 MHz, 25°C): $\delta$ = 163.42, 134.40, 129.00, 123.48, 77.21, 71.93, 70.78, 70.56, 70.51, 69.27, 59.02. ESI-MS: calcd for $C_{23}H_{35}NO_{10}$ 503.23 $[M+H_2O]^+$, found 503.61.

## Compound 6

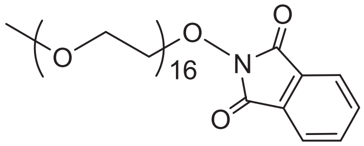

**6**

*N*-hydroxyphthalimide (3.98 mmol, 650 mg) was dissolved in acetonitrile (13 mL) and the solution was heated up to reflux. Triethylamine (0.56 mL) was then added followed by compound **2** (3.32 mmol, 3.0 g). The mixture was stirred for 10 h at reflux. The solvent was then evaporated and water was added (60 mL). The aqueous mixture was extracted three times with dichloromethane (30 mL). The resulting organic phase was then washed with a pH 12 aqueous solution (80 mL), dried over sodium sulfate and further evaporation under reduced pressure afforded pure compound **6** (2.08 g, 70%) as a yellow oil. $^1$H NMR (CDCl$_3$, 400 MHz, 25°C): δ = 7.84-7.82 (m, 2H), 7.75-7.73 (m, 2H), 4.37 (t, $^3J$=4.6 Hz, 2H), 3.86 (t, $^3J$=4.6 Hz, 2H), 3.66-3.56 (m, 60H), 3.37 (s, 3H); $^{13}$C NMR (CDCl$_3$, 100 MHz, 25°C): δ = 163.48, 134.48, 129.05, 123.53, 77.27, 71.99, 70.82, 70.61, 69.35, 59.08; ESI-MS: calcd for $C_{41}H_{71}NO_{19}$ 899.47 $[M+H_2O]^+$, found: 899.88.

## Compound 7

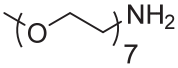

**7**

Compound **3** (2.82 mmol, 1.35 g) was dissolved in THF (40.5 mL) and aqueous hydrazine (5.5 mL) was added slowly. The mixture was stirred for 4 h at room temperature. The solvent was evaporated and water was added (110 mL). The aqueous phase was extracted three times with chloroform (110 mL) and the combined organic layer was dried over sodium sulfate. Further evaporation under reduced pressure afforded pure compound **7** (783 mg, 75%) as a yellow-brown oil. $^1$H NMR (CDCl$_3$, 400 MHz, 25°C): δ = 3.64-3.50 (m, 26H), 3.38 (s, 3H), 2.86 (t, $^3J$=4.8 Hz, 2H); $^{13}$C NMR (CDCl$_3$, 100 MHz, 25°C): δ = 77.20, 72.71, 71.84, 70.49, 70.46, 70.40, 70.31, 70.27, 70.20, 70.10, 70.03, 61.54, 58.94; ESI-MS: calcd for $C_{15}H_{33}NO_7$ 340.23

$[M+H]^+$, found: 340.40.

### *Compound 8*

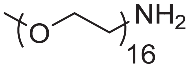

**8**

Compound **4** (3.81 mmol, 3.35 g) was dissolved in THF (100 mL) and aqueous hydrazine (7.4 mL) was added slowly. The mixture was stirred for 4 h at room temperature. The solvent was evaporated and water was added (250 mL). The aqueous phase was extracted three times with chloroform (250 mL) and the combined organic layer was dried over sodium sulfate. Further evaporation under reduced pressure afforded pure compound **8** (2.28 g, 80%) as a yellow-brown oil. $^1$H NMR ($CDCl_3$, 400 MHz, 25°C): $\delta$ = 3.64-3.50 (m, 62H), 3.36 (s, 3H), 2.90 (t, $^3J$=4.8 Hz, 2H); $^{13}$C NMR ($CDCl_3$, 100 MHz, 25°C): $\delta$ = 77.20, 72.71, 71.84, 70.49, 70.46, 70.40, 70.31, 70.27, 70.20, 70.10, 70.03, 61.54, 58.94; ESI-MS: calcd for $C_{33}H_{69}NO_{16}$ 736.46 $[M+H]^+$, found: 736.64.

### *Compound 9*

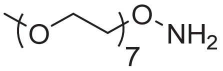

**9**

Compound **5** (4.87 mmol, 2.41 g) was dissolved in THF (72.4 mL) and aqueous hydrazine (9.5 mL) was added slowly. The mixture was stirred for 4 h at room temperature. The solvent was evaporated and water was added (200 mL). The aqueous phase was extracted three times with chloroform (200 mL) and the combined organic layer was dried over sodium sulfate. Further evaporation under reduced pressure afforded pure compound **9** (1.26 g, 71%) as a yellow-brown oil. $^1$H NMR ($CDCl_3$, 400 MHz, 25°C): $\delta$ = 3.87-3.85 (m, 2H), 3.70-3.58 (m, 24H), 3.56-3.54 (m, 2H), 3.38 (s, 3H); $^{13}$C NMR ($CDCl_3$, 100 MHz, 25°C): $\delta$ = 77.20, 72.7, 71.84, 70.49, 70.46, 70.40, 70.31, 70.27, 70.20, 70.10, 70.03, 61.54, 58.94; ESI-MS: calcd for $C_{15}H_{33}NO_8$ 356.22 $[M+H]^+$, found: 356.41.

### Compound 10

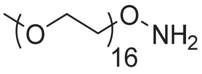

**10**

Compound **6** (1.40 mmol, 1.25 g) was dissolved in THF (37.5 mL) and aqueous hydrazine (2.7 mL) was added slowly. The mixture was stirred for 4 h at room temperature. The solvent was evaporated and water was added (100 mL). The aqueous phase was extracted three times with chloroform (100 mL) and the combined organic layer was dried over sodium sulfate. Further evaporation under reduced pressure afforded pure compound **10** (750 mg, 70%) as a yellow-brown oil. $^1$H NMR ($CDCl_3$, 400 MHz, 25°C): δ = 3.91-3.89 (m, 2H), 3.69-3.59 (m, 60H), 3.55-3.53 (m, 2H), 3.37 (s, 3H); $^{13}$C NMR ($CDCl_3$, 100 MHz, 25°C): δ = 77.20, 72.71, 71.84, 70.49, 70.46, 70.40, 70.31, 70.27, 70.20, 70.10, 70.03, 61.54, 58.94; ESI-MS: calcd for $C_{33}H_{69}NO_{17}$ 752.46 $[M+H]^+$, found: 752.81.

### Compound 11

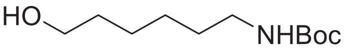

**11**

Di-*tert*-butyl-dicarbonate (17.0 mmol, 3.72 g) was added into a solution of 6-amino-1-hexanol (17.0 mmol, 2.00 g) in THF (10 mL) at 0 °C. This reaction was stirred overnight from 0 °C to room temperature and monitored by TLC analysis. The solvent was then evaporated. The residue was dissolved in $CH_2Cl_2$ (55 mL) and the organic phase was extracted with saturated $NH_4Cl$ (110 mL) and NaCl (65 mL). The organic solution was dried over $Na_2SO_4$ and further evaporation under reduced pressure provided compound **11** (3.18 g, 86%) as a yellow oil. $R_f$ (cyclohexane/EtOAc 3/1) = 0.3; $^1$H NMR ($CDCl_3$, 400 MHz, 25°C): δ = 3.61 (t, $^3J$=6.4 Hz, 2H), 3.09 (t, $^3J$=6.8 Hz, 2H), 1.58-1.50 (m, 2H), 1.48-1.45 (m, 2H), 1.42 (s, 9H), 1.39-1.29 (m, 4H); $^{13}$C NMR ($CDCl_3$, 100 MHz, 25°C): δ = 156.28, 79.21, 62.65, 40.51, 32.70, 30.18, 28.56, 26.55, 25.46; ESI-MS: calcd for $C_{11}H_{23}NO_3$ 240.17 $[M+Na]^+$, found: 240.11.

### Compound 12

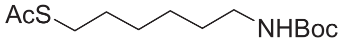

**12**

Compound **11** (0.23 mmol, 50.0 mg) and triphenyl phosphine (0.25 mmol, 66.4 mg) were dissolved in THF (1.1 mL). The mixture was cooled down to 0 °C. Diisopropyl azodicarboxylate (DIAD, 0.25 mmol, 49.8 μL) and thioacetic acid (0.25 mmol, 18.0 μL) were then added dropwise. The reaction was stirred from 0 °C to room temperature overnight and monitored by TLC. The reaction mixture was then evaporated, and the residue was purified by flash chromatogram ($SiO_2$, cyclohexane/ethyl acetate: 50/1 → 10/1) to yield compound **12** (42.8 mg, 68%) as a slight yellow oil. $R_f$ (cyclohexane/EtOAc 3/1) = 0.5; $^1$H NMR ($CDCl_3$, 400 MHz, 25°C): δ = 3.07 (t, $^3J$=7.1 Hz, 2H), 2.83 (t, $^3J$=7.3 Hz, 2H), 2.30 (s, 3H), 1.58-1.51 (m, 2H), 1.48-1.44 (m, 2H), 1.42 (s, 9H), 1.37-1.26 (m, 4H); $^{13}$C NMR ($CDCl_3$, 100 MHz, 25°C): δ = 195.79, 155.81, 78.83, 40.31, 30.47, 29.75, 29.26, 28.82, 28.26, 28.23, 26.10; ESI-MS: calcd for $C_{13}H_{25}NO_3S$ 298.16 $[M+Na]^+$, found: 298.08.

### Compound 13

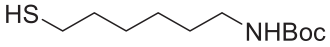

**13**

A solution of sodium thiomethoxide (1.36 mmol, 96.4 mg) in dry methanol (7.55 mL) was added dropwise to a solution of compound **12** (1.36 mmol, 374.6 mg) in dry tetrahydrofurane (30.2 mL) at 0 °C under an argon atmosphere. The reaction was stirred for 20 min at 0 °C and then up room temperature for 1 h. Upon completion (monitoring by TLC), the mixture was evaporated and the residue was carefully kept under argon for next step. $R_f$ (n-pentane/EtOAc 3/1) = 0.4; $^1$H NMR ($CDCl_3$, 400 MHz, 25°C): δ = 3.08 (t, $^3J$=5.6 Hz, 2H), 2.49 (t, $^3J$=7.0 Hz, 2H), 1.64-1.55 (m, 2H), 1.49-1.47 (m, 2H), 1.42 (s, 9H), 1.35-1.24 (m, 4H).

### Compound 14

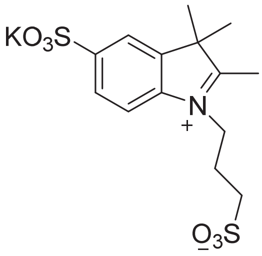

**14**

**2,3,3-trimethyl-1-(3-sulfonatopropyl)-*3H*-indolinium-5-sulfonate:** Potassium 2,3,3-trimethyl-*3H*-indole-5-sulfonate (40.27 mmol; 10.0 g) and 1,3-propane sultone (84.56 mmol; 10.3 g) were mixed in 1,2-dichlorobenzene (141 mL) and the reaction mixture was heated to 120 °C for 3 days under an argon atmosphere. The mixture was then cooled down to room temperature, the precipitate was filtered and washed with diethylether (800 mL) to give practically pure compound **14** (11.4 g, 72%) as a red solid. $^1$H NMR (DMSO-d$_6$, 400 MHz, 25°C): δ = 8.01 (d, $^4J$=1.0 Hz, 1H), 7.97 (d, $^3J$=8.4 Hz, 1H), 7.80 (dd, $^3J$=8.4 Hz, $^4J$=1.4 Hz, 1H), 4.63 (t, $^3J$=7.9 Hz, 2H), 2.83 (s, 3H), 2.62 (t, $^3J$=6.5 Hz, 2H), 2.19-2.11 (m, 2H), 1.54 (s, 6H); $^{13}$C NMR (DMSO-d$_6$, 100 MHz, 25°C): δ = 197.83, 149.09, 141.81, 141.30, 126.50, 120.80, 115.10, 57.87, 54.21, 48.81, 25.54, 22.08, 14.14; ESI-MS: calcd for $C_{14}H_{19}NO_6S_2$ 360.06 [M+H]$^+$, found: 360.05.

### Compound 15

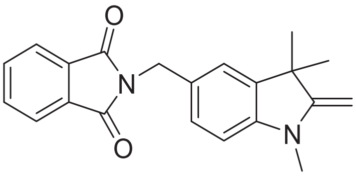

**15**

*N*-hydroxymethylphthalimide (66 mmol, 11.80 g) was added portionwise over a period of 45 min to a stirred solution of Fischer's base (66 mmol, 11.53 g) in concentrated sulfuric acid (60 mL) at room temperature. Upon dissolution of the hydroxymethyl compound, the solution was stirred for 70 hours at room temperature before being poured onto ice-water. Basification with dilute ammonia (2M, 150 mL) gave a yellow solid which was shaken up with diethylether (300 mL) to give an ether-soluble fraction and an insoluble residue. Both of these fractions were found to be mixtures of two isomeric phthalimides, the ether insoluble fraction consisting predominantly of one isomer. Recrystallization of this solid from ethanol-dichloromethane (100 mL, 4:1) gave compound **15** (13.1 g, 60%) as a yellow powder. $^1$H NMR (CDCl$_3$, 400 MHz, 25°C): δ = 7.83-7.81 (m, 2H), 7.67-7.69 (m, 2H), 7.27 (dd, $^3J$=8.0 Hz, $^4J$=1.8 Hz, 1H), 7.19 (d, $^4J$=1.7 Hz, 1H), 6.45 (d, $^3J$=8.0 Hz, 1H), 4.76 (s, 2H), 3.82 (s, 2H), 2.99 (s, 3H), 1.31 (s, 6H); $^{13}$C NMR (CDCl$_3$, 100 MHz, 25°C): δ = 168.19, 162.86, 146.18, 138.03, 133.83, 132.28, 128.77, 126.45, 123.24, 122.87, 104.60, 73.39, 44.07, 41.65, 29.88, 28.77; ESI-MS: calcd for $C_{21}H_{20}N_2O_2$ 333.15 [M+H]$^+$, found: 332.80.

### Compound 16

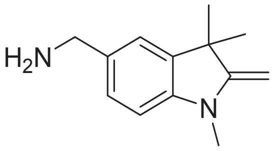

**16**

Compound **15** (12.0 mmol, 4.00 g) was heated up overnight under reflux in concentrated hydrochloric acid (28 mL). After cooling to room temperature, the precipitate was filtered off and the filtrate was basified with ammonia (108 mL). Extraction of this aqueous solution with diethylether (361 mL) and further evaporation under reduced pressure yielded compound **16** (2.13 g, 88%) as a yellow viscous oil. $^1$H NMR (CDCl$_3$, 400 MHz, 25°C): δ = 7.06-7.04 (m, 2H), 6.48 (d, $^3J$=8.4 Hz, 1H), 3.83 (s, 2H), 3.78 (s, 2H), 3.03 (s, 3H), 1.34 (s, 6H); $^{13}$C NMR (CDCl$_3$, 100 MHz, 25°C): δ = 163.03, 145.49, 138.06, 133.45, 126.40, 121.03, 104.60, 72.93, 46.45, 44.12, 29.92, 28.81; ESI-MS: calcd for $C_{13}H_{18}N_2$ 203.15 [M+H]$^+$, found: 203.11.

### Compound 17

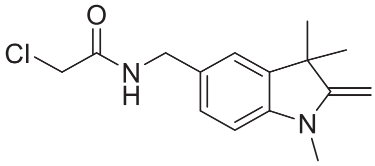

**17**

A solution of compound **16** (10.9 mmol, 2.20 g) and triethylamine (1.53 mL) in dichloromethane (217 mL) was added dropwise to a stirred solution of chloroacetyl chloride (870 µL) in dichloromethane (44 mL) at 0 °C under argon. After 3 h, the solution was diluted with dichloromethane (435 mL) and washed twice with 1N hydrochloric acid (869 mL). Neutralization of the aqueous acidic layer with a 2N sodium hydroxide solution (435 mL), followed by extraction with $Et_2O$ (1.3 L). Further evaporation under reduced pressure give compound **17** (1.96 g, 65%) as an oil, which rapidly turned reddish purple in air. This oil was used without further purification for the preparation of compound **19**. $^1H$ NMR ($CDCl_3$, 400 MHz, 25°C): $\delta$ = 7.01 (d, $^3J$=7.6 Hz, 1H), 6.97 (s, 1H), 6.44 (d, $^3J$=8.0 Hz, 1H), 4.34 (d, $^3J$=6.0 Hz, 1H), 4.02 (s, 2H), 3.82 (s, 2H), 2.98 (s, 3H), 1.31 (s, 6H); $^{13}C$ NMR ($CDCl_3$, 100 MHz, 25°C): $\delta$ = 181.02, 165.72, 162.31, 145.92, 138.00, 127.37, 126.88, 121.65, 104.51, 73.45, 45.65, 43.67, 29.71, 28.59; ESI-MS: calcd for $C_{15}H_{19}ClN_2O$ 279.12 $[M+H]^+$, found: 279.06.

### Compound 18

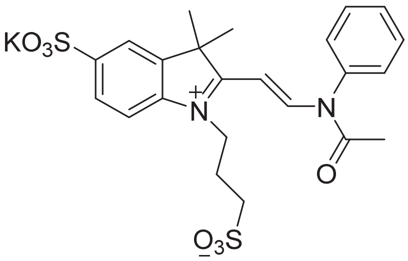

**18**

A mixture of compound **14** (5.55 mmol, 2.0 g) and *N,N*-diphenylformamidine (25.5 mmol, 5.0 g) in acetic acid-acetic anhydride (25 mL, 1:2) was heated to reflux for two hours. After that time, the solvents were evaporated and the product was washed with acetone until compound **18** was obtained (1.96 g, 70%) as a yellow powder. $^{1}$H NMR (DMSO-d$_6$, 400 MHz, 25°C): δ = 8.68 (d, $^{3}J$=12.2 Hz, 1H), 7.82 (s, 1H), 7.67 (d, $^{3}J$=8.3 Hz, 1H), 7.51-7.48 (m, 5H), 7.28 (brd, $^{3}J$=6.8 Hz, 1H), 6.22 (d, $^{3}J$=12.7 Hz, 1H), 4.23 (brt, $^{3}J$=6.4 Hz, 2H), 2.62 (t, $^{3}J$=7.1 Hz, 2H), 2.06-2.03 (m, 2H), 1.71 (s, 6H), [3 protons are hidden by the residual DMSO signal]; $^{13}$C NMR (MeOD, 100 MHz, 25°C): δ = 180.62, 154.18, 144.28, 142.40, 139.57, 131.44, 131.36, 130.42, 129.90, 128.40, 128.18, 125.33, 124.22, 121.58, 121.38, 119.41, 54.94, 51.26, 44.51, 28.86, 23.94, 23.79; ESI-MS: calcd for $C_{23}H_{25}N_2O_7S_2$ 506.11 [M+H]$^+$, found: 506.95.

### *Compound 19*

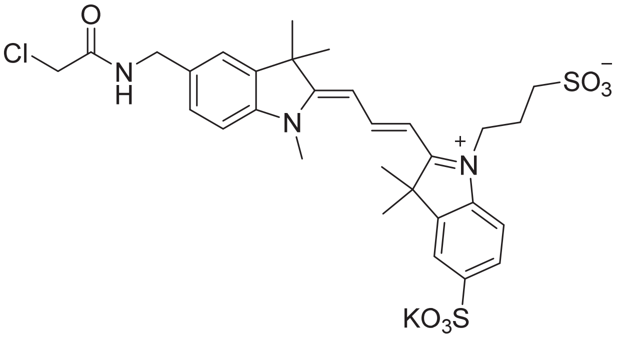

**19**

A mixture of compound **17** (3.38 mmol, 1.07 g) and compound **18** (3.38 mmol, 1.94 g) was heated at 130 °C in acetic anhydride (29 mL) under argon for 45 min. The mixture was then cooled to room temperature, and the resulting precipitate was separated by filtration. The crude mixture was purified by preparative HPLC to yield compound **19** (987 mg, 45%) as a purple solid. $^{1}$H NMR (MeOD, 400 MHz, 25°C): δ = 8.49 (dd, $^{3}J$=13.4, 13.4 Hz, 1H), 7.87-7.83 (m, 2H), 7.46 (d, $^{3}J$=1.2 Hz, 1H), 7.40-7.36 (m, 2H), 7.31 (d, $^{3}J$=8.4 Hz, 1H), 6.54 (d, $^{3}J$=13.2 Hz, 1H), 6.50 (d, $^{3}J$=14.0 Hz, 1H), 4.44 (s, 2H), 4.30 (brt, $^{3}J$=8.0 Hz, 2H), 4.06 (s, 2H), 3.67 (s, 3H), 2.95 (t, $^{3}J$=6.6 Hz, 2H), 2.24 (brt, $^{3}J$=7.2 Hz, 2H), 1.74 (s, 6H), 1.72 (s, 6H); $^{13}$C NMR (MeOD, 100 MHz, 25°C): δ = 183.85, 177.08, 144.71, 144.60, 144.05, 143.64, 142.34, 141.26, 137.05, 128.69, 128.47, 122.44, 121.72, 121.57, 116.84, 112.46, 109.64, 105.26, 61.74, 56.37, 50.85, 45.64, 44.43, 40.13, 28.52, 28.40, 26.64, 24.63; ESI-MS: calcd for $C_{30}H_{35}ClN_3O_7S_2$ 648.16 [M]$^-$, found: 648.17.

### *Compound 20*

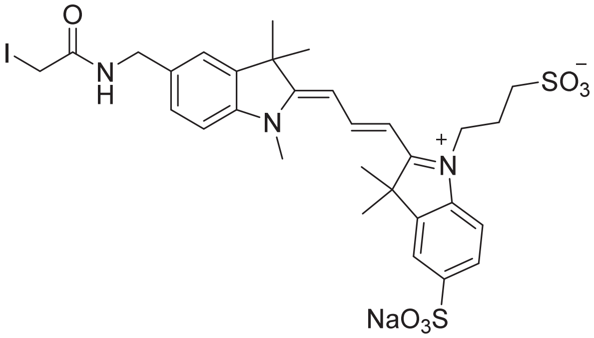

**20**

A mixture of compound **19** (0.26 mmol, 170 mg) and sodium iodide (1.97 mmol, 294 mg) in methanol (5 mL) was refluxed for 3 hours. The crude mixture was cooled to room temperature, filtered and evaporated and the purple solid was kept in vacuo overnight for next step. $^1$H NMR (MeOD, 400 MHz, 25°C): δ = 8.48 (dd, $^3J$=13.2, 13.2 Hz, 1H), 7.92 (s, 1H), 7.88 (d, $^3J$=7.0 Hz, 1H), 7.49 (s, 1H), 7.43-7.31 (m, 3H), 6.58 (d, $^3J$=13.2 Hz, 1H), 6.55 (d, $^3J$=13.2 Hz, 1H), 4.41 (s, 2H), 4.31 (t, $^3J$=7.4 Hz, 2H), 3.73 (s, 2H), 3.69 (s, 3H), 2.96 (t, $^3J$=6.6 Hz, 2H), 2.20 (brt, $^3J$=7.2 Hz, 2H), 1.74 (s, 6H), 1.72 (s, 6H); $^{13}$C NMR (MeOD, 100 MHz, 25°C): δ = 178.51, 176.30, 172.22, 153.20, 145.64, 144.18, 144.03, 143.57, 142.73, 139.51, 130.15, 129.11, 123.51, 122.24, 113.60, 112.49, 106.34, 104.82, 63.64, 51.76, 51.12, 44.92, 44.85, 33.19, 29.26, 28.97, 24.83; ESI-MS: calcd for $C_{30}H_{35}IN_3O_7S_2$ 740.09 [M]$^-$, found: 740.10.

### *Compound 21*

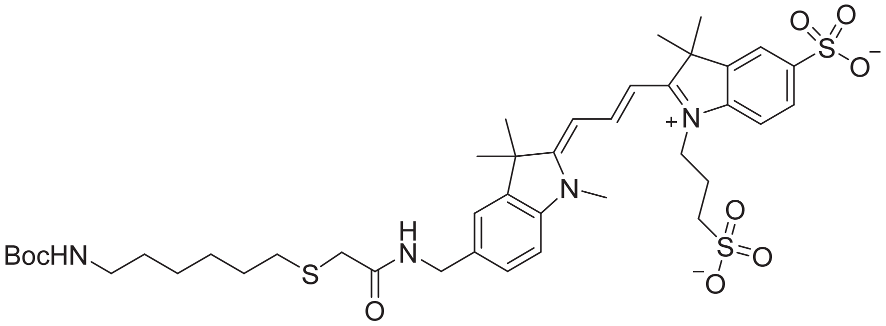

**21**

Potassium carbonate (1.14 mmol, 159.6 mg), compound **13** (0.76 mmol, 177.1 mg) and compound **20** (0.38 mmol, 281.0 mg) were dissolved in DMF (32 mL). The reaction mixture was stirred at room temperature overnight and monitored by

UPLC-MS. Further evaporation under reduced pressure and purification by preparative HPLC afforded compound **21** (72.7 mg, 23%) as a purple solid. $^1$H NMR (MeOD, 400 MHz, 25°C): δ = 8.58-8.51 (m, 1H), 7.92 (s, 1H), 7.90 (d, $^3J$= 1.6 Hz, 1H), 7.52 (s, 1H), 7.45-7.35 (m, 2H), 7.36 (d, $^3J$=8.4 Hz, 1H), 6.60 (d, $^3J$=13.2 Hz, 1H), 6.55 (d, $^3J$=13.6 Hz, 1H), 4.47 (s, 2H) , 4.36 (t, $^3J$=8.0 Hz, 2H), 3.73 (s, 3H), 3.23 (s, 2H), 3.04-2.98 (m, 4H), 2.59 (t, $^3J$=7.3 Hz, 2H), 2.28-2.21 (m, 2H), 1.79 (s, 6H), 1.77 (s, 6H), 1.63-1.56 (m, 2H), 1.42 (s, 9H), 1.39-1.26 (m, 6H); $^{13}$C NMR (MeOD, 100 MHz, 25°C): δ = 177.65, 175.55, 172.88, 158.58, 152.39, 144.86, 143.57, 143.25, 142.80, 141.99, 138.75, 129.52, 128.35, 123.00, 121.49, 112.83, 111.79, 105.56, 104.09, 79.86, 50.98, 50.39, 44.08, 41.37, 36.33, 33.58, 32.40, 30.94, 30.28, 29.56, 28.97, 28.55, 28.22, 27.49, 24.15; ESI-MS: calcd for $C_{41}H_{57}N_4O_9S_3$ 845.33 $[M]^-$, found: 845.60.

### Compound 22

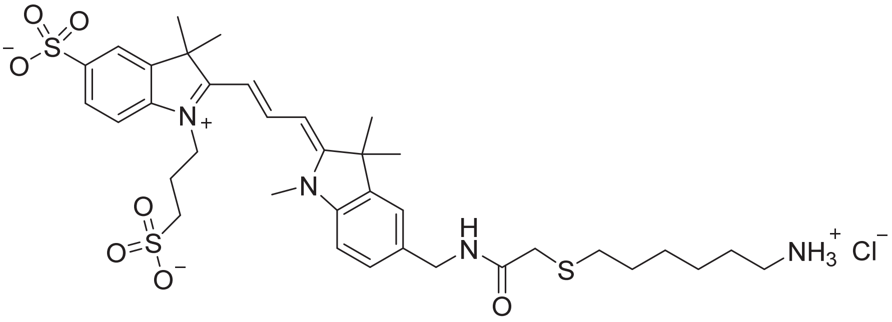

**22**

Acetyl chloride (500 µL) was added dropwise to a solution of compound **21** (0.015 mmol, 12.7 mg) in methanol (500 µL) at 0 °C. The reaction mixture was stirred at 0 °C for 30 min and monitored by UPLC-MS. Further evaporation under reduced pressure afforded compound **22** as a purple solid, which was pure enough to be used as such in the next step. $^1$H NMR (MeOD, 400 MHz, 25°C): δ = 8.58-8.51 (m, 1H), 7.92 (s, 1H), 7.90 (d, $^3J$=1.6 Hz, 1H), 7.52 (s, 1H), 7.45-7.41 (m, 2H), 7.36 (d, $^3J$= 8.4 Hz, 1H), 6.60 (d, $^3J$=13.2 Hz, 1H), 6.55 (d, $^3J$=13.6 Hz, 1H), 4.47 (s, 2H), 4.36 (t, $^3J$=8.0 Hz, 2H), 3.73 (s, 3H), 3.23 (s, 2H), 3.01 (t, $^3J$=6.8 Hz, 2H), 2.91 (t, $^3J$=7.3 Hz, 2H), 2.62 (t, $^3J$=7.3 Hz, 2H), 2.29-2.22 (m, 2H), 1.78 (s, 6H), 1.75 (s, 6H), 1.67-1.59 (m, 4H), 1.46-1.39 (m, 4H); $^{13}$C NMR (MeOD, 100 MHz, 25°C): δ = 177.65, 175.55, 172.88, 152.39, 144.86, 143.57, 143.25, 142.80, 141.99, 138.75, 129.52, 128.35, 123.00, 121.49, 112.83, 111.79, 105.56, 104.09, 50.98, 50.39, 44.19, 40.85, 36.17, 33.44, 32.61, 30.04, 29.28, 28.62, 28.49, 28.27, 27.08, 24.15; ESI-MS: calcd for $C_{36}H_{50}N_4O_7S_3$ 745.28 $[M]^-$, found: 745.37.

### Compound 23

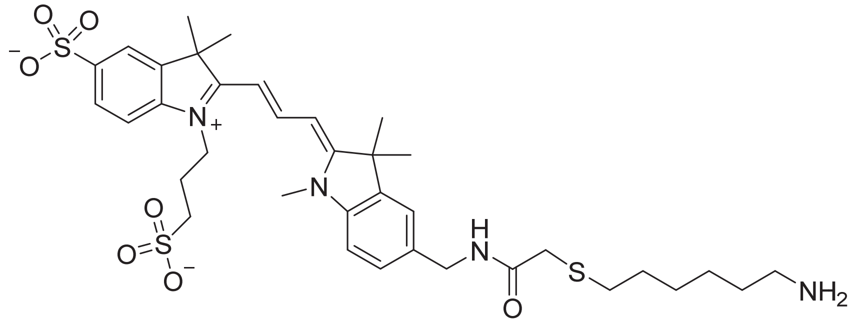

**23**

*N,N*-diisopropylethylamine (DIPEA, 3.9 μL) was added dropwise to a solution of compound **22** (0.022 mmol, 17.5 mg) in methanol (1 mL). The reaction was stirred at 50 °C for 2 h. Further evaporation under reduced pressure afforded compound **23** (15.6 mg, 95%) as a purple solid. $^1$H NMR (MeOD, 400 MHz, 25°C): δ = 8.54 (dd, $^3J$=13.2, 13.2 Hz, 1H), 7.92 (s, 1H), 7.90 (d, $^3J$=7.0 Hz, 1H), 7.52 (s, 1H), 7.45-7.35 (m, 3H), 6.60 (d, $^3J$=13.2 Hz, 1H), 6.55 (d, $^3J$=13.2 Hz, 1H), 4.47 (s, 2H), 4.36 (t, $^3J$=7.4 Hz, 2H), 3.73 (s, 3H), 3.23 (s, 2H), 3.01 (t, $^3J$=7.0 Hz, 2H), 2.91 (t, $^3J$=7.3 Hz, 2H), 2.59 (t, $^3J$=7.3 Hz, 2H), 2.28-2.21 (m, 2H), 1.79 (s, 6H), 1.77 (s, 6H), 1.66-1.59 (m, 4H), 1.47-1.29 (m, 4H); $^{13}$C NMR (MeOD, 100 MHz, 25°C): δ = 176.14, 174.22, 171.60, 151.00, 143.29, 141.71, 141.30, 140.48, 137.02, 128.00, 126.85, 121.31, 119.97, 111.22, 110.24, 103.90, 102.55, 49.39, 48.85, 42.51, 39.27, 34.68, 31.89, 30.83, 28.41, 27.71, 27.09, 26.99, 26.71, 25.51, 22.46; ESI-MS: calcd for $C_{36}H_{49}N_4O_7S_3$ 745.28 $[M]^-$, found: 744.96.

### Compound 24

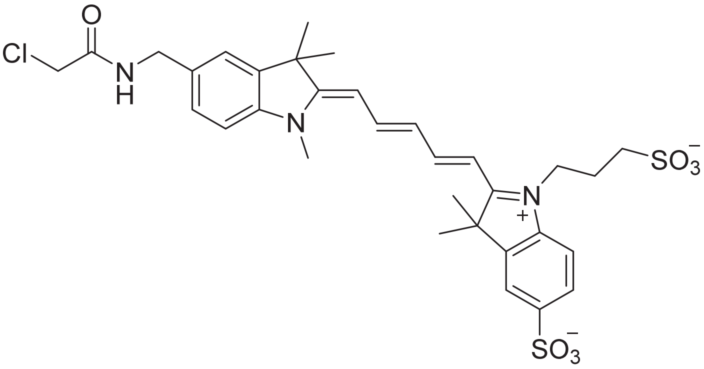

**24**

A mixture of compound **14** (7.83 mmol, 2.82 g) and malonaldehyde dianilide hydrochloride (3.53 mmol, 920 mg) in acetic acid-acetic anhydride (14 mL, 1:2) was heated to reflux for 2 hours. The resulting mixture was mixed with compound **17** (7.03 mmol, 1.96 g) and heated to 120 °C for 20 min. After cooling down to room temperature, diethyl ether (99 mL) was added and the resulting precipitate was purified by preparative HPLC to yield compound **24** (987 mg, 41%) as a blue solid. $^1$H NMR (MeOD, 400 MHz, 25°C): δ = 8.35-8.24 (m, 2H), 7.88-7.86 (m, 2H), 7.50 (s, 1H), 7.42-7.34 (m, 3H), 6.71 (dd, $^3J$=12.3, 12.3 Hz, 1H), 6.41-6.36 (m, 2H), 4.50 (s, 2H), 4.35-4.31 (m, 2H), 4.14 (s, 2H), 3.70 (s, 3H), 3.04-3.02 (m, 2H), 2.26 (brt, $^3J$=7.3 Hz, 2H), 1.75 (s, 6H), 1.73 (s, 6H); $^{13}$C NMR (MeOD, 100 MHz, 25°C): δ = 176.95, 173.06, 169.36, 156.61, 154.87, 145.22, 143.35, 143.30, 142.06, 142.01, 137.79, 129.25, 128.03, 127.71, 122.83, 121.29, 112.43, 110.85, 106.09, 104.09, 73.88, 50.95, 50.00, 44.14, 32.04, 28.02, 27.61, 26.57, 24.53, 13.87; ESI-MS: calcd for $C_{32}H_{37}ClN_3O_7S_2$ 674.17 [M]$^-$, found: 674.17.

### Compound 25

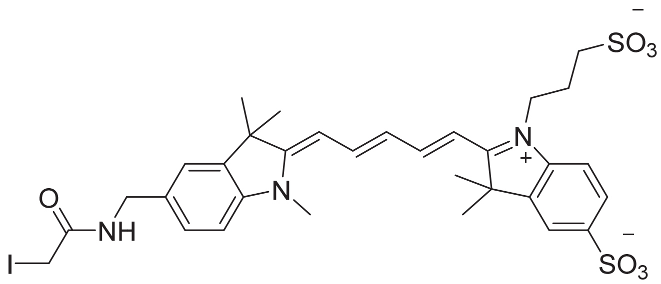

**25**

A mixture of compound **24** (0.791 mmol, 534 mg) and sodium iodide (7.117 mmol, 1.07 g) was refluxed in methanol (16 mL) for 3 hours. The crude mixture was cooled down to room temperature and filtered. The methanolic solid was then evaporated providing a blue solid which was pure enough to be used as such in the next step. $^{1}$H NMR (MeOD, 400 MHz, 25°C): δ = 8.39-8.28 (m, 2H), 7.91-7.89 (m, 2H), 7.42 (s, 1H), 7.40-7.32 (m, 3H), 6.75 (dd, $^{3}J$=12.4, 12.4 Hz, 1H), 6.42 (d, $^{3}J$=13.6 Hz, 2H), 4.50 (s, 2H), 4.33 (t, $^{3}J$=7.4 Hz, 2H), 3.78 (s, 2H), 3.70 (s, 3H), 3.02 (t, $^{3}J$=6.4 Hz, 2H), 2.27-2.20 (m, 2H), 1.77 (s, 6H), 1.74 (s, 6H); $^{13}$C NMR (MeOD, 100 MHz, 25°C): δ = 177.27, 173.27, 171.65, 156.91, 155.06, 145.56, 143.64, 143.58, 142.73, 142.31, 138.25, 129.42, 128.32, 128.00, 122.92, 121.55, 112.74, 111.12, 106.44, 104.29, 70.62, 51.29, 50.26, 44.41, 32.36, 28.32, 27.90, 26.83, 24.14; ESI-MS: calcd for $C_{32}H_{37}IN_3O_7S_2$ 766.11 [M]$^-$, found: 766.10.

### *Compound 26*

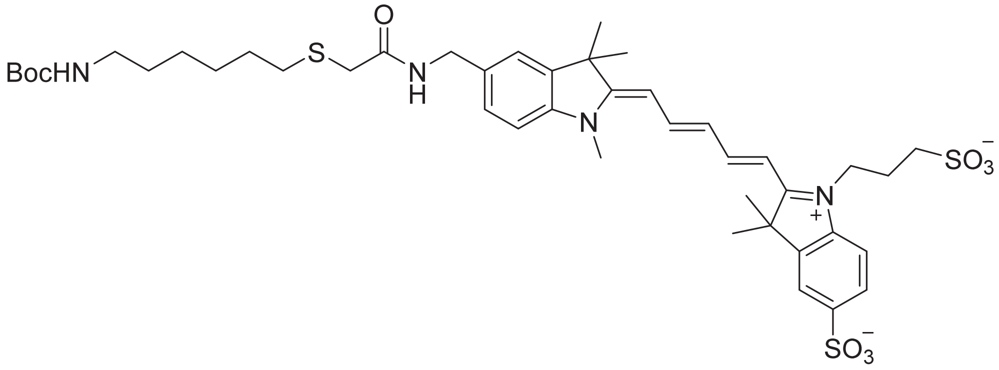

**26**

Potassium carbonate (1.14 mmol, 159.6 mg), compound **13** (0.76 mmol, 177.1 mg) and compound **25** (0.38 mmol, 291.3 mg) were dissolved in DMF (32 mL). The reaction mixture was stirred at room temperature overnight and monitored by UPLC-MS. Further evaporation under reduced pressure and purification by preparative HPLC afforded compound **26** (99.4 mg, 30%) as a blue solid. $^{1}$H NMR (MeOD, 400 MHz, 25°C): δ = 8.34-8.23 (m, 2H), 7.88 (d, $^{3}J$= 1.6 Hz, 1H), 7.86 (s, 1H), 7.48 (s, 1H), 7.39 (d, $^{3}J$= 8.0 Hz, 1H), 7.35 (d, $^{3}J$= 8.4 Hz, 1H), 7.31 (d, $^{3}J$= 8.0 Hz, 1H), 6.69 (t, $^{3}J$=12.4 Hz, 1H), 6.40-6.35 (m, 2H), 4.46 (s, 2H) , 4.30 (t, $^{3}J$=7.8 Hz, 2H), 3.67 (s, 3H), 3.22 (s, 2H), 3.02-2.98 (m, 4H), 2.59 (t, $^{3}J$=7.4 Hz, 2H), 2.27-2.20

(m, 2H), 1.74 (s, 6H), 1.72 (s, 6H), 1.62-1.55 (m, 2H), 1.48-1.27 (m, 15H); $^{13}$C NMR (MeOD, 100 MHz, 25°C): δ = 177.00, 173.25, 172.93, 158.65, 156.71, 155.00, 145.34, 143.41, 142.75, 142.17, 138.42, 129.36, 128.16, 127.87, 122.93, 121.41, 112.54, 111.01, 106.23, 104.23, 79.92, 51.07, 50.14, 44.13, 41.41, 36.39, 33.64, 32.20, 30.97, 30.32, 29.59, 28.97, 28.18, 27.83, 27.51, 24.03; ESI-MS: calcd for $C_{43}H_{59}N_4O_9S_3$ 870.34 [M]$^-$, found: 870.93.

### *Compound 27*

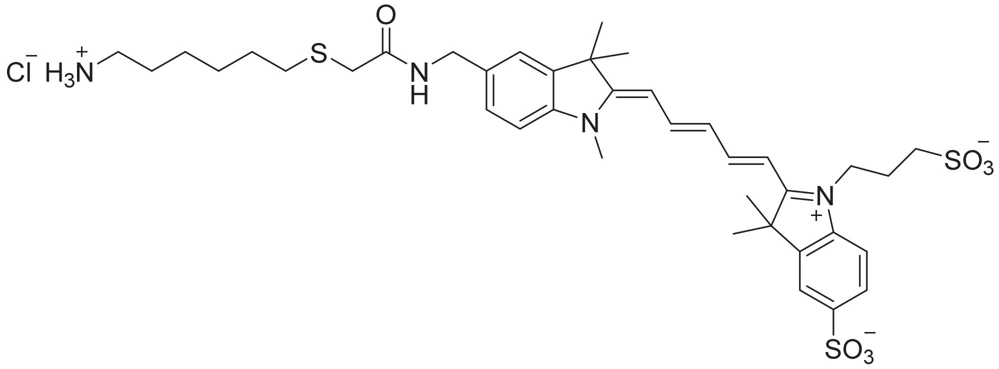

**27**

Acetyl chloride (500 µL) was added dropwise to a solution of compound **26** (0.015 mmol, 11.6 mg) in methanol (500 µL) at 0 °C. The mixture was stirred at 0 °C for 30 min and monitored by UPLC-MS. Further evaporation under reduced pressure afforded compound **27** as a blue solid, which was pure enough to be used as such in the next step. $^1$H NMR (MeOD, 400 MHz, 25°C): δ = 8.54-8.43 (m, 2H), 7.91-7.89 (m, 2H), 7.50 (s, 1H), 7.39-7.31 (m, 3H), 6.60 (t, $^3J$=12.0 Hz, 1H), 6.50 (d, $^3J$= 13.1 Hz, 2H), 4.45 (s, 2H), 4.35 (t, $^3J$=6.5 Hz, 2H), 3.67 (s, 5H), 2.92 (t, $^3J$=6.4 Hz, 2H), 2.61-2.55 (m, 4H), 2.23-2.16 (m, 2H), 1.69 (s, 6H), 1.68 (s, 6H), 1.68-1.61 (m, 2H), 1.56-1.54 (m, 2H), 1.39-1.35 (m, 4H); $^{13}$C NMR (MeOD, 100 MHz, 25°C): δ = 177.13, 173.31, 172.49, 156.67, 155.58, 145.21, 143.30, 142.48, 141.93, 141.39, 138.11, 129.38, 128.56, 127.74, 122.56, 120.38, 112.20, 110.01, 105.37, 104.01, 70.41, 61.99, 50.50, 49.95, 44.22, 33.05, 32.20, 31.54, 31.15, 30.28, 29.25, 27.82, 26.84, 26.48, 24.34, 23.22; ESI-MS: calcd for $C_{38}H_{52}N_4O_7S_3$ 771.29 [M]$^-$, found: 771.29.

### *Compound 28*

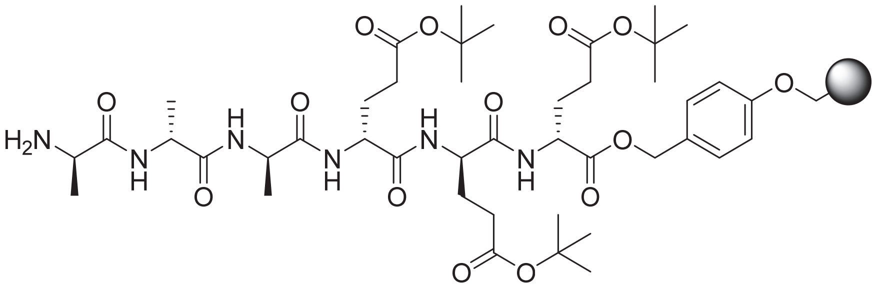

**28**

Standard solid phase peptide synthesis was performed using microwave assisted solid phase peptide synthesis with a CEM Liberty 1$^{TM}$ microwave synthesizer starting with a Fmoc-L-Glu-MPPA(Wang) resin (0.62 mmol/g). A typical synthesis was done on a 1.0 mmol scale. For each amino acid, double couplings were performed at 70 ºC and 35 W (microwave power) for 5 min using 4-fold molar excess of each Fmoc L-amino acid (10 mL of a 0.2 M solution in DMF), HBTU (4 mL of a 0.5 M solution in DMF) and DIPEA (2 mL of a 2 M solution in NMP). Fmoc groups were deprotected with 2 successive treatments with 20 vol% piperidine solution in DMF (15 mL, 70 ºC for 3 min, 55 W). At the end of the synthesis, a small amount of resin was submitted to a cleavage solution of TFA/$H_2O$/TIPS: 9.5/0.25/0.25 vol% and the crude peptide was isolated after precipitation in diethyl ether in order to check the purity of the peptide using UPLC-MS analysis and $^1$H NMR. $^1$H NMR ($D_2O$, 400 MHz, 25 °C): $\delta$ = 4.42-4.27 (m, 5H), 4.12-4.07 (m, 1H), 2.51-2.46 (m, 6H), 2.25-1.95 (m, 6H), 1.54 (d, $^3J$=7.2 Hz, 3H), 1.41-1.39 (m, 6H); $^{13}$C NMR ($D_2O$, 100 MHz, 25 °C): $\delta$ = 177.38, 177.28, 175.82, 174.82, 174.45, 173.00, 172.69, 170.52, 167.20, 52.91, 49.66, 49.55, 48.81, 30.19, 30.13, 30.04, 26.19, 16.44, 16.35; ESI-MS: calcd for $C_{24}H_{39}N_6O_{13}$ 619.25 $[M+H]^+$, found: 619.46.

### Compound 29

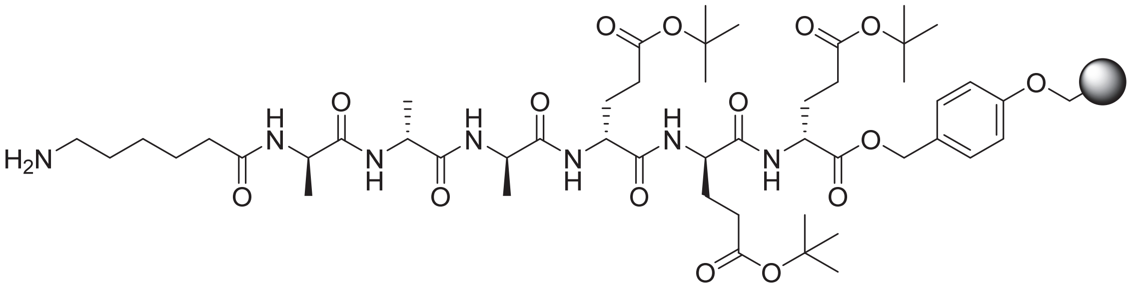

**29**

Standard solid phase peptide synthesis was performed using microwave assisted solid phase peptide synthesis with a CEM Liberty 1$^{TM}$ microwave synthesizer starting with a Fmoc-L-Glu-MPPA(Wang) resin (0.62 mmol/g). A typical synthesis was done on a 1.0 mmol scale. For each amino acid, double couplings were performed at 70 ºC and 35 W (microwave power) for 5 min using 4-fold molar excess of each Fmoc L-amino acid (10 mL of a 0.2 M solution in DMF), HBTU (4 mL of a 0.5 M solution in DMF) and DIPEA (2 mL of a 2 M solution in NMP). Fmoc groups were deprotected with 2 successive treatments with 20 vol% piperidine solution in DMF (15 mL, 70 ºC for 3 min, 55 W). At the end of the synthesis, a small amount of resin was submitted to a cleavage solution of TFA/$H_2O$/TIPS: 9.5/0.25/0.25 vol% and the crude peptide was isolated after precipitation in diethyl ether in order to check the purity of the peptide using UPLC-MS analysis and $^1$H NMR. $^1$H NMR ($D_2O$, 400 MHz, 25 °C): δ = 4.38-4.31 (m, 3H), 4.28-4.20 (m, 3H), 2.95 (t, $^3J$=7.7 Hz, 2H), 2.47-2.41 (m, 6H), 2.26 (t, $^3J$=7.5 Hz, 2H), 2.21-1.90 (m, 6H), 1.67-1.55 (m, 4H), 1.36-1.32 (m, 11H); $^{13}$C NMR (D2O, 400 MHz, 25 °C): δ = 177.26, 177.12, 176.63, 175.62, 175.18, 174.90, 174.81, 173.00, 172.71, 167.08, 52.92, 52.75, 49.72, 49.59, 48.86, 39.24, 34.86, 30.15, 30.00, 26.39, 26.11, 25.05, 24.54, 16.45, 16.34; ESI-MS: calcd for $C_{30}H_{50}N_7O_{14}$ 732.33 $[M+H]^+$, found: 732.51.

### Compound 30

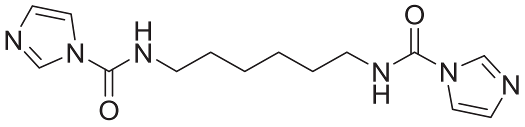

**30**

1,6-diaminohexane (8.61 mmol, 1.00 g) and *N,N'*-carbonyldiimidazole (18.07 mmol, 2.93 g) were dissolved in THF (18.1 mL). The mixture was stirred at room temperature for 21 h and monitored by $^1$H NMR. Further evaporation and recrystallization in ethyl acetate afforded compound **30** (2.10 g, 80%) as a white powder. $^1$H NMR (MeOD, 400 MHz, 25°C): δ = 8.24 (s, 2H), 7.60 (d, $^3J$=2.7 Hz, 2H), 7.05 (d, $^3J$=2.5 Hz, 2H), 3.37 (t, $^3J$=7.2 Hz, 4H), 1.70-1.63 (m, 4H), 1.45 (t, $^3J$=7.4 Hz, 4H); $^{13}$C NMR (MeOD, 100 MHz, 25°C): δ = 150.93, 137.52, 130.17, 117.90, 41.85, 30.38, 27.59; ESI-MS: calcd for $C_{14}H_{20}N_6O_2$ 305.16 $[M+H]^+$, found: 305.09.

### Compound 31

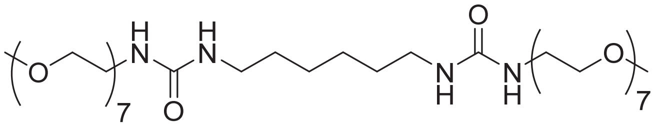

**31**

Compound **30** (1.23 mmol, 375 mg) and compound **7** (3.08 mmol, 1.08 g) were dissolved in dry $CH_2Cl_2$ (30 mL) and the reaction mixture was refluxed for 2 days. After cooling down to room temperature, further evaporation under reduced pressure and purification by preparative HPLC provided compound **31** (583 mg, 56%) as a slight yellow solid. $^1$H NMR ($CDCl_3$, 400 MHz, 25°C): δ = 3.63-3.51 (m, 52H), 3.35 (s, 6H), 3.34 (t, $^3J$=4.0 Hz, 4H), 3.15 (t, $^3J$=6.7 Hz, 4H), 1.46 (t, $^3J$=6.3 Hz, 4H), 1.32 (t, $^3J$=3.0 Hz, 4H); $^{13}$C NMR ($CDCl_3$, 100 MHz, 25°C): δ = 159.13, 72.10, 70.97, 70.70, 70.52, 70.27, 59.16, 40.33, 39.82, 30.26, 26.17; ESI-MS: calcd for $C_{38}H_{78}N_4O_{16}$ 870.54 $[M+Na]^+$, found: 870.13.

### Compound 32

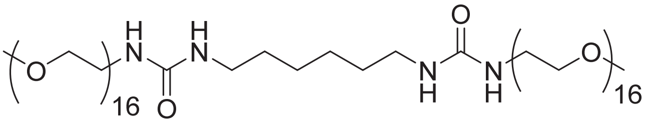

**32**

Compound **30** (0.80 mmol, 244 mg) and compound **8** (2.00 mmol, 1.50 g) were dissolved in dry $CH_2Cl_2$ (20 mL) and the reaction mixture was refluxed for 2 days. After cooling down to room temperature, further evaporation under reduced pressure and purification by preparative HPLC afforded compound **32** (459 mg, 35%) as a slight yellow solid. $^1$H NMR ($CDCl_3$, 400 MHz, 25°C): $\delta$ = 3.63-3.51 (m, 124H), 3.36 (s, 6H), 3.34 (t, $^3J$=4.0 Hz, 4H), 3.14 (t, $^3J$=5.3 Hz, 4H), 1.46 (t, $^3J$=4.1 Hz, 4H), 1.32 (t, $^3J$=4.7 Hz, 4H); $^{13}$C NMR ($CDCl_3$, 100 MHz, 25°C): $\delta$ = 159.08, 72.13, 70.96, 70.75, 70.54, 70.28, 59.20, 40.37, 39.81, 30.27, 26.15; ESI-MS: calcd for $C_{74}H_{150}N_4O_{34}$ 1640.01 $[M+H]^+$, found: 1640.39.

### Compound 33

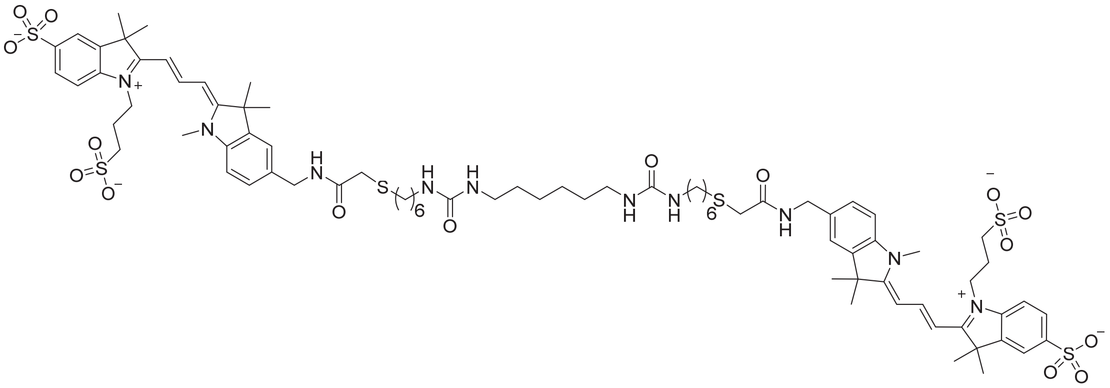

**33**

Compound **22** (0.046 mmol, 36.0 mg) and compound **30** (0.023 mmol, 7.0 mg) were dissolved in dry DMF (1.5 mL), followed by the addition of DIPEA (8.0 μL). The reaction mixture was stirred at 50 °C under argon for 32 hours and monitored by UPLC-MS. Further evaporation under reduced pressure followed by purification using preparative HPLC afforded compound **33** (11.5 mg, 30%) as a purple solid. $^1$H NMR (MeOD, 400 MHz, 25°C): $\delta$ = 8.58-8.51 (m, 2H), 7.92 (s, 2H), 7.90 (d, $^3J$= 1.6 Hz, 2H), 7.52 (s, 2H), 7.45-7.35 (m, 4H), 7.36 (d, $^3J$= 8.4 Hz, 2H), 6.60 (d, $^3J$=13.2

Hz, 2H), 6.55 (d, $^3J$=13.6 Hz, 2H), 4.47 (s, 4H), 4.36 (t, $^3J$=8.0 Hz, 4H), 3.73 (s, 6H), 3.23 (s, 4H), 3.06 (t, $^3J$=7.0 Hz, 8H), 3.01 (t, $^3J$=7.0 Hz, 4H), 2.59 (t, $^3J$=7.3 Hz, 4H), 2.28-2.21 (m, 4H), 1.79 (s, 12H), 1.77 (s, 12H), 1.60-1.53 (m, 4H), 1.47-1.40 (m, 8H), 1.38-1.30 (m, 12H); $^{13}$C NMR (MeOD, 100 MHz, 25°C): δ = 177.71, 175.80, 172.93, 161.44, 152.47, 144.86, 143.73, 143.35, 142.88, 142.07, 138.78, 129.59, 128.41, 123.02, 121.56, 112.80, 111.78, 105.50, 104.19, 56.02, 51.01, 50.47, 50.00, 44.18, 41.06, 36.44, 33.64, 32.36, 31.40, 30.36, 29.65, 28.57, 28.28, 27.71, 27.59, 24.17, 13.32; ESI-MS: calcd for $C_{80}H_{110}N_{10}O_{16}S_6$ 829.32 $[M]^{2-}$, found: 829.46.

### Compound 34

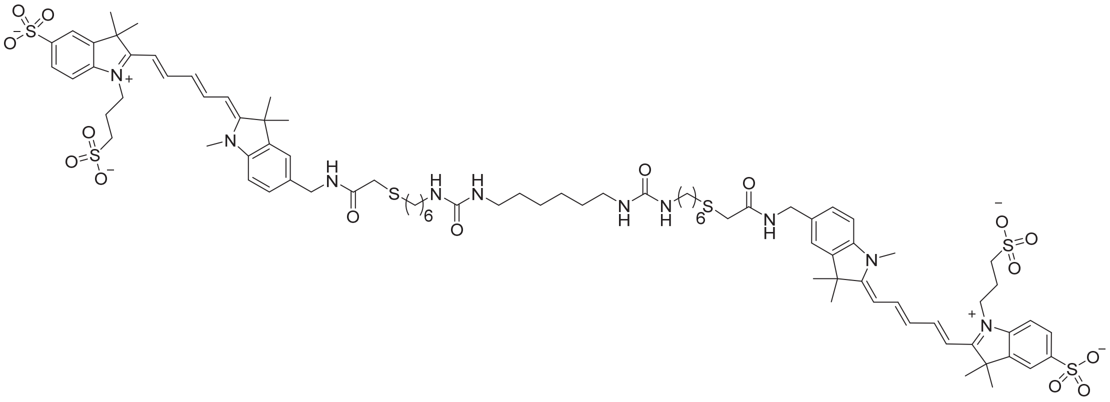

**34**

Compound **27** (0.046 mmol, 37.2 mg) and compound **30** (0.023 mmol, 7.0 mg) were dissolved in dry DMF (1.5 mL), followed by the addition of DIPEA (8.0 µL). The reaction mixture was stirred at 50 °C under argon for 32 hours and monitored by UPLC-MS. Further evaporation under reduced pressure followed by purification using preparative HPLC afforded compound **34** (7.9 mg, 20%) as a blue solid. $^1$H NMR (MeOD, 400 MHz, 25°C): δ = 8.33-8.22 (m, 4H), 7.86-7.84 (m, 4H), 7.48 (s, 2H), 7.38 (d, $^3J$= 8.0 Hz, 2H), 7.35-7.30 (m, 4H), 6.68 (t, $^3J$= 12.4 Hz, 2H), 6.37 (d, $^3J$=14.0 Hz, 4H), 4.55 (s, 2H), 4.44 (s, 4H), 4.29 (t, $^3J$=7.2 Hz, 4H), 3.67 (s, 6H), 3.22 (s, 4H), 3.09-3.04 (m, 8H), 3.00 (t, $^3J$=6.6 Hz, 4H), 2.57 (t, $^3J$=7.4 Hz, 4H), 2.27-2.19 (m, 4H), 1.72 (s, 12H), 1.70 (s, 12H), 1.60-1.53 (m, 4H), 1.46-1.41 (m, 8H), 1.38-1.32 (m, 12H); $^{13}$C NMR (MeOD, 100 MHz, 25°C): δ = 177.04, 173.25, 172.94, 161.44, 156.76, 155.04, 145.36, 143.44, 142.79, 142.19, 138.47, 129.42, 128.19, 127.93, 122.93, 121.43, 112.56, 111.02, 106.28, 104.25, 56.01, 51.10, 50.16, 50.00, 44.14, 41.04, 36.47, 33.65, 32.34, 31.43, 31.34, 30.35, 29.64, 28.23, 27.87, 27.73, 27.55, 24.05, 13.32; ESI-MS: calcd for $C_{84}H_{114}N_{10}O_{16}S_6$ 855.84 $[M]^{2-}$, found: 855.27.

### Compound 35

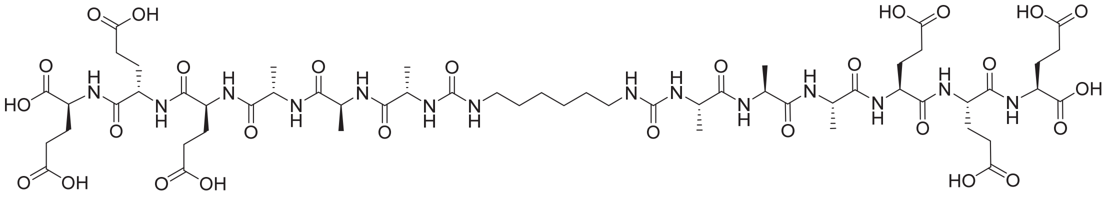

**35**

Resin **28** (0.86 mmol) and compound **30** (0.41 mmol, 124.8 mg) were dissolved in 1-methyl-2-pyrrolidinone (NMP, 20 mL). This reaction was stirred at 45°C for 48 h and monitored by UPLC-MS (for that, some resin beads were taken out and cleaved using a mixture of TFA, $H_2O$, and TIPS (95:2.5:2.5) before UPLC analysis). The reaction solution was then drained off and the resulting peptidyl resin was washed with DMF (4 times). Cleavage from the resin and deprotection of **35** was performed twice for 1 h with a mixture of TFA, $H_2O$, and TIPS (30 mL, 95:2.5:2.5). Both cleavage mixtures and two subsequent $CH_2Cl_2$ washings (2 × 20 mL) were filtered into a round-bottom flask. The combined solution was concentrated under reduced pressure and cold ether was then added to precipitate crude **35**. The precipitate was centrifuged, and the supernatant liquid was removed by decantation. After washing with ether (3 times) to remove residual TFA, the precipitate was dried overnight under vacuum. Purification of the crude mixture by preparative HPLC afforded compound **35** (172.9 mg, 30%), as a white powder. $^1H$ NMR ($D_2O$, 400 MHz, 25°C): $\delta$ = 4.44-4.31 (m, 10H), 4.17-4.12 (m, 2H), 3.12 (t, $^3J$=6.8 Hz, 4H), 2.49 (t, $^3J$=6.3 Hz, 12H), 2.25-1.97 (m, 12H), 1.49-1.46 (m, 4H), 1.44-1.32 (m, 22H); $^{13}C$ NMR ($D_2O$, 100 MHz, 25°C): $\delta$ = 181.45, 181.19, 180.85, 178.28, 176.64, 175.01, 174.88, 173.56, 172.73, 158.85, 55.16, 53.62, 50.13, 49.75, 49.47, 39.74, 33.15, 29.15, 28.19, 27.66, 27.45, 25.64, 17.16, 16.51; ESI-MS: calcd for $C_{56}H_{88}N_{14}O_{28}$ 1427.59 $[M+Na]^+$, found: 1427.09.

## Compound 36

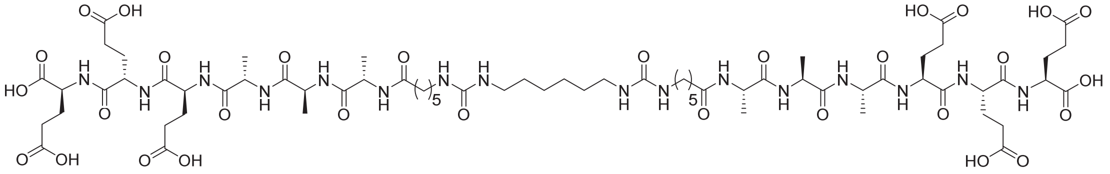

**36**

Resin **29** (0.83 mmol) and compound **30** (0.40 mmol, 121.7 mg) were dissolved in 1-methyl-2-pyrrolidinone (NMP, 20 mL). This reaction was stirred at 45°C for 24 h and monitored by UPLC-MS (For that, some resin beads were taken out and cleaved using a mixture of TFA, $H_2O$, and TIPS (95:2.5:2.5) before UPLC analysis). The reaction solution was then drained off and the resulting peptidyl resin was washed with DMF (4 times). Cleavage from the resin and deprotection of **36** was performed twice for 1 h with a mixture of TFA, $H_2O$, and TIPS (30 mL, 95:2.5:2.5). Both cleavage mixtures and two subsequent $CH_2Cl_2$ washings (2 × 20 mL) were filtered into a round-bottom flask. The combined solution was concentrated under reduced pressure and cold ether was then added to precipitate crude **36**. The precipitate was centrifuged, and the supernatant liquid was removed by decantation. After washing with ether (3 times) to remove residual TFA, the precipitate was dried under vacuum for overnight. Purification of the crude mixture by preparative HPLC afforded compound **36** (359.0 mg, 55%), as a white powder. $^1$H NMR ($D_2O$, 400 MHz, 25°C): $\delta$ = 4.39-4.27 (m, 10H), 4.22-4.18 (m, 2H), 3.09 (t, $^3J$=6.0 Hz, 8H), 2.40-2.32 (m, 12H), 2.30 (t, $^3J$=7.2 Hz, 4H), 2.20-1.89 (m, 12H), 1.65-1.58 (m, 4H), 1.51-1.45 (m, 8H), 1.42-1.30 (m, 26H); $^{13}$C NMR ($D_2O$, 100 MHz, 25°C): $\delta$ = 180.62, 180.48, 180.29, 178.07, 177.00, 175.12, 174.95, 174.74, 173.45, 172.66, 160.78, 54.87, 53.48, 49.67, 49.50, 39.81, 39.69, 35.17, 32.61, 29.10, 28.91, 27.79, 27.22, 25.61, 25.46, 24.90, 16.50; ESI-MS: calcd for $C_{68}H_{110}N_{16}O_{30}$ 1631.77 $[M+H]^+$, found: 1631.48.

### *Compound 37*

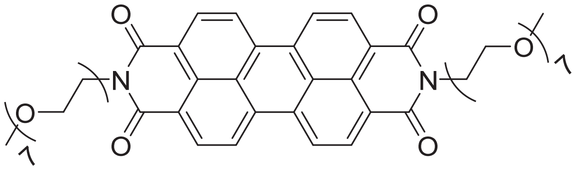

**37**

Compound **7** (1.97 mmol, 688 mg) and 3,4,9,10-perylenetetracarboxylic dianhydride (PTCDA, 1.97 mmol, 773 mg) were dissolved in pyridine (15 mL), and the reaction mixture was heated to reflux for 24 h. The mixture was then cooled down to room temperature, diluted with dichloromethane (100 mL) and then filtered through Celite to remove the excess of PTCDA. The filtrate was concentrated under reduced pressure and crude product was purified by preparative HPLC to yield compound **37** (176 mg, 17%) as a red solid. $^1$H NMR (CDCl$_3$, 400 MHz, 25°C): $\delta$ = 8.62 (d, $^3J$=8.0 Hz, 4H), 8.54 (d, $^3J$=7.6 Hz, 4H), 4.45 (t, $^3J$=6.0 Hz, 4H), 3.85 (t, $^3J$=6.0 Hz, 4H), 3.72-3.50 (m, 48H), 3.34 (s, 6H); $^{13}$C NMR (CDCl$_3$, 100 MHz, 25°C): $\delta$ = 163.6, 134.8, 131.6, 129.6, 126.6, 123.4, 123.3, 72.2, 70.8, 70.4, 68.1, 59.3, 39.6; ESI-MS: calcd for $C_{54}H_{70}N_2O_{18}$ 1057.45 [M+Na]$^+$, found: 1057.25; MALDI-TOF: calcd for $C_{54}H_{70}N_2O_{18}$ 1057.45 [M+Na]$^+$, found: 1057.55.

### *Compound 38*

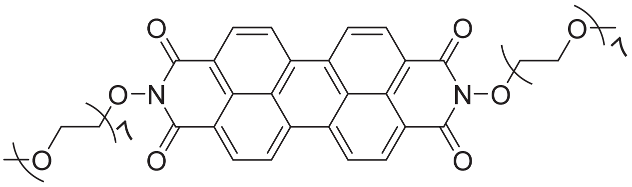

**38**

Compound **9** (0.74 mmol, 271 mg) and 3,4,9,10-perylenetetracarboxylic dianhydride (PTCDA, 0.74 mmol, 290 mg) were dissolved in pyridine (6 mL), and the reaction mixture was heated to reflux for 24 h. The mixture was then cooled down to room temperature, diluted with dichloromethane (40 mL) and then filtered through Celite to remove the excess of PTCDA. The filtrate was concentrated under reduced pressure and crude product was purified by preparative HPLC to yield compound **38** (212 mg, 52%) as a red solid. $^1$H NMR (CDCl$_3$, 400 MHz, 25°C): δ = 8.70 (d, $^3J$=8.0 Hz, 4H), 8.65 (d, $^3J$=6.8 Hz, 4H), 4.47 (t, $^3J$=4.6 Hz, 4H), 3.96 (t, $^3J$=4.6 Hz, 44H), 3.73 (t, $^3J$=4.8 Hz, 4H), 3.68-3.57 (m, 40H), 3.52 (t, $^3J$=4.6 Hz, 4H), 3.35 (s, 6H); $^{13}$C NMR (CDCl$_3$, 100 MHz, 25°C): δ= 159.7, 134.0, 131.4, 128.0, 125.6, 123.2, 76.3, 71.9, 70.6, 70.5, 70.4, 69.1, 59.0; ESI-MS: calcd for $C_{54}H_{70}N_2O_{20}$ 1089.44 [M+Na]$^+$, found: 1089.31; MALDI-TOF: calcd for $C_{54}H_{70}N_2O_{20}$ 1089.44 [M+Na]$^+$, found: 1089.40.

### Compound 39

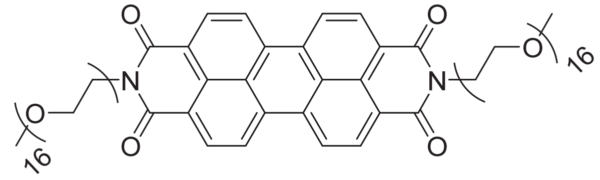

**39**

Compound **8** (0.93 mmol, 700 mg) and 3,4,9,10-perylenetetracarboxylic dianhydride (PTCDA, 0.93 mmol, 365 mg) were dissolved in pyridine (7 mL), and the reaction mixture was heated to reflux for 24 h. The mixture was then cooled down to room temperature, diluted with dichloromethane (60 mL) and then filtered through Celite to remove the excess of PTCDA. The filtrate was concentrated under reduced pressure and crude product was purified by preparative HPLC to yield compound **39** (135 mg, 16%) as a red solid. $^1$H NMR (CDCl$_3$, 400 MHz, 25°C): δ = 8.68 (d, $^3J$=8.0 Hz, 4H), 8.63 (d, $^3J$=8.0 Hz, 4H), 4.45 (t, $^3J$=6.1 Hz, 4H), 3.84 (t, $^3J$=6.0 Hz, 4H), 3.72-3.51 (m, 120 H), 3.36 (s, 6H); $^{13}$C NMR (CDCl$_3$, 100 MHz, 25°C): δ = 163.5, 134.7, 131.5, 129.5, 126.5, 123.4, 123.3, 72.1, 70.8, 70.3, 68.1, 59.2, 39.5; ESI-MS: calcd for $C_{90}H_{142}N_2O_{36}$ 1849.92 [M+Na]$^+$, found: 1849.78; MALDI-TOF: calcd for $C_{90}H_{142}N_2O_{36}$ 1849.92 [M+Na]$^+$, found: 1849.49.

### Compound 40

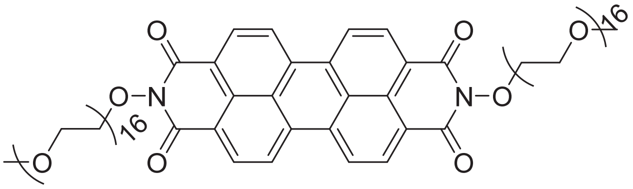

**40**

Compound **10** (0.65 mmol, 495 mg) and 3,4,9,10-perylenetetracarboxylic dianhydride (PTCDA, 0.65 m mol, 255 mg) were dissolved in pyridine (5 mL), and the reaction mixture was heated to reflux for 24 h. The mixture was then cooled down to room temperature, diluted with dichloromethane (40 mL) and then filtered through Celite to remove the excess of PTCDA. The filtrate was concentrated under reduced pressure and crude product was purified by preparative HPLC to yield compound **40** (118 mg, 19%) as a red solid. $^1$H NMR ($CDCl_3$, 400 MHz, 25°C): δ = 8.73 (d, $^3J$=8.0 Hz, 4H), 8.68 (d, $^3J$=8.2 Hz, 4H), 4.47 (t, $^3J$= 4.6 Hz, 4H), 3.97 (t, $^3J$=4.6 Hz, 4H), 3.73 (t, $^3J$=4.8 Hz, 4H), 3.67-3.57 (m, 112H), 3.52 (t, $^3J$=4.6 Hz, 4H), 3.36 (s, 6H); $^{13}$C NMR ($CDCl_3$, 100 MHz, 25°C): δ = 160.0, 134.6, 131.7, 128.4, 126.3, 123.6, 123.5, 76.3, 72.0, 70.8, 70.6, 69.3, 59.1; ESI-MS: calcd for $C_{90}H_{142}N_2O_{38}$ 1881.92 $[M+Na]^+$, found: 1881.71; MALDI-TOF: calcd for $C_{90}H_{142}N_2O_{38}$ 1881.91 $[M+Na]^+$, found: 1881.85.

## *Compound 41*

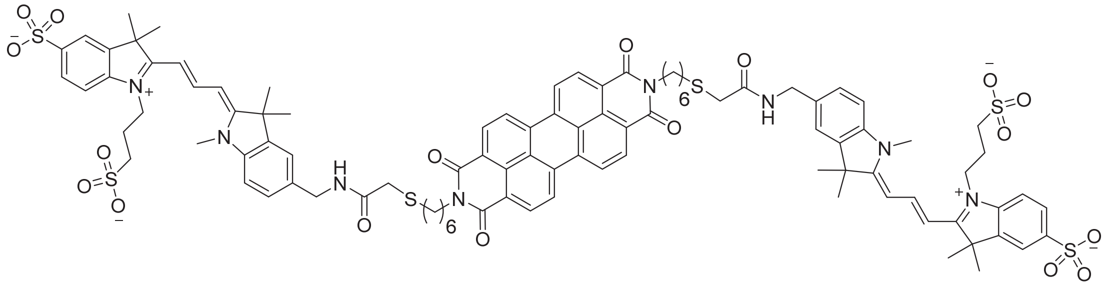

**41**

Compound **22** (0.022 mmol; 40.0 mg) and 3,4,9,10-perylenetetracarboxylic dianhydride (PTCDA, 0.011 mmol, 4.3 mg) were dissolved in pyridine (6 mL). The mixture was sonicated for 10 min and heated up to 110 °C for 12 h in a microwave oven (P = 200 W). After that time, milliQ-$H_2O$ (6 mL) was added, and the mixture was further reacted at 110 °C for 24 h using microwave technology (P = 200 W). The reaction was monitored by UPLC-MS. Further evaporation under reduced pressure and purification by preparative HPLC yielded compound **41** (3.0 mg, 15%) as a dark purple solid. ESI-MS: calcd for $C_{96}H_{102}N_8O_{18}S_6$ 923.78 $[M]^{2-}$, found: 923.85. Compound **41** was poorly soluble in most deuterated organic solvents and in $D_2O$, flattening of all the signals was observed. Therefore, this compound was only analyzed by LC-MS.

## Compound 42

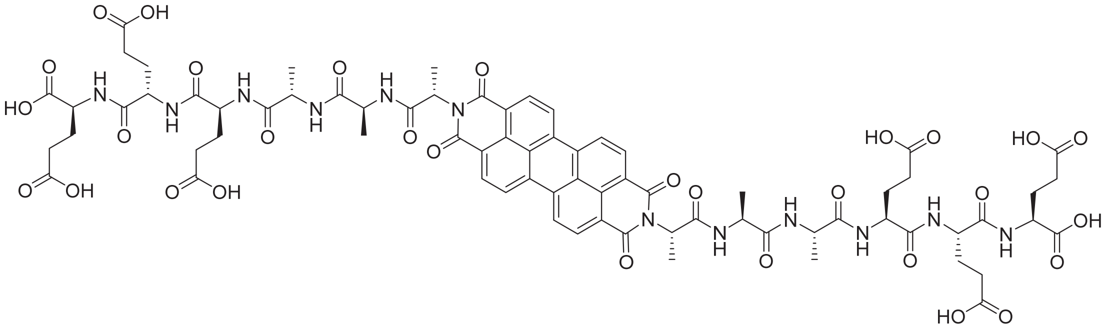

**42**

PTCDA (0.41 mmol, 160.9 mg), imidazole (8.19 mmol, 557.6 mg) and zinc acetate dihydrate (0.123 mmol, 27.0 mg) were added to a solution of resin **28** (0.86 mmol) and DIPEA (151 µL) in DMF (30 mL). This reaction was stirred at 100°C for 3 days under an argon atmosphere. The reaction solution was then drained off and the resulting peptidyl resin was washed with DMF (4 times). Cleavage from the resin and deprotection of **42** was performed twice for 1 h with a mixture of TFA, $H_2O$, and TIPS (30 mL, 95:2.5:2.5). Both cleavage mixtures and two subsequent $CH_2Cl_2$ washings (2 × 20 mL) were filtered into a round-bottom flask. The combined solution was concentrated under reduced pressure and cold ether was then added to precipitate crude **42**. The precipitate was centrifuged, and the supernatant liquid was removed by decantation. After washing with ether (3 times) to remove residual TFA, the precipitate was dried overnight under vacuum. Purification of the crude mixture by preparative HPLC afforded compound **42** (163.3 mg, 25%), as a red powder. $^1$H NMR ($CDCl_3$/TFA-d 2/1, 400 MHz, 25°C): $\delta$ = 8.85 (d, $^3J$=8.0 Hz, 4H), 8.79 (d, $^3J$=8.0 Hz, 4H), 6.01-5.93 (m, 2H), 4.79-4.59 (m, 10H), 2.90 (t, $^3J$=5.6 Hz, 2H), 2.62 (t, $^3J$=4.0 Hz, 8H), 2.42 (t, $^3J$=7.2 Hz, 4H), 2.30-2.23 (m, 2H), 2.21-2.05 (m, 6H), 1.98-1.90 (m, 2H), 1.82 (d, $^3J$=7.2 Hz, 6H), 1.60 (d, $^3J$=7.2 Hz, 6H), 1.52 (d, $^3J$=7.2 Hz, 6H); $^{13}$C NMR ($CDCl_3$/TFA-d 2/1, 100 MHz, 25°C): $\delta$ = 181.49, 181.45, 181.16, 178.52, 177.32, 176.93, 175.87, 175.22, 175.04, 166.87, 138.33, 135.28, 131.71, 128.78, 126.60, 124.21, 55.32, 55.17, 54.14, 53.06, 52.61, 52.42, 37.84, 37.73, 31.78, 31.63, 31.44, 28.54, 28.34, 27.79, 18.01, 15.51; ESI-MS: calcd for $C_{72}H_{80}N_{12}O_{30}$ 1615.50

$[M+Na]^+$, found: 1615.03.

### Compound 43

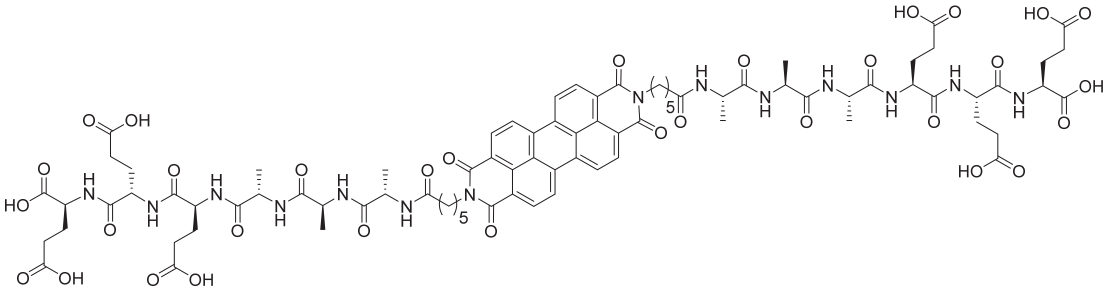

**43**

PTCDA (0.40 mmol, 157.0 mg), imidazole (7.90 mmol, 539.1 mg) and zinc acetate dihydrate (0.119 mmol, 26.1 mg) were added to a solution of resin **29** (0.83 mmol) and DIPEA (145 µL) in DMF (30 mL). This reaction was stirred at 100°C for 2 days under an argon atmosphere. The reaction solution was then drained off and the resulting peptidyl resin was washed with DMF (4 times). Cleavage from the resin and deprotection of **43** was performed twice for 1 h with a mixture of TFA, $H_2O$, and TIPS (30 mL, 95:2.5:2.5). Both cleavage mixtures and two subsequent $CH_2Cl_2$ washings (2 × 20 mL) were filtered into a round-bottom flask. The combined solution was concentrated under reduced pressure and cold ether was then added to precipitate crude **43**. The precipitate was centrifuged, and the supernatant liquid was removed by decantation. After washing with ether (3 times) to remove residual TFA, the precipitate was dried overnight under vacuum. Purification of the crude mixture by preparative HPLC afforded compound **43** (364.0 mg, 50%), as a red powder. $^1$H NMR ($CDCl_3$/TFA-d 2/1, 400 MHz, 25°C): δ = 4.69 (t, $^3J$=5.1 Hz, 4H), 4.60 (t, $^3J$=7.2 Hz, 2H), 4.54-4.44 (m, 6H), 4.20 (t, $^3J$=7.7 Hz, 4H), 2.53 (t, $^3J$=6.7 Hz, 8H), 2.48 (t, $^3J$=7.0 Hz, 4H), 2.37-1.94 (m, 16H), 1.73-1.88 (m, 8H), 1.46-1.33 (m, 22H); $^{13}$C NMR ($CDCl_3$/TFA-d 2/1, 100 MHz, 25°C): δ = 179.58, 179.52, 179.44, 176.68, 175.15, 174.79, 173.41, 173.11, 165.85, 136.27, 133.44, 129.74, 126.86, 124.70, 122.64, 53.52, 53.42, 52.38, 50.37, 50.31, 41.54, 35.60, 29.93, 29.79, 29.63, 27.37, 26.93, 26.69, 26.45, 26.06. 25.25, 16.86, 16.72, 16.60; ESI-MS: calcd for $C_{84}H_{102}N_{14}O_{32}$ 1841.68 $[M+Na]^+$, found: 1841.28.

# ANNEXES

# 1. Additional characterizations for compound 37

## a. UV-Vis experiments

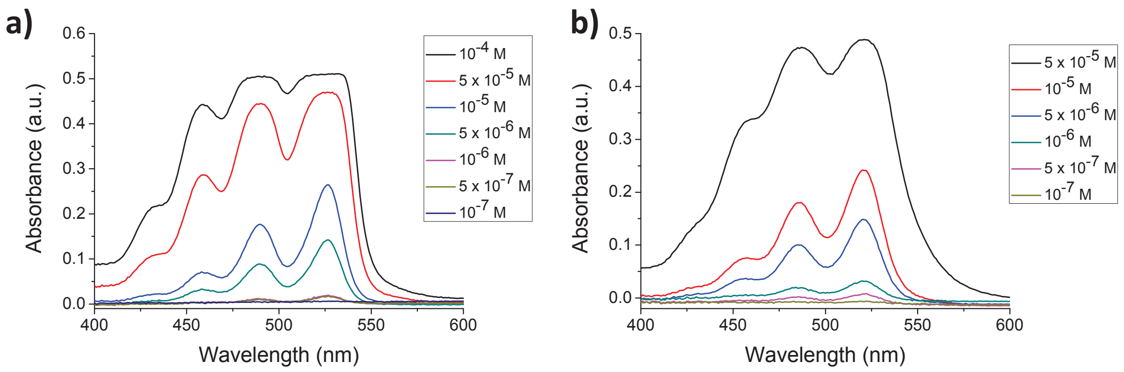

**Figure 118 |** a) UV-Vis spectra of a $CDCl_3$ solution of PBI-$PEG_7$ with concentrations ranging from $10^{-7}$ (dark blue) up to $10^{-4}$ mol/L (black); b) UV-Vis spectra of a $CD_3OD$ solution of PBI-$PEG_7$ with concentrations ranging from $10^{-7}$ (light brown) up to $5 \times 10^{-5}$ mol/L (black).

## b. Fluorescence experiments

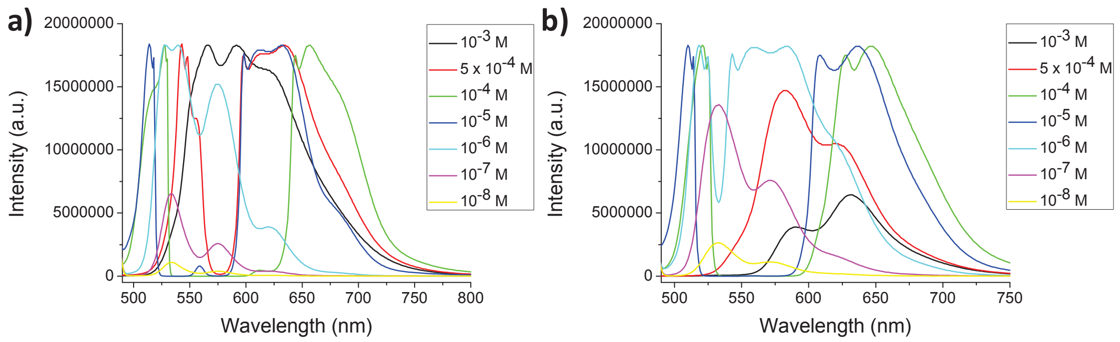

**Figure 119 |** a) Fluorescent spectra of PBI-$PEG_7$ in $CDCl_3$ for concentrations of $10^{-8}$ mol/L up to $10^{-3}$ mol/L (black), $\lambda_{ex}$=483 nm; b) Fluorescent spectra of PBI-$PEG_7$ in $CD_3OD$ for concentrations of $10^{-8}$ mol/L up to $10^{-3}$ mol/L (black), $\lambda_{ex}$=483 nm.

## c. TEM imaging

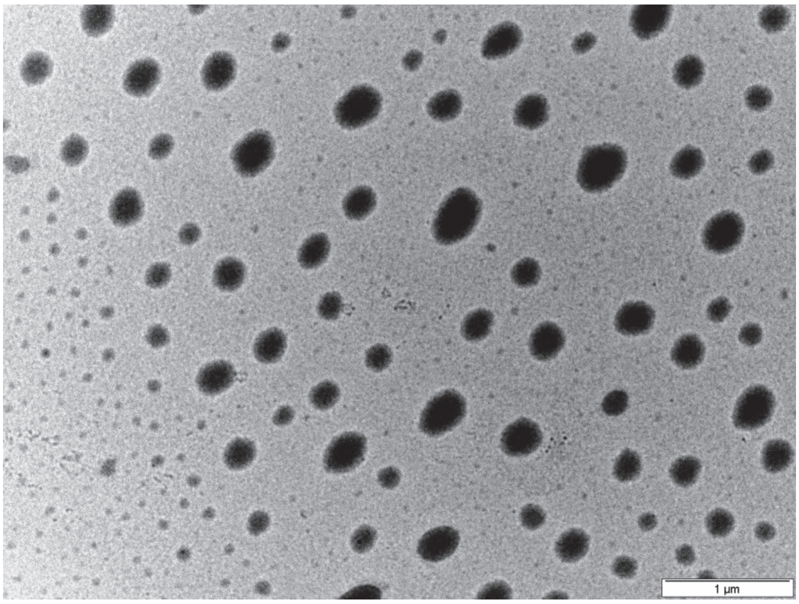

**Figure 120 |** TEM imaging of PBI-PEG$_7$ in $D_2O$ (Scale bar: 1 μm)

## 2. Additional characterizations for compound 38

### a. $^1$H NMR

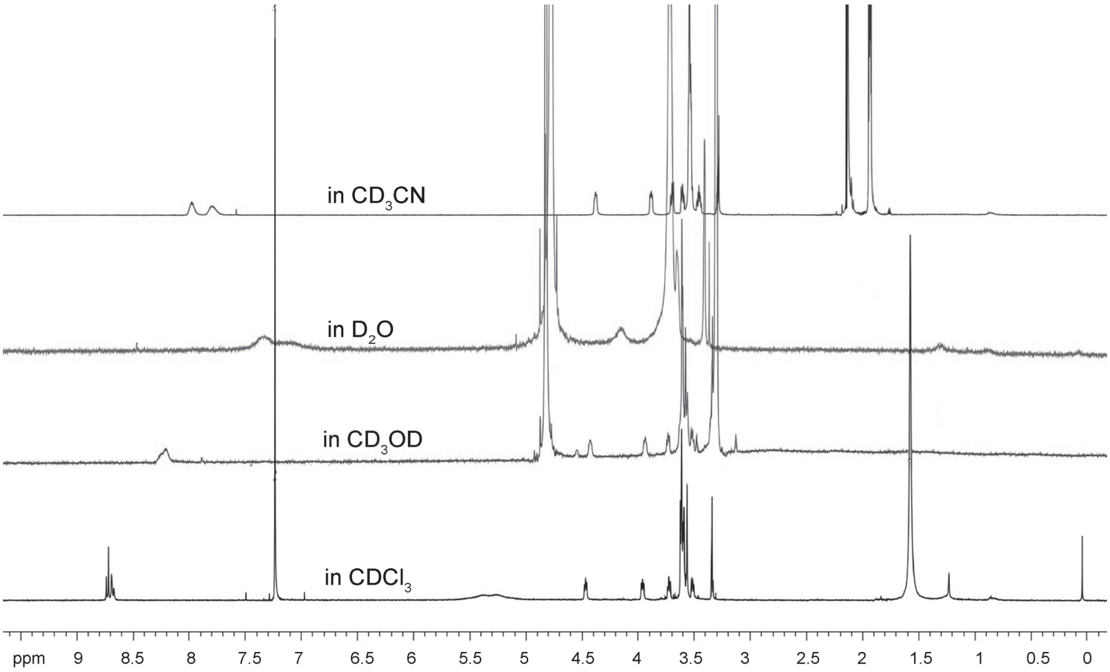

**Figure 121 |** $^1$H NMR spectra of $10^{-3}$ M PBI-OPEG$_7$ in different solvent.

## b. UV-Vis experiments

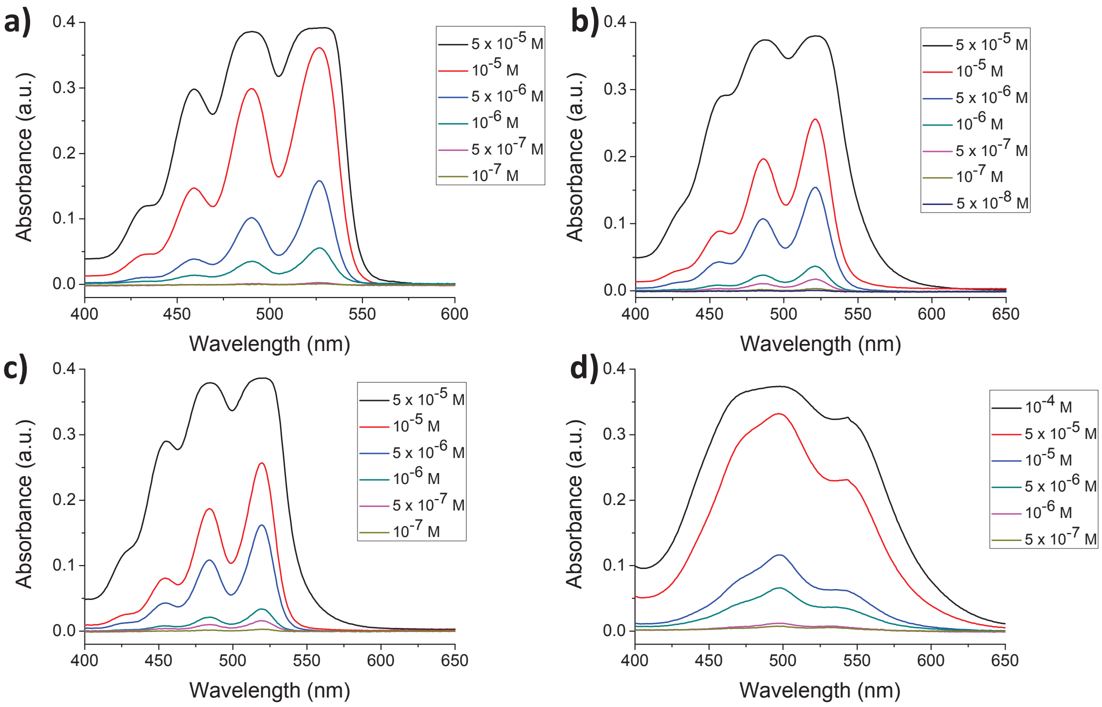

**Figure 122 |** a) UV-Vis spectra of a $CDCl_3$ solution of PBI-OPEG$_7$ with concentrations ranging from $10^{-7}$ (light brown) up to $5 \times 10^{-5}$ mol/L (black); b) UV-Vis spectra of a $CD_3OD$ solution of PBI-OPEG$_7$ with concentrations ranging from 5 x $10^{-8}$ (dark blue) up to $5 \times 10^{-5}$ mol/L (black); c) UV-Vis spectra of a $CD_3CN$ solution of PBI-OPEG$_7$ with concentrations ranging from $10^{-7}$ (light brown) up to $5 \times 10^{-5}$ mol/L (black); d) UV-Vis spectra of a $D_2O$ solution of PBI-OPEG$_7$ with concentrations ranging from 5 x $10^{-7}$ (light brown) up to $10^{-4}$ mol/L (black).

## c. Fluorescence experiments

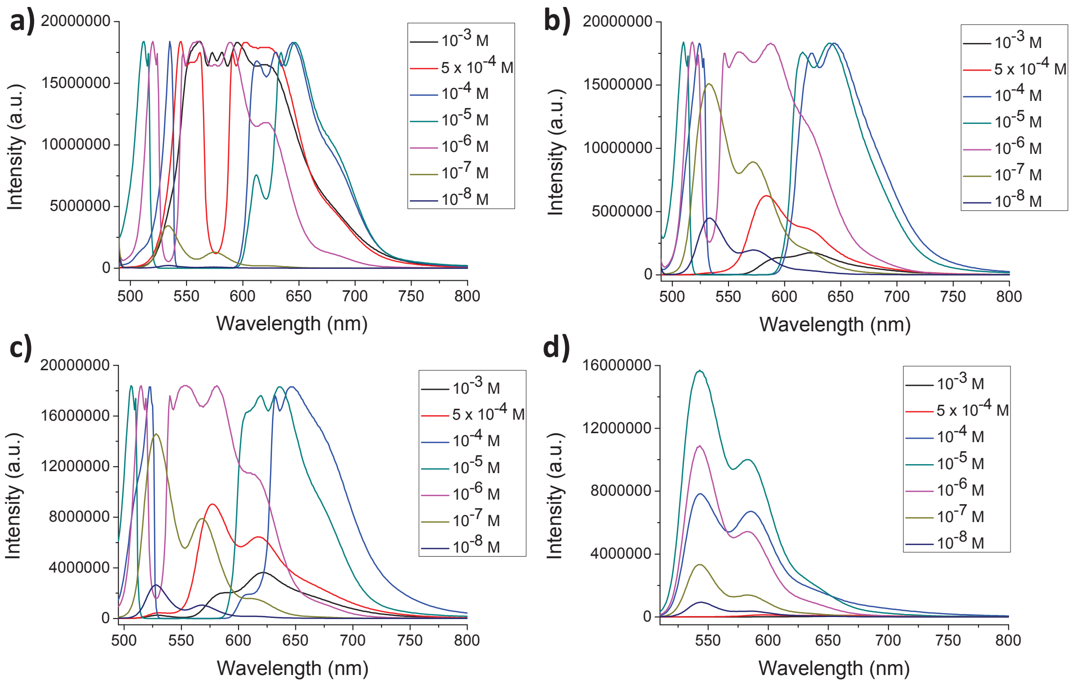

**Figure 123 |** a) Fluorescent spectra of PBI-OPEG$_7$ in CDCl$_3$ for concentrations of $10^{-8}$ mol/L up to $10^{-3}$ mol/L (black), $\lambda_{ex}$=483 nm; b) Fluorescent spectra of PBI-OPEG$_7$ in CD$_3$OD for concentrations of $10^{-8}$ mol/L up to $10^{-3}$ mol/L (black), $\lambda_{ex}$=483 nm; c) Fluorescent spectra of PBI-OPEG$_7$ in CD$_3$CN for concentrations of $10^{-8}$ mol/L up to $10^{-3}$ mol/L (black), $\lambda_{ex}$=483 nm; d) Fluorescent spectra of PBI-OPEG$_7$ in D$_2$O for concentrations of $10^{-8}$ mol/L up to $10^{-3}$ mol/L (black), $\lambda_{ex}$=498 nm.

## 3. Additional characterizations for compound 39

### a. $^1$H NMR

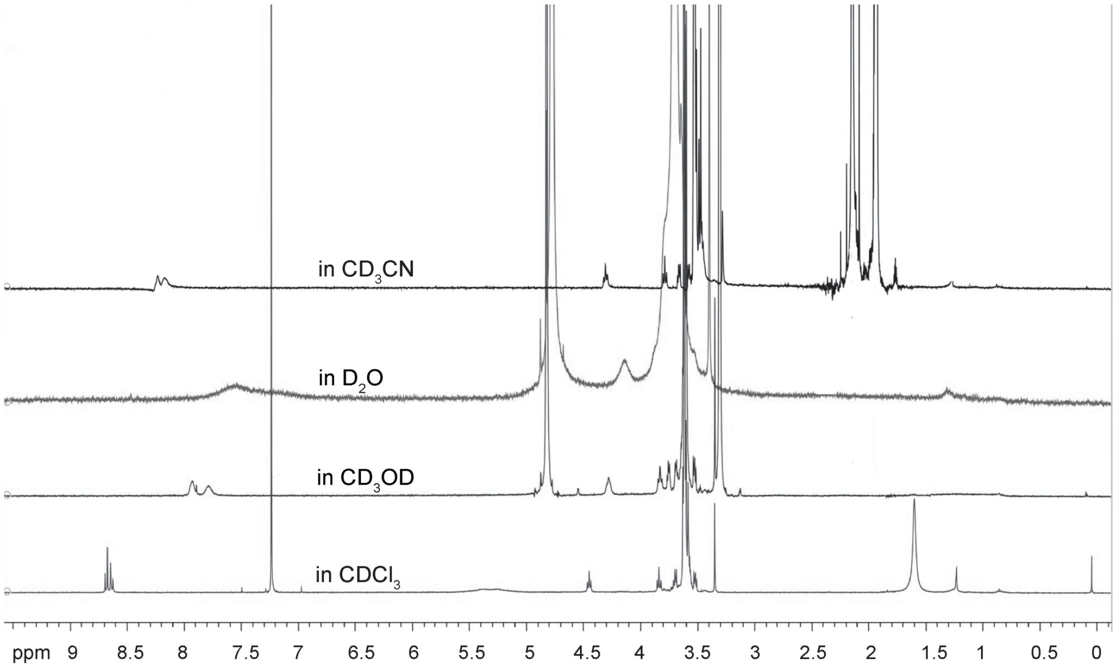

**Figure 124 |** $^1$H NMR spectra of PBI-PEG$_{16}$ in different solvents at $10^{-3}$ M.

## b. UV-Vis experiments

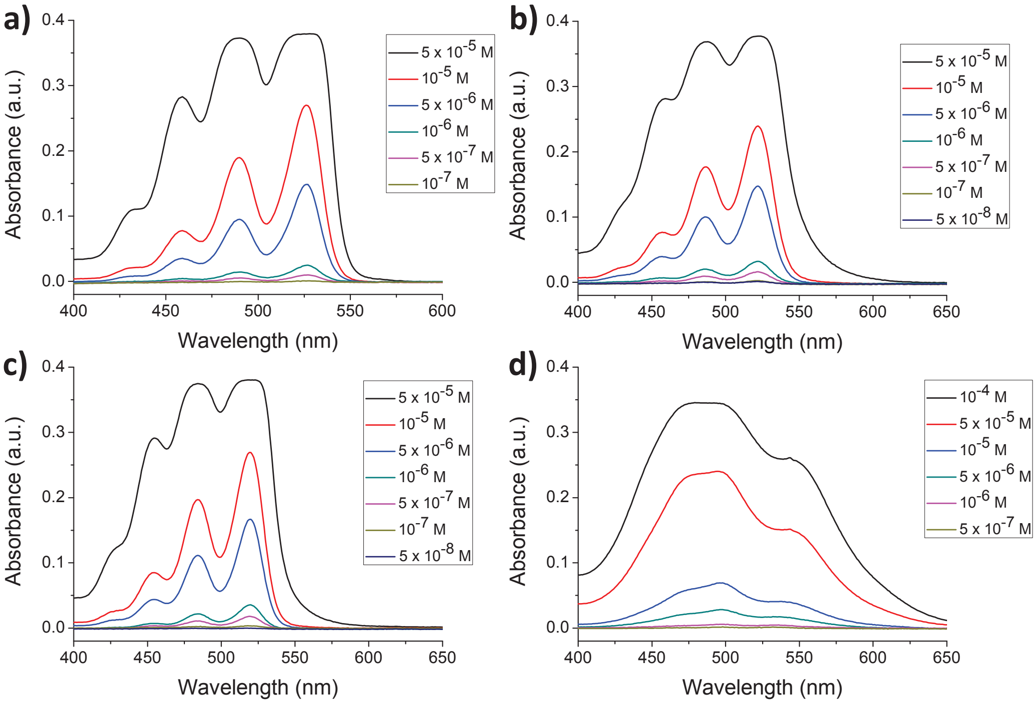

**Figure 125 |** a) UV-Vis spectra of a $CDCl_3$ solution of PBI-$PEG_{16}$ with concentrations ranging from $10^{-7}$ (light brown) up to 5 × $10^{-5}$ mol/L (black); b) UV-Vis spectra of a $CD_3OD$ solution of PBI-$PEG_{16}$ with concentrations ranging from 5 x $10^{-8}$ (dark blue) up to 5 × $10^{-5}$ mol/L (black); c) UV-Vis spectra of a $CD_3CN$ solution of PBI-$PEG_{16}$ with concentrations ranging from 5 x $10^{-8}$ (dark blue) up to 5 × $10^{-5}$ mol/L (black); d) UV-Vis spectra of a $D_2O$ solution of PBI-$PEG_{16}$ with concentrations ranging from 5 x $10^{-7}$ (light brown) up to $10^{-4}$ mol/L (black).

## c. Fluorescence experiments

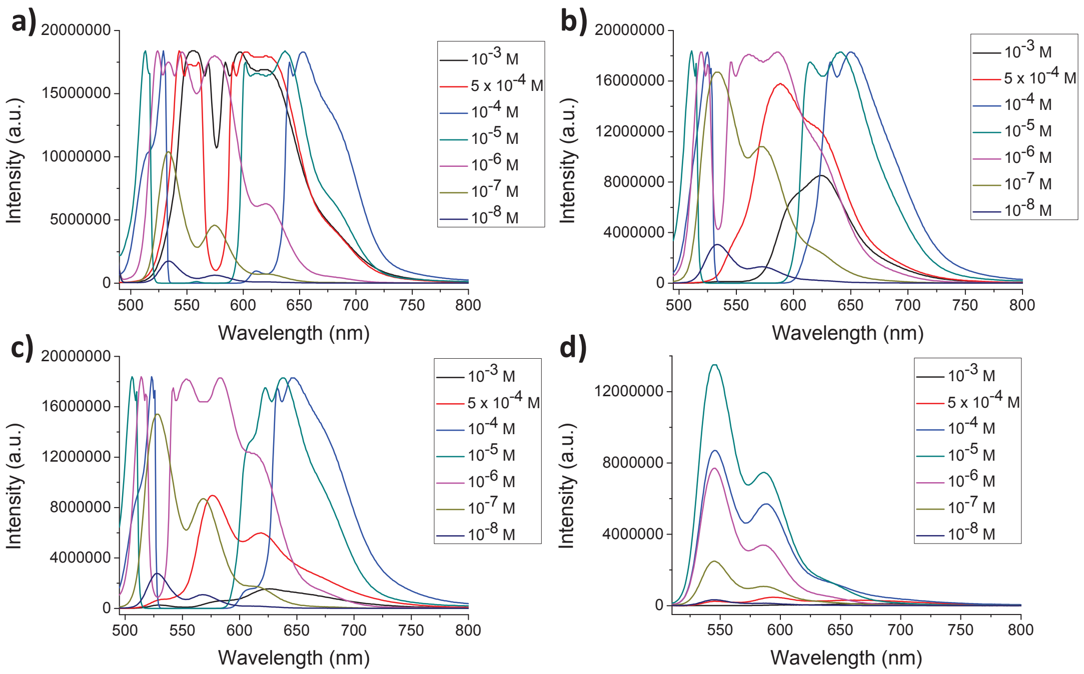

**Figure 126 |** a) Fluorescent spectra of PBI-PEG$_{16}$ in CDCl$_3$ for concentrations of $10^{-8}$ mol/L up to $10^{-3}$ mol/L (black), $\lambda_{ex}$=483 nm; b) Fluorescent spectra of PBI-PEG$_{16}$ in CD$_3$OD for concentrations of $10^{-8}$ mol/L up to $10^{-3}$ mol/L (black), $\lambda_{ex}$=483 nm; c) Fluorescent spectra of PBI-PEG$_{16}$ in CD$_3$CN for concentrations of $10^{-8}$ mol/L up to $10^{-3}$ mol/L (black), $\lambda_{ex}$=483 nm; d) Fluorescent spectra of PBI-PEG$_{16}$ in D$_2$O for concentrations of $10^{-8}$ mol/L up to $10^{-3}$ mol/L (black), $\lambda_{ex}$=498 nm.

## 4. Additional characterizations for compound 40

### a. UV-Vis experiments

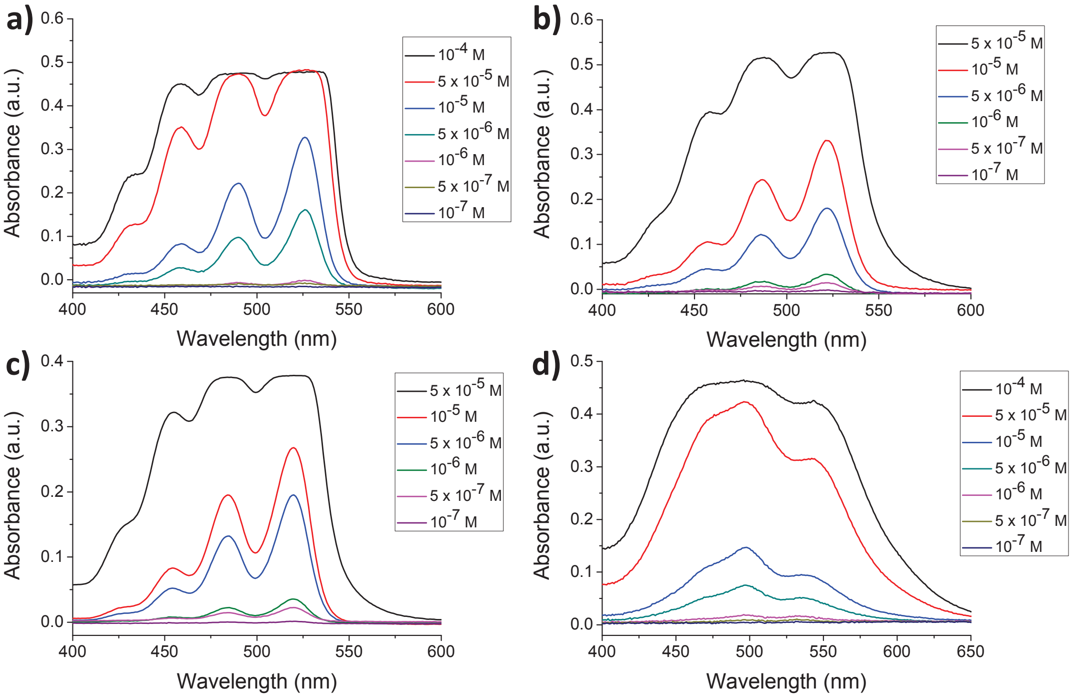

**Figure 127 |** a) UV-Vis spectra of a $CDCl_3$ solution of PBI-OPEG$_{16}$ with concentrations ranging from $10^{-7}$ (dark blue) up to $10^{-4}$ mol/L (black); b) UV-Vis spectra of a $CD_3OD$ solution of PBI-OPEG$_{16}$ with concentrations ranging from $10^{-7}$ (purple) up to 5 × $10^{-5}$ mol/L (black); c) UV-Vis spectra of a $CD_3CN$ solution of PBI-OPEG$_{16}$ with concentrations ranging from $10^{-7}$ (purple) up to 5 × $10^{-5}$ mol/L (black); d) UV-Vis spectra of a $D_2O$ solution of PBI-OPEG$_{16}$ with concentrations ranging from 5 x $10^{-7}$ (dark blue) up to $10^{-4}$ mol/L (black).

## b. Fluorescence experiments

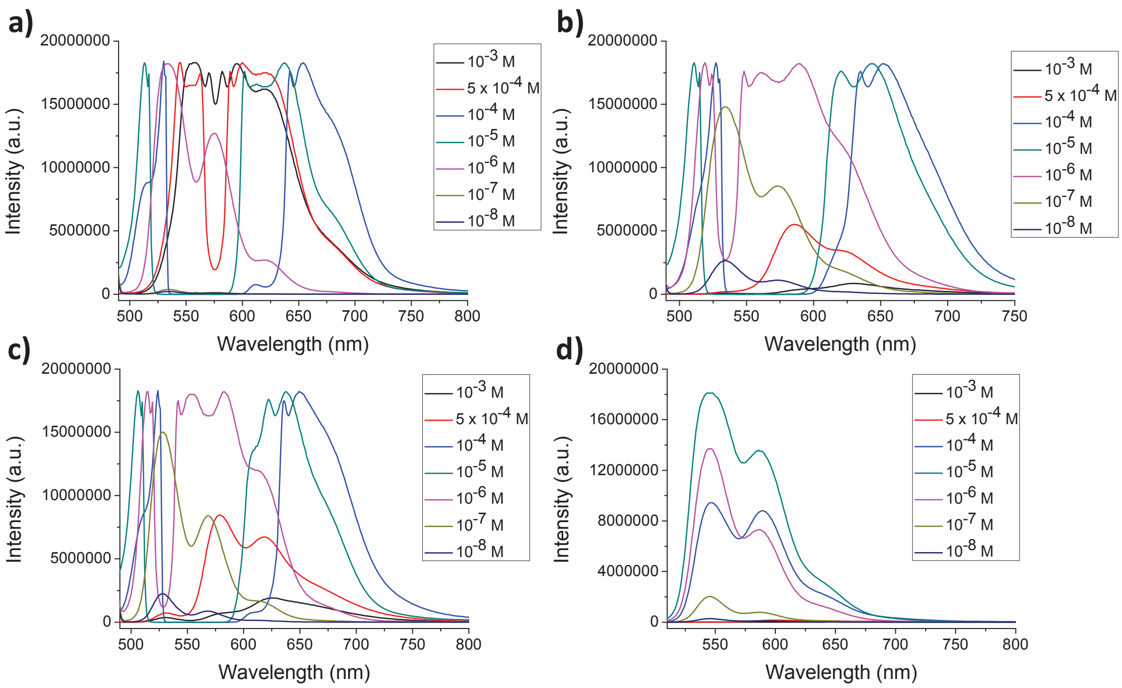

**Figure 128 |** a) Fluorescent spectra of PBI-OPEG$_{16}$ in $CDCl_3$ for concentrations of $10^{-8}$ mol/L up to $10^{-3}$ mol/L (black), $\lambda_{ex}$=483 nm; b) Fluorescent spectra of PBI-OPEG$_{16}$ in $CD_3OD$ for concentrations of $10^{-8}$ mol/L up to $10^{-3}$ mol/L (black), $\lambda_{ex}$=483 nm; c) Fluorescent spectra of PBI-OPEG$_{16}$ in $CD_3CN$ for concentrations of $10^{-8}$ mol/L up to $10^{-3}$ mol/L (black), $\lambda_{ex}$=483 nm; d) Fluorescent spectra of PBI-OPEG$_{16}$ in $D_2O$ for concentrations of $10^{-8}$ mol/L up to $10^{-3}$ mol/L (black), $\lambda_{ex}$=498 nm.

Yunjie XIANG

# Towards Multifunctional Supramolecular Copolymers

## Résumé

Le but de cette thèse était de comprendre l'organisation supramoléculaire et le possible réarrangement dynamique de copolymères supramoléculaires multifonctionnels. Ainsi, nous avons synthétisé diverses molécules présentant un cœur urée ou pérylène fonctionalisé par différentes chaines latérales afin de combiner des propriétés de structuration, de fluorescence et de bioreconnaissance dans une même chaine de polymère supramoléculaire. En combinant différentes techniques de spectroscopie, de diffusion du rayonnement et de microscopie, nous avons montré que des molécules avec un même cœur mais des chaines latérales différentes conduisaient à des nanostructures différentes comme des rubans vrillés, des plaques 2D ou encore des fibres branchées. Enfin, plusieurs unités monomériques avec un même cœur mais des chaines latérales différentes ont été mélangées pour former des copolymères supramoléculaires multifonctionnels. La formation préférentielle d'une nanostructure unique dictée par un des monomères a été démontrée selon un mécanisme de tri dit social (« social self-sorting »).

Chimie supramoléculaire, Auto-assemblage, Polymères supramoléculaires fonctionnels, Copolymères supramoléculaires multifonctionnels, Spectroscopies optiques, Microscopies, Diffusion du rayonnement, « Social Self-sorting ».

## Résumé en anglais

The goal of this thesis was to understand the supramolecular organization and the possible dynamic rearrangement of multifunctional supramolecular copolymers. To this end, we have developed a series of building blocks based on urea or perylene cores with various lateral side chains for combining structuring, fluorescence, and biorecognition properties in a single supramolecular polymer chain. Using a combination of spectroscopy, scattering, and microscopy techniques, we have shown that molecules with a same core but different lateral chains can lead to the formation of various nanostructures such as twisted ribbons, 2D plates, or branched fibers. Ultimately, by combining monomeric units with different functional side chains, multifunctional supramolecular copolymers have been obtained. Whereas radiation scattering and imaging techniques were used to demonstrate that one of the monomer can dictate the formation of a preferential nanostructure, optical spectroscopies revealed that the polymerization process of our systems indeed occurs via social self-sorting.

Supramolecular chemistry, Self-assembly, Functional supramolecular polymers, Multifunctional supramolecular copolymers, Optical Spectroscopies, Microscopies, Scattering techniques, Social self-sorting.